ESCOLA DE DOUTORAMENTO
INTERNACIONAL DA USC

Alessandra
Gioventù

Tese de doutoramento

Tests of Lepton Flavour Universality with Semileptonic D and B decays at the LHCb experiment

Santiago de Compostela, 2023

Programa de Doutoramento en Física Nuclear e de Partículas

TESE DE DOUTORAMENTO

TESTS OF LEPTON FLAVOUR UNIVERSALITY WITH SEMILEPTONIC D AND B DECAYS AT THE LHCB EXPERIMENT

Alessandra Gioventù

ESCOLA DE DOUTORAMENTO INTERNACIONAL DA UNIVERSIDADE DE SANTIAGO DE COMPOSTELA

PROGRAMA DE DOUTORAMENTO EN FÍSICA NUCLEAR E DE PARTÍCULAS

SANTIAGO DE COMPOSTELA

ANO 2023

DECLARACIÓN DO AUTOR/A DA TESE

D./Dna. **Alessandra Gioventù**

Título da tese: **Tests of Lepton Flavour Universality with Semileptonic D and B decays at the LHCb experiment**

Presento a miña tese, seguindo o procedemento axeitado ao Regulamento, e declaro que:

1) A tese abarca os resultados da elaboración do meu traballo.
2) De ser o caso, na tese faise referencia ás colaboracións que tivo este traballo.
3) Confirmo que a tese non incorre en ningún tipo de plaxio doutros autores nin de traballos presentados por min para a obtención doutros títulos.
4) A tese é a versión definitiva presentada para a súa defensa e coincide a versión impresa coa presentada en formato electrónico

E comprométome a presentar o Compromiso Documental de Supervisión no caso de que o orixinal non estea na Escola.

En **Santiago de Compostela**, **17 de Febreiro de 2023**.

Sinatura electrónica

AUTORIZACIÓN DO DIRECTOR/TITOR DA TESE

D./Dna. **Cibrán Santamarina Ríos**

En condición de: **Titor/a e director/a**

Título da tese: **Tests of Lepton Flavour Universality with Semileptonic D and B decays at the LHCb experiment**

INFORMA:

Que a presente tese, correspóndese co traballo realizado por D/Dna Alessandra Gioventù, baixo a miña dirección/titorización, e autorizo a súa presentación, considerando que reúne os requisitos esixidos no Regulamento de Estudos de Doutoramento da USC, e que como director/titor desta non incorre nas causas de abstención establecidas na Lei 40/2015.

En **Santiago de Compostela**, **17 de Febreiro de 2023**

Sinatura electrónica

AUTORIZACIÓN DO DIRECTOR/TITOR DA TESE

D./Dna. **Antonio Romero Vidal**

En condición de: **Director/a**

Título da tese: **Tests of Lepton Flavour Universality with Semileptonic D and B decays at the LHCb experiment**

INFORMA:

Que a presente tese, correspóndese co traballo realizado por D/Dna Alessandra Gioventù, baixo a miña dirección/titorización, e autorizo a súa presentación, considerando que reúne os requisitos esixidos no Regulamento de Estudos de Doutoramento da USC, e que como director/titor desta non incorre nas causas de abstención establecidas na Lei 40/2015.

En **Santiago de Compostela**, **17 de Febreiro de 2023**

Sinatura electrónica

Every new discovery is just a reminder:
we're all small and stupid.

Jobu Tupaki - "Everything Everywhere All at Once", D. Kwan and D. Scheinert (2022)

Acknowledgements

During these years I had the opportunity to meet and collaborate with people who inspire me everyday and whom I learned a lot from. I hope I am able to express all my gratitude in few words and not to miss anyone.

First of all, I would like to thank my supervisors, Cibrán and Antonio, for all their dedication to my professional and personal growth during these years. I'm also very grateful to Abraham for all the support and the insightful conversations. Thank you to all the LHCb group at IGFAE who welcomed and supported me since day one. Thank you to both seniors and juniors for always collaborate and participate.

I would also like to thank my fellow colleagues of the $R_{\mu/e}$ analysis, Adam, Lorenzo, Holly, Lucia and Federico for their help during all the analysis steps. Special thanks to Adam and for accepting to write the report for the International mention and to Lorenzo for also accepting to be in the thesis committee. Thanks should also go to Ricardo for bringing very good perspectives for the $R_{\mu/e}$ analysis and for the patience he had during his period here at IGFAE.

I would also like to thank the colleagues of the $R(D^{(*)0})$ analysis for their help during these years. Special thanks to all subgroup members of the hadronic $R(H_c)$ analyses subgroup, particularly to Guy, Donal and Olivier, for all the lively discussions from which I learned a lot and for the help in the development of the HLT2 lines for the LHCb Upgrade I. Thank you very much to Suzanne and Julián for their patience and their work as MiCo during the last two years and also to the other fellow developers from the SLB working group.

Besides, I would like to thank the Charm and SLB conveners for their comments who helped us improve both analyses and for their endorsement when I applied to conferences. Hoping to not forget anyone, thanks to: Michael, Dominik, Marianna, Lucia, Greg, Michel, Marcello, Marta, Donal and Anna. I also would like to thank all the LHCb collaborators I had the pleasure to meet during Collaboration weeks and conferences. Special thanks to Carla who accepted to be in my thesis committee.

I also would like to thank the people from the LHCb Bologna group, Vincenzo, Angelo and Fabio. They introduced me to flavour physics and the LHCb experiment, guided me during my master thesis preparation and welcomed me for a two week stay in 2021. Thank you for your support and patience. Thank you also to the former Bologna people Serena, Lorenzo and Federico, without your company the stay at CERN wouldn't be so good.

I thank the financial support provided by the "Programa de ayuda para contratos predoctorales para la formacon de doctores", of the "Ministerio de Universidades", which founded my contract at USC and my stay at CERN in 2021. Thank also to thank the IFGAE for founding my first years of PhD and my stay in Bologna with the "2021 IGFAE call for Travels and Visitors grant".

Para los agradecimientos más personales, quiero utilizar una mezcla entre castellano

e italiano, para ser coherente con mi manera de hablar los idiomas ibéricos y pido perdón preventivamente por las tildes perdidas. Primero agradezco muchísimo haber empezado esta aventura hace 4 años sin saber qué esperarme. Gracias Santiago por acogerme como una hija y por hacerme conocer mi segunda familia y una cultura nueva que me enriquece cada día más.

Mil gracias a mis compañerxs de aventura Óscar, Julián y Bea por todo y para empezar*a minha familia galega*. Gracias a María por toda la ayuda durante mis primeros meses y más adelante, a Vero por hacer cada día más soleado, a Saúl, Arnau, Juan y Carlos por las conversaciones, y a los del 26 por las locuras. Gracias a los compis del piso de Saint Genis con lxs que compartí la vida de CERN.

Gracias a toda mi red afectiva expandida entre Santiago, Cattolica, Bologna y Ginebra por ayudarme a encontrar mi equilibrio entre el trabajo y la vida misma y por seguirme en todas mis ideas, también las más locas. In ordine random (e dimenticandomi sicuramente di qualcuno): Delby, Pit, Marina, Octavio, Sunny, Silvia, Ghita, Jess, Uxi, Alex, Susana, Luisa, Bea, Arnau, Antía, Tomás, Serena, Federico, Michela, Lorena, Giulia, Vale, Pindi, Miguel, Gela, Irene... Os quiero. Quería agradecer también Mercè y lxs compañerxs de circo, porque me ayudaron a aprender que también yo puedo volar.

Infine, però non per questo meno importante, vorrei ringraziare la mia famiglia. Vorrei ringraziare soprattutto i miei genitori Manuela e Bruno, che, siano 0, 1718 km o 5125.05 km i chilometri di distanza, mi sono sempre accanto. Vi voglio bene. Alessandra

Abstract

In The Standard Model of particle physics (SM), the coupling between the leptons and the gauge bosons is independent of the lepton generation. This SM feature is called Lepton Flavour Universality (LFU) and finding processes that violate it could be a sign of new physics (NP). Recent experimental results on LFU tests with $b \to c\ell\nu_\ell$ and $b \to s\ell\ell$ transitions show a tension from the theoretical predictions. This thesis aims to test LFU by studying two different processes involving D and B meson decays and using data recorded by the LHCb experiment.

The LHCb experiment is dedicated to perform heavy flavour physics measurements and it is an excellent place to search for indirect evidences of NP. The LHCb experiment collected data from proton-proton collisions in two runs, Run 1 (2010-2012) and Run 2 (2015-2018). The combination of the two data samples corresponds to an integrated luminosity of 9 fb^{-1}. The LHCb Upgrade I detector started to take data in 2022, aiming to record an integrated luminosity of 50 fb^{-1} (300 fb^{-1}) by the end of 2030 (2040). It is programmed to run at an instantaneous luminosity of 2×10^{33} cm^2 s^{-1}, implying a higher multiplicity of inelastic pp collisions. The LHCb Upgrade I features a fully software-based trigger system, making software development and trigger line migration crucial. In this thesis, aiming to optimise LFU studies in $H_b \to H_c\tau^+\nu_\tau$ decays, where the τ lepton is reconstructed by its $\tau^+ \to \pi^+\pi^-\pi^+\overline{\nu}_\tau$ decay and H_b (H_c) is a b-(c-) hadron, trigger lines for these processes are implemented.

The goal of the first LFU test is to measure the branching fraction ratio $R_{\mu/e}$, defined as $R_{\mu/e} = \mathcal{B}(D^0 \to K^-\mu^+\nu_\mu)/\mathcal{B}(D^0 \to K^-e^+\nu_e)$. D^0 candidates are selected from $D^{*+} \to D^0\pi^+$ decays and the undetected neutrino is accounted for using two reconstruction methods. The value of $R_{\mu/e}$ is obtained as the ratio of the signal $D^0 \to K^-\ell^+\nu_\ell$ decays multiplied by their respective efficiencies. The value of $R_{\mu/e}$ is blinded, resulting in $x.xxx \pm 0.003 \pm 0.013$, where the first uncertainty is due to statistics and the second contribution is an estimation of the systematic uncertainty.

The second study aims to test LFU considering $B^- \to D^{(*)0}\tau^-\overline{\nu}_\tau$ decays, where the τ is reconstructed using $\tau^+ \to \pi^+\pi^-\pi^+\overline{\nu}_\tau$ decays. The observables sensitive to LFU $R(D^0)$ and $R(D^{*0})$, defined as $R(D^{(*)0}) = \mathcal{B}(B^- \to D^{(*)0}\tau^-\overline{\nu}_\tau)/\mathcal{B}(B^- \to D^{(*)0}\ell^-\overline{\nu}_\ell)$, are measured simultaneously. To select signal candidates, it is of paramount importance to model the main background contributions. These are due to doubly-charmed decays, $B \to DDX$, where a D_s^+, a D^+ or a D^0 meson decays inclusively into 3 pions. In this thesis, a model to control inclusive $D_s^+ \to \pi^+\pi^-\pi^+(X)$ decays is implemented. This is a reweighting procedure to correct the simulation accounting for the main $D_s^+ \to \pi^+\pi^-\pi^+(X)$ decay modes. The relative branching fractions obtained from the model agree with the

PDG [1] within uncertainties. Finally, the blinded results for $R(D^0)$ and $R(D^{*0})$ are respectively $x.xx \pm 0.093 \pm 0.034\%$ and $x.xx \pm 0.024 \pm 0.029\%$, where the first contribution to the uncertainty is due to statistics and the second is the systematic uncertainty.

This thesis is structured as follows. The **introduction** is reported in Ch. 1. The **hypotheses** are reported in detail in Ch. 2, which reports the theoretical principles, and in Ch. 3, which reports the current experimental status. The **objectives**, **methodology** and **results** of the thesis are addressed in the specific sections of the analyses chapters, Ch. 5 and 6. For the the $D^0 \to K^-\ell^+\nu_\ell$ analysis the objectives and methodology are reported in Sec. 5.1 and the results are reported in Sec. 5.9, while for the $R(D^{(*)0})$ the objectives and methodology are in Sec. 6.1 and the results in Sec. 6.11. Besides, the description of the LHCb detector and how its data are recorded is reported in Ch. 4. The LHCb Upgrade I detector description and the trigger selection for the upgrade are reported in Ch. 7. Finally, the thesis **conclusions** are reported in Ch. 8 and the **thesis summary in Galician** in Appendix C. All the abbreviations and acronyms used throughout this thesis are listed after the lists of figures and tables. Finally, at the end of the document the **bibliography** is reported.

Resumo

No Modelo Estándar de Física de Partículas (SM) o acoplamento entre os leptóns e os bosóns *gauge* é independente da xeración á que pertencen os leptóns. Esta característica do SM chámase Universalidade Leptónica de Sabor (LFU) e atopar procesos que a infrinxan podería ser un sinal de nova física (NP). Os resultados experimentais recentes en probas de LFU con transicións $b \to c\ell\nu_\ell$ e $b \to s\ell\ell$ mostran unha tensión coas predicións teóricas. Esta tese pretende probar LFU estudando dous procesos diferentes que implican desintegracións de mesóns D e B, utilizando os datos tomados polo experimento LHCb do CERN.

O experimento LHCb está deseñado para realizar medicións de partículas pesadas e é un excelente lugar para buscar evidencias indirectas de NP. O experimento recolleu datos de colisións protón-protón en dúas etapas, Run 1 (2010-2012) e Run 2 (2015-2018). A combinación das dúas mostras de datos corresponde a unha luminosidade integrada de 9 fb^{-1}. O detector LHCb Upgrade I comezou a tomar datos en 2022, co obxectivo de acumular unha luminosidade integrada de 50 fb^{-1} (300 fb^{-1}) para finais de 2030 (2040). O detector está programado para funcionar cunha luminosidade instantánea de $2 \times 10^{33}\ \text{cm}^2\,\text{s}^{-1}$, o que implica unha maior multiplicidade das colisións inelásticas de pp. O LHCb Upgrade I presenta un sistema de *trigger* totalmente baseado en *software*, o que fai que o desenvolvemento do mesmo e o deseño das liñas de *trigger* sexan cruciais. Nesta tese, co obxectivo de optimizar os estudos de LFU en desintegracións $H_b \to H_c\tau^+\nu_\tau$, onde o τ lepton é reconstruído pola súa desintegración $\tau^+ \to \pi^+\pi^-\pi^+\overline{\nu}_\tau$ e H_b (H_c) é un hadrón con un quark b (c), propóñense e desenvólvense liñas de *trigger* para estes procesos.

O obxectivo da primeira proba de LFU desta tese é medir a razón de fracción de ramificación $R_{\mu/e}$, definida como $R_{\mu/e} = \mathcal{B}(D^0 \to K^-\mu^+\nu_\mu)/\mathcal{B}(D^0 \to K^-e^+\nu_e)$. Os candidatos D^0 son seleccionados de desintegracións de $D^{*+} \to D^0\pi^+$ e o neutrino non detectado é contabilizado mediante dous métodos de reconstrución independentes. O valor de $R_{\mu/e}$ obtense como a relación entre o numero das dúas canles de sinal $D^0 \to K^-\ell^+\nu_\ell$ multiplicados polas súas respectivas eficiencias. O valor de $R_{\mu/e}$ está cegado e resulta en $x.xxx \pm 0,003 \pm 0,013$, onde a primeira incerteza é de natureza estatística e a segunda é unha estimación dos efectos sistemáticos.

O segundo estudo ten como obxectivo probar LFU tendo en conta as desintegracións $B \to D^{(*)0}\tau^+\nu_\tau$, onde o τ é reconstruído empregando desintegracións $\tau^+ \to \pi^+\pi^-\pi^+\overline{\nu}_\tau$. Os observables sensibles a LFU son as razóns de fraccións de ramificación $R(\overline{D}^0)$ e $R(\overline{D}^{*0})$, definidas como $R(D^{(*)0}) = \mathcal{B}(B \to \bar{D}^{(*)0}\tau^+\nu_\tau)/\ \mathcal{B}(B \to \bar{D}^{(*)0}\ell^+\nu_\ell)$. Estas mídense simultáneamente. Para separar os decaimentos do sinal é de suma importancia modelar as principais contribucións de fondo. Estas débense a desintegracións dobremente encan-

tadas, onde un mesón D_s^+, un D^+ ou un D^0 decae no vértice de desintegración 3π. Nesta tese, proponse un modelo para controlar os decaementos inclusivos $D_s^+ \to \pi^+\pi^-\pi^+(X)$. Este é un procedemento de reponderación para corrixir os eventos de simulación polos principais modos de decaimento $D_s^+ \to \pi^+\pi^-\pi^+(X)$. As fraccións de ramificación relativas obtidas do modelo concordan co PDG [1] dentro das súas incertezas. Finalmente, os resultados cegados para $R(D^0)$ e $R(D^{*0})$ son, respectivamente, $x.xx \pm 0.093 \pm 0.034\%$ e $x.xx \pm 0.024 \pm 0.029\%$, onde a primeira contribución á incerteza é debido á estatística e a segunda é a incerteza sistemática.

Esta tese estrutúrase do seguinte xeito. A **introdución** aparece en Capítulo 1. As **hipóteses** infórmanse en detalle no Capítulo 2, que informa dos principios teóricos, e en Capítulo 3, que informa do estado experimental actual. Os **obxectivos**, a **metodoloxía** e os **resultados** da tese abórdanse nas seccións específicas dos capítulos de análise, Capítulo 5 e Capítulo 6. Para a análise dos decaementos $D^0 \to K^-\ell^+\nu_\ell$, os obxectivos e a metodoloxía indícanse en Sección 5.1 e a os resultados aparecen en Sección 5.9, mentres que para o $R(D^{(*)0})$ os obxectivos e a metodoloxía están en Sección 6.1 e os resultados en Sección 6.11. Ademais, a descrición do detector LHCb e como se rexistran os seus datos indícase en Capítulo 4. Os detalles do detector LHCb Upgrade I e a selección do *trigger* para a actualización do detector infórmanse en Capítulo 7. Finalmente, as **conclusións** da tese aparecen en Capítulo 8 e o **resumo da tese en galego** no Apéndice C. Todas as abreviaturas e acrónimos empregados ao longo desta tese están listados no despois das listas de figuras e táboas. Finalmente, ao final do documento infórmase da **bibliografía**.

Resumen

En el Modelo Estándar de la física de partículas (SM), el acoplamiento entre los leptones y los bosones de gauge es independiente de la generación de leptones. Esta característica del SM se denomina Universalidad del Sabor del Leptón (LFU) y encontrar procesos que la violen podría ser una señal de nueva física (NP). Resultados experimentales recientes sobre pruebas de LFU con transiciones $b \to c\ell\nu_\ell$ y $b \to s\ell\ell$ muestran una tensión respecto a las predicciones teóricas. Esta tesis pretende probar LFU estudiando dos procesos diferentes que implican decaimientos de mesones D y B, utilizando datos registrados por el experimento LHCb.

El experimento LHCb se dedica a realizar medidas de física de sabores pesados y es un lugar excelente para buscar evidencias indirectas de NP. El experimento LHCb recogió datos de colisiones protón-protón en dos tomas, Run 1 (2010-2012) y Run 2 (2015-2018). La combinación de las dos muestras de datos corresponde a una luminosidad integrada de 9 fb^{-1}. El detector LHCb Upgrade I comenzó a tomar datos en 2022, con el objetivo de registrar una luminosidad integrada de 50 fb^{-1} (300 fb^{-1}) a finales de 2030 (2040). Está programado para funcionar a una luminosidad instantánea de 2×10^{33} $\text{cm}^2\,\text{s}^{-1}$, lo que implica una mayor multiplicidad de colisiones pp inelásticas. El LHCb Upgrade I un sistema de *trigger* totalmente basado en software, por lo que el desarrollo de software y la migración de la línea de *trigger* son cruciales. En esta tesis, con el objetivo de optimizar los estudios de LFU en decaimientos $H_b \to H_c\tau^+\nu_\tau$, donde el leptón τ es reconstruido por su decaimiento $\tau^+ \to \pi^+\pi^-\pi^+\overline{\nu}_\tau$ y H_b (H_c) es un hadrón con un quark b (c), se implementan líneas de *trigger* para estos procesos.

El objetivo de la primera prueba LFU es medir el ratio de fracción de ramificación $R_{\mu/e}$, definido como $R_{\mu/e} = \mathcal{B}(D^0 \to K^-\mu^+\nu_\mu)/\mathcal{B}(D^0 \to K^-e^+\nu_e)$. Los candidatos D^0 se seleccionan a partir de las desintegraciones $D^{*+} \to D^0\pi^+$ y el neutrino no detectado se contabiliza utilizando dos métodos de reconstrucción independientes. El valor de $R_{\mu/e}$ se obtiene como el cociente entre el numero de eventos de las desintegraciones de señal $D^0 \to K^-\ell^+\nu_\ell$ multiplicado por sus respectivas eficiencias. El valor de $R_{\mu/e}$ se ciega, resultando $x.xxx \pm 0.003 \pm 0.013$, donde la primera incertidumbre se debe a la estadística y la segunda contribución es una estimación de la incertidumbre sistemática.

El segundo estudio pretende probar la LFU considerando las desintegraciones $B \to D^{(*)0}\tau^+\nu_\tau$, donde el τ se reconstruye usando desintegraciones $\tau^+ \to \pi^+\pi^-\pi^+\overline{\nu}_\tau$. Los observables sensibles a LFU $R(\overline{D}^0)$ y $R(\overline{D}^{*0})$, definidos como la razón de fracciones de ramificación $R(D^{(*)0}) = \mathcal{B}(B \to \bar{D}^{(*)0}\tau^+\nu_\tau)/\ \mathcal{B}(B \to \bar{D}^{(*)0}\ell^+\nu_\ell)$, se miden simultáneamente. Para separar las desintegraciones de señal, es de vital importancia modelar las principales contribuciones de fondo. Éstas se deben a desintegraciones doblemente encantadas, en las

que un mesón D_s^+, D^+ o D^0 desintegra en el vértice de desintegración 3π. En esta tesis se implementa un modelo para controlar las desintegraciones inclusivas $D_s^+ \to \pi^+\pi^-\pi^+(X)$. Se trata de un procedimiento de reponderación para corregir la simulación teniendo en cuenta los principales modos de desintegración $D_s^+ \to \pi^+\pi^-\pi^+(X)$. Las fracciones de bifurcación relativas obtenidas a partir del modelo concuerdan con la PDG [1] dentro de las incertidumbres. Finalmente, los resultados ciegos para $R(D^0)$ y $R(D^{*0})$ son respectivamente $x.xx \pm 0.093 \pm 0.034\%$ y $x.xx \pm 0.024 \pm 0.029\%$, donde la primera contribución a la incertidumbre es debida a la estadística y la segunda es la incertidumbre sistemática.

Este tesis está estructurada como sigue. La **introducción** se encuentra en el Capítulo 1. Las **hipótesis** se detallan en el Capítulo 2, donde se presentan los principios teóricos, y en el Capítulo 3, donde se informa del actual estado de los resultados experimentales. Los **objetivos**, la **metodología** y los **resultados** de la tesis se abordan en las secciones específicas de los capítulos de análisis, Capítulo 5 y 6. Para el análisis de $D^0 \to K^-\ell^+\nu_\ell$, los objetivos y metodología del análisis se informan en la Sección 6.1.1 y los resultados en Sección 5.9; mientras que para el analálisis de $R(D^{(*)0})$ los objetivos y metodología se enforman en la Sección 6.1 y los en la Sección 6.11. La descripción del detector LHCb Upgrade I y la selección del trigger para la actualización se reportan en el Capítulo 4 y la selección del *trigger* para la actualización se reportan en en el Capítulo 7. Finalmente, las **conclusiones** de la tesis se informan en el Capítulo 8 y el **resumen de la tesis en gallego** se encuentra en el Apéndice C. Todas las abreviaturas y acrónimos utilizados a lo largo de esta tesis se listan en la sección siguiente a las listas de figuras y tablas. Finalmente, en la sección final del documento se informa la **bibliografía**.

Index

1

Introduction

Lepton Flavour Universality (LFU) is a key feature of the Standard Model (SM) of particle physics. It states that the coupling between leptons and gauge bosons is independent of the lepton generation. Many new physics scenarios predict the violation of LFU, therefore testing it is a powerful probe of the SM.

The LHCb experiment has proven to be a valuable tool for searching for new physics. LHCb has collected data corresponding to an integrated luminosity of 9 fb^{-1} in its first two data-taking periods, since 2010 until 2018. The upgraded detector, LHCb Upgrade I, started operating in 2022 and is planned to reach an integrated luminosity of ~ 300 fb^{-1} by the end of $\sim$ 2040. One of the main changes in the Upgrade I is the introduction of a full software-based trigger system. Therefore, the software development and the migration of the trigger lines to the new framework is of high importance. In this thesis, the development of the lines for $H_b \to H_c \tau \nu_\tau$ decays is presented, where H_b and H_c are a b- and c-hadrons, and the τ is reconstructed with the 3-prong $\tau^+ \to \pi^+\pi^-\pi^+\overline{\nu}_\tau$ final state.

This thesis focuses on two LHCb data analyses testing LFU in semileptonic decays of B and D mesons. The first analysis aims to test LFU by measuring the branching fraction ratio $R_{\mu/e}$ using $D^0 \to K^-\ell^+\nu_\ell$ decays, the first LFU test in the charm sector at a hadron collider. The second analysis is a simultaneous measurement of the observables $R(D^0)$ and $R(D^{*0})$ using $B^+ \to \overline{D}^{(*)0}\tau^+\nu_\tau$ decays, where the τ candidates are selected using the $\tau^+ \to \pi^+\pi^-\pi^+\overline{\nu}_\tau$ decay, namely 3-prong. The main contribution of this thesis to the analysis of $R(D^{(*)0})$ is a model to control the background contributions from inclusive $D_s^+ \to \pi^+\pi^-\pi^+(X)$ decays. In fact, the major sources of background in this analysis are due to D_s^+ decays: doubly-charmed $B \to \overline{D}^0 D_s^{(*)+}(X)$ and $D_s^+ \to \pi^+\pi^-\pi^+(X)$ decays.

Besides, understanding the relative contributions of inclusive decays of the D_s^+ meson is crucial for other $R(H_c)$ analyses.

This thesis is structured as follows. The theoretical principles at the basis of this study are reported in Chap. 2, while the current experimental status is presented in Ch. 3. In Ch. 4, the LHC is described, focusing on the LHCb experiment and its operation. The test of LFU using $D^0 \to K^-\ell^+\nu_\ell$ decays is reported in Ch. 5 and the one with $B^+ \to \overline{D}^{(*)0}\tau^+\nu_\tau$ decays in Ch. 6. The Run 3 trigger lines for $H_b \to H_c\tau\nu_\tau$ decays, with 3-prong τ decays, are discussed in Ch. 7 together with the description of the LHCb Upgrade I detector. The conclusions and the prospects for future measurements are collected in Ch. 8. Additional material is presented in App. A and B for the $R_{\mu/e}$ and $R(D^{(*)0})$ measurements, respectively.

2

Theoretical and phenomenological motivation

In this chapter, an overview of the theoretical principles that are the base of this thesis is presented. The fundamental elements of the Standard Model (SM) of particle physics are introduced in Sec. 2.1. Special emphasis is put in the concept of Lepton Flavour Universality (LFU), introduced in Sec. 2.2. The phenomenology of the $D^0 \to K^-\ell^+\nu_\ell$ and $\overline{B} \to D^*\ell^-\overline{\nu}_\ell$ decays, where ℓ represents a charged lepton, is presented in Secs. 2.2.3 and 2.2.4, respectively.

2.1 The Standard Model of particle physics

The SM is the theoretical model describing the dynamics of the fundamental constituents of the Universe, the elementary particles, and their fundamental interactions, *i.e.* the *forces*, with the exception of gravity. The SM is a quantum field theory (QFT) defining particles (fields) by their interactions (couplings) with each other and their quantum numbers, such as charge, colour, flavour, spin, etc. Fundamental particles are differentiated in two groups: fermions and bosons.

- **Bosons** have an integer spin and follow the Bose-Einstein statistics. The dynamics of a boson field $\psi(x)$ are based on the Klein-Gordon equation[1],

$$(\partial_\mu \partial^\mu + m^2)\psi(x) = 0, \tag{2.1}$$

[1] In this document natural units, with $c = 1$, are considered.

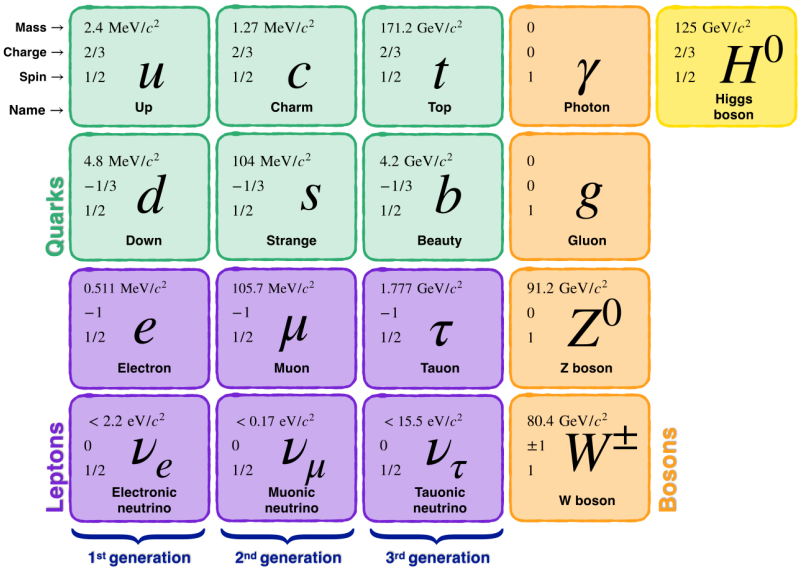

Figure 2.1: Scheme of Standard Model particles. For each particle the mass, the electric charge and the spin values are reported [1].

where the index μ accounts for the four x^μ space-time coordinates and m is the mass of the spin 1 ($S = 1$) particle. In the SM, bosons with $S = 1$, such as the photon γ, $W^\pm$ and Z, represent the mediators of the forces and are shown in orange in Fig. 2.1. The Higgs boson H^0, with $S = 0$ and shown in the yellow block of Fig. 2.1, is associated with the spontaneous symmetry breaking mechanism (SSB) that gives mass to the particles, described in Sec. 2.1.1.1.

- **Fermions** have semi-integer spin and obey to Fermi-Dirac statistics. The dynamics of fermions with $S = 1/2$ is described by the Dirac equation

$$(i\gamma^\mu \partial_\mu - m)\psi(x) = 0, \tag{2.2}$$

where γ^μ are the Dirac matrices, ∂^μ the partial derivative with respect to the μ-coordinate. Matter and antimatter particles are defined by positive and negative energy solutions to the Dirac equation, respectively. In total, in the SM, there are 12 fermions and 12 antifermions, with spin 1/2. These are organised in three families or generations, visible in the columns of Fig. 2.1. The first generation of fermions consists of the u and d quarks, the electron e and the electron neutrino ν_e. These are basic constituents of the stable matter surrounding us (protons and neutrons). Particles from the second and third generations have the same properties of their first generation correspondents but they have increasingly higher mass. This rule is valid for quarks and charged leptons, because the SM assumes that neutrinos are massless.

Fermions are further organised in quarks and leptons, represented by the green and purple blocks of Fig. 2.1 respectively. Leptons (e, μ, τ) and the three respective neutrinos (ν_e, ν_μ and ν_τ) interact only via electroweak force. The six quarks, u, d, s, c, b and t, interact also via the strong force. Quarks combine to create composite particles, named hadrons. These take different names, based on their composition: mesons ($q\overline{q}$), baryons (qqq), tetraquarks ($qq\overline{qq}$) [2] or pentaquarks ($qqqq\overline{q}$) [3], where q ($\overline{q}$) indicates any of the six quark (antiquark) flavours, and not necessarily the same when repeated.

The SM is described by a Lagrangian density $\mathcal{L}_{SM}$ invariant under non-abelian local gauge transformations. The local gauge symmetry group for the SM is

$$\mathcal{G}_{SM} = \mathrm{SU}(3)_C \times \mathrm{SU}(2)_L \times \mathrm{U}(1)_Y. \tag{2.3}$$

The $\mathrm{SU}(3)_C$ group corresponds to strong nuclear interactions, being C the colour charge of the strong interaction. This is called quantum chromodynamics and its Lagrangian is denoted as $\mathcal{L}_{\mathrm{QCD}}$. The $\mathrm{SU}(2)_L \times \mathrm{U}(1)_Y$ symmetry group is the base of the Glashow-Weinberg-Salam model (GWS) [4–6], describing electroweak interactions, where Y is the hypercharge of the electromagnetic group and L denotes the left chirality of the weak force. In general, properties of fundamental interactions between elementary particles arise from symmetry features. For example, one of the reasons of the presence of only left chirality in weak interactions comes from parity violation [7].

In the Lagrangian formalism, $\mathcal{L}_{SM}$ can be split into two terms: the interaction term $\mathcal{L}_I$ and the non-interacting or free particle term $\mathcal{L}_0$:

$$\mathcal{L} = \mathcal{L}_0 + \mathcal{L}_I. \tag{2.4}$$

By applying the least action to the free Lagrangian $S_0 = \int \mathrm{d}x^4 \mathcal{L}_0$, it is possible to obtain the free particle equations for quarks and leptons, Eqs. (2.1) and (2.2), respectively. Generally, the effect of the interaction term in decay processes is evaluated perturbatively.

2.1.1 Electroweak interactions

Electroweak interactions are described by the Glashow-Weinberg-Salam model (GWS), which is based on the $\mathrm{SU}(2)_L \times \mathrm{U}(1)_Y$ symmetry group. Its Lagrangian, $\mathcal{L}_{\mathrm{GWS}}$, can be divided in four components:

$$\mathcal{L}_{\mathrm{GWS}} = \mathcal{L}_B + \mathcal{L}_f + \mathcal{L}_H + \mathcal{L}_Y, \tag{2.5}$$

where the first term is relative to the kinetic energies and self-interactions of bosons ($\mathcal{L}_B$), the second, $\mathcal{L}_f$, to the kinetic energy of the fermions and their coupling with the boson fields. Then, the $\mathcal{L}_H$ term concerns the masses couplings between the gauge bosons $W^\pm$, Z, γ and the Higgs boson, H^0, and $\mathcal{L}_Y$ describes the leptons and quarks masses and couplings. The kinematics of the gauge bosons is described by the term $\mathcal{L}_B$. Being $B_{\mu\nu}$

the boson field tensor and $W^{a\mu\nu}$ the weak isospin field tensor, with $a = 1,\ 2,\ 3$, the Lagrangian $\mathcal{L}_B$ can be written as

$$\mathcal{L}_B = -\frac{1}{4}W^{a\mu\nu}W^a_{\mu\nu} - \frac{1}{4}B^{\mu\nu}B_{\mu\nu}. \tag{2.6}$$

The second term of the $\mathcal{L}_{\text{GWS}}$ Lagrangian, $\mathcal{L}_f$, describes the kinematics of the fermions and their interaction with the gauge bosons. Assuming a sum over j generations when the index is repeated, $\mathcal{L}_f$ is given by

$$\mathcal{L}_f = \bar{Q}^j i\not{D}_L Q^j + \overline{u}^j_R i\not{D}_R u^j_R + \overline{d}^j_R i\not{D}_R d^j_R + \bar{L}^j i\not{D}_L L^j + \bar{e}^j_R i\not{D}_R e^j_R, \tag{2.7}$$

where $\not{D} \equiv \gamma^\mu D_\mu$ is the contracted form of the covariant derivatives D_μ. Fermions are represented by the right-handed singlets u_R and d_R for up- and down-type quarks and e_R for leptons, with isospin $T = 0$, and the left-handed doublets Q^j and L^j. These have $T = 1/2$ and the third component $T_3 = \pm 1/2$ for up and down-type fields, respectively, and can be written as

$$Q^j_L = P_L Q^j = \begin{pmatrix} u^j \\ d^j \end{pmatrix}_L \quad \text{and} \tag{2.8}$$

$$L^j_L = P_L L^j = \begin{pmatrix} \nu^j \\ e^j \end{pmatrix}_L, \tag{2.9}$$

where $P_{L,R} = (1 \mp \gamma_5)/2$ is the left (right) parity projector. The covariant derivatives $D_{L\mu}$ and $D_{R\mu}$ of Eq. (2.7) are defined as

$$D_{L\mu} = \partial_\mu + igW^a_\mu \frac{\sigma^a}{2} + ig'\frac{Y}{2}B_\mu, \tag{2.10}$$

$$D_{R\mu} = \partial_\mu + ig'\frac{Y}{2}B_\mu, \tag{2.11}$$

where σ^a are the Pauli matrices, and g and g' are the coupling constants. The electromagnetic charge Q of a field can be defined as a function of the hypercharge Y and the third coordinate of the weak isospin T_3:

$$Q = \frac{Y}{2} + T_3. \tag{2.12}$$

From this definition it is possible to obtain the values of the hypercharges of all fermionic doublets and singlets according to their electromagnetic charge, collected in Tab. 2.1.

The third term in $\mathcal{L}_{\text{GWS}}$ is the Higgs Lagrangian $\mathcal{L}_H$, describing the Higgs field and its coupling with the electroweak bosons:

$$\begin{aligned} \mathcal{L}_H &= (D^\mu\Phi^\dagger)(D_\mu\Phi) - V(\Phi^\dagger\Phi) \\ &= (D^\mu\Phi^\dagger)(D_\mu\Phi) - \left(-\mu^2\Phi^\dagger\Phi + \frac{\lambda^2}{2}(\Phi^\dagger\Phi)^2\right), \end{aligned} \tag{2.13}$$

f	T_3	Y	Q
u_L	$1/2$	$1/3$	$2/3$
d_L	$-1/2$	$1/3$	$-1/3$
u_R	0	$4/3$	$2/3$
d_R	0	$-2/3$	$-1/3$
ν_L	$1/2$	-1	0
e_L	$-1/2$	-1	-1
e_R	0	-2	-1

Table 2.1: Quantum numbers for each fermion. The third component of the weak isospin T_3, the hypercharge Y and electromagnetic charge Q are represented.

where λ and μ are real parameters and Φ is the Higgs SU(2) doublet, with hypercharge 1,

$$\Phi = \begin{pmatrix} \phi^+ \\ \phi^0 \end{pmatrix} , \tag{2.14}$$

where the two components have different electromagnetic charges. It follows that the covariant derivative operating on ϕ^+ is the left-handed,

$$D_\mu = \partial_\mu + igW_\mu^a \frac{\sigma^a}{2} + ig' \frac{Y}{2} B_\mu. \tag{2.15}$$

The last term of the GWS model Lagrangian, $\mathcal{L}_Y$, concerns Yukawa interactions between the fermion fields and the Higgs doublet Φ. Assuming again a sum over repeated indexes, it has the following form

$$\mathcal{L}_Y = -\lambda_d^{ij} \overline{Q}^i \Phi d_R^j - \lambda_u^{ij} \overline{Q}^i (i\sigma^2 \Phi) u_R^j - \lambda_e^{ij} \overline{L}^i \Phi e_R^j + \text{h.c.} , \tag{2.16}$$

where $\lambda_{d,u,e}^{ij}$ are general complex matrices of the Yukawa couplings and h.c. corresponds to the Hermitian conjugate.

2.1.1.1 The Brout-Englert-Higgs mechanism

Particle masses are generated through the spontaneous symmetry breaking (SSB) of the local gauge symmetry $\mathrm{SU(2)}_L \times \mathrm{U(1)}_Y$ [8, 9]. Using the SU(2) gauge invariance, it is possible to reduce the four degrees of freedom of the Φ field to one. The Higgs doublet can be written in the unitarity gauge and then expanded around its own vacuum expectation value (VEV). The Higgs potential $V(\Phi^\dagger \Phi)$ has a continuum of minima when the condition

$$\Phi^\dagger \Phi = \frac{\mu^2}{\lambda^2} \equiv \frac{v^2}{2}, \tag{2.17}$$

is satisfied, where the vacuum expectation value of Φ is $v/\sqrt{2} \simeq 246\,\text{GeV}$. Then Φ becomes

$$\Phi(x) = \frac{1}{\sqrt{2}} \begin{pmatrix} 0 \\ v + H(x) \end{pmatrix}, \tag{2.18}$$

where $H(x)$ is the invariant Higgs field, which is scalar and real. At this point, the Lagrangian is no longer gauge invariant on SU(2). Moreover, because of the Goldstone theorem, stating that massless scalars occur whenever a continuous symmetry of a physical system is spontaneously broken, there will be one massless and three Goldstone bosons. The gauge fields are redefined as

$$W_\mu^\pm = \frac{W_\mu^1 \mp i W_\mu^2}{\sqrt{2}}, \tag{2.19}$$

$$Z_\mu = W_\mu^3 \cos\theta_\text{W} - B_\mu \sin\theta_\text{W}, \tag{2.20}$$

$$A_\mu = W_\mu^3 \sin\theta_\text{W} + B_\mu \cos\theta_\text{W}, \tag{2.21}$$

where the Weinberg angle θ_W is introduced ($\sin^2\theta_\text{W} \simeq 0.23$). Therefore, substituting in Eq. (2.18), the Lagrangian $\mathcal{L}_H$ of Eq. (2.13) becomes:

$$\mathcal{L}_H = -\frac{1}{8} g^2 v^2 (W^{+\mu} W_\mu^+ + W^{-\mu} W_\mu^-) - \frac{1}{8} v^2 (g^2 + g'^2) Z^\mu Z_\mu - \frac{1}{2} \lambda^2 v^2 H^2. \tag{2.22}$$

As a consequence, the masses of the gauge bosons are

$$M_H = \lambda v, \tag{2.23}$$

$$M_W = \frac{1}{2} g v, \tag{2.24}$$

$$M_Z = \frac{1}{2} v \sqrt{g^2 + g'^2}, \tag{2.25}$$

$$M_\gamma = 0. \tag{2.26}$$

After the SSB, also the Yukawa coupling Lagrangian $\mathcal{L}_Y$ of Equation (2.16) changes to

$$\mathcal{L}_Y = -\frac{v}{\sqrt{2}} \lambda_d^{ij} \overline{d}_L^i d_R^j - \frac{v}{\sqrt{2}} \lambda_u^{ij} \overline{u}_L^i u_R^j - \frac{v}{\sqrt{2}} \lambda_e^{ii} \overline{e}_L^i e_R^i + \text{h.c.} \tag{2.27}$$

Thus, the mass of the lepton e^i is proportional to the coupling between the lepton and the Higgs boson

$$M_{e^i} = \frac{v}{\sqrt{2}} \lambda_e^{ii}. \tag{2.28}$$

Since the neutrino field does not appear in the Lagrangian after the SSB, it remains massless in the SM framework. Because of observed neutrino oscillations [10–12], neutrinos are known not to be massless. Hence, a similar mechanism to quark mass generation is introduced in the next section.

2.1.1.2 Quark and lepton mixing

Quark masses are generated differently than lepton ones. The part of $\mathcal{L}_Y$ in Eq. (2.27) involving quarks can be written as

$$\mathcal{L}_{Y,quarks} = -\frac{v}{\sqrt{2}}\lambda_d^{ij}\overline{d}_L^i d_R^j - \frac{v}{\sqrt{2}}\lambda_u^{ij}\overline{u}_L^i u_R^j, \tag{2.29}$$

where the two flavour eigenstates u^i and d^i do not correspond to physical particles. In order to obtain the mass eigenstates, $\lambda_{u,d}$ matrices are diagonalised [13, 14]. This is done by introducing the unitary matrices $U_{u,d}$ and $W_{u,d}$

$$\lambda_{u,d}\lambda_{u,d}^\dagger = U_{u,d}D_{u,d}^2U_{u,d}^\dagger, \tag{2.30}$$
$$\lambda_{u,d}^\dagger\lambda_{u,d} = W_{u,d}D_{u,d}^2W_{u,d}^\dagger, \tag{2.31}$$

where $D_{u,d}$ are diagonal matrices. Hence

$$\lambda_{u,d} = U_{u,d}D_{u,d}W_{u,d}^\dagger. \tag{2.32}$$

Using this and defining the quark fields as

$$\begin{aligned} u_L^i &= U_u^{ij}u_L^{j,phys}, \\ u_R^i &= W_u^{ij}u_R^{j,phys}, \\ d_L^i &= U_d^{ij}d_L^{j,phys}, \\ d_R^i &= W_d^{ij}d_R^{j,phys}, \end{aligned} \tag{2.33}$$

it is possible to substitute the following terms in the Yukawa Lagrangian $\mathcal{L}_Y$ of Eq. (2.29):

$$\mathcal{L}_{Y,quarks} = -\frac{v}{\sqrt{2}}D_u^{ii}\overline{u}^{i,phys}u^{i,phys} - \frac{v}{\sqrt{2}}D_d^{ii}\overline{d}^{i,phys}d^{i,phys}. \tag{2.34}$$

Therefore, quark masses are defined as

$$m_{u,d}^i = \frac{v}{\sqrt{2}}D_u^{ii}. \tag{2.35}$$

Replacing weak eigenstates quark fields with mass eigenstates has another important effect, when considering currents. The fermionic Lagrangian $\mathcal{L}_f$ can be re-written using the term

$$-\frac{g}{\sqrt{2}}(J^{+\mu}W_\mu^+ + J^{-\mu}W_\mu^-) - \frac{g}{\cos\theta_W}J^{N\mu}Z_\mu, \tag{2.36}$$

where $J^{\pm\mu}$ and $J^{N\mu}$ represent the charged and neutral currents, respectively. They are defined as

$$J^{+\mu} = \overline{\nu}_L^a\gamma^\mu e_L^a + \overline{u}_L^a\gamma^\mu d_L^a, \tag{2.37}$$
$$J^{-\mu} = \text{h.c.}(J^{+\mu}),$$
$$J^{N\mu} = \sum_{a,f}\bar{f}^a\frac{\gamma^\mu}{2}\left[T_3 - (T_3 - 2\sin^2\theta_W Q)\gamma^5\right]f^a, \tag{2.38}$$

where f^a stands for a generic fermion (neutrino, electron or quark) of the a-th generation, T_3 its weak isospin and Q its electromagnetic charge.

Using the mass eigenstate, the terms involving quarks in the charged current of Eq. (2.37) can be written as

$$J^{+\mu}_{quarks} = \overline{u}^{i,phys}_L (U^\dagger_u U_d)^{ij} \gamma^\mu d^{j,phys}_L, \tag{2.39}$$

where the matrix $U^\dagger_u U_d \equiv V_{\rm CKM}$ is the Cabibbo-Kobayashi-Maskawa matrix (CKM). The charged-current interaction Lagrangian for quarks can now be written in this way:

$$\mathcal{L}_{cc,quarks} = -\frac{g}{\sqrt{2}} \begin{pmatrix} \overline{u}_L & \overline{c}_L & \overline{t}_L \end{pmatrix} \begin{pmatrix} V_{ud} & V_{us} & V_{ub} \\ V_{cd} & V_{cs} & V_{cb} \\ V_{td} & V_{ts} & V_{tb} \end{pmatrix} \gamma^\mu \begin{pmatrix} d_L \\ s_L \\ b_L \end{pmatrix} W^+_\mu + \text{h.c.}, \tag{2.40}$$

where the spinors represent the physical quark fields and the V_{ij} elements are complex numbers. As a consequence, the $W^\pm$ bosons mediate interactions between up-type and down-type quarks and also between different families, so that the quark flavour can change in weak interactions. Every element of the CKM matrix describes the coupling strength between two different quarks. For example $|V_{tb}| \simeq 1$ and $|V_{ub}| \simeq 0.004$, means that the coupling between t and b quarks is very strong as compared to the u and b quarks coupling.

Accounting for unitarity, the CKM matrix can be parameterised with three mixing angles θ_{ij} and a CP-violating[2] phase δ. Defining $s_{ij} = \sin\theta_{ij}$ and $c_{ij} = \cos\theta_{ij}$, the CKM matrix becomes

$$V_{\rm CKM} = \begin{pmatrix} c_{12}c_{13} & s_{12}c_{13} & s_{13}e^{-i\delta} \\ -s_{12}c_{23} - c_{12}s_{23}s_{13}e^{i\delta} & c_{12}c_{23} - s_{12}s_{23}s_{13}e^{i\delta} & s_{23}c_{13} \\ s_{12}s_{23} - c_{12}s_{23}s_{13}e^{i\delta} & -c_{12}s_{23} - s_{12}c_{23}s_{13}e^{i\delta} & c_{23}c_{13} \end{pmatrix}. \tag{2.41}$$

Experimentally it is known that $s_{13} \ll s_{23} \ll s_{12} \ll 1$. For this reason, a parameterisation proposed by L. Wolfenstein [15], which takes into account the hierarchy of the matrix elements, can be used. With this parameterisation, the CKM matrix becomes

$$V_{\rm CKM} = \begin{pmatrix} 1 - \lambda^2/2 & \lambda & A\lambda^3(\rho - i\eta) \\ -\lambda & 1 - \lambda^2/2 & A\lambda^2 \\ A\lambda^3(1 - \rho - i\eta) & -A\lambda^2 & 1 \end{pmatrix} + \mathcal{O}(\lambda^4), \tag{2.42}$$

where

$$s_{12} = \lambda = \frac{|V_{us}|}{\sqrt{|V_{ud}|^2 + |V_{us}|^2}},\ s_{23} = A\lambda^2 = \lambda \left|\frac{V_{cb}}{V_{us}}\right| \text{ and } s_{13}e^{i\delta} = V^*_{ub} = A\lambda^3(\rho + i\eta). \tag{2.43}$$

It is possible to evaluate the CKM matrix elements through different tree-level processes. For example, V_{ud} is obtained studying β decays, while V_{tb} is known from the branching

[2] The CP transformation is a combination of the parity transformation P and charge conjugation C, being q the electromagnetic charge of the field ψ, $C\psi(q) = \psi(-q)$.

ratio of the $t \to W^+ b$ transition. According to the latest available measurements [1], the magnitudes of the CKM matrix elements are known to be

$$|V_{\mathrm{CKM}}| = \begin{pmatrix} 0.97435 \pm 0.00016 & 0.22500 \pm 0.00067 & 0.00369 \pm 0.00011 \\ 0.22486 \pm 0.00067 & 0.97349 \pm 0.00016 & 0.04182^{+0.00085}_{-0.00074} \\ 0.00857^{+0.00020}_{-0.00018} & 0.04110^{+0.00083}_{-0.00072} & 0.999118^{+0.000031}_{-0.000036} \end{pmatrix}. \tag{2.44}$$

Finally, the CKM matrix shows another important feature of the electroweak theory: the non existence of Flavour-Changing Neutral Currents (FCNC) at tree level in the SM [13, 16]. In fact, after substituting the mass eigenstates in Eq. (2.38) it is clear that a fermion only interacts with its antiparticle or an identical fermion in neutral-current interactions. This is possible thanks to the unitarity of $U_{u,d}$ and $W_{u,d}$.

Concerning the lepton sector, since neutrinos are not massless due to oscillation [10–12], a similar treatment can be done. Therefore, it is possible to apply the same arguments of quark mixing to the lepton sector and define a mixing matrix. This is the Pontecorvo-Maki-Nakagawa-Sakata (PMNS) matrix [17],

$$\begin{pmatrix} \nu_e \\ \nu_\mu \\ \nu_\tau \end{pmatrix} = V_{\mathrm{PMNS}} \begin{pmatrix} \nu_1 \\ \nu_2 \\ \nu_3 \end{pmatrix} = \begin{pmatrix} V_{e1} & V_{e2} & V_{e3} \\ V_{\mu 1} & V_{\mu 2} & V_{\mu 3} \\ V_{\tau 1} & V_{\tau 2} & V_{\tau 3} \end{pmatrix} \begin{pmatrix} \nu_1 \\ \nu_2 \\ \nu_3 \end{pmatrix}. \tag{2.45}$$

Taking all of the above into account, the diagonalisation of the mass matrices in the Yukawa interaction between the Higgs field and the fermion fields yields to the mixing matrices V_{CKM} and V_{PMNS}. This can be considered the only source of difference in the coupling between the weak bosons and the three fermion generations. This feature is further investigated in Sec. 2.2.

2.1.2 Quantum chromodynamics

Quantum chromodynamics (QCD) is the theory describing the strong interactions between quarks and gluons. QCD is a Yang-Mills [18] non-abelian quantum field theory based on the exact and unbroken colour-SU(3) local gauge symmetry. The QCD Lagrangian is:

$$\mathcal{L}_{\mathrm{QCD}} = \sum_f \overline{\psi}_f \left(i\gamma^\mu \partial_\mu - g_s \gamma^\mu \frac{\lambda^C}{2} A^C_\mu - m_f \right) \psi_f - \frac{1}{4} A^{C\mu\nu} A^C_{\mu\nu}, \tag{2.46}$$

where ψ_f is a triplet in the SU(3) space of quark spinors of flavour f and mass m_f, g_s is the strong coupling constant, A^C_μ are the massless gluon fields (C = 1, ..., 8), $A^{C\mu\nu}$ are the gluon field strength tensors and λ^C are the eight Gell-Mann matrices, generators of the SU(3) group. The strong coupling constant α_s depends on the exchanged momentum q^2 at one-loop level,

$$\alpha_s(q^2) = \frac{g_s^2}{4\pi} = \frac{4\pi}{(11 - \frac{2}{3} n_f) \log(q^2 / {\Lambda_{\mathrm{QCD}}}^2)}, \tag{2.47}$$

where n_f is the number of active flavours and $\Lambda_{\rm QCD}$ is the energy scale of strong interactions, which is about 200 MeV experimentally. The magnitude of the coupling decreases with increasing q^2 or with decreasing distances. As a consequence, quarks and gluons behave as quasi-free particles at high energies, when $q \gg \Lambda_{\rm QCD}$, while at low energies, $q \ll \Lambda_{\rm QCD}$, the coupling becomes very high. This means that only at high energies quark-gluon interactions can be treated perturbatively, performing an expansion in series of $\alpha_s = g_s/4\pi$.

Nonetheless, non-perturbative studies of QCD are possible. These are performed by using lattice QCD (LQCD). In the LQCD approach, space-time is discretised in a lattice hypercube. The quark fields are placed on the lattice nodes and the gauge fields connect them. In this way, by calculating the path integral between sites, it is possible to perform non-perturbative calculations. The efficiency of the algorithm and the computing resources available are the main limitation of LQCD.

2.1.3 Limitations of the Standard Model

The SM successfully describes fundamental particles and their interactions. Results on precise SM tests have validated the theory up to the electroweak scale. However, the SM does not include some important phenomena that have been observed, showing hints that it could be itself an effective theory of a more fundamental one.

In the SM there is a large number of 18 canonical free parameters. These are the 12 fermion masses, the electromagnetic coupling strength, the Weinberg angle $\theta_{\rm W}$, the strong interaction coupling g_s, the vaccum expectation value v, the Higgs mass and the CKM mixing angles and the *CP* violation phase δ_{CP}. In addition to these other free parameters could arise, raising the total amount to 26. These are the three neutrino masses, the mixing angles and the *CP* violation phase of the PMNS matrix. Another free parameter that can be considered is the *CP* violation of the strong interaction. Experimentally this has not been observed, but the SM does not rule it out, making the strong *CP* problem one of the most puzzling questions of particle physics.

A good evidence of physics beyond the SM is the existence of dark matter and dark energy in the Universe. This has been inferred by studying the universe expansion and the position of the galaxies and has been further confirmed by cosmology measurements. Moreover, gravity is the only fundamental interaction that is not included in the model.

Furthermore, as already mentioned in Sec. 2.1.1.2, neutrinos are predicted to be massless but oscillation measurements have proven that the mass is non-zero. The main question arising from this result is if the oscillation is related to the nature of neutrinos or if it is the result of an unknown mechanism. Even if they are obtained similarly, the CKM and the PMNS matrices are very different. The first is almost diagonal, while $V_{\rm PMNS}$ is not. Besides, *CP* violation in the SM is allowed only by the complex phases of $V_{\rm CKM}$ and $V_{\rm PMNS}$. This is not enough to explain the observed matter-antimatter asymmetry in the Universe. In fact, *CP* violation is one of the conditions that would lead to *baryogenesis* [19]. Matter and antimatter are considered to have the same concentration in the Universe just after

the inflation, one of its early stages, but an excess of matter caused its dominance over antimatter.

All this considered, new physics (NP) is needed to explain these and more unanswered questions in particle physics. Currently, several NP searches are ongoing. These include direct searches of new particles or indirect searches of new processes, such as Lepton Flavour Universality tests.

2.2 Lepton Flavour Universality

In the SM, the three generations of charged leptons are identical except for their masses. The electroweak gauge bosons γ, $W^{\pm}$ and Z couple in the same manner with the three lepton generations. This peculiarity is known as Lepton Flavour Universality (LFU). This feature is related to the SM structure $\mathrm{SU}(3)_C \times \mathrm{SU}(2)_L \times \mathrm{U}(1)_Y \xRightarrow{SSB} \mathrm{SU}(3)_C \times \mathrm{U}(1)_{EM}$, hence it is a very good laboratory of NP searches.

LFU can be probed comparing the coupling in the leptonic decays of muons and tauons, $\mu^- \to e^- \overline{\nu}_e \nu_\mu$ and $\tau^- \to \ell^- \overline{\nu}_\ell \nu_\tau$. This is done in Sec. 2.2.1. Heavy flavoured hadrons decays, containing a b-quark or a c-quark, form a more complicated picture because of the QCD term in the interaction Lagrangian and quark mixing. The theoretical framework used to explain these transitions is presented in Sec. 2.2.2.

2.2.1 LFU in leptonic decays

In the SM, universality can be tested by considering the leptonic decays of muons and tauons. Fig. 2.2(a) represents the Feynman diagram of the $\mu^- \to e^- \overline{\nu}_e \nu_\mu$ decay. This includes two weak vertices: $\mu^- \nu_\mu W^-$ and $W^- e^- \overline{\nu}_e$. The muon decay rate is

$$\Gamma(\mu^- \to e^- \overline{\nu}_e \nu_\mu) = \frac{G_{\mathrm{F}}^2 m_\mu^5}{192\pi^3} \times f\left(\frac{m_e^2}{m_\mu^2}\right), \tag{2.48}$$

where $f(x) = 1 - 8x + 8x^3 - x^4 - 12x^2 \log x$ is a phase-space correction factor [20, 21] and G_{F} is the Fermi constant. The latter is given by

$$G_{\mathrm{F}} = \frac{g^2\sqrt{2}}{8M_W^2} = 1.16638 \times 10^{-5}\,\mathrm{GeV}^{-2}. \tag{2.49}$$

If the electron and the muon couplings were different, Eq. (2.48) can be written as

$$\Gamma(\mu^- \to e^- \overline{\nu}_e \nu_\mu) = \frac{1}{\tau_\mu} = \frac{G_{\mathrm{F}}^\mu G_{\mathrm{F}}^e m_\mu^5}{192\pi^3} \times f\left(\frac{m_e^2}{m_\mu^2}\right), \tag{2.50}$$

where G_{F}^e and G_{F}^μ are the weak couplings of the W^- with the e and the μ, respectively. Similarly, for the $\tau^- \to e^- \overline{\nu}_e \nu_\tau$ decay, represented in Fig. 2.2(b), the decay rate is

$$\Gamma(\tau^- \to e^- \overline{\nu}_e \nu_\tau) = \frac{G_{\mathrm{F}}^\tau G_{\mathrm{F}}^e m_\tau^5}{192\pi^3} \times f\left(\frac{m_e^2}{m_\tau^2}\right). \tag{2.51}$$

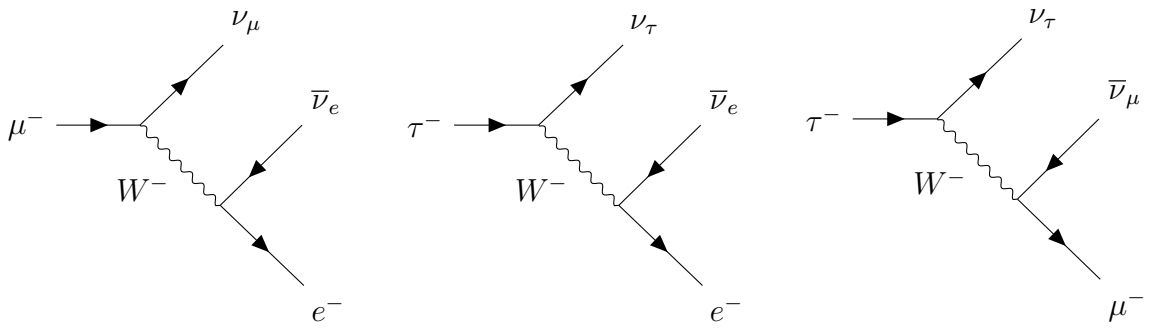

(a) $\mu^- \to e^- \overline{\nu}_e \nu_\mu$ (b) $\tau^- \to e^- \overline{\nu}_e \nu_\tau$ (c) $\tau^- \to \mu^- \overline{\nu}_\mu \nu_\tau$

Figure 2.2: Feynman diagrams of μ and τ leptonic decays.

Lepton	m_ℓ (MeV/c^2)	τ ($\times 10^{-6}$ s)
e	$0.5109989461 \pm 0.000000031$	stable
μ	105.658375 ± 0.000025	2.1969811 ± 0.0000022
τ	177686 ± 12	$(0.2903 \pm 0.0005) \times 10^{-6}$

Table 2.2: Lepton mass and mean lifetime values [1].

Since the τ can decay into several modes, other than the electronic one, the mean lifetime τ_τ can be written as a function of all the partial decay rates, Γ_i, of the i contributions,

$$\frac{1}{\tau_\tau} = \Gamma = \sum_i \Gamma_i. \tag{2.52}$$

Hence, the branching fraction $\mathcal{B}(\tau^- \to e^- \overline{\nu}_e \nu_\tau)$ is given by the ratio of the partial width to the total decay rate Γ

$$\mathcal{B}(\tau^- \to e^- \overline{\nu}_e \nu_\tau) = \frac{\Gamma(\tau^- \to e^- \overline{\nu}_e \nu_\tau)}{\Gamma} = \Gamma(\tau^- \to e^- \overline{\nu}_e \nu_\tau) \times \tau_\tau. \tag{2.53}$$

Substituting Eq. (2.53) into Eq. (2.51), the τ lifetime is obtained as

$$\tau_\tau = \frac{192\pi^3}{G_{\mathrm{F}}^\tau G_{\mathrm{F}}^e m_\tau^5} \mathcal{B}(\tau^- \to e^- \overline{\nu}_e \nu_\tau). \tag{2.54}$$

At this point, it is possible to compare the μ and τ lifetimes of Eqs. (2.50) and (2.51), obtaining

$$\frac{G_{\mathrm{F}}^\tau}{G_{\mathrm{F}}^\mu} = \frac{m_\mu^5 \tau_\mu}{m_\tau^5 \tau_\tau} \mathcal{B}(\tau^- \to e^- \overline{\nu}_e \nu_\tau). \tag{2.55}$$

Therefore, it is possible to evaluate the coupling strength by comparing the Fermi constant ratios and substituting the known values of the branching fraction $\mathcal{B}(\tau^- \to e^- \overline{\nu}_e \nu_\tau) =$

$(17.82 \pm 0.04)\%$ [1] and the mass and the lifetime values collected in Tab. 2.2. Experimentally, the muon and tauon weak charged-current coupling strength is measured

$$\frac{G_{\mathrm{F}}^{\tau}}{G_{\mathrm{F}}^{\mu}} = 1.002 \pm 0.003. \tag{2.56}$$

Comparing the τ decays to the electron and the muon mode and accounting for phase space differences, the $G_{\mathrm{F}}^{e}/G_{\mathrm{F}}^{\mu}$ ratio can be obtained. Since $\mathcal{B}(\tau^- \to \mu^- \overline{\nu}_{\mu} \nu_{\tau}) = (17.39 \pm 0.04)\%$, the muon to electron coupling strength ratio for weak charged-currents is

$$\frac{G_{\mathrm{F}}^{e}}{G_{\mathrm{F}}^{\mu}} = 1.000 \pm 0.004. \tag{2.57}$$

Both Eq. (2.56) and (2.57) are compatible with the LFU hypothesis.

2.2.2 Heavy flavoured semileptonic decays

Semileptonic decays of heavy flavoured hadrons are a very good laboratory of indirect NP searches. The amplitude of the semileptonic decay of a meson M_{Qq} into a state containing a meson $M_{q'q}$ can be written as a term proportional to the product of a leptonic current L_{μ} and a hadronic current H_{μ}. In particular, if the exchanged four-momentum, q^2, is much smaller than the mass, M_W, of the $W^{\pm}$ boson, the amplitude can be written as

$$\mathcal{M} = -i \frac{G_{\mathrm{F}}}{\sqrt{2}} V_{Qq'} L^{\mu} H_{\mu}, \tag{2.58}$$

where $V_{Qq'}$ is the V_{CKM} matrix element involved in the $Q \to q' \ell \nu_{\ell}$ transition. The leptonic and hadronic currents are given by

$$L^{\mu} = \bar{\ell} \gamma^{\mu} (1 - \gamma_5) \nu_{\ell}, \tag{2.59}$$

$$H_{\mu} = \langle M_{q'q}(p') | \, j_{\mu}^{H} \, | M_{Qq}(p) \rangle \,, \tag{2.60}$$

where j_{μ}^{H}, a four-component current, can be expressed in term of Lorentz-invariant quantities, combinations of $(p_{\mu} + p'_{\mu})$, q_{μ} and q^2.

Since the two mesons also interact strongly, the hadronic current contains some terms that parameterise the non-perturbative behaviour of QCD. These terms are called form factors (FF) and describe the hadronisation of quarks and gluons. The FF depend on the given initial and final states and they are measurable experimentally. For B or D (both with spin zero) decays to pseudoscalar or vector mesons, $B(D) \to P \ell \nu_{\ell}$, $B(D) \to V \ell \nu_{\ell}$, the FF that apply for different spin-parity final state mesons are listed in Tab. 2.3.

In the SM, semileptonic transitions can occur, as illustrated in the diagrams of Figs. 2.3 and 2.4. By considering the weak current of the process (see Sec. 2.1.1.2), which can be charged, defined in Eq. (2.37), or neutral, defined in Eq. (2.38), it is possible to separate them in two sets:

J^P	Operator	Form factors
0^-	γ_μ	f_0, f_+
0^+	$\sigma_{\mu\nu}$	f_T
1^-	γ_μ	A_0, A_1, A_2
1^-	$\gamma_\mu\gamma_5$	V
1^-	$\sigma_{\mu\nu}$	T_1, T_2
1^-	$\sigma_{\mu\nu}\gamma_5$	T_1

Table 2.3: List of form factors B or D decays $B(D) \to H\ell\nu_\ell$, where H is a meson of spin-parity J^P. When $J^P = 0^-$ the hadron is called a pseudoscalar, while vector mesons have $J^P = 1^-$.

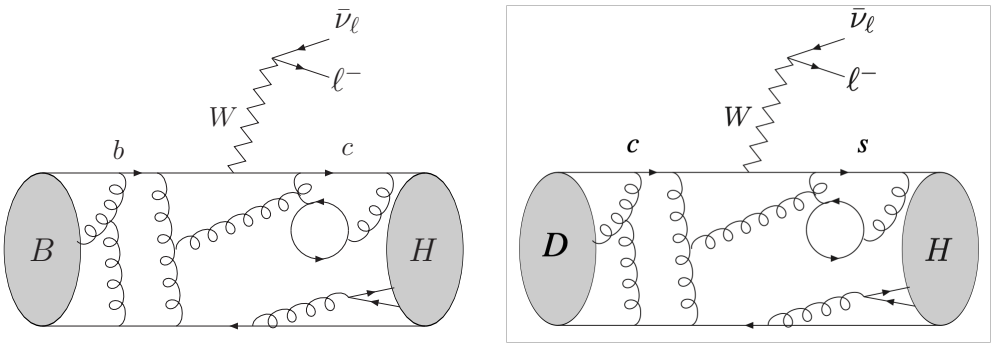

(a) $b \to c\ell^-\overline{\nu}_\ell$ (b) $c \to s\ell^-\overline{\nu}_\ell$

Figure 2.3: Feynman diagrams for $b \to c\ell^-\overline{\nu}_\ell$ (left) and $c \to s\ell^-\overline{\nu}_\ell$ (right) transitions [22].

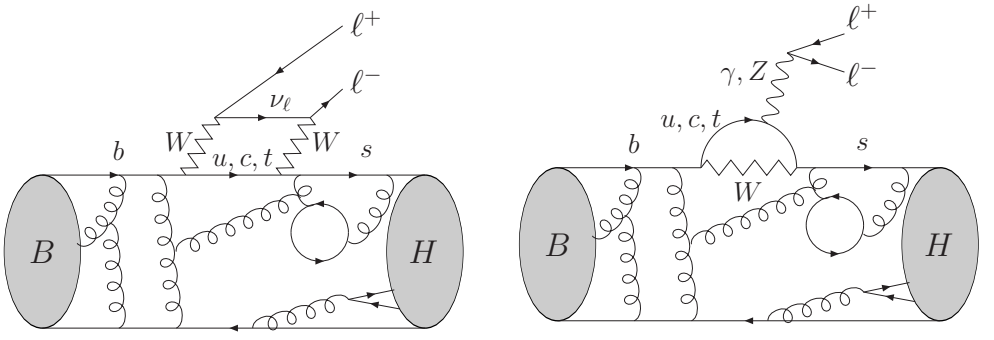

(a) (b)

Figure 2.4: Feynman diagrams for FCNC processes in the SM. Left: loop diagram with a W exchange. Right: penguin diagram with a Z or γ exchange [22].

- **Flavour Changing Charged Current** (FCCC) processes. In the SM they occur at tree level, as schematised in Fig. 2.3 for $b \to c\ell^-\overline{\nu}_\ell$ and $c \to s\ell^-\overline{\nu}_\ell$, respectively. Only a single $V_{\rm CKM}$ matrix element is involved in these transitions: V_{cb} or V_{cs}. The experimental status of FCCC decays is reported in Sec. 3.2.

- **Flavour Changing Neutral Current** (FCNC) processes. Because of the hierarchy of the $V_{\rm CKM}$ matrix, they cannot occur at tree level in the SM [13, 16]. Figure 2.4 shows the possible SM Feynman diagrams for $b \to s\ell^+\ell^-$ transitions. These can proceed through an exchange of a W^+/W^- box, Fig. 2.4(a), or a Z/γ penguin, Fig. 2.4(b). In this case, it is possible to express the CKM matrix contribution as the product of a leading element, $V_{tb}V_{ts}^*$, and a less favoured term, namely Cabibbo-suppressed, $V_{ub}V_{us}^*$. The experimental status of these measurements is reported in Sec. 3.3.

The preferred experimental observables to test LFU are ratios of decay rates with different lepton flavours in the final states (ℓ, ℓ'), such as

$$R(q^2) = \frac{\mathrm{d}\Gamma^{(\ell')}}{\mathrm{d}q^2} \Big/ \frac{\mathrm{d}\Gamma^{(\ell)}}{\mathrm{d}q^2}. \tag{2.61}$$

One of the main advantages of these observables is that form factor parameterisation uncertainties partially cancel out in the ratio. Besides, if there are neutrinos in the final state, only neutrinos from one generation are considered, making any contribution of neutrino mixing negligible.

2.2.2.1 Effective Field Theory approach

Considering the different scales involved in electroweak and strong interactions, one can decide to adopt an Effective Field Theory approach (EFT) to build the theoretical framework describing semileptonic hadron decays [23, 24]. In particular, the Heavy Quark Effective Theory (HQET) is an effective theory aiming to describe the interaction between a single heavy quark ($Q = b$, c) and a light quark [25].

The idea is analogue to Fermi's description of the β decay: an effective theory where the weak interactions are approximated by point-like couplings, governed by the dimensional coupling constant $G_{\rm F}$. Only at energies much larger than the masses of hadrons, the effects of the intermediate vector bosons, $W^\pm$ and Z, can be resolved. Therefore, if the existence of a NP particle is assumed, only the effect at the lower energy scale can be considered.

The starting point of HQET is the approximation of the mass of the heavy quark m_Q as infinite. Hence, this acts like a stationary source of colour charge. The effective Lagrangian is then constructed by expanding the QCD Lagrangian $\mathcal{L}_{\rm QCD}$ in a power series of $1/m_Q$ and neglecting higher-order terms, as far as $m_Q \gg \Lambda_{\rm QCD}$. This is particularly useful to calculate the form factors of decays involved in the transitions. In fact, the momentum transferred between the two quarks is small, leaving the colour source stationary to a good approximation.

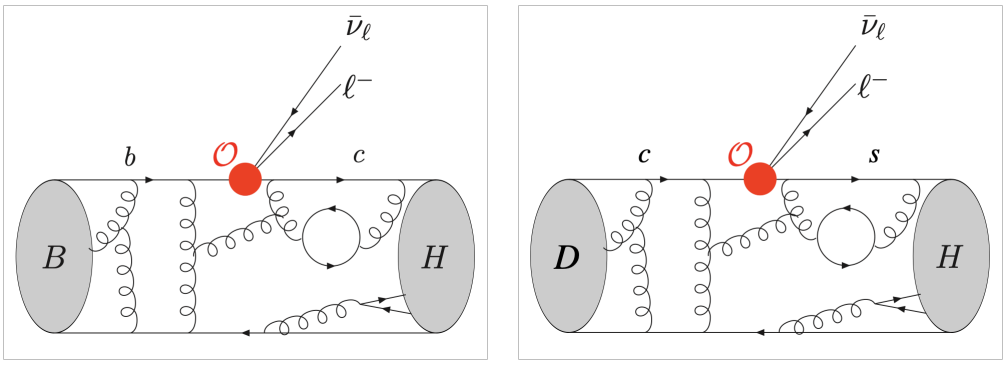

(a) $b \to c\ell^-\overline{\nu}_\ell$ (b) $c \to s\ell^-\overline{\nu}_\ell$

Figure 2.5: Feynman diagrams of $b \to c\ell^-\overline{\nu}_\ell$ (left) and $c \to s\ell^-\overline{\nu}_\ell$ (right) transitions in HQET approach [22]. The red dot corresponds to the local operator coupling two quarks and two leptons.

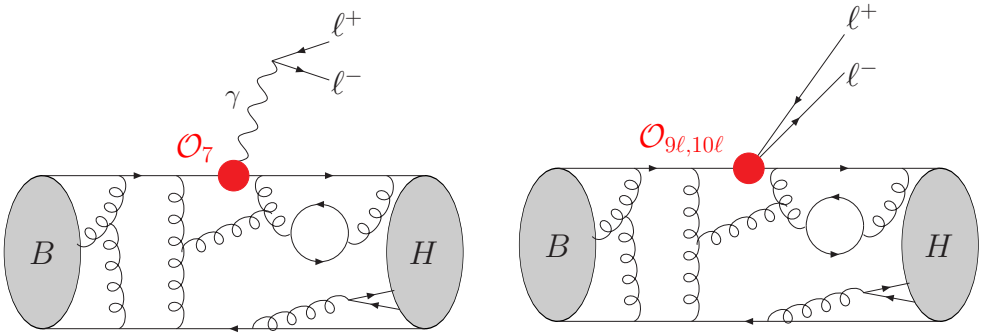

(a) (b)

Figure 2.6: Feynman diagrams of possible FCNC processes in HQET approach [22]. The red dot corresponds to the local operator $\mathcal{O}$.

This approach can be applied to both FCCC and FCNC transitions, as shown in the effective diagrams of Figs. 2.5 and 2.6. Since this thesis is centred on FCCC transitions, only the effective Lagrangians and the respective operators for D and B meson transitions are described (Sec. 2.2.3 and 2.2.4) and only the experimental status of FCNC transitions is presented in Sec. 3.3.

Considering that the fermion fields propagate over a distance larger than the factorisation scale, the four-fermion point interaction Lagrangian for $b \to c\ell^-\overline{\nu}_\ell$ transitions can be parameterised as

$$\mathcal{L}_{eff}(b \to c\ell^-\overline{\nu}_\ell) = \frac{4G_F}{\sqrt{2}} V_{cb} \sum_{\ell=e,\mu,\tau} \sum_i \mathcal{C}_i^\ell \mathcal{O}_i^\ell + \text{h.c.}\,, \tag{2.62}$$

where the index i runs over the $\mathcal{O}_i^\ell$ operators and Wilson Coeffients $\mathcal{C}_i^\ell$ [26]. These coefficients encode the energetic modes and the massive fields, so it is possible to obtain

the couplings of the mesons to the SM gauge bosons, or possible NP mediators, using perturbative methods. In terms of Feynman diagrams, the SM diagram of Fig. 2.3(a) becomes the one represented in Fig. 2.5(a). In the SM framework, due to LFU, the leading 4-fermion operator for $B \to V\ell\nu_\ell$ decays is

$$\mathcal{O}^{SM} = (\bar{c}\gamma_\mu P_L b)\left(\bar{\ell}\gamma^\mu P_L \nu_\ell\right), \tag{2.63}$$

where $P_{L,R}$ are the chirality projection operators introduced in Sec. 2.1.1, corresponding to the $V-A$ structure of the weak interaction. The normalisation is chosen in order to have $\mathcal{C}^{SM} = 1$.

The same procedure can be followed for $c \to s\ell^-\overline{\nu}_\ell$ transitions. Fig. 2.5(b) represents the Feynman diagram obtained with the effective field theory approach, to be compared with Fig. 2.3(b). For these, the SM Lagrangian is

$$\mathcal{L}_{eff}(c \to s\ell^-\overline{\nu}_\ell) = -\frac{4G_{\rm F}}{\sqrt{2}} V_{cs} \sum_{\ell=e,\ \mu,\ \tau} \sum_i \mathcal{C}_i^\ell \mathcal{O}_j^\ell + \text{h.c.}\,, \tag{2.64}$$

where

$$\mathcal{O}^{SM} = (\overline{s}\gamma_\mu P_L c)\left(\bar{\ell}\gamma^\mu P_L \nu_\ell\right), \tag{2.65}$$

$$\mathcal{C}^{SM} = 1. \tag{2.66}$$

This framework can be extended to include NP effects by defining effective operators and by allowing a shift of the Wilson coefficients. The Wilson coefficients considered in NP models and the form factors of D and B meson decays studied in this thesis are discussed in Secs. 2.2.3 and 2.2.4, respectively.

2.2.3 Phenomenology of $D \to K\ell\nu_\ell$ decays

The $c \to s\ell\nu_\ell$ transition considered in this thesis is $D^0 \to K^-\ell^+\nu_\ell$. The D^0 meson, formed by a $c\overline{u}$ quark pair, decays into a charged kaon, a pseudoscalar meson with spin parity $J^P = 0^-$. In this section this is referred as $D \to K\ell\nu_\ell$.

The observable to test LFU with these transitions is the ratio of decay rates

$$\begin{aligned} R_{\mu/e}(q^2) &= \frac{\mathrm{d}\Gamma^{(\mu)}}{\mathrm{d}q^2} \Big/ \frac{\mathrm{d}\Gamma^{(e)}}{\mathrm{d}q^2} \\ &= \frac{\mathrm{d}\Gamma(D \to K\mu\nu_\mu)}{\mathrm{d}q^2} \Big/ \frac{\mathrm{d}\Gamma(D \to Ke\nu_e)}{\mathrm{d}q^2}, \end{aligned} \tag{2.67}$$

and the theoretical predictions for these decays can be found in Ref. [27].

In the SM, the effective Lagrangian is given by Eq. (2.64). The relevant operators are

$$\mathcal{O}^{(\ell)}_{L(R)} = \left(\bar{s}P_{L(R)}c\right)\left(\bar{\nu}_\ell P_R \ell\right), \tag{2.68}$$

and the scalar Wilson coefficient is defined as

$$\mathcal{C}_S^{(\ell)} = \mathcal{C}_R^{(\ell)} + \mathcal{C}_L^{(\ell)}. \tag{2.69}$$

The differential decay rate for the $D \to K\ell\nu_\ell$ process is given by the formula

$$\frac{\mathrm{d}\Gamma^{(\ell)}}{\mathrm{d}q^2} = \frac{G_\mathrm{F}^2 |V_{cs}|^2 |\mathbf{q}| q^2}{96\pi^3 m_D^2} \left(1 - \frac{m_\ell^2}{q^2}\right)^2 \left[|h_0(q^2)|^2 \left(1 + \frac{m_\ell^2}{2q^2}\right) + \frac{3m_\ell^2}{2q^2} |h_t(q^2)|^2 \right], \tag{2.70}$$

where q^2 and $\mathbf{q}$ are respectively the 4-momentum and the 3-momentum transferred to the 2-lepton system in the D meson rest frame and $h_{0,t}$ are the hadronic helicity amplitudes for $D \to K\ell\nu_\ell$ decays. These are defined as

$$h_0(q^2) = \frac{\sqrt{\lambda(m_D^2, m_K^2, q^2)}}{\sqrt{q^2}} f_+(q^2), \tag{2.71}$$

$$h_t(q^2) = \left(1 + g_s^{(\ell)} \frac{q^2}{m_\ell (m_s - m_c)}\right) \frac{m_D^2 - m_K^2}{\sqrt{q^2}} f_0(q^2), \tag{2.72}$$

being $f_{+,0}(q^2)$ the form factors, m_s and m_c the s and c masses and g_s the strong coupling constant. Substituting Eqs. (2.71) and (2.72) into Eq. (2.70), the decay rate becomes

$$\begin{aligned} \frac{\mathrm{d}\Gamma^{(\ell)}}{dq^2} =& \frac{G_\mathrm{F} |V_{cs}|^2}{24\pi^3} \frac{(q^2 - m_\ell^2)^2 |\mathbf{p}_K|}{q^4 m_D^2} \\ &\times \left[\left(1 + \frac{m_\ell^2}{q^2}\right) m_D^2 |\mathbf{p}_K|^2 |f_+(q^2)|^2 + \frac{3m_\ell^2}{8q^2} (m_D^2 - m_K^2)^2 |f_0(q^2)|^2 \right], \end{aligned} \tag{2.73}$$

where $\mathbf{p}_K$ is the three-momentum of the kaon in the D rest frame. The mass of the lepton over the D mass squared suppresses the terms with the scalar form factor $f_0(q^2)$. Hence, the decay rate depends only on the vector form factor $f_+(q^2)$ and can be written as

$$\frac{\mathrm{d}\Gamma^{(\ell)}}{\mathrm{d}q^2} = \frac{G_\mathrm{F}}{24\pi^3} |\mathbf{p}_K|^3 |V_{cs}|^2 |f_+(q^2)|^2. \tag{2.74}$$

The dependence on q^2 of the scalar form factor has been calculated by LQCD groups [28, 29]. One of these groups has published the latest prediction for the $R_{\mu/e}$ value, reported in Sec. 3.2.1 together with the experimental status of LFU tests with D mesons.

2.2.3.1 Form factors parameterisations

As mentioned in Sec. 2.2.2, form factors depend on the initial and the final states and there are various alternatives to parameterise these functions. In this thesis, two parameterisation models are considered for the $f_+(q^2)$ form factor: the Isgur-Nathan-Scora-Grinstein-Wisen model (ISGW2) and the modified pole parameterisation (BK).

The ISGW2 model [30, 31] is the one usually chosen to simulate hadron semileptonic decays. The parameter values are obtained with calculations based on the constituent quark models and QCD sum rules. Its predictions are reported in Ref. [31].

The modified pole parameterisation (BK) [32] is developed assuming that the transition is governed by the heavy meson D. The form factor $f_+(q^2)$ has a pole at m^2_{pole} and other possible contributions are accounted for by adding effective poles. The form factor is then parameterised as

$$f_+^{\mathrm{BK}}(x) = \frac{f_+(0)}{(1-\frac{q^2}{m^2_{\mathrm{pole}}})(1-\alpha_{\mathrm{BK}}\frac{q^2}{m^2_{\mathrm{pole}}})}, \tag{2.75}$$

where $x = q^2/m^2_{\mathrm{pole}}$, $f_+(0)$ is the form factor value at $q^2 = 0$ and α_{BK} is a positive parameter. The values for $f_+(0)$, α_{BK} and m_{pole} are obtained both with experimental measurements and LQCD calculations (see Sec. 3.2.1).

2.2.4 Phenomenology of $B \to D^{(*)}\ell\nu_\ell$ decays

Tests of LFU with $b \to c\ell\nu_\ell$ transitions are performed by studying the ratio observables $R(H_c)$, where H_c is the charm meson, either a D or a D^* meson in this specific case. This is defined as

$$\begin{aligned} R(H_c) &= \frac{\mathrm{d}\Gamma^{(\tau)}}{\mathrm{d}q^2}\Big/\frac{\mathrm{d}\Gamma^{(\ell)}}{\mathrm{d}q^2} \\ &= \frac{\mathrm{d}\Gamma(B\to H_c\tau\nu_\tau)}{\mathrm{d}q^2}\Big/\frac{\mathrm{d}\Gamma(B\to H_c\ell\nu_\ell)}{\mathrm{d}q^2}, \end{aligned} \tag{2.76}$$

where ℓ stands for either a muon or an electron. As aforementioned, since the spin-parities of D^* and the D mesons are different, the decay rates are calculated following different approaches. In the case of the D meson, this is performed similarly to the previous section, being both the B and D mesons two pseudoscalars. Therefore, the decay rate $\mathrm{d}\Gamma^{(\tau)}/\mathrm{d}q^2$ depends on the $f_+(q^2)$ and $f_0(q^2)$ form factors.

For the D^* meson case, for instance, the decay rate of $B \to D^*\tau\nu$ is calculated in Ref. [33]. From the effective Lagrangian of Eq. (2.62), the differential decay rate is expressed as

$$\begin{aligned} \frac{\mathrm{d}\Gamma^{(\tau)}}{\mathrm{d}q^2} =& \frac{G_{\mathrm{F}}^2|V_{cb}|^2|\mathbf{p}\,|q^2}{96\pi^3 m_B^2}\left(1-\frac{m_\tau^2}{q^2}\right)^2 \\ &\times\left[\left(|H_{++}|^2+|H_{--}|^2+|H_{00}|^2\right)\left(1+\frac{m_\tau^2}{2q^2}\right)+\frac{3}{2}\frac{m_\tau^2}{q^2}|H_{0t}|^2\right], \end{aligned} \tag{2.77}$$

where $\mathbf{p}$ is the 3-momentum of the D^* meson in the B rest frame, q^2 the transfer momentum and $H_{mn}(q^2)$ are the helicity amplitudes. For $B \to D^*\ell\nu_\ell$ transitions, these relevant

form factors are the axial A_0, A_1, A_2 and the vector V (see Tab. 2.3). Hence, the helicity amplitudes can be written as

$$\begin{aligned} H^{\rm SM}_{\pm\pm}(q^2) &= (m_B + m_{D^*})A_1(q^2) \mp \frac{2m_B}{m_B + m_{D^*}}|\mathbf{p}\,|V(q^2)\,, \\ H^{\rm SM}_{00}(q^2) &= \frac{1}{2m_{D^*}\sqrt{q^2}}\left[(m_B^2 - m_{D^*}^2 - q^2)(m_B + m_{D^*})A_1(q^2) - \frac{4m_B^2|\mathbf{p}\,|^2}{m_B + m_{D^*}}A_2(q^2)\right]\,, \\ H^{\rm SM}_{0t}(q^2) &= \frac{2m_B|\mathbf{p}\,|}{\sqrt{q^2}}A_0(q^2)\,. \end{aligned} \tag{2.78}$$

Besides, one interesting helicity amplitude that can be affected by NP is the H_{0t} term. In Ref. [33] a NP coupling $g_{SL,SR}$ is introduced in the operator $\mathcal{O}_{V\ell}$ of Eq. (2.63), obtaining

$$H_{0t} = H^{\rm SM}_{0t}\left[1 + (g_{SR} - g_{SL})\frac{q^2}{m_b + m_c}\right]\,. \tag{2.79}$$

All this considered, $R(D^*)$ (2.76) can be written as a function of the helicity amplitudes as

$$R(D^*) = \left(1 - \frac{m_\tau^2}{q^2}\right)\left[\left(1 + \frac{m_\tau^2}{q^2}\right) + \frac{3m_\tau^2}{2q^2}\frac{|H_{0t}|^2}{|H_{++}|^2 + |H_{--}|^2 + |H_{00}|^2}\right]\,. \tag{2.80}$$

2.2.4.1 Form factors parameterisations

In the HQET framework, the helicity amplitudes, H, can be expressed as a function of a recoil variable, w, defined as

$$w \equiv v_B \cdot v_{D^*} = \frac{m_B^2 + m_{D*}^2 - q^2}{2m_B m_{D*}}, \tag{2.81}$$

where v_B^μ, and $v_{D^*}^\mu$ are the B and D^* meson 4-velocities, respectively. The D^* meson minimum recoil in the B rest frame, hence the largest allowed value for q^2, corresponds to the value $w = 1$. At this point, it is possible to define an universal form factor, $h_{A_1}(w)$,

$$h_{A_1}(w) = A_1(q^2)\frac{1}{\xi}\frac{2}{w+1}\,, \tag{2.82}$$

and ratios $R_{0,1,2}(w)$, so that the form factors can be rewritten as

$$A_0(q^2) = \frac{R_0(w)}{\xi}h_{A_1}(w)\,, \tag{2.83}$$

$$A_2(q^2) = \frac{R_2(w)}{\xi}h_{A_1}(w)\,, \tag{2.84}$$

$$V(q^2) = \frac{R_1(w)}{\xi}h_{A_1}(w)\,, \tag{2.85}$$

where $\xi = 2\sqrt{m_B m_{D^*}}/(m_B + m_{D^*})$.

As for $D \to K\ell\nu_\ell$ decays, several models have been developed to parameterise these form factors. The approaches considered in this thesis are the Caprini-Lellouch-Neubert (CLN) parameterisation [34] and the Boyd-Grinstein-Lebed (BGL) parameterisation [35–37].

The CLN model provides a parameterisation valid within $\approx 2\%$ uncertainty taking into account the heavy quark mass correction $1/m_Q$ near $w = 1$ [38]. Introducing the variable z

$$z = (\sqrt{w+1} - \sqrt{2})/(\sqrt{w+1} + \sqrt{2}), \tag{2.86}$$

the form factor variations of Eqs. (2.82) (2.83) (2.84) and (2.85) can be written as

$$h_{A_1}(w) = h_{A_1}(1)\left[1 - 8\rho^2 z + (53\rho^2 - 15)z^2 - (231\rho^2 - 91)z^3\right], \tag{2.87}$$

$$R_1(w) = R_1(1) - 0.12(w-1) + 0.05(w-1)^2, \tag{2.88}$$

$$R_2(w) = R_2(1) + 0.11(w-1) - 0.06(w-1)^2, \tag{2.89}$$

$$R_0(w) = R_0(1) - 0.11(w-1) + 0.01(w-1)^2. \tag{2.90}$$

In the BGL model [35–37], semileptonic decays are represented by the combination of resonant poles and non-analytic structures, multiplied by Taylor series encoding the momentum transfer, q^2. A parameterisation of the form factors around $z = 0$ is performed.

Therefore, Eqs. (2.82) (2.83) (2.84) and (2.85) are transformed into

$$h_{A_1}(w) = \frac{f(w)}{\sqrt{m_B m_{D^*}(1+w)}}, \tag{2.91}$$

$$R_0(w) = m_{D^*}\left(\frac{1+w}{1+m_{D^*}/m_B}\right)\frac{\mathcal{F}_\infty}{f}, \tag{2.92}$$

$$R_1(w) = (1+w)m_{D^*}m_B\frac{g(w)}{f(w)}, \tag{2.93}$$

$$R_2(w) = \frac{w-r}{w-1}\frac{\mathcal{F}(w)}{m_B(w-1)f(w)}. \tag{2.94}$$

Here, the three functions $f(w)$, $g(w)$ and $\mathcal{F}_\infty(w)$ are defined as

$$f(z) = \frac{1}{P_{1+}(z)\phi_f(z)}\sum_{n=0}^{\infty} a_n^f z^n, \tag{2.95}$$

$$g(z) = \frac{1}{P_{1-}(z)\phi_g(z)}\sum_{n=0}^{\infty} a_n^g z^n, \tag{2.96}$$

$$\mathcal{F}_1(z) = \frac{1}{P_{1+}(z)\phi_{\mathcal{F}_1}(z)}\sum_{n=0}^{\infty} a_n^{\mathcal{F}_1} z^n, \tag{2.97}$$

$$\mathcal{F}_2(z) = \frac{1}{P_{1-}(z)\phi_{\mathcal{F}_2}(z)}\sum_{n=0}^{\infty} a_n^{\mathcal{F}_2} z^n, \tag{2.98}$$

where $P_{1\pm}(z)$ are Blaschke[3] factors and the $\phi_{f,g,\mathcal{F}}(z)$ functions are introduced to remove poles in the contour of $z = 1$ [36]. For decays with light leptons, $R_0(w)$ is neglected, affecting only decays with τ.

[3]Blaschke factors are products of the form $(z - z_i)/(1 - \bar{z}z_i)$. For instance $P_0 = P_1 = \prod_{j=5}^{8} \frac{z-z_j}{1-\bar{z}z_j}$ and $P_2 = P_3 = \prod_{j=1}^{4} \frac{z-z_j}{1-\bar{z}z_j}$.

3

Latest experimental results

This chapter provides an overview of the current experimental status of tests of Lepton Flavour Universality. Before presenting the various measurements, a brief description of the heavy flavour experiments at e^+e^- colliders is given in Sec. 3.1. Then tests on FCCC decays are described in Sec. 3.2, $c \to s\ell\nu_\ell$ transitions in Sec. 3.2.1 and $b \to c\ell\nu_\ell$ in Sec. 3.2.2. Finally, results concerning FCNC transitions are reported in Sec. 3.3.

3.1 Experimental landscape

Lepton Flavour Universality has been investigated by performing several measurements and theoretical studies. In the heavy quark sector several measurements have been performed at different experimental conditions, at both hadron (LHCb) and e^+e^- (B Factories, BESIII) colliders.

B factories are e^+e^- colliders aiming to study heavy flavoured hadron decays. The experiments, such as BaBar, Belle and Belle II, have a 4π acceptance and they operate at a centre-of-mass energy close to the $\Upsilon(4S)$ mass of 10.58 GeV. The $\Upsilon(4S)$ is a $b\bar{b}$ resonance decaying into a B^+B^- or a $B^0\overline{B}^0$ pair. Aiming to study CP violation, the $\Upsilon(4S)$ resonance is boosted, so that the two beams have different energies: 9 and 3.1 GeV at BaBar and 8 and 3.5 GeV at Belle. The BaBar experiment, at the SLAC accelerator, took data between 1998 and 2008, corresponding to an integrated luminosity of about 433 fb^{-1}. The Belle experiment run between 1999 and 2010, collecting a data sample corresponding to an integrated luminosity of about 711 fb^{-1}. Recently, the Belle detector

underwent an upgrade. The upgraded Belle II detector started to run in 2019. The data sample collected until August 2022 corresponds to 363 fb^{-1} [39].

At B Factories, B mesons are reconstructed using a tagging technique. One meson of the pair, B_{tag}, is fully reconstructed by using hadronic or semileptonic decays while the other particles of the event are due to the decays of the B_{signal} meson. In case there is a neutrino in the signal final state, fully reconstructing the B_{tag} decay (using hadronic decays) allows to obtain the missing information.

Recent measurements of charm hadron decays have been performed by the BESIII experiment. This is a 4π spectrometer at the BEPC II e^+e^- collider, designed to study charm, charmonium and light hadrons decays. It operates at a centre-of-mass energy of 3.78 GeV and an instantaneous luminosity of about $10^{33}\,\text{cm}^{-2}\,\text{s}^{-1}$. The reconstruction methods employed to study D meson decays are analogous to the B Factories ones.

At hadron colliders, the techniques to reconstruct heavy hadrons are different. The specific case of the LHCb experiment is described in detail in Ch. 4.

3.2 LFU tests in FCCC transitions

As introduced in Sec. 2.2.2, the decays analysed in this thesis are charged current processes. The experimental status of these measurements, performed with D and B meson decays, are reported in Sec. 3.2.1 and 3.2.2, respectively.

3.2.1 D meson decays

As introduced in Sec. 2.2.3, the main observable considered as a LFU probe is the ratio $R_{\mu/e}$, defined in Eq. (2.67). Experimentally, $R_{\mu/e}$ can be measured using D meson decays to s- or d-hadrons (H) as

$$R_{\mu/e} = \frac{\mathcal{B}(D \to H\mu^+\nu_\mu)}{\mathcal{B}(D \to He^+\nu_e)}, \tag{3.1}$$

where D stands for a D^0 or a $D^\pm$ meson. A list of the branching fractions of $D \to H\ell^+\nu_\ell$ decays is reported in Tab. 3.1.

The first SM prediction for $R_{\mu/e}$ with $D^0 \to K^-\ell^+\nu_\ell$ decays is $R_{\mu/e} = 0.976 \pm 0.002$ [27]. This was recently updated by LQCD calculations [29] to $R_{\mu/e} = 0.9779 \pm 0.0002(\text{latt}) \pm 0.0050(\text{EM})$, where the first contribution to the uncertainty is specific to the lattice and the second one is due to electromagnetic corrections. Figure 3.1 represents the SM prediction of $R_{\mu/e}$ as a function of the q^2 together with the latest BESIII measurement. Recently BESIII measured $R_{\mu/e}$ using $D^0 \to K^-\ell^+\nu_\ell$ and $D^0 \to \pi^-\ell^+\nu_\ell$ decays [40, 42]. For the K measurement, $R^K_{\mu/e}$ is $0.974 \pm 0.037 \pm 0.012$, where the first contribution to the uncertainty is due to statistics and the second to the systematic uncertainties, while when there is a π in the final state $R^\pi_{\mu/e} = 0.922 \pm 0.0.30 \pm 0.022$. Both results are in agreement with the SM predictions within 2 standard deviations. In

Channel	$\mathcal{B}(D \to H\mu^+\nu_\mu)$ (%)		$\mathcal{B}(D \to He^+\nu_e)$ (%)	
$D^0 \to K^-\ell^+\nu_\ell$	$3.413 \pm 0.019 \pm 0.035$	[40]	3.049 ± 0.026	[1]
$D^0 \to K^{*-}\ell^+\nu_\ell$	1.89 ± 0.24	[1]	2.15 ± 0.16	[1]
$D^+ \to \overline{K}^0\ell^+\nu_\ell$	$8.72 \pm 0.07 \pm 0.18$	[41]	8.72 ± 0.09	[1]
$D^0 \to \pi^-\ell^+\nu_\ell$	$0.272 \pm 0.008 \pm 0.006$	[42]	$0.295 \pm 0.004 \pm 0.003$	[43]
$D^+ \to \pi^0\ell^+\nu_\ell$	$0.350 \pm 0.011 \pm 0.010$	[42]	0.372 ± 0.017	[1]

Table 3.1: Previous measurements of $\mathcal{B}(D \to H\ell^+\nu_\ell)$. The first contribution to the uncertainty is the statistics, while the second term, when present, represents the systematic uncertainty.

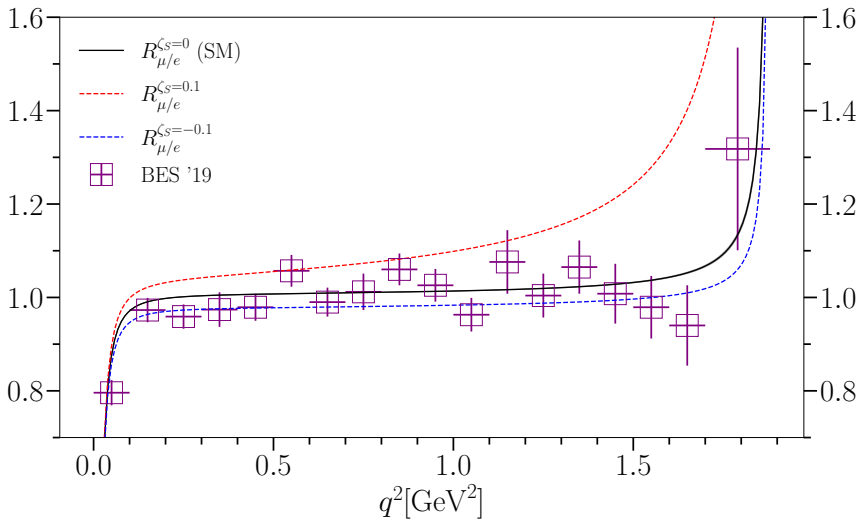

Figure 3.1: $R_{\mu/e}$ predictions as a function of q^2 [29]. The black line represents the SM prediction, and the points with the uncertainties, BESIII measurement. The red and blue lines correspond to $R_{\mu/e}$ when the Wilson coefficient takes two possible values, respectively $\zeta_S^\mu = \mathcal{C}_S^{(\mu)}/(m_c - m_s) = \pm 0.1$ GeV^{-1}, with $m_{c(s)}$ standing for the $c\,(s)$ quark mass.

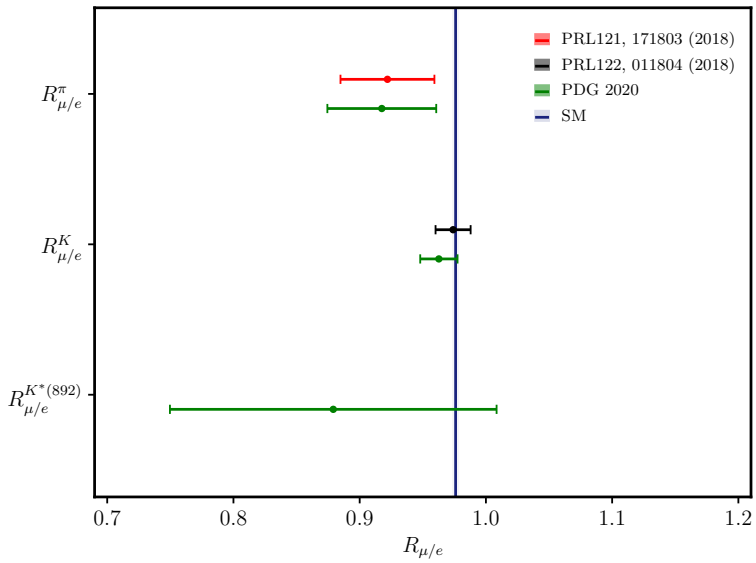

Figure 3.2: State of the art of $R_{\mu/e}$ measurement performed considering different signal final states, namely $R^{\pi}_{\mu/e}$, $R^{K}_{\mu/e}$ and $R^{K^*}_{\mu/e}$. The green points are the values of $R_{\mu/e}$ obtained by comparing the averaged measurements [1], shown in red and black for $D^0 \to \pi^-\ell^+\nu_\ell$ and $D^0 \to K^-\ell^+\nu_\ell$ decays, respectively. The SM prediction from Ref. [27] is represented by the vertical blue line and its uncertainty is represented by the thickness. Note that the contribution to the uncertainty due to QED corrections is not accounted for.

Fig. 3.2, the $R_{\mu/e}$ measurements and the SM predictions are represented. In addition to the experimental measurements, also the averages taken from Ref. [1] are reported.

3.2.2 B hadron decays

LFU tests using $b \to c\ell\nu_\ell$ transitions have been performed by different experiments. For the full q^2 region and generic b- and c-hadrons, H_b and H_c, the ratio observable of Eq. (2.76) can be written as

$$R(H_c) = \frac{\mathcal{B}(H_b \to H_c\tau^+\nu_\tau)}{\mathcal{B}(H_b \to H_c\ell'^+\nu_{\ell'})}, \tag{3.2}$$

where ℓ' stands for μ or e. Tau leptons decay through different channels, as shown in Tab. 3.2, hence, it is possible to reconstruct them in different manners and each one presents different advantages and disadvantages. The main τ decay channels used in LFU tests are the following:

- **Leptonic** $\tau^- \to \mu^-\overline{\nu}_\mu\nu_\tau$ and $\tau^- \to e^-\overline{\nu}_e\nu_\tau$ decays with a charged lepton and a neutrino in the final state. Experimentally, signal events are selected by requiring a

Channel	$\mathcal{B}$ ($\times 10^{-3}$)
$\tau^- \to \mu^- \overline{\nu}_\mu \nu_\tau$	17.39 ± 0.04
$\tau^- \to e^- \overline{\nu}_e \nu_\tau$	17.82 ± 0.04
$\tau^- \to \pi^- \pi^0 \nu_\tau$	25.49 ± 0.09
$\tau^- \to \pi^- \nu_\tau$	10.82 ± 0.05
$\tau^- \to \pi^- \pi^+ \pi^- \nu_\tau$	9.02 ± 0.05
$\tau^- \to \pi^- \pi^+ \pi^- \pi^0 \nu_\tau$	4.49 ± 0.05

Table 3.2: Branching fraction measurements of τ decays for the different modes [1].

charm hadron, in addition to a μ or an e. In this way, $R(H_c)$ is extracted from a single dataset containing both the signal and normalisation channels. The main background contributions are due to inclusive $B \to H_c D(X)$ decays with $D \to \ell'^+ \overline{\nu}_\ell \nu_\tau$ and $B \to H_c^{**} \ell \nu_\ell$ decays, with $H_c^{**} \to H_c(X)$, where X represents any possible unreconstructed particle. This reconstruction method has been used for the $R(D^*)$, $R(D)$ and $R(J/\psi)$ measurements [44–52].

- **Hadronic** decays contain two neutrinos in the final state. Signal events can have one or three pions and are called 1-prong and 3-prong, respectively. Three 3-prong $\tau^- \to \pi^- \pi^+ \pi^- \nu_\tau$ and $\tau^- \to \pi^- \pi^+ \pi^- \pi^0 \nu_\tau$ modes enable the τ vertex reconstruction, therefore are preferred to the 1-prong ones. One of the biggest source of background is due to B hadrons decaying into doubly-charmed final states $H_b \to H_c D(X)$, where the D meson decay inclusively into three pions. Besides, one of the main differences from the reconstruction with leptonic decays is that the $H_b \to H_c \mu \nu_\mu$ and $H_b \to H_c e \nu_e$ channels are not measured simultaneously with the τ final state. Therefore, the branching fraction values are taken from external measurements. This reconstruction method has been used for the $R(D^*)$, $R(D)$ and $R(\Lambda_c^+)$ measurements [53–55].

$R(H_c)$ has been measured both at B Factories, by Belle and BaBar, and at the LHC by LHCb. In particular, LHCb measured $R(J/\psi)$ and $R(\Lambda_c^+)$ using LHC Run 1 data sample, corresponding to an integrated luminosity of 3 fb^{-1} [52, 55]. A value of $R(J/\psi)$ equal to $0.71 \pm 0.17 \pm 0.18$, where the first term of the uncertainty is due to statistics and the second to the systematics, is found. This lies within 2 standard deviations above the SM predicted range of $(0.25, 0.30)$ [56–59]. Concerning $R(\Lambda_c^+)$, the result is $0.242 \pm 0.026 \pm 0.040 \pm 0.059$, with the third uncertainty term due to external measurements, in agreement with the SM expectations.

Concerning the $R(D)$ and $R(D^*)$ observables, these are predicted to be $R(D) = 0.298 \pm 0.004$ and $R(D^*) = 0.254 \pm 0.005$, respectively, by different groups [38, 60–68]. In Figs. 3.3 and 3.4 these values are compared with the experimental measurements published

Experiment (year)		τ decay	R(D^*)	R(D)	Total corr.
BaBar (2012)	[44, 45]	$\tau^- \to \ell'^- \overline{\nu}_\ell \nu_\tau$	$0.332 \pm 0.024 \pm 0.018$	$0.440 \pm 0.058 \pm 0.042$	-0.27
Belle (2015)	[46]	$\tau^- \to \mu^- \overline{\nu}_\mu \nu_\tau$	$0.293 \pm 0.038 \pm 0.015$	$0.375 \pm 0.064 \pm 0.026$	-0.49
LHCb (2015)	[47]	$\tau^- \to \ell'^- \overline{\nu}_\ell \nu_\tau$	$0.336 \pm 0.027 \pm 0.030$	-	-
Belle (2017)	[48, 49]	$\tau^- \to \ell'^- \overline{\nu}_\ell \nu_\tau$	$0.270 \pm 0.035\ ^{+0.028}_{-0.025}$	-	-
LHCb (2018)	[53, 54]	$\tau^- \to \pi^-\pi^+\pi^-(\pi^0)\nu_\tau$	$0.283 \pm 0.019 \pm 0.029$	-	-
Belle (2019)	[50]	$\tau^- \to \ell'^- \overline{\nu}_\ell \nu_\tau$	$0.283 \pm 0.018 \pm 0.014$	$0.307 \pm 0.037 \pm 0.016$	-0.51
LHCb (2022)	[51]	$\tau^- \to \ell'^- \overline{\nu}_\ell \nu_\tau$	$0.281 \pm 0.018 \pm 0.024$	$0.441 \pm 0.060 \pm 0.066$	-0.43
Average	[60]	all	$0.285 \pm 0.010 \pm 0.008$	$0.358 \pm 0.025 \pm 0.012$	-0.29

Table 3.3: Experimental status of $R(D)$ and $R(D^*)$ measurement. The first contribution to the uncertainty is the statistics, while the second one, when present, represents the systematic uncertainty.

by Belle, BaBar and LHCb. The τ reconstruction mode is specified in Tab. 3.3 together with the measurements.

Finally, by considering all the aforementioned measurements the average of the combination of $R(D)$ and $R(D^*)$ equals to

$$R(D) = 0.358 \pm 0.025 \pm 0.012, \tag{3.3}$$

$$R(D^*) = 0.285 \pm 0.010 \pm 0.008. \tag{3.4}$$

The first contribution to the uncertainty is due to statistics and the second to the systematic ones. These two values have a correlation of -0.29, as visible in the slope of the red ellipse in Fig. 3.4. The $R(D)$ and $R(D^*)$ measurements exceed the SM prediction by 2.16 and 2.26 standard deviations, respectively. The combined measurement differs from the SM predictions by about 3.2 standard deviations.

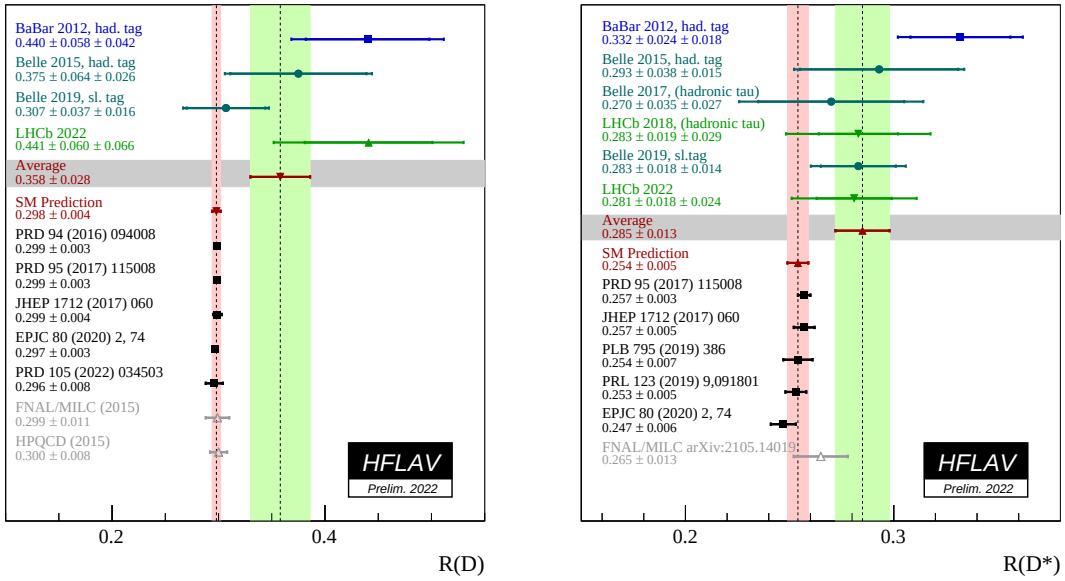

(a) (b)

Figure 3.3: Average and predictions for $R(D)$ and $R(D^*)$ [38, 60–69].

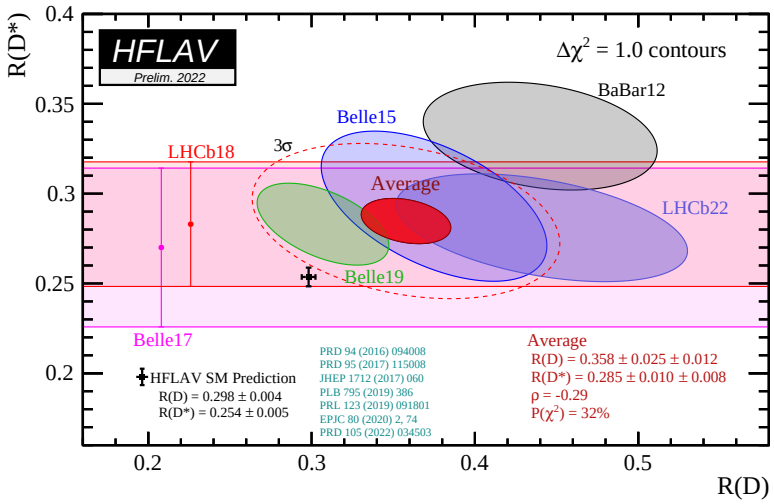

Figure 3.4: State of the art average of the combination of $R(D)$ and $R(D^*)$ [60]. The combined $R(D)$ and $R(D^*)$ measurements are represented by the ellipses, while the single measurements with a point. The SM prediction is represented by the black point and the average of all the experimentl resuts is the red ellipse, at 3.2σ from the prediction.

3.3 LFU tests in FCNC transitions

As mentioned in Sec. 2.2.2, FCNC processes occur only at loop level. Since they are higly suppressed, $b \to s\ell\ell$ transitions are very good probes of physics beyond the SM. The observable $R(H_s)$ is defined in a given interval of q^2 as

$$R(H_s) = \frac{\int_{q^2_{min}}^{q^2_{max}} \frac{\mathrm{d}\Gamma}{\mathrm{d}q^2}(H_b \to H_s\mu^+\mu^-)\,\mathrm{d}q^2}{\int_{q^2_{min}}^{q^2_{max}} \frac{\mathrm{d}\Gamma}{\mathrm{d}q^2}(H_b \to H_s e^+e^-)\,\mathrm{d}q^2}, \tag{3.5}$$

where H_s is the strange hadron and q^2 is the transfer momentum of the di-lepton system. The SM predicts $R(H_s)$ close to unity, and in the case of K and K^*, with an uncertainty of the order of 1% [70–73].

Differently from $R(H_c)$, the third lepton generation is not investigated. Nevertheless, one of the main challenges of these analyses is the presence of electrons in the final state. These loose energy through *bremsstrahlung* radiation, so the invariant mass shapes and reconstruction efficiency are different than the muon ones. In LHCb the electron reconstruction is treated using a *bremsstrahlung* recovery algorithm, described in Sec. 4.3.1.1.

Since these measurements are performed in bins of q^2, experimentally it is possible to take advantage of resonant states decaying into the dilepton final states, such as J/ψ and $\psi(2S)$. The q^2 intervals containing these resonances can be used as control regions. This has been the case in all the measurements performed until now by BaBar, Belle and LHCb. In particular, the latter fully exploits the double ratio

$$R(H_s) = \frac{\mathcal{B}(H_b \to H_s\mu^+\mu^-)}{\mathcal{B}(H_b \to H_s J/\psi(\to \mu^+\mu^-))} \Bigg/ \frac{\mathcal{B}(H_b \to H_s e^+e^-)}{\mathcal{B}(H_b \to H_s J/\psi(\to e^+e^-))}\,. \tag{3.6}$$

Some studied decays are $B \to K^{(*)}\ell^+\ell^-$ and $\Lambda_b^0 \to pK^-\ell^+\ell^-$. The experimental results for these decays are listed in Tab. 3.4 together with the considered q^2 ranges.

Previous $R(K^{(*)})$ measurements from LHCb [74, 75] showed tensions with the SM predictions. However, they have been overruled by the simultaneous $R(K)$ and $R(K^*)$ results [76, 77], which employ the full data sample. These are in agreement with the SM within one standard deviation.

In addition to ratios, B anomalies are investigated also by measuring other observables. These correspond to differential decay rates and angular variables [70, 78]. Angular analyses of $B \to K^*\mu^+\mu^-$ decays have been performed by Belle and at LHC by the CMS, ATLAS and LHCb collaborations [79–84]. The majority of the observables are in agreement with the SM predictions. Nevertheless, angular observable P_5' measurements with $B^0 \to K^{*0}\mu^+\mu^-$ and $B^+ \to K^{*+}\mu^+\mu^-$ decays [79, 80] show tension with the SM of more than 2 standard deviations. Besides, recent measurements of differential decay rates performed by LHCb agree with the SM predictions within 2 standard deviations [85–88]. The attention on B anomalies has not stemmed. More results on these decay modes are expected in the next future, foreseeing to have a final understanding of these processes.

Observable	Measurement	q^2 range (GeV/c^2)	Experiment (year)	
$R(K^*)$	$0.83 \pm 0.17 \pm 0.05$	—	Belle (2009)	[89]
$R(K^*)$	$1.06^{+0.48}_{-0.33} \pm 0.08$	(0.10, 8.12)	BaBar (2012)	[90]
$R(K^*)$	$1.18^{+0.55}_{-0.37} \pm 0.10$	> 10.11	BaBar (2012)	[90]
$R(K^{*0})$	$0.66^{+0.11}_{-0.07} \pm 0.03$	(0.045, 1.1)	LHCb (2017)	[74]
$R(K^{*0})$	$0.69^{+0.11}_{-0.05} \pm 0.03$	(1.1, 6.0)	LHCb (2017)	[74]
$R(K^*)$	$0.90^{+0.27}_{-0.21} \pm 0.10$	(0.1, 8.0)	Belle (2019)	[91]
$R(K^*)$	$1.03^{+0.52}_{-0.32} \pm 0.10$	(15.0, 19.0)	Belle (2019)	[91]
$R(K^{*+})$	$0.70^{+0.18+0.03}_{-0.13-0.04}$	(1.1, 6.0)	LHCb (2021)	[92]
$R(K^{*0})$	$0.927^{+0.093+0.034}_{-0.087-0.033}$	(0.045, 1.1)	LHCb (2022)	[76, 77]
$R(K^{*0})$	$1.027^{+0.072+0.027}_{-0.068-0.027}$	(1.1, 6.0)	LHCb (2022)	[76, 77]
$R(K)$	$1.03 \pm 0.19 \pm 0.10$	—	Belle (2009)	[89]
$R(K)$	$0.74^{+0.40}_{-0.31} \pm 0.06$	(0.10, 8.12)	BaBar (2012)	[90]
$R(K)$	$1.43^{+0.65}_{-0.44} \pm 0.12$	> 10.11	BaBar (2012)	[90]
$R(K^+)$	$1.03^{+0.28}_{-0.024} \pm 0.01$	(1.1, 6.0)	Belle (2021)	[93]
$R(K^+)$	$0.846^{+0.042+0.013}_{-0.039-0.012}$	(1.1, 6.0)	LHCb (2021)	[75]
$R(K)$	$0.994^{+0.090+0.027}_{-0.082-0.029}$	(0.045, 1.1)	LHCb (2022)	[76, 77]
$R(K)$	$0.949^{+0.042+0.023}_{-0.041-0.023}$	(1.1, 6.0)	LHCb (2022)	[76, 77]
$R(K^0_S)$	$0.66^{+0.20+0.02}_{-0.14-0.04}$	(1.1, 6.0)	LHCb (2021)	[92]
$R(pK^-)$	$0.86^{+0.14}_{-0.11} \pm 0.05$	(1.1, 6.0)	LHCb (2019)	[94]

Table 3.4: Summary of LFU tests in FCNC transitions.

4

The LHC and the LHCb experiment

LHCb is one of the four main experiments at the Large Hadron Collider (LHC) at CERN (European Organization for Nuclear Research). The LHC is an accelerator and a circular collider, situated near Geneva, across the French-Swiss border. In this chapter, after an introduction of the LHC in Sec. 4.1, a detailed description of the LHCb detector and its sub-detectors is given in Sec. 4.2. Finally, a description of how the information from the detector is collected and set up for analyses is given in Sec. 4.3.

4.1 The Large Hadron Collider

The Large Hadron Collider is a two ring hadron accelerator, installed in a 27-kilometres long tunnel built during the decade of 1980 for the Large Electron Positron (LEP) collider, which completed its data taking in 2001. The tunnel is situated between 45 m and 170 m below the surface. For a more detailed description of the LHC see Ref. [95].

The LHC is designed to collide protons and heavy ions at unprecedented energies: protons up to a centre-of-mass energy of 14 TeV, with an instantaneous luminosity of $10^{34}\,\mathrm{cm}^{-2}\,\mathrm{s}^{-1}$; and heavy-ions, such as in Pb-Pb collisions, which happen at a centre-of-mass of 2.8 TeV per nucleon with a peak luminosity of $10^{27}\,\mathrm{cm}^{2}\,\mathrm{s}^{-1}$. In this thesis, only proton-proton collisions are being described and investigated.

Since 2010 LHC has delivered data in different runs. During Run 1 (2010-2012), protons have collided at a centre-of-mass energy of $\sqrt{s} = 7$ TeV in 2010-2011 and $\sqrt{s} = 8$ TeV in 2012. Run 2 data-taking took place between 2015 and 2018, and the energy was increased to $\sqrt{s} = 13$ TeV. After three years of shutdown (LS2), Run 3 started on the 5^{th}

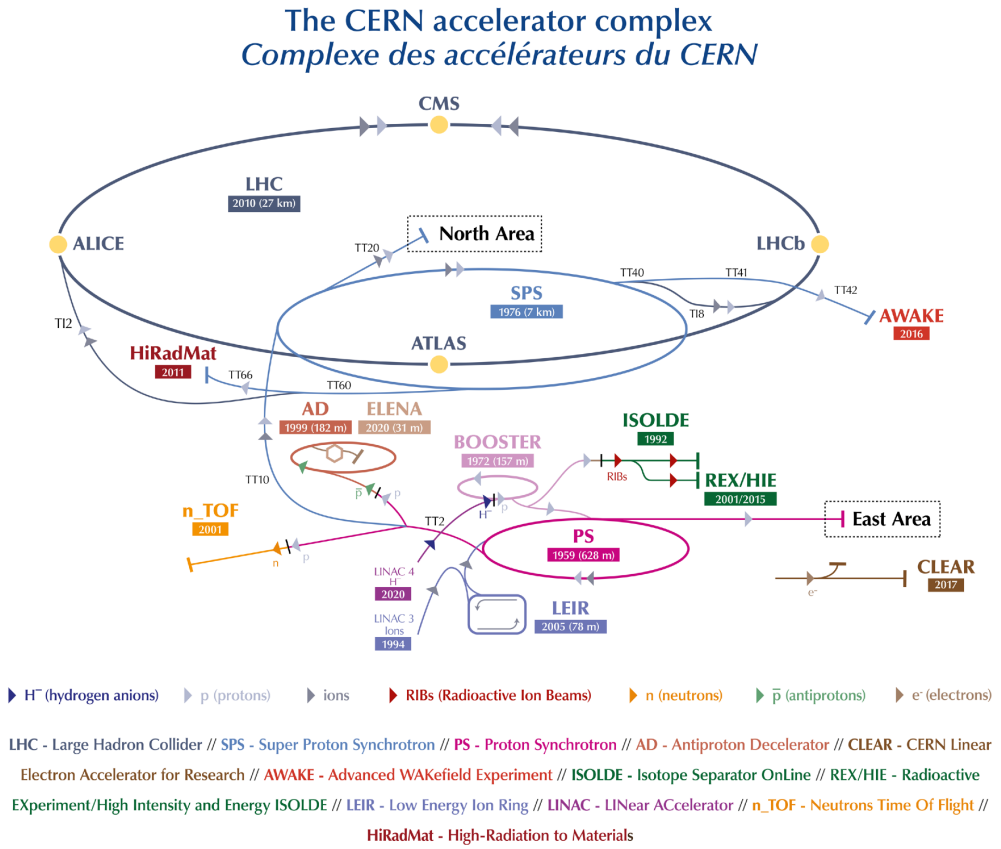

Figure 4.1: Schematic view of the CERN accelerator complex [96].

of July 2022, with the first collisions at a centre-of-mass energy of $\sqrt{s} = 13.5$ TeV. More information about Run 3 and the LHCb upgrade can be found in next chapter, Sec. 7.1.

The LHC machine is composed by two separate rings in which two counter-rotating proton beams circulate. Superconducting magnets maintain the circular trajectory producing magnetic field around 8 T. In order to ensure the highest performances, these are kept at a temperature of 1.9 K ($-271.3°$C) using a cryostat of superfluid He.

The colliding protons are obtained from ionised hydrogen atoms. Protons are accelerated in consecutive steps by a complex system of machines, as shown in Fig. 4.1. First, protons are injected in the LINAC 2 (replaced by LINAC 4 in 2020), a linear accelerator. Afterwards, protons, organised in small packages, enter the Proton Synchrotron Booster (PSB) with an energy of 50 MeV. The PSB can accelerate protons at energies up to 1 GeV. After this, the protons are injected in the Proton Synchrotron (PS), reaching an energy of 26 GeV. Next, they are passed to the Super Proton Synchrotron (SPS) where they are accelerated up to an energy of 450 GeV, before being finally injected to the LHC (TI2 and TI8). Here they are accelerated up to the final energy before collision. In the

LHC, hadrons are organised in small packages, named *bunches*. At the nominal operation regime, the LHC rings store 2808 proton bunches per ring, each one containing about 1.1 10^{11} protons, colliding at a 40 MHz frequency (*i.e.* a collision every 25 ns).

In order to induce hadronic collisions, the beams are slightly deviated at four points of the LHC, where the main LHC experiments are situated: ATLAS (A Toroidal LHC Apparatus), CMS (Compact Muon Solenoid), ALICE (A Large Ion Collider Experiment) and LHCb (Large Hadron Collider beauty).

ATLAS [97] and CMS [98] are general-purpose detectors (GPDs), having a wide range of physics in their program. The discovery of the Higgs boson in 2012 [99, 100] is their most remarkable achievement. In addition to the search and the study of the properties of the Higgs, their program spans to search for new physics particles, dark matter, long lived particles and more. Their design is optimised to study unstable heavy particles, which usually have large transverse momentum with respect to the beam direction.

ALICE [101] is mainly designed to study the strong interaction in the Quark Gluon Plasma (QGP). It is optimised to operate in a high multiplicity environment, detecting the products of heavy ion collisions at high energies.

Finally, the LHCb experiment [102] is mainly dedicated to heavy flavour physics measurements. Its primary goal is to look for indirect evidence of new physics in *CP*-violating processes and rare decays of beauty and charm hadrons [103]. In particular, LHCb was the first experiment to observe *CP* violation in the charm sector [104] and in the B_s^0 system [105,106]. Nevertheless, LHCb has demonstrated that it is capable of having a wider physics program, unforeseen before the beginning of data-taking. This includes heavy-ion collisions studies [107], precise measurement of SM properties, such as the W^+ boson mass [108], studies of spectroscopy with observation of new resonances compatible with tetraquarks and pentaquarks [2, 3, 109], studies of semitauonic decays [47, 53, 54] and searches in the dark sector [110].

4.2 The LHCb detector

The LHCb experiment [102] is designed and optimised for the study of heavy flavour hadrons. It is a single-arm forward spectrometer, in contrast to the other LHC experiments.

The detector geometry is chosen based on the direction of the $b\bar{b}$ pair production. In a pp collision, the outgoing b quarks are strongly boosted along the beam-line, because of the average imbalance in momentum of the two partons. As a consequence, the b hadrons at the LHC are produced in the same forward or backward hemisphere and with a small angle with respect to the beam direction. The spectrometer geometrical acceptance lies between 10 and 300 mrad in the horizontal plane xz and between 10 and 250 mrad in the vertical plane (yz). This is clear in Fig. 4.2(a), representing $b\bar{b}$ pairs produced at $\sqrt{s}$ of 14 TeV as a function of their angle, simulated by Pythia [111]. The difference between horizontal and vertical acceptances is due to the fact that the horizontal plane is also the

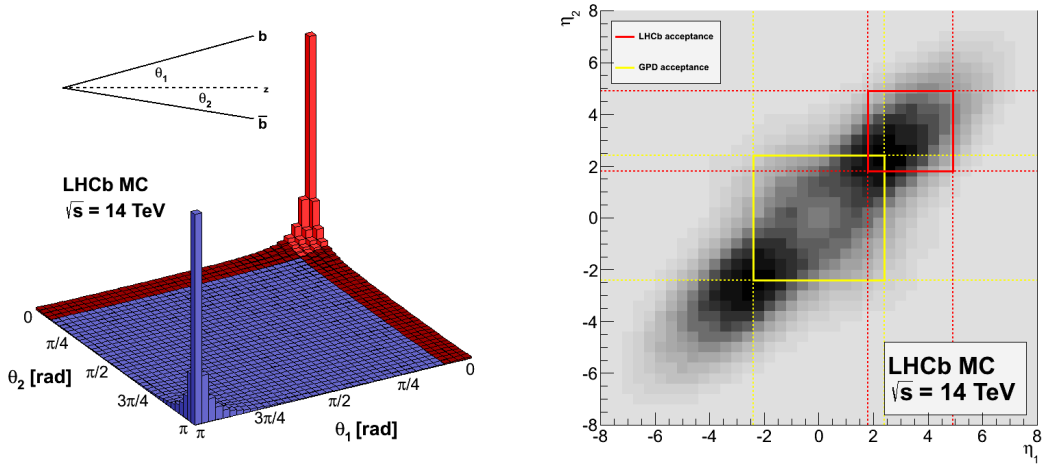

(a) (b)

Figure 4.2: Left: angular distribution of $b\bar{b}$ pair production in pp collisions at $\sqrt{s} = 14$ TeV. Right: comparison of LHCb pseudorapidity coverage of $b\bar{b}$ pairs vs a standard GPD [112].

bending plane for the charged particles deflected by the magnetic field (see Sec. 4.2.5). The geometrical acceptance can be written in terms of pseudorapidity η, which is defined as

$$\eta = -\ln \tan\left(\frac{\theta}{2}\right) \,, \, , \tag{4.1}$$

where θ is the angle between the particle and the beam axis. For tracks inside the LHCb geometrical acceptance $2 < \eta < 5$. The LHCb acceptance, compared to a general GPD, allows to maximise the number of $b\bar{b}$ pairs, as shown in Fig. 4.2(b).

In addition to the acceptance an important feature that differentiates LHCb from the GPDs is the luminosity. Flavour physics measurements rely on highly precise vertex resolution, so the the average number of pp interactions in visible events, the *pile-up*, is required to be very low. On average, only about one visible pp interaction per bunch crossing (named μ [113]) is allowed, resulting in a pile-up of about 1.5. Otherwise, operating at higher pile-up would increase the occupancy, complicating the reconstruction and the discrimination of signal and background events. Therefore, the LHCb detector operates at an average instantaneous luminosity of 4×10^{32} cm^{-2} s^{-1}, one order of magnitude lower than ATLAS and CMS, as shown in Fig. 4.3. During Run 1 and Run 2 data-taking LHCb recorded an integrated luminosity of about 3 fb^{-1} and 6 fb^{-1}, respectively.

In Fig. 4.4 a schematic view of the LHCb detector, with its sub-detectors and the magnet, is represented. Based on the functionality, they can be divided into two categories: the tracking and the particle identification (PID) systems.

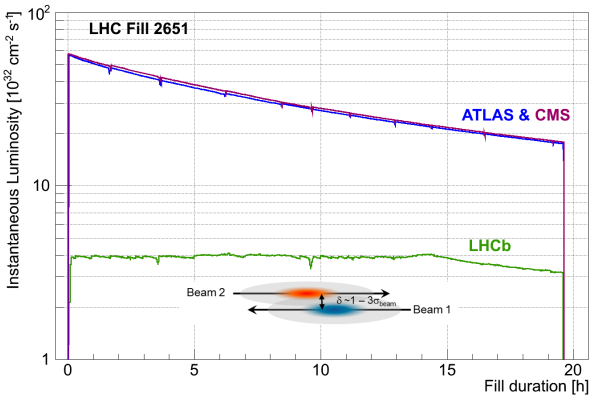

Figure 4.3: Instantaneous luminosity for ATLAS (blue), CMS (purple) and LHCb (green) during LHC fill 2651 as a function of time [114].

- **Tracking systems:** VELO (VErtex LOcator), Tracker Turicensis (TT) and T1-T3 stations. The VELO is a system which identifies the primary and secondary interaction vertices and it is situated around the beam interaction point. The Tracker Turicensis (TT) is placed before the magnet and the other three station after it. Each station is divided in two parts, the Inner Tracker (IT), which, together with the TT, forms the Silicon Tracker (ST), and the Outer Tracker (OT). The ST and OT tasks are the reconstruction of the tracks and the measurement of the particle's momentum.

  The tracking systems are described in more detail in Sections 4.2.1, 4.2.3, 4.2.4, respectively. Finally, track reconstruction is described in detail in Sec. 4.3.1

- **PID systems:** The particle identification is composed of two Ring Imaging Cherenkov detectors (RICH1 and RICH2), the calorimeters system and five muon stations (M1–M5). RICH1, the first Cherenkov detector, is placed immediately after the VELO, while the second, RICH2, is placed after the Tracking Stations. The main task of the two RICH detectors is the discrimination of pions, kaons, and protons, that they achieve for particles with momentum up to 150 GeV/c. The calorimeters system is divided in four sub-detectors: Scintillator Pad Detector (SPD), Pre-Shower (PS) and Electromagnetic and Hadronic calorimeters (named ECAL and HCAL, respectively). The system measures the energy of the particles that hit the sub-detectors. While the ECAL measures e^+, e^- and γ energies, the HCAL measures hadrons energies. At the end of the LHCb detector five MultiWire Proportional Chambers (MWPCs), spaced with iron filters, are used to identify muons.

  The PID systems are described in detail in Sec. 4.2.2, 4.2.6 and 4.2.7. LHCb particle identification methods are described in Sec. 4.3.2.

- **The magnet** is fundamental for both tracking and PID. Magnetic fields deflect the

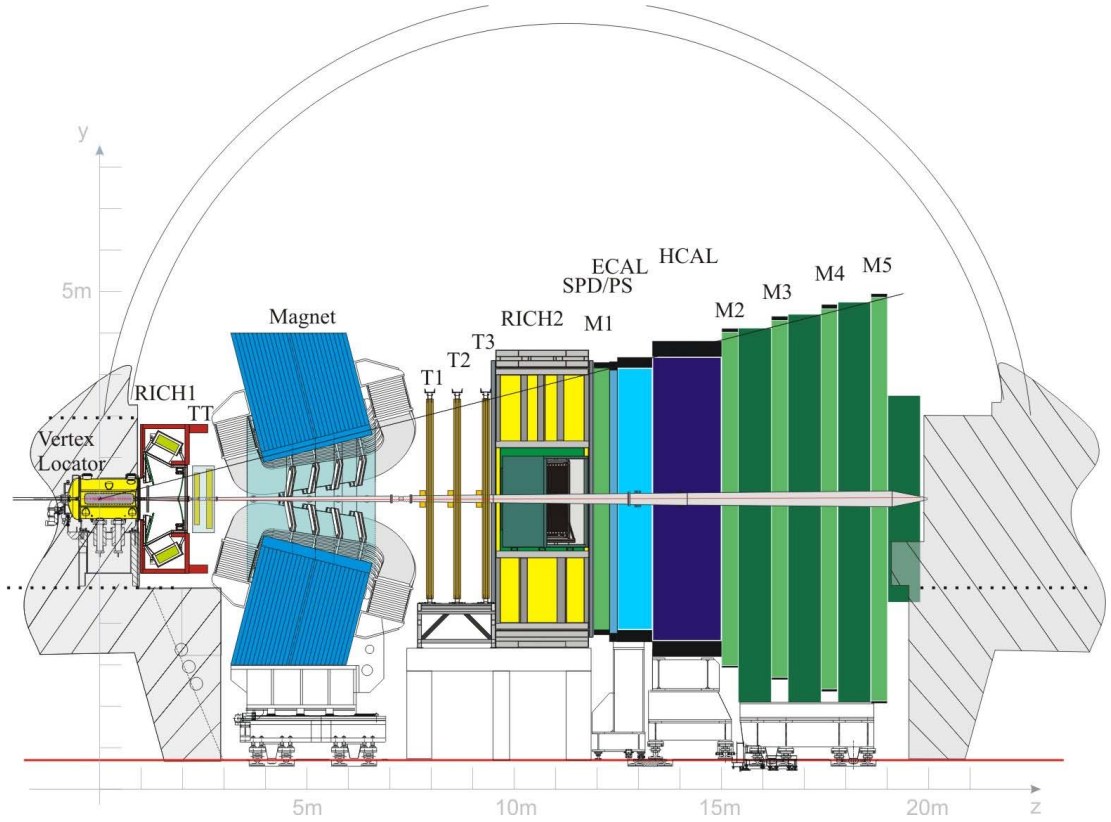

Figure 4.4: Schematic view of the LHCb detector. From left to right: VELO, RICH1, TT, Magnet, the three Tracking Stations, RICH2, SPD, PS, Electromagnetic Calorimeter (ECAL), Hadronic Calorimeter (HCAL) and the five Muon Stations [102].

trajectory of charged particles. The curvature is used to measure the momentum and the verse to extract the charge of the particle. The LHCb magnet is described in Sec. 4.2.5.

Moreover, an important feature for the detector is the ability to discriminate events of interest from the dominant background. For this goal, the first step is done by the trigger system, described in detail in Sec. 4.2.8. Finally, in section 4.3, the LHCb software and workflow are presented.

4.2.1 Vertex Locator (VELO)

The main signature of b-hadron decays at LHCb is the large mean distance of flight, typically about 1 cm. Therefore, measuring with high precision the position of the interaction vertices is crucial. This allows to select signal events and reject most of the background in a high multiplicity environment.

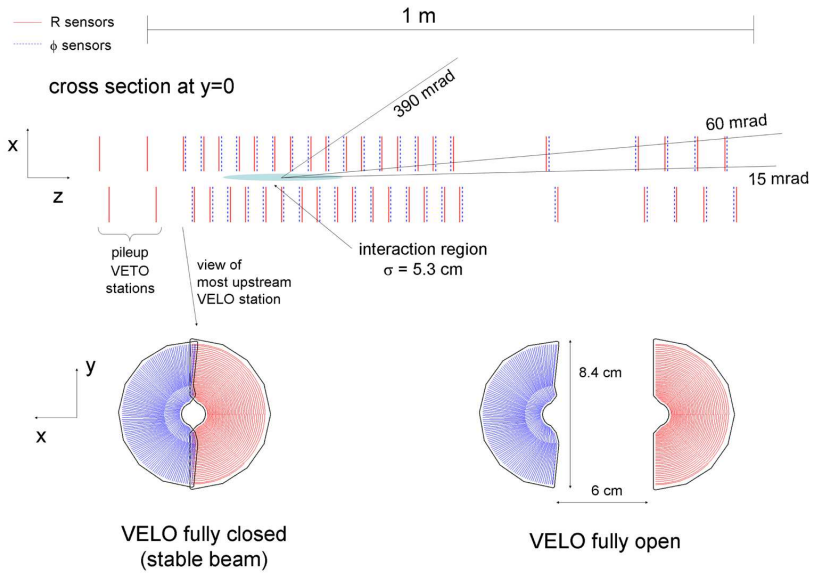

Figure 4.5: Top: xz plane section of the VELO silicon sensors at $y = 0$. Bottom: frontal view of the modules in the closed (left) and open positions (right) [102].

The VELO [115, 116] sub-detector is located close to the pp interaction region, surrounding the beam pipe. It is composed of 21 circular silicon modules, installed perpendicularly along the beam line, as shown in the top part of Fig. 4.5. The modules are situated in a secondary vacuum, separated from the primary LHC vacuum where the primary collisions occur. The region facing the beam (named RF foil) is only 0.3 mm thick, in order to minimise the degradation of the momentum measurement of particles due to multiple scattering, .

Each VELO sensor is divided in two halves and installed on a movable device in order to allow to change the position during different phases of the experiment, as represented in the bottom part of Fig. 4.5. During the beam-stabilisation, the VELO is in the "open" configuration. The VELO is closed during the data-taking phase and the two parts of the modules are partly overlapped in order to achieve a better geometrical coverage. In this configuration, the distance between the centre of the modules and the beam pipe is 7 mm, smaller than the aperture required by the LHC during injection.

The modules are composed by two planes of 220 µm thick silicon micro-strip sensors, able to measure the radial distance from the beam (R) and the polar angle (ϕ) of hits generated by the ionising particles that cross the VELO. The coordinate z is simply measured knowing what module gives a signal for a particular hit.

The R sensors are divided in four parts per half, each one covering about 45°. The micro-strips composing these are modelled in a semi-circular shape and their width increases as the distance from the centre becomes greater, because the majority of the

particles are expected to be near the beam axis (*i.e.* in high η regions). The micro-strips width ranges from 40 µm near the center to 92 µm far from the beam.

The ϕ sensors are divided in an inner and an outer region. The latter starts at a radius of 17.25 mm and its pitch is set to be roughly half (39.3 µm) than that of the inner region, which is 78.3 µm and ends at the same radius. In order to improve pattern recognition, the two regions have different skew to the radial direction: the inner one is tilted by 20° and the other by 10°. Furthermore, to improve the track reconstruction, the longitudinally adjacent ϕ sensors have opposite skew to each other.

The performances of the VELO detector have been analysed using the the data collected in 2010 and 2011 [117]. The resolution on the x and y hit coordinates ranges from 40 µm to 10 µm depending on the number of tracks used to form a vertex, while the resolution on the z coordinate ranges from 250 µm to 50 µm, for the same reason.

4.2.2 The Ring-Imaging Cherenkov detectors (RICH)

For the discrimination of charged pions, kaons and protons in a momentum range between few GeV/c up to about 150 GeV/c, two Ring Imaging Cherenkov detectors are used: RICH1, installed immediately after the VELO, and RICH2, positioned after the tracking stations [118].

Cherenkov detectors are composed by chambers filled with a fluid or other refractive medium and instrumented with photon detectors, exploiting the light emitted by particles that travel faster than light in that medium. The Cherenkov photon emission angle θ_C depends on the refraction index n of the radiator by

$$\cos(\theta_C) = \frac{1}{\beta n}, \tag{4.2}$$

where $\beta = v/c$ is the particle velocity with respect to the speed of light in vacuum. From this relation, it is possible to notice that Cherenkov light is emitted only by those particles with $c/n < v < c$. For instance, if $v = c/n$ then $\cos(\theta_C) = 1$ and so $\theta_C = 0$, while if $v = c$ then $\cos(\theta_C) = 1/n$ and so $\theta_C = \arccos(1/n)$. Thus, it is evident that for particles approaching the speed of light the Cherenkov angle will saturate at the value $\theta_C = \arccos(1/n)$. For these reasons, it is necessary to have different refraction index radiators in order to discriminate particles in a wide range of momenta.

RICH1 is optimised to identify tracks with medium-low momentum, between 1 GeV/c and about 50 GeV/c. The structure of the apparatus is reported in the left part of Fig. 4.6. The RICH1 is placed immediately after the VELO and its geometrical acceptance (between 25 mrad to 330 mrad) is enough to cover the LHCb detector acceptance. There are two different types of radiators inside RICH1, as shown in Fig. 4.6(a). The first one is a 5 cm thick Aerogel layer, in yellow, with a refraction index $n = 1.03$, which is suitable for low momentum particles. The second radiator is gaseous C_4F_{10} (light blue, $n = 1.0015$) filling the remaining part of the detector and it is employed to detect particles with momenta up to 50 GeV/c.

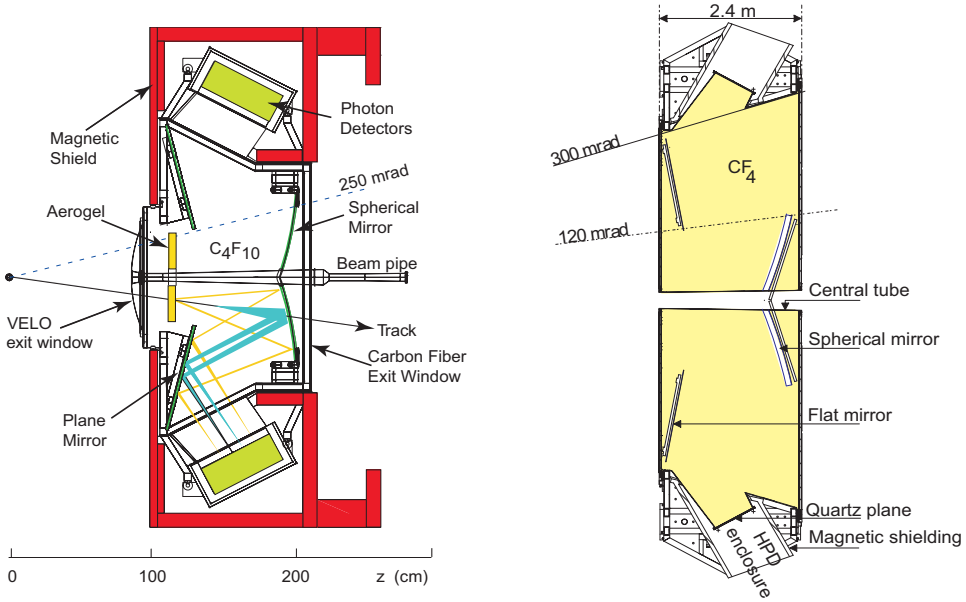

(a) (b)

Figure 4.6: Overview of the RICH1 (left) and the RICH2 (right) detectors [102].

RICH2 is located behind the last tracking station and has the structure shown in Fig. 4.6(b). Its geometrical acceptance covers the region of the detector where most of high momentum particles are found: 120 mrad in the vertical plane and 100 mrad in the horizontal plane. The radiator chosen is gaseous CF_4, with a refraction index $n = 1.00046$, optimal for the higher momentum region, up to about 150 GeV/c. Fig. 4.7 represents Cherenkov emission angles as a function of the momentum for the different RICH radiators.

Thanks to a system composed of spherical and plane mirrors, the Cherenkov photons emitted in both detectors are conveyed onto a lattice of photo-detectors, the Hybrid Photon Detectors (HPDs). The HPDs are placed in both sub-detectors outside the LHCb detector acceptance and they are shielded against the residual magnetic field. This feature is particularly important for RICH1, since the residual magnetic field is not negligible. The shielding is necessary in order to allow the HPDs to operate properly: the photo-electrons could be bent by the residual magnetic field reducing the HPDs performances. This configuration allows to have optimal results with rise and fall times of the signal of about 1 ns.

4.2.3 The Silicon Tracker (ST)

The Silicon Tracker covers the region close to the beam pipe. It is composed by two silicon micro-strip detectors: the Tracker Turicensis (TT) and the Inner Tracker (IT) [119].

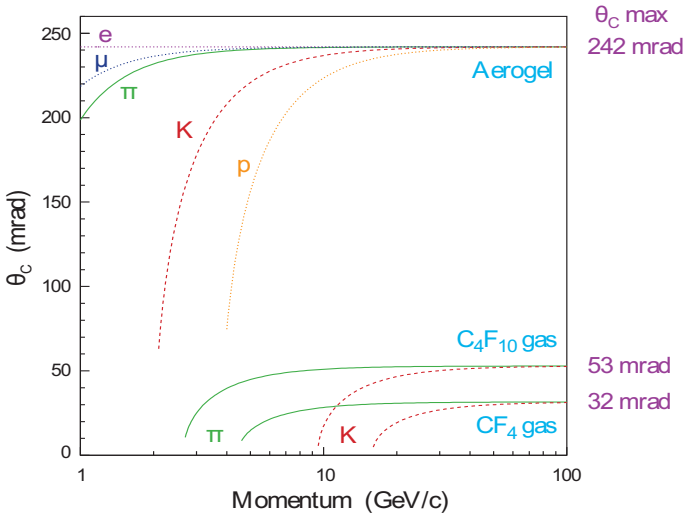

Figure 4.7: Reconstructed Cherenkov emission angles as a function of momentum for the RICH radiators [102].

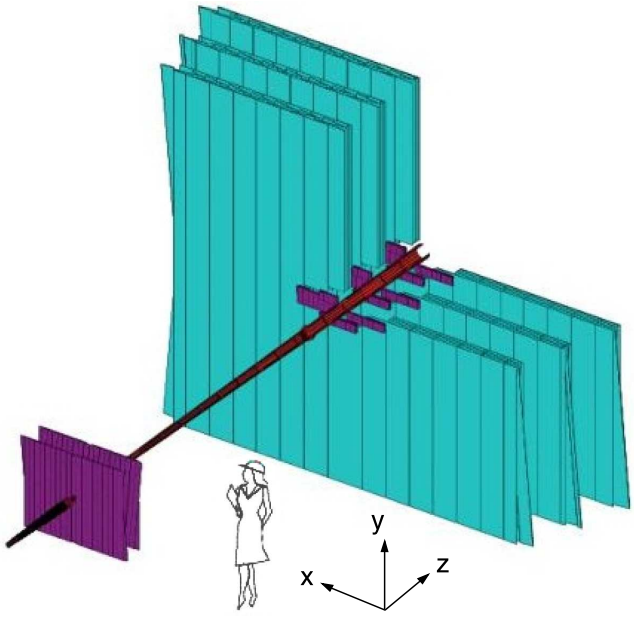

Figure 4.8: Tracking stations location with respect to the beam pipe. OT represented in cyan and ST (TT and IT) in violet [102].

These are visible in Fig. 4.8, in violet.

The TT is situated after the RICH1 detector and before the magnet. The TT's goal is to provide reference segments used to combine the track reconstructed in the tracking stations with those reconstructed in the VELO, in order to improve the momentum and position resolution. The dipole magnet produces an integrated magnetic field of 0.15 Tm in the space between the VELO and the TT station, so the track transverse momentum can be estimated with a resolution of $\delta p_{\mathrm{T}}/p_{\mathrm{T}} = 25\%$ at $p_{\mathrm{T}} = 1\,\mathrm{GeV}/c$. The system is composed by four stations, divided in two groups called respectively TTa and TTb, at a distance of about 30 cm one from the other and placed approximately 2.4 m after the beam interaction region. Each station covers a rectangular region of about 120 cm in height and about 150 cm in width. In the first and fourth stations the strips are parallel to the vertical plane, while in the second and third stations they are tilted by $+5°$ (u-layer) and $-5°$ (v-layer) respectively, in order to improve the precision of the track reconstruction.

The Inner Tracker is composed by the three inner parts of the stations T1, T2 and T3. Each IT station is arranged around the beam pipe and consists of four individual detector boxes, each one containing four detection layers. Each detection layer is composed by seven detector modules and each module is formed by one or two silicon sensors and a readout hybrid. The detection layers are positioned in the same way as the TT. On the other hand, the side boxes have two ladders of micro-strips, with those of the lower sensor connected in series with those of the upper sensor to a single readout channel, while the top and bottom boxes have only one micro-strips ladder. The total IT size is about 1.2 m in the bending plane and about 40 cm in the vertical plane.

4.2.4 The Outer Tracker (OT)

The Outer Tracker [120] is a gas-filled straw tube detector, covering about 99% of the summed surface of the T1-T3 tracker stations, as shown in Fig. 4.8. For each tracking station there are four planes of straw tubes arranged in the same way as the TT and IT silicon micro-strip sensors: the first and the fourth with tubes parallel to the vertical plane, while the second and the third with tubes tilted by $\pm 5°$ (u-layer and v-layer). Each plane is composed of two rows of tubes, arranged in a honeycomb structure. These tubes have a radius of 5 mm and are filled with a mixture of $\mathrm{Ar}/\mathrm{CF}_4/\mathrm{CO}_2$. The anode wire is supported and centred with a precision better than 100 µm by locator pieces at the tube ends. Unlike other tracking detectors here described, the OT measures drift times rather than pulse heights. Due to the limited drift speed of the gas mixture, the readout time window exceeds a single LHC bunch crossing interval. The OT spacial resolution is better than 200 µm.

4.2.5 Magnet

The LHCb magnet is placed between the TT and the first tracking station T1, as seen in Fig. 4.4. It is a warm dipole, made of non superconducting material, which

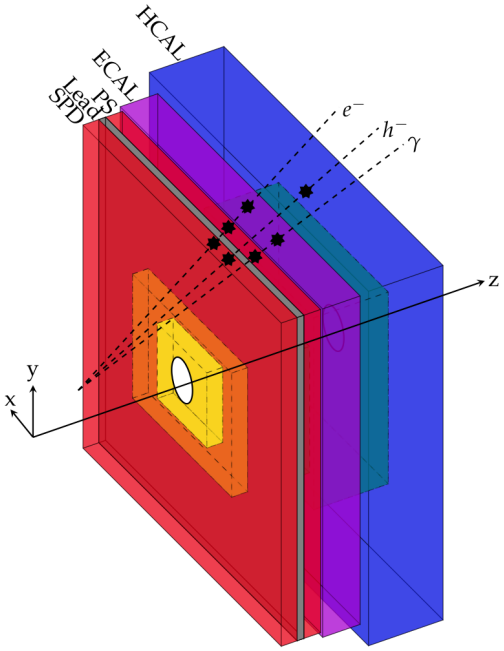

Figure 4.9: Schematic view of the energy deposit in the calorimeters sub-detectors for different particles [123].

does not require very low temperatures to operate [121]. The magnet geometry has been chosen considering the detector acceptance. It is formed by two coils shaped in order to widen as the z coordinate increases, as can be seen in the top part of Fig. 4.15(a). The magnetic field is oriented along the y coordinate, perpendicular to the x-z plane, referred to as the bending plane. The maximum intensity of the magnetic field is about 1 T, and the magnetic field integral is 4 Tm. In order to allow the evaluation of any left-right asymmetry in the detector, the polarity of the magnetic field is flipped during the data-taking.

4.2.6 Calorimeters

The calorimeters system is used to measure hadrons, electron and photon energies. As a consequence, it gives information for their identification and it provides important information for the Level-0 (L0) trigger (see Sec. 4.2.8.1), evaluating hadron, electron and photon transverse energy E_{T}. The calorimeter system is divided into four sub-detectors [122], sketched in Fig. 4.9: Scintillator Pad Detector (SPD), Pre-Shower (PS), Electromagnetic Calorimeter (ECAL) and Hadronic Calorimeter (HCAL).

Each sub-detector is divided into regions with different dimensions and sensors sizes, as summarised in Fig. 4.10. In order to reach a compromise between occupancy and the number of read-out channels, the sensor size increases with the distance from the beam

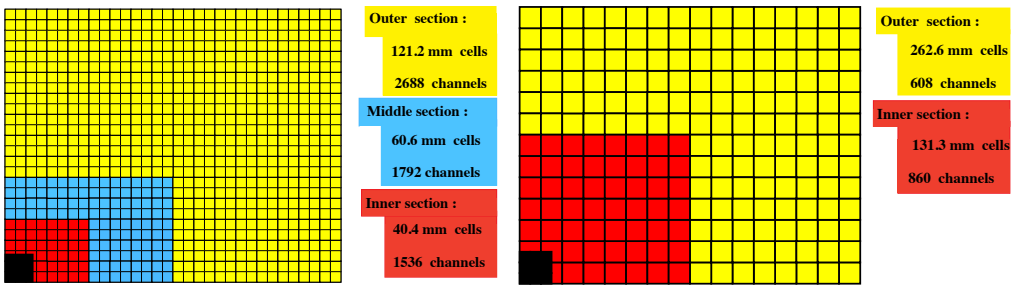

Figure 4.10: Segmentation of the calorimeters system for SPD, PS and ECAL on the left and HCAL on the right. Only a quarter of the detector is shown, the bottom-left point correspond to the beam pipe [102].

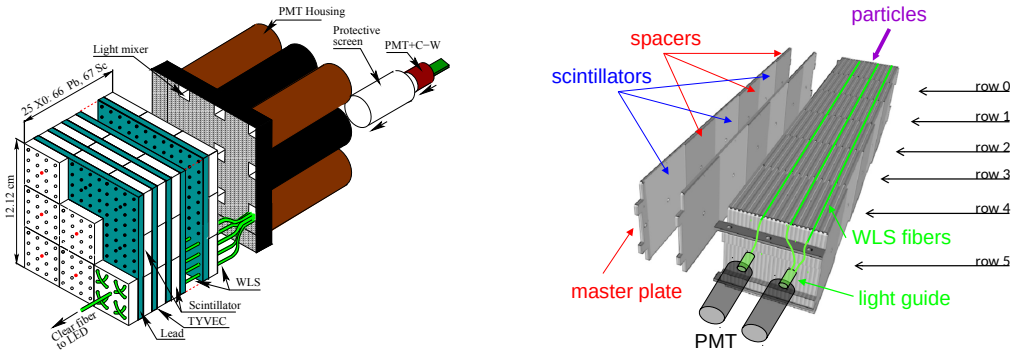

(a) (b)

Figure 4.11: Overview of the modules for HCAL (left) and the HCAL (right) detectors. Figures extracted from [125].

pipe. SPD, PS and ECAL are divided in inner, middle and outer regions, while HCAL is divided in two parts (inner and outer).

The **SPD** and the **PS** are made of scintillating materials and are auxiliary to the electromagnetic calorimeter. The SPD is used to discriminate between charged and neutral, by exploiting the fact that neutral particles do not emit light when crossing a scintillator. The PS is used to obtain a better discrimination between electrons and pions. Both detectors consist of about 6000 scintillating pads with a thickness of 15 mm, interspaced with a 2.5 radiation lengths (X_0), which corresponds to the distance over which the energy of an electron is reduced by a factor $1/e$ only due radiation loss [124]. The scintillating pads are interspaced with a lead converter. The light produced is collected using wavelength-shifting fibers (WLS), used to transmit the light to multi-anode photomultipliers (MAPMTs) located outside the detector.

The **ECAL** is a sampling calorimeter built using Shashlik technology and separated in

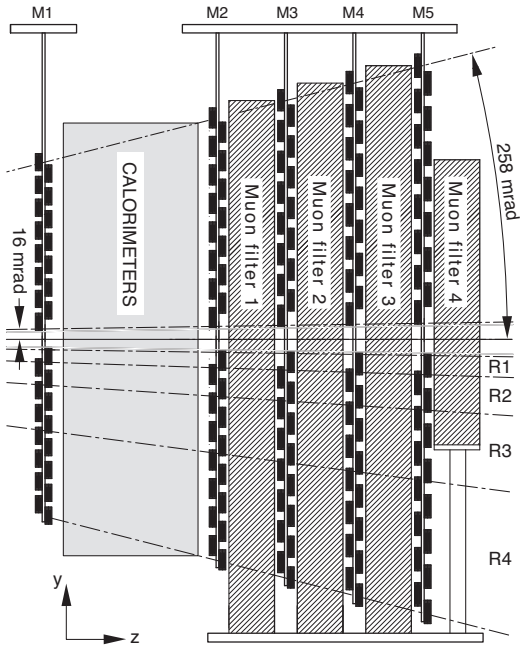

Figure 4.12: Overview of the muon sub-detector in the y-z plane, showing the division in R1-R4 regions [102].

independent modules [126,127]. These are sampling calorimeters in which the scintillation light is conveyed by WLS fibers running perpendicularly to the converter/absorber plates. This technique offers the advantages of an easy assembly, good hermiticity and fast time response. Each ECAL module, as shown in Fig. 4.11(a), is composed of 66 lead converter layers (2 mm thick), each one installed between two plastic scintillator layers 4 mm thick, resulting in about 25 radiation lengths and 1.1 nuclear interaction lengths. The WLS fibers bring the light produced by the scintillator material to the read-out photo-multipliers in the back part of the module. In the inner region, each module has a section of 4×4 cm^2, with 9 read-out channels per module; the middle region contains modules with a section of 6×6 cm^2 and 4 read-out channels. Finally, the outer region is composed of 12×12 cm^2 modules with one channel each.

The **HCAL** main task it to measure the energies of hadronic showers, thus providing fundamental information for the Level-0 trigger (see Sec. 4.2.8). The HCAL structure is very similar to that of the ECAL. As represented in Fig. 4.11(b), each module is composed of scintillator layers 4 mm thick, interleaved with steel layers 16 mm thick. This corresponds to roughly 5.6 nuclear interaction lengths in total. The module section is 13×13 cm^2 for the inner region and 26×26 cm^2 for the outer region.

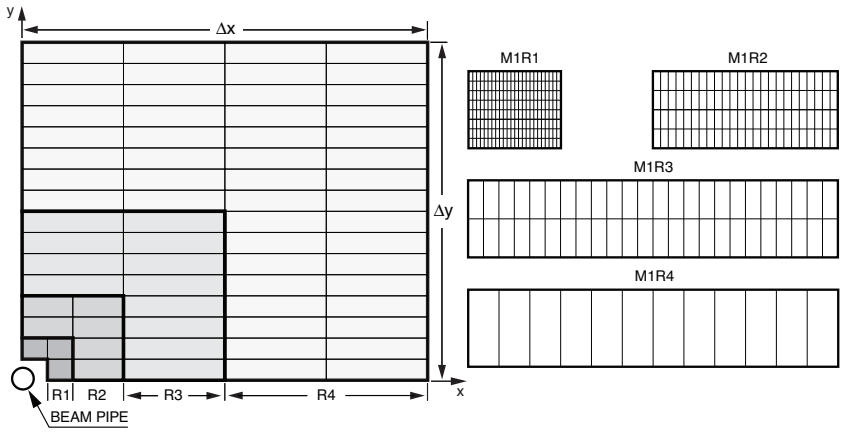

Figure 4.13: Frontal view of a muon station section, where each rectangle represents a chamber (left) and the different segmentation types of the four chambers (right) [102].

4.2.7 Muon stations

To discriminate muons against the abundant hadronic background, muon candidates are formed from aligned hits in each of the five stations of the sub-detector, shown in Fig. 4.12. These stations cover an angular acceptance of 300 mrad in the horizontal plane and 200 mrad in the vertical plane. The geometrical efficiency for the detection of muons coming from b-hadron decays is nearly 46% [128]. In order to avoid possible muon multiple scattering effects, which could modify the particle trajectory, the first muon station M1 is placed before the calorimeters. The remaining four muon station (M2-M5) are placed after the calorimeter system, at the end of the LHCb detector.

In the the inner region of the M1 station, triple-Gas Electron Multiplier (GEM) detectors are employed, while all the other chambers are Multi-Wire Proportional Chambers (MWPC). In total, the detector contains 1380 MWPCs, each has four overlapped gaps, 5 mm thick and with a distance between wires of about 2 mm. The triple-GEM detector consists of three GEM foils sandwiched between anode and cathode planes.

Each muon station is divided into four regions R1-R4, where R1 is the closest to the beam pipe, as it is represented in both Fig. 4.12 and Fig. 4.13. The dimension of the chambers and the segmentation of each region increase as the distance from the beam pipe becomes greater. In particular, the segmentation increases in a ratio $1 : 2 : 4 : 8$ (see Fig. 4.13). As a consequence, the charged particle occupancy is expected to be about the same in each region.

4.2.8 Trigger

In order to accept selected candidates while rejecting most of the background events at the same time, a sophisticated trigger system is fundamental. The LHCb trigger has

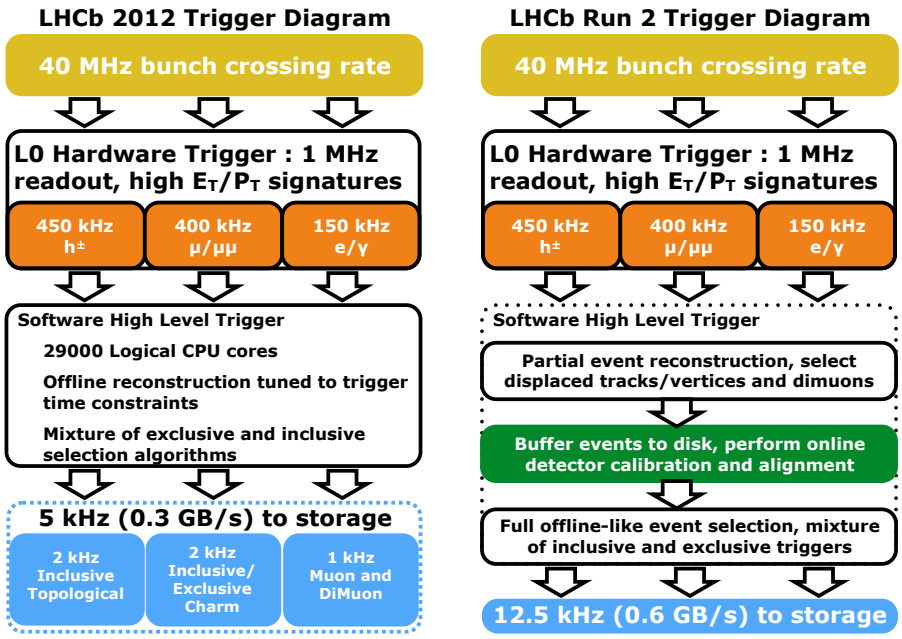

Figure 4.14: The LHCb trigger scheme for Run 1 (left) and Run 2 (right) [131].

been developed to work at the 40 MHz bunch crossing frequency of the LHC (during Run 1 and Run 2) and to reduce it to a rate manageable by the LHCb software framework [129].

The instantaneous luminosity of LHCb operation is lower than the one of CMS and ATLAS, as seen in Fig. 4.3. In any case, physical events occurs at about $\sim$ 10 MHz, so the only way to reach the desired performance is to divide the trigger into different levels, each processing the output of the previous. In particular, the LHCb trigger system is divided into three levels: the first level, implemented the hardware, Level-0 (L0), and the software trigger, separated in two levels, High Level Trigger 1 (HLT1) and High Level Trigger 2 (HLT2). The software package for the HLT is called Moore.

A summary of the trigger strategies used is reported in Fig. 4.14, where Run 1 strategy is on the left and the Run 2 on the right. The hardware trigger reduces the rate from 40 MHz, to an output of 1 MHz. Afterwards, the events are filtered by the High Level Trigger, resulting in an output rate of about 12 MHz (5 MHz) in Run 2 (Run 1). The output of the Run 2 trigger rate is distributed in three different streams: the *full, Turbo* and *TurCal* streams [130]. Events entering the *full* stream have a trigger reconstruction with a low quality to fit into online time constraints and are reconstructed offline by a separate application, persisting the information from all the subdetectors. In the *Turbo* streams the reconstruction can occur also at the trigger level. Hence, for the *Turbo* and the *TurCal* (*Turbo* + *calibration*) streams, a reduced format of the event is persisted. A detailed description of the various trigger levels for Run 2 is given in this section.

L0 trigger	E_T/p_T threshold			SPD threshold
	2015	2016	2017	
Hadron	> 3.6 GeV	> 3.7 GeV	> 3.46 GeV	< 450
Photon	> 2.7 GeV	> 2.78 GeV	> 2.47 GeV	< 450
Electron	> 2.7 GeV	> 2.4 GeV	> 2.11 GeV	< 450
Muon	> 2.8 GeV	> 1.8 GeV	> 1.35 GeV	< 450
Muon high p_T	> 6.0 GeV	> 6.0 GeV	> 6.0 GeV	none
Dimuon	> 1.69 GeV^2	> 2.25 GeV^2	> 1.69 GeV^2	< 900

Table 4.1: L0 trigger E_T/p_T thresholds used in 2015, 2016 and 2017 for the different trigger lines [131].

4.2.8.1 Level-0 Trigger

The L0 trigger is based on custom electronics, and it is designed to perform a first filtering of the events, aiming to an output rate of only 1 MHz. L0 uses information coming mainly from the tracking and from the calorimeters system. At this level, the trigger decides to keep or discard events based on measurements of p_T and E_T of the particles composing the event. Three independent systems running in parallel are used to discriminate electrons and photons (SPD/PS and ECAL output), hadrons (HCAL output) and muons (muon stations). A summary of the E_T/p_T requirements for the L0 trigger lines in Run 2 is given in Table 4.1.

Furthermore, since in 2010 and 2011 the detector worked at an input rate four times larger than originally planned, a system to reject high-occupancy events was developed and implemented in the L0 trigger. Thanks to its fast response, the SPD can be used to roughly estimate the number of charged particles per event, accepting only events with less than 600 hits in SPD.

4.2.8.2 The High Level Trigger 1

HLT1 is the second trigger level and it is software based. It aims to filter events in an inclusive way and to reduce the rate of accepted events to 50 kHz, starting from an input rate of about 1 MHz, given by the L0 level. The HLT1 is devoted to the reduction of the input rate from the L0 trigger to a more manageable level by rejecting events with an OT occupancy larger than 20%. In fact, these events would take more than the 25 ms allowed to the HLT1 to take a decision. After this first rough selection, the remaining events are reconstructed, considering the following:

- The particles produced in high-mass b-hadrons decays have larger total, p, and transverse, p_T, momentum compared to other hadrons composed by light quarks.

- The average decay length of b-hadrons produced at the LHC is about 1 cm. Hence,

their decay products have a large impact parameter (IP) with respect to their primary vertex (PV).

- There is at least one final state particle with large p, p_{T} and IP in each b-hadron decay.

- The VELO reconstruction time is fast enough to allow the full information on the primary vertex to be used by the HLT1.

- The full reconstruction can be performed only for a limited number of tracks, because of time limitations.

The last two points are the reason why the reconstruction is divided in two steps. Firstly, VELO tracks and PV are reconstructed. These tracks are selected requiring large IP with respect to the closest PV and a minimum number of hits in the VELO. The track is rejected if the difference between the expected number of hits and the observed number of hits in the VELO is greater than a certain threshold. For example, a typical choice of the requirements is: IP $> 125\,\mu$m, $N^{\mathrm{hits}}_{\mathrm{obs}} > 9$ and $N^{\mathrm{hits}}_{\mathrm{exp}} - N^{\mathrm{hits}}_{\mathrm{obs}} < 3$. Afterwards, forward reconstructed tracks are further selected, requiring minimal p and p_{T} thresholds. Finally, remaining tracks are fitted using a bi-directional Kalman filter to obtain an offline-quality value for the track χ^2 and an offline-quality covariance matrix. This allows a cut on the square significance, χ^2, of the impact parameter IP, *i.e.* χ^2_{IP}. This is the χ^2 of the distance of a track from the PV and it is very efficient in rejecting background contributions, while the track χ^2 is suitable in rejecting ghost tracks (see Sec. 4.3.1).

4.2.8.3 The High Level Trigger 2

The last trigger level, HLT2, is also a completely software based trigger. It takes its input from HLT1 and reduces it to an output rate of about 12 kHz, applying an exclusive selection. The output of HLT2 is finally sent to mass storage. HLT2 filtering is mainly based on three inclusive selections, the so-called topological lines.

The main strategy of topological lines is to build multibody candidates. For all tracks the pion mass hypothesis is adopted. To form a two-body object two particles are combined if they fulfil a cut on the distance of their closest approach (DOCA), for example DOCA $< 0.15\,$mm. After that, if another particle fulfils the DOCA requirement it is added to the two-body object to form a three-body object, and so on, creating n-body objects. This procedure saves CPU time with respect to combining n particles directly.

The HLT2 also contains selection lines exploiting tracks identified as muons. Di-muon candidates are formed and, depending on their mass, selection requirements are applied on the flight distance and p_{T} of the candidate. Single muon candidates are accepted requiring a large p_{T} or a combination of χ^2(IP) and p_{T} requirements.

4.2.8.4 Trigger variables

Trigger information is stored in two boolean variables: TOS and TIS, defined as follow.

- **Trigger On Signal, TOS.** If the particle or a combination of particles have fired the trigger, the TOS variable is `True`. For the i^{th} track t_i of a set of tracks $t_1, ..., t_n$, TOS is defined as

$$\text{TOS}(t_1, ..., t_n) = \text{TOS}(t_1) \texttt{ OR } ... \texttt{ OR } \text{TOS}(t_n) \tag{4.3}$$

  where `OR` represent the logic `OR`.

- **Trigger Independent from Signal, TIS.** If in the event at least another particle passes the trigger requirements, the TIS variable is `True`. For the set of tracks $t_1, ..., t_n$, $\text{TIS}(t_1, ..., t_n)$ cannot be explicitly calculated in terms of $\text{TIS}(t_i)$, since it is not possible to know what particle fires the trigger a priori nor if it is included in $t_1, ..., t_n$.

- **TISTOS.** Combination of TIS and TOS requirements, usually a logic `OR`. Only the events that pass the TIS requirement or the TOS one are saved.

4.3 Reconstruction, PID and software

In this section the framework and techniques used for track reconstruction (Sec. 4.3.1) and particle identitification (PID) (Sec. 4.3.2) are described. Afterwards, in Sec. 4.3.3, the LHCb data and simulation workflow for Run 1 and Run 2 is reported in detail together with a description of the software used.

4.3.1 Track reconstruction at LHCb

In LHCb the trajectories of the charged particles traversing the tracking system are reconstructed from hits in the VELO, TT, IT and OT detectors. As illustrated in Fig. 4.15(a), the tracks are divided in the following categories:

- **Long tracks:** particles generating hits in all tracking sub-detectors.

- **VELO tracks:** particles producing hits only inside the VELO. Since these tracks have a wide angle with respect to the beam pipe, they exit from the detector geometrical acceptance just after the VELO. Moreover, these tracks are used to reconstruct primary vertices with the VELO.

- **Upstream tracks:** tracks produced by particles with a low momentum, producing hits in the VELO and in the TT and kicked off the geometrical acceptance of the

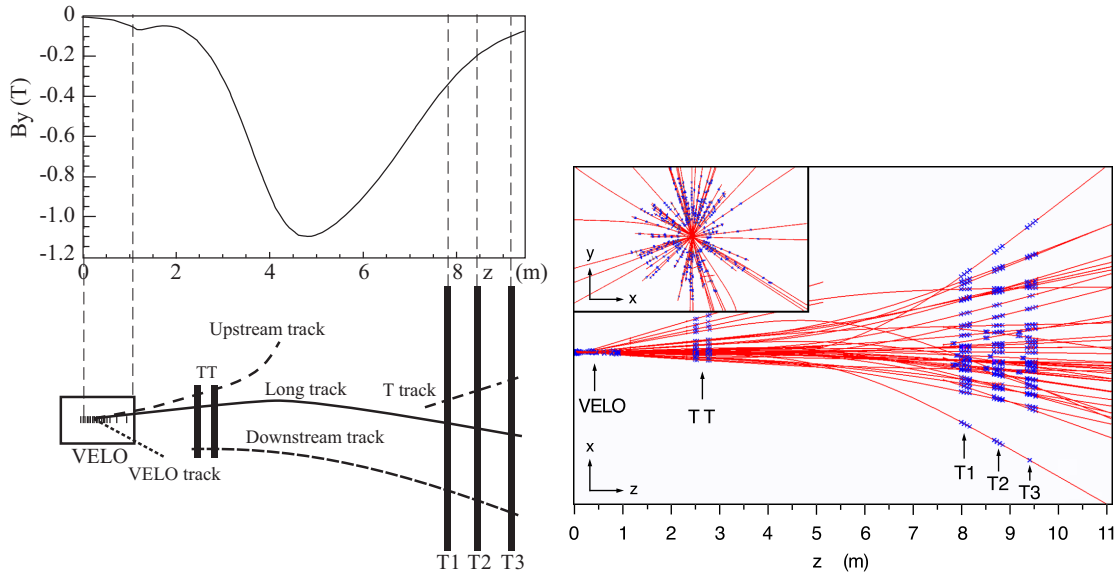

(a) (b)

Figure 4.15: Fig. 4.15(a): Schematic illustration of the various track types (bottom) and main magnetic field component (B_y) as a function of the z coordinate (top). Fig. 4.15(b): Display of the reconstructed tracks (red) and assigned hits (blue) in an event in the xz plane and zoom on the VELO region in xy plane [102].

detector by the magnetic field. It is possible to measure their momentum thanks to the VELO residual magnetic field, even if the measurement is affected by a 20% relative uncertainty.

- **Downstream tracks:** Long lived neutral particles can decay between the VELO and the TT, producing charged particles that generate hits in the TT and in the three tracking stations (T1, T2 and T3).

- **T tracks:** tracks which have hits only in the tracking stations are classified as T tracks.

The reconstructed tracks are then fitted using a Kalman filter. The fit takes into account multiple scattering and corrects for energy loss due to ionisation. The χ^2 per degree of freedom of the fit is used to determine the quality of the reconstructed track.

Fake or *ghost tracks* are defined as the tracks that do not correspond to the trajectory of a charged particle. Because of the large extrapolation distance in traversing the magnet, most of these fake tracks originate from wrong associations between VELO tracks and tracks in the T stations.

The track reconstruction efficiency is measured using a tag-and-probe technique with $J/\psi \to \mu^+\mu^-$ decays [132]. In this method one of the daughter particles, the "tag", is fully reconstructed, while the other muon, the "probe" leg, is only partially reconstructed. An

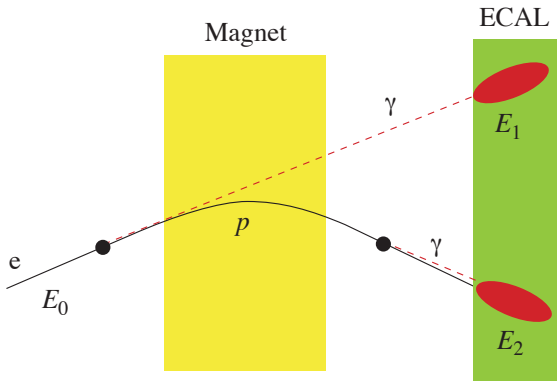

Figure 4.16: Bremsstrahlung energy loss of electrons in LHCb. Black: electron track, red: bremsstrahlung photons trajectory and energy deposit in the ECAL [102].

invariant mass fit is then performed to reconstruct J/ψ candidates. Afterwards, a search for a long track match for the partially reconstructed probe is made and, if found, the candidate is marked as efficient. Finally the efficiency is obtained as the ratio of efficient candidates over the total number of candidates.

4.3.1.1 Electron track reconstruction and Bremsstrahlung recovery

Electrons may lose their energy through Bremsstrahlung radiation before the magnet or when passing through the magnet, as seen in Fig. 4.16. Therefore, long tracks cannot be used for the reconstruction. Hence, a custom tag-and-probe method has been developed [133]. This exploits VELO tracks to reconstruct electrons as long tracks. This utilises a control sample of $B^+ \to J/\psi(\to e^+e^-)K^+$ decays and the reconstruction efficiency of VELO tracks obtained in Ref. [117].

One electron of the $B^+ \to J/\psi(\to e^+e^-)K^+$ decay is fully reconstructed and paired with the K to form the tag side. The other one is reconstructed only in the VELO and used to probe the detection and the reconstruction efficiency.

A kinematic fit is performed for both the tag and probe momentum, by applying a combined J/ψ and B^+ mass constraint and the resulting efficiency is determined as a function of this estimate. This results in a $\mathcal{O}(5\%)$ resolution with respect to the generated momentum information. In order to correct the simulated sample to take into account the energy loss, the efficiency ratio r, is introduced:

$$r = \frac{\varepsilon_{\text{data}}}{\varepsilon_{\text{simulation}}}, \tag{4.4}$$

which is determined as a function of the probe momentum kinematics.

In addition, a kinematical binning in p_{T}, η and ϕ is considered in order to unfold efficiencies. Two ϕ regions are defined by considering the VELO RF-foil: **RF-foil region** for $|\phi - \pi/2| < \pi/8$ or $|\phi + \pi/2| < \pi/8$ and **Non-RF-foil region** for all other phase

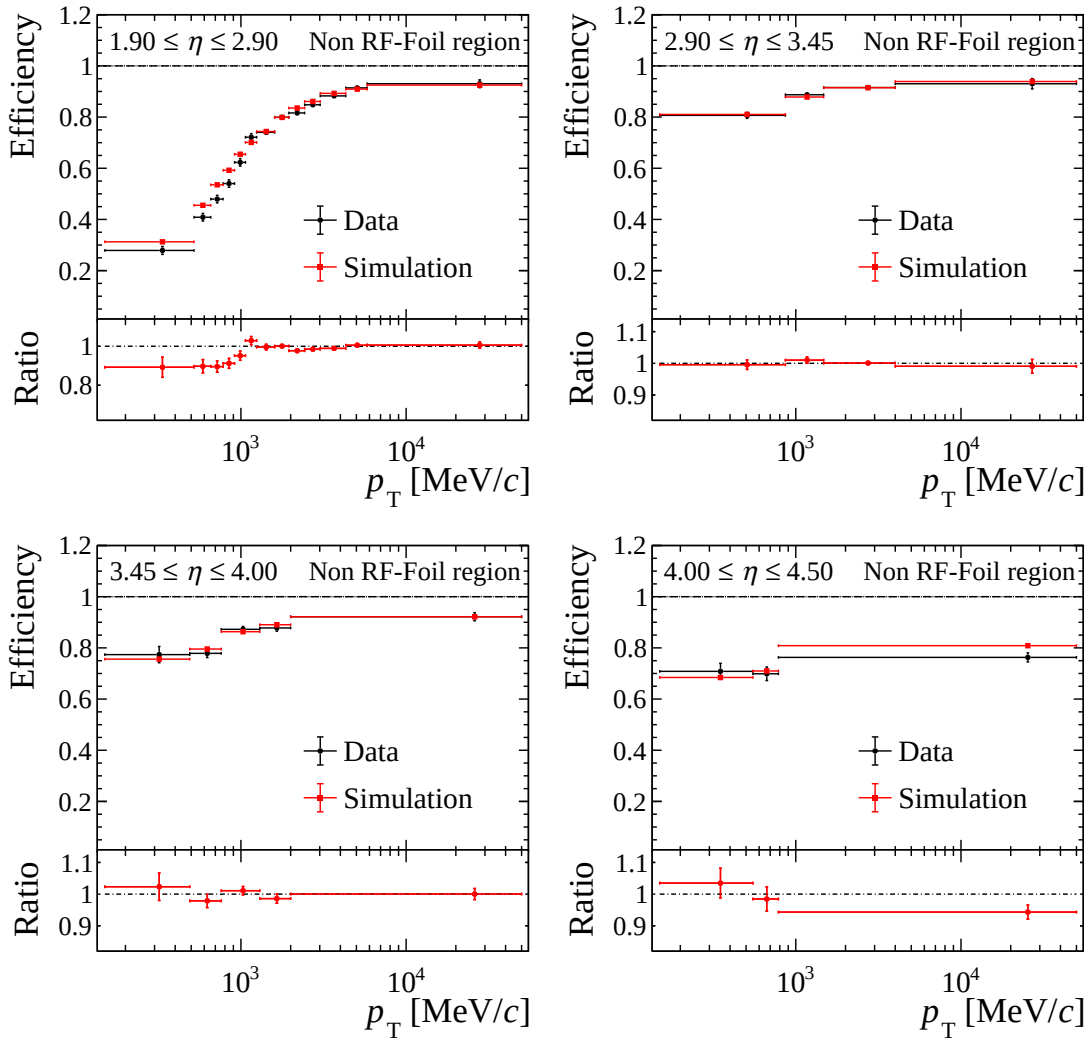

Figure 4.17: Electron detection efficiency (top) and data-simulation efficiency ratio (bottom) in $p_{\mathrm{T}} - \eta$ bins in data and simulation for electrons which do not travel parallel to the RF-foil [133].

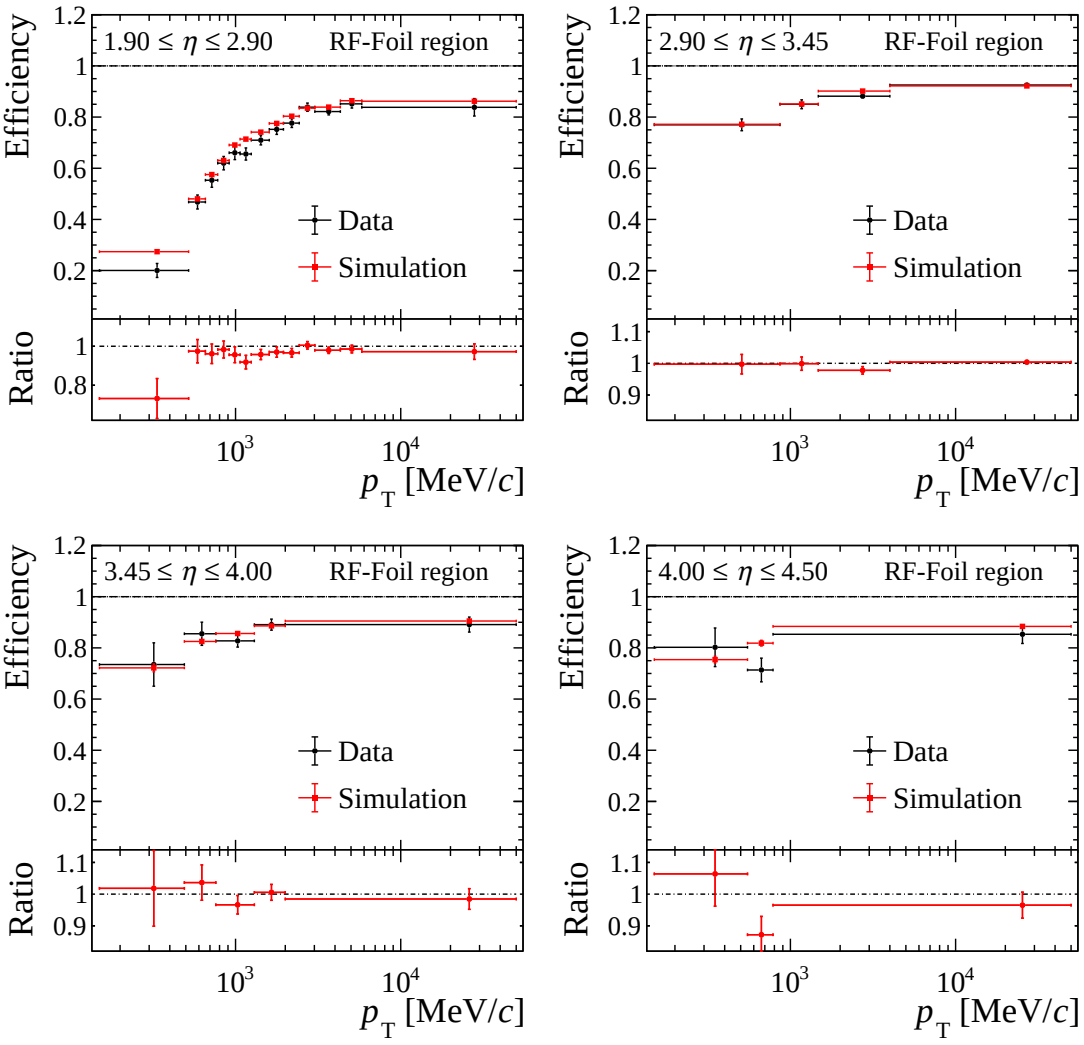

Figure 4.18: Electron detection efficiency (top) and data-simulation efficiency ratio (bottom) in $p_{\mathrm{T}} - \eta$ bins in data and simulation for electrons which travel parallel to the RF-foil [133].

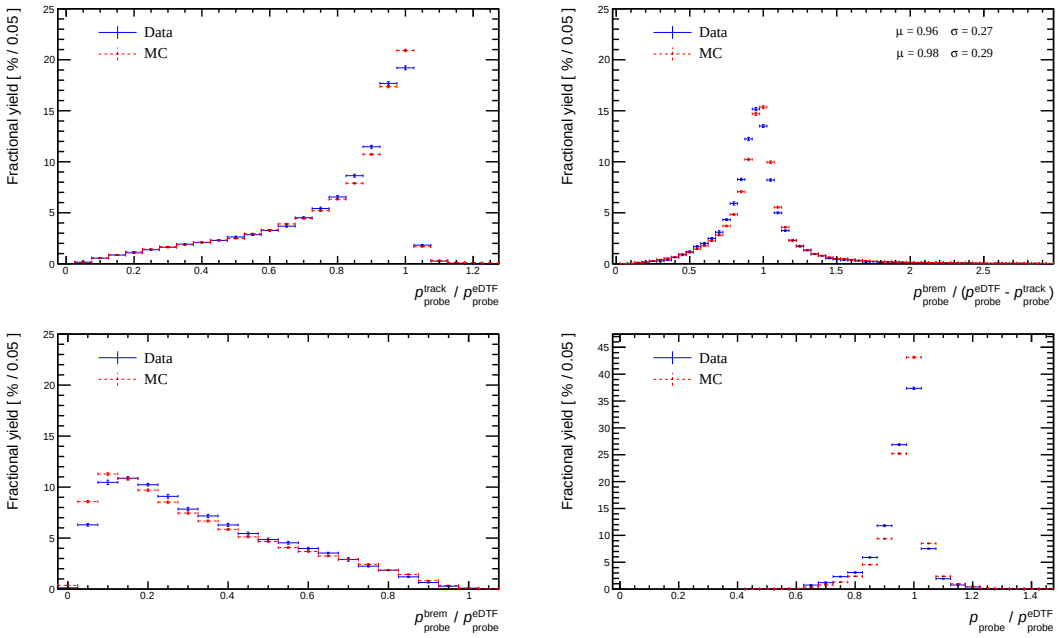

Figure 4.19: Performance of electrons in terms of $p_{\text{track}}/p_{\text{eDTF}}$ (top left), $p_{\text{brem}}/(p_{\text{eDTF}} - p_{\text{track}})$ (top right), $p_{\text{brem}}/p_{\text{eDTF}}$ (bottom left) and p/p_{eDTF} (bottom right) in simulation (red) versus data (blue).

space. Figs. 4.17 and 4.18 report the electron efficiency and efficiency ratios in the different kinematical bins for RF-Foil and Non-RF-Foil regions, respectively.

After the efficiency correction of the reconstruction it is possible that there is still a residual difference between simulation and data due to bremsstrahlung energy loss. An additional study on bremsstrahlung with $B \to J/\psi(\to e^+e^-)K^+$ decays is performed.

In order to compare the performance of reconstructed electrons in data and simulation, the following variables are defined:

- $p_{\text{track}}/p_{\text{eDTF}}$ *Track performance*, obtained as the electron reconstruction efficiency, where p_{track} is the reconstructed track momentum and p_{eDTF} is the estimated true electron momentum, determined with a B^+ and J/ψ mass constraint.

- $p_{\text{brem}}/(p_{\text{eDTF}}-p_{\text{track}})$ *Relative bremsstrahlung recovery*, where p_{brem} is the bremsstrahlung photons momentum.

- $p_{\text{brem}}/p_{\text{eDTF}}$ *Absolute bremsstrahlung recovery.*

- p/p_{eDTF} *Relative particle performance*, where p is the particle momentum, including track and bremsstrahlung recovery.

A fit on the $J/\psi K^+$ invariant mass with the J/ψ-mass-constraint is performed to obtain their distributions, collected in Fig. 4.19. This additional method allows to introduce correction factors to apply to the MC simulation when this does not model data correctly.

4.3.2 Particle identification

At LHCb, particle identification (PID) is performed by a combination of information from the RICH detectors, the calorimeters and the muon stations.

- **RICH detectors.** By combining the information from the tracking systems with the Cherenkov angle a measurement of the mass can be performed. Since this is not an effective method to assess mass in high multiplicity regions, a likelihood is assigned ($\mathcal{L}^{\text{RICH}}$). This is obtained by an iterative algorithm [134], starting from the assumption that the number of observed photoelectrons is Poisson distributed. At the first step all tracks are assumed as pions, then the mass hypothesis is changed to another particle type (e, μ, p, K). Finally, the mass hypothesis that gives the highest $\mathcal{L}$ is chosen.

- **Calorimeters.** In Fig. 4.9 the interaction of hadrons, electrons and photons with the calorimeters is represented. The most discriminating variables are the energy deposit in ECAL or HCAL, the presence of SPD hits and the PS energy. Also in this case, a likelihood is calculated ($\mathcal{L}^{\text{CALO}}$).

- **Muon stations.** The muon identification requires different combinations of hits as a function of the momentum. For $3 < p < 3.5\,\text{GeV}/c$ hits in M1-M3 are required. When $3.5 < p < 4.5\,\text{GeV}/c$ hits in M1-M4 are required and, finally, hits in all the five stations are required for $p > 4.5\,\text{GeV}/c$. After this, complex algorithms compute the muon likelihood for each muon track, used as a particle-identification discriminator ($\mathcal{L}^{\text{MUON}}$).

At this point, a global PID likelihood is defined as the product of the three contributions. For example, for a kaon track the likelihood $\mathcal{L}(K)$ is defined as

$$\mathcal{L}^{\text{PID}}(K) = \mathcal{L}^{\text{RICH}}(K) \cdot \mathcal{L}^{\text{CALO}}(\text{not an } e) \cdot \mathcal{L}^{\text{MUON}}(\text{not a } \mu) \tag{4.5}$$

Initially, the pion mass hypothesis is assigned to each charged track. The final PID is calculated starting from this hypothesis. For a particle x, with a likelihood $\mathcal{L}(x)$, the PID variable, also known as DLL, is defined as

$$\text{PID}(x) \equiv \text{DLL}(x) = \Delta\text{LL}(\pi - x) = \ln\left(\frac{\mathcal{L}^{\text{PID}}(x)}{\mathcal{L}^{\text{PID}}(\pi)}\right). \tag{4.6}$$

In addition to PID, ProbNN variables are utilised in LHCb analyses. These variables are evaluated from the output of a neural network, combining all information from the subdetectors and taking into account also correlations between different signatures and fake tracks. They are not used for online processing but in offline selection requirements.

In order to obtain PID efficiencies for a set of requirements, the standard approach is to use PIDCalib algorithms [135] to a calibration sample. In particular, a fit to the mass spectrum of the particle is performed and then the efficiencies are extracted by using the sPlot technique [136].

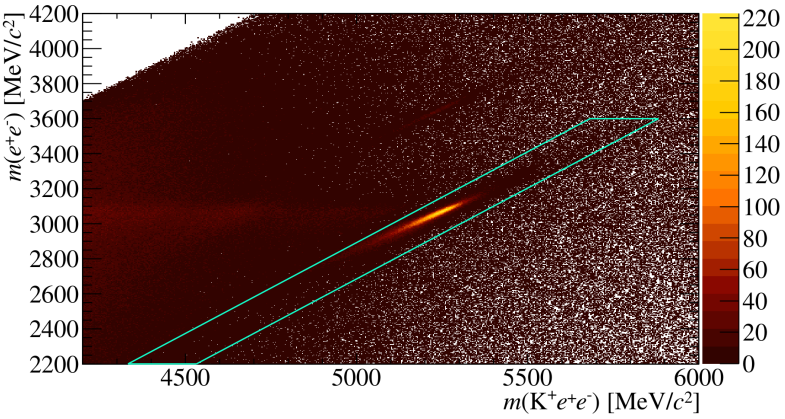

Figure 4.20: The $m(J/\psi)-m(B^+)$ plane for the electron calibration sample. The diagonal cut around the J/ψ peak is shown [123].

4.3.2.1 Electron identification

Electron PID is affected by Bremsstrahlung radiation loss, so a tag-and-probe method with $B^+ \to J/\psi(\to e^+e^-)K^+$ decays is used. This method was first developed by Ref. [123] and we refer to it for a more detailed description. The events are selected so that the tail of the J/ψ mass distribution depends only on bremsstrahlung effects by requiring that the J/ψ mass stands in the range $[2250, 3600]$ MeV/c^2 and that the deconvoluted B^+ mass fulfils: $|m(B^+) - m(J/\psi) - 2182.3| < 100$ MeV/c^2. This selection is visible is the diagonal of Fig. 4.20. Afterwards, fits to the J/ψ distribution are performed requiring a hard PID cut on one electron and scanning the other PID variable with a set of increasingly larger cuts.

4.3.3 LHCb software and workflow

The LHCb data follow a specific flow, summarised in Fig. 4.21, designed to maximise the data acquisition efficiency and quality. Each step is controlled by a specific application processing data event-by-event and using the output of the previous step, as follows:

i. **Trigger.** It is implemented in the Moore software. The detailed description of the trigger is in Sec. 4.2.8.

ii. **Reconstruction.** Trigger selected data enter the Brunel application in order to transform the detector hits into objects such as tracks and clusters. These objects are stored into an output file in a data summary tape (DST) format, which contains the full event information (reconstructed objects and raw data)

iii. **Stripping.** Data are further filtered through a set of selections implemented in the so called *stripping lines*, and applied by the DaVinci software, which writes out data either in the DST or micro-DST (μDST) format. In order to save disk space and

speed up the access, the output files are grouped into streams which contain similar selections.

In addition to the data flow, Fig. 4.21 show also the steps followed by the simulated events. Before being processed by MOORE, these are first simulated and then digitised by their specific software.

The LHCb simulation framework is called GAUSS [137] and consist in three steps:

1. **Generation.** The *pp* collisions in LHCb are generated with the PYTHIA software [138]

2. **Decays** are emulated by the EVTGEN software [139] and are identified by a numerical string, named *event number*. At this point, final-state radiation in the simulated samples is introduced by using the PHOTOS package [140].

3. **Detector.** The interaction between the product of the decays and the detector is simulated by GEANT4 [141, 142] software. In order to adapt the simulated sample to the detector status of the targeted sample. At this point, the detector conditions are identified by using two databases: the detector description database (DDDB) and the condition database (CondDB).

Afterwards, GAUSS output is passed to BOOLE [137], which digitises the simulated data. BOOLE output has the same format provided by the experiment electronics and the DAQ system, readable by the trigger. From this step ahead, both the data and the simulated sample follow the same processing.

For the simulated sample, several techniques can be used in order to save disk space or computing time, based on the aim of the analysis. For instance, filtered decay production allows to save disk memory by writing only the events passing the specific trigger/stripping decisions. Besides, in order to reduce computing time, the ReDecay algorithm [143] is used in large Monte Carlo productions. In this case, the underlying event, the one that does not participate in the simulated decay, is re-used in order to speed up simulation and up to 100 events can be simulated with the same underlying event. Furthermore, if additional studies which do not need the complete simulation are needed, the RapidSim [144] software is used. This is a fast Monte Carlo generator designed for heavy-quark hadron decays. It can also be used in combination with EVTGEN for form factors studies, as in Sec. 5.4.2 and 6.5.3. In both analyses of this thesis, all of the strategies above are employed and specified in the respective sections.

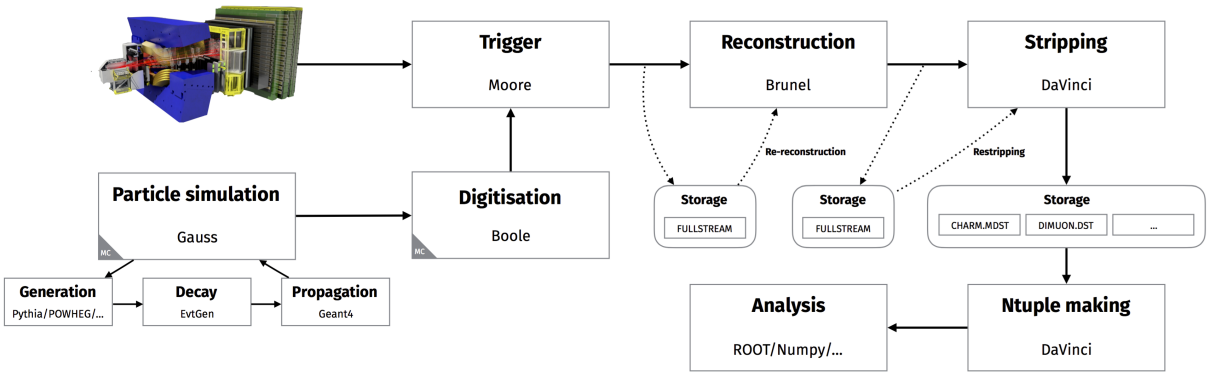

Figure 4.21: The LHCb data flow and the software used at each different step [102].

5

Test of Lepton Flavour Universality with the $D^0 \to K^-\ell^+\nu_\ell$ decay

5.1 Introduction and analysis overview

Lepton Flavour Universality can be tested studying branching fraction ratios, as stated in Sec. 2.2. For $c \to s\ell\nu_\ell$ transitions, the observable considered is $R_{\mu/e}$, defined in Eq. (2.67). This analysis aims to perform a LFU test by using $D^0 \to K^-\ell^+\nu_\ell$ decays, so the $R_{\mu/e}$ observable can be written as the ratio of branching fractions

$$R_{\mu/e} = \frac{\mathcal{B}(D^0 \to K^-\mu^+\nu_\mu)}{\mathcal{B}(D^0 \to K^-e^+\nu_e)}. \tag{5.1}$$

The topology for $D^0 \to K^-\ell^+\nu_\ell$ decays is represented in Fig. 5.1. D^0 candidates are originated from *prompt* $D^{*+} \to D^0\pi^+$ decays. The D^{*+} meson decays through strong interaction into a D^0 meson and a soft charged pion. D^{*+} candidates are selected to originate directly from the pp interaction point (PV), namely *prompt*. The pion flies through the detector producing a track with an average momentum of about 5 GeV/c, *i.e. soft* pion. Finally, the D^0 weakly decays after a flight of some centimetres forming a secondary decay vertex (SV), displaced from the primary vertex. Note that charge conjugate decays are implied, unless explicitly stated. The main challenges of this study are due to the presence of an electron and the presence of neutrinos in the final states.

Electrons lose energy through *bremsstrahlung* radiation, so the resolution and detection efficiency are lower than for muons (see Sec. 4.3.1.1 and Sec. 4.3.2.1). Therefore,

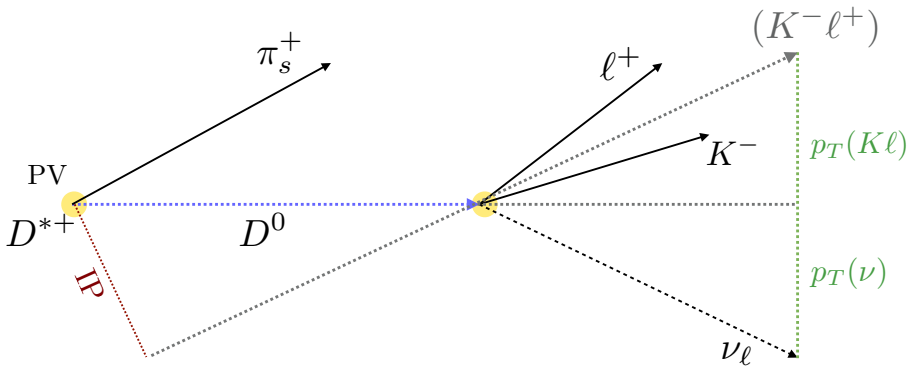

Figure 5.1: Topology of the $D^{*+} \to D^0(\to K^-\ell^+\nu_\ell)\pi^+$ decay chain. The scale is arbitrary for displaying purposes.

instead of measuring the muon over electron branching fraction ratio, $R_{\mu/e}$, the inverse $R_{e/\mu}$ is preferred:

$$R_{e/\mu} = R_{\mu/e}^{-1} = \frac{\mathcal{B}(D^0 \to K^- e^+ \nu_e)}{\mathcal{B}(D^0 \to K^- \mu^+ \nu_\mu)}. \tag{5.2}$$

Besides, in order to take into account the presence of neutrinos, two strategies have been developed: the cone closure method and the "Global Fit" method, described in detail in Sec. 5.5.

The value of $R_{e/\mu}$ is obtained by dividing the number of signal events, N_e and N_μ, and correcting them by the efficiency $\varepsilon_{tot}(\ell)$,

$$R_{e/\mu} = \frac{N(D^0 \to K^- e^+ \nu_e)}{N(D^0 \to K^- \mu^+ \nu_\mu)} \times \frac{\varepsilon_{tot}(\mu)}{\varepsilon_{tot}(e)}. \tag{5.3}$$

This strategy to obtain the branching fraction ratio is very similar to other LFU tests, such as the $R(D^{(*)0})$ analysis (Chap. 6). Two fit frameworks to obtain the signal $D^0 \to K^-\ell^+\nu_\ell$ yields are developed. Once the evaluation of both strategies is completed, one of the two fit methods will be used as baseline and the other as a cross-check.

The efficiencies of Eq. (5.3) are obtained as the product of all the possible contributions,

$$\varepsilon_{tot}(\ell) = \varepsilon_{acc} \cdot \varepsilon_{rec|acc} \cdot \varepsilon_{sel|rec} \cdot \varepsilon_{PID|sel}. \tag{5.4}$$

The LHCb acceptance is accounted for in ε_{acc}; $\varepsilon_{rec|acc}$ stands for the reconstruction efficiency after forming the candidates from the decay in the LHCb acceptance; $\varepsilon_{sel|rec}$ is the selection efficiency, after all trigger, stripping and offline selection criteria, and $\varepsilon_{PID|sel}$ stands for the particle identification efficiency after the selection efficiency. Each of the individual selection efficiencies relies on the step before. They are calculated from MC

simulation, except for the PID efficiency, which is calculated from dedicated data samples, either using PIDCalib (see Sec. 4.3.2) algorithms or other methods specifically developed for this analysis, as introduced in Sec. 4.3.2.1. Finally, in order to exploit the sensitivity of $R_{e/\mu}$ to new physics, this study will be done in bins of the dilepton mass squared, q^2. This is not included in this thesis, where preliminary results are presented in the integrated q^2 region.

This chapter is structured following the workflow of the analysis. First, the data and simulation samples are described in Sec. 5.2; the selection and the correction to MC simulation in Sec. 5.3 and Sec. 5.4, respectively. The two neutrino estimation methods are reported in Sec. 5.5. Afterwards, in Sec. 5.6, the two fits frameworks are described. The efficiencies calculation is reported in Sec. 5.7 and the systematic uncertainties evaluation in Sec. 5.8. Finally, the preliminary results are reported in Sec. 5.9.

5.2 Datasets and Monte Carlo Samples

This analysis is based on 1.9 fb^{-1} of data from $\sqrt{s} = 13$ TeV pp collisions, collected in 2015 and 2016. The simulated samples are produced with different conditions and techniques (for definitions see Sec. 4.3.3):

- **Unfiltered, Full MC production.** Small sample where the full event is simulated. This is used primarily to calculate efficiencies and the list of generated events is reported in Tables 5.1 and 5.2.

- **Filtered MC production.** These simulation samples can be divided into two sets: the ones where the full event is simulated and the ones employing the ReDecay algorithm (see Sec. 4.3.3). The statistics are collected in Tables 5.3 and 5.4, respectively. These samples are used to create the templates for the model used to describe the data.

In addition to these samples, RapidSim is used to generate high-statistics datasets to understand possible background contributions and to perform a specific study to assess the knowledge of the $D^0 \to K$ form factors (see Secs. 4.3.3 and 5.4.2). Besides, a dataset with D^0 candidates reconstructed from unphysical $D^0 \to K^+\ell^+\nu_\ell$ events, named *same sign* sample, is produced. This is used as a template to account for misreconstructed D^0 decays.

Event Number	Decay Channel	Events on Disk 2016 MU	Events on Disk 2016 MD	Events on Disk, 2015 MU	Events on Disk 2015 MD
27173001	$D^0 \to K^-\mu^+\nu_\mu$	1757357	1751390	253319	250762
27583002	$D^0 \to K^-e^+\nu_e$	1754493	1875792	255211	252302
27573400	$D^0 \to K^-\mu^+\nu_\mu\pi^0$	1755411	1761490	250375	260807
27583400	$D^0 \to K^-e^+\nu_e\pi^0$	1754476	1754852	253322	251688
27572001	$D^0 \to K^{*-}(892)\mu^+\nu_\mu$	1757228	1754780	250714	255133
27582401	$D^0 \to K^{*-}(892)e^+\nu_e$	1753008	1751410	255111	250535
27573001	$D^0 \to \pi^-\mu^+\nu_\mu$	1758546	1776455	251751	254891
27583000	$D^0 \to \pi^-e^+\nu_e$	1751546	1756658	250005	253560
27265000	$D^0 \to K^-3\pi$	1750349	1755986	2290588	2240118
27163002	$D^0 \to K^-K^+$	1750891	1786642	252813	255834
27263400	$D^0 \to K^-\pi^+\pi^0$	1755598	1750809	252529	250794
27163403	$D^0 \to \pi^-\pi^+\pi^0$	1751894	1756054	255142	256274
27163003	$D^0 \to K^-\pi^+$	0	0	0	0

Table 5.1: Statistics for unfiltered MC sample simulated with "Sim09b" conditions divided by magnet polarity (MU and MD) and year.

Event Number	Decay Channel	Events on Disk 2016 MU	Events on Disk 2016 MD	Events on Disk, 2015 MU	Events on Disk 2015 MD
27173001	$D^0 \to K^-\mu^+\nu_\mu$	1740356	1750989	280306	288072
27583002	$D^0 \to K^-e^+\nu_e$	1875587	1748598	251094	254133
27573400	$D^0 \to K^-\mu^+\nu_\mu\pi^0$	2026650	1739936	298839	253240
27583400	$D^0 \to K^-e^+\nu_e\pi^0$	1722348	1750569	249355	251429
27572001	$D^0 \to K^{*-}(892)\mu^+\nu_\mu$	1754794	1750024	273106	253452
27582401	$D^0 \to K^{*-}(892)e^+\nu_e$	1873126	1753739	243241	262132
27573001	$D^0 \to \pi^-\mu^+\nu_\mu$	1888217	1750705	251923	252152
27583000	$D^0 \to \pi^-e^+\nu_e$	1979092	1750623	292319	252400
27265000	$D^0 \to K^-3\pi$	1909908	1747757	0	0
27163002	$D^0 \to K^-K^+$	1740354	1750979	248428	255388
27263400	$D^0 \to K^-\pi^+\pi^0$	1751518	1750178	244947	294331
27163403	$D^0 \to \pi^-\pi^+\pi^0$	1737653	1752298	258601	289322
27163003	$D^0 \to K^-\pi^+$	1700924	2166440	0	0

Table 5.2: Statistics for the unfiltered MC sample simulated with "Sim09c" conditions divided by magnet polarity (MU and MD) and year.

Event Number	Decay Channel	Events on Disk 2016 MU	Events on Disk 2016 MD	Events on Disk, 2015 MU	Events on Disk 2015 MD
27173001	$D^0 \to K^-\mu^+\nu_\mu$	11623403	11977451	3952502	3966032
27583002	$D^0 \to K^-e^+\nu_e$	11122782	11300357	3727281	3743492
27573400	$D^0 \to K^-\mu^+\nu_\mu\pi^0$	1473166	1499180	473952	472468
27583400	$D^0 \to K^-e^+\nu_e\pi^0$	1547160	1535216	535733	543947
27572001	$D^0 \to K^{*-}(892)\mu^+\nu_\mu$	1466473	1462343	491081	493422
27582401	$D^0 \to K^{*-}(892)e^+\nu_e$	1476926	1535617	488721	495099
27573001	$D^0 \to \pi^-\mu^+\nu_\mu$	1678539	1661043	596633	582078
27583000	$D^0 \to \pi^-e^+\nu_e$	1609798	1626996	532033	532289
27265000	$D^0 \to K^-3\pi$	1734691	1734892	594887	632390
27163002	$D^0 \to K^-K^+$	1752472	1731698	610782	652465
27263400	$D^0 \to K^-\pi^+\pi^0$	1639073	1634226	541689	544136
27163403	$D^0 \to \pi^-\pi^+\pi^0$	1709870	1705663	599475	597178
27163003	$D^0 \to K^-\pi^+$	1784653	1746340	706220	658483

Table 5.3: Statistics for the filtered MC sample simulated with "Sim09c" conditions divided by magnet polarity (MU and MD) and year.

Event Number	Decay Channel	Events on Disk 2016 MU	Events on Disk 2016 MD	Events on Disk, 2015 MU	Events on Disk 2015 MD
27573077	$D^0 \to K^-\mu^+\nu_\mu$	10004396	10007010	1364077	1401219
27583006	$D^0 \to K^-e^+\nu_e$	10066692	10058587	2030907	2011919
27573405	$D^0 \to K^-\mu^+\nu_\mu\pi^0$	2506086	2526952	854615	850234
27583403	$D^0 \to K^-e^+\nu_e\pi^0$	2609219	2809935	869612	856946
27773404	$D^0 \to K^{*-}(892)\mu^+\nu_\mu\pi^0$	2656914	3510065	803216	813436
27783403	$D^0 \to K^{*-}(892)e^+\nu_e\pi^0$	2515040	2509786	806015	812241
27573006	$D^0 \to K^{*-}(892)(\to \pi^-K^0)\mu^+\nu_\mu\pi^0$	2545011	2556842	993323	1033711
27583005	$D^0 \to K^{*-}(892)(\to \pi^-K^0)e^+\nu_e\pi^0$	2500744	2508475	854955	856589
27573009	$D^0 \to \pi^-\mu^+\nu_\mu$	2695531	2749902	876953	905693
27583007	$D^0 \to \pi^-e^+\nu_e$	2617830	2631406	878287	878430
27465006	$D^0 \to K^-3\pi$	2537435	2513534	843893	857350
27163178	$D^0 \to K^-K^+$	911921	914927	559028	552540
27263403	$D^0 \to K^-\pi^+\pi^0$	446841	516739	215158	217034
27163409	$D^0 \to \pi^-\pi^+\pi^0$	1081993	1087766	368142	368677
27163179	$D^0 \to K^-\pi^+$	505287	503286	385696	340434

Table 5.4: Statistics for the filtered ReDecay MC sample simulated with "Sim09e" conditions divided by magnet polarity (MU and MD) and year.

5.3 Selection

The selection criteria are chosen in order to be as much unbiased as possible with respect to the muon and the electron modes. Hence, analogue requirements are applied for the two leptons. The selection process can be separated into different steps. First, events must pass the trigger and the stripping requirements, listed and motivated in Sec. 5.3.1. Afterwards, in order to reduce the contribution of misidentified or combinatorial background, other requirements are applied. These are collected in Sec. 5.3.2.

5.3.1 Stripping and Trigger

The first step requires the trigger to be fired at all three levels: hardware L0, and software HLT1 and HLT2. First, D^* candidates are selected by a TIS or TOS logic, introduced in Sec. 4.2.8. At the final trigger level, events with three charged tracks (h), attributable to events like $D^* \to D^0(\to hh(X))\pi^+$, are selected. The specific trigger lines are listed:

- L0: D^{*+} selected independent from signal (TIS) `OR` a K triggered on signal (TOS) (`Dstar_L0_TIS || K_L0_TOS`),
- HLT1: K track triggered on signal, $K^{\text{track}}_{\text{TOS}}$(HLT1), (`K_Hlt1Track_TOS`),
- HLT2: select inclusive $D^{*+} \to D^0(\to hh(X))\pi^+$ events (`Dstar_Hlt2CharmHadInclDst2PiD02HHX_TOS`).

The L0 and HLT1 efficiencies are expected to cancel in the $R_{e/\mu}$ ratio. On the other hand, HLT2 efficiencies are calculated separately for electron and muon modes (Sec. 5.7).

After trigger acceptance, the events are preselected by a dedicated stripping line (see Sec. 4.3.3). For the $D^0 \to K^-\ell^+\nu_\ell$ signal, events with a D^0, a charged kaon and a lepton are selected with the specific requirements listed in Tab. 5.5.

Cut	Value
K	
p	> 3 GeV/c
p_{T}	> 800 MeV/c
PID(K)	> 5
PID($K - \mu$)	> 5
PID($K - p$)	> 5
χ^2_{IP}	> 9
Track Ghost Prob	< 0.35
π	
p	> 1 GeV/c
p_{T}	> 300 MeV/c
PID(e)	< 5
χ^2_{IP}	< 9
Track Ghost Prob	< 0.35
e	
p_{T}	> 500 MeV/c
PID(e)	> 0
Track Ghost Prob	< 0.35
μ	
p_{T}	> 500 MeV/c
PID(μ)	> 3
PID($K - \mu$)	< 0
PID($\mu - p$)	> 0
Track Ghost Prob	< 0.35
D^0 daughters, $K\ell$	
PV Separation (χ^2_{PV})	> 100
DIRA(PV)	> 0.999
Δz(SV $-$ PV)	> 0
D^* daughters, $K\ell\pi$	
Combination: Δm	< 405 MeV/c^2
Combination: χ^2_{DOCA}	< 20
Mother cut: Δm	< 400 MeV/c^2
Vertex χ^2/ndf	< 9

Table 5.5: Stripping selection criteria.

In the stripping selection, since the D^0 vertex is displaced from the D^{*+} one, requirements are applied to the χ^2 of the distance of the track with respect to the PV, the $\chi^2_{\rm IP}$ of the K^- and the π^+. Besides, the D^0 daughters, $K^-\ell^+$, must fulfil requirements on the $\chi^2_{\rm PV}$, the DIRA[1] and the distance between their vertex and the PV must be greater than 0. The D^{*+} candidates must have a deconvoluted mass $\Delta m = m(D^{*+}) - m(h) < 400\,\text{MeV}/c^2$, where h is one of the daughters, while the combination of the daughters must have a Δm greater than $405\,\text{MeV}/c^2$. Requirements on the particle identification[2] and the momentum of the single tracks are applied. Finally, the probability of them being a ghost track must be lower than 0.35. In addition to this, the same set of requirements is applied to select nonphysical $D^0 \to K^+\ell^+\nu_\ell$ candidates, namely "same-sign" (SS). This sample is used to control possible contributions to the combinatorial background in the final fit, see 5.6 .

5.3.2 Offline selection

In order to further reduce any misidentification or combinatorial backgrounds, a tighter set of requirements is applied offline. For instance, two-body D^0 decays and some three body D^0 decays which appear in the two-body spectrum may be misidentified as the signal decay. To reduce this contribution the following procedure is applied. The momentum asymmetry between the K^- and ℓ^+ candidates, defined as

$$\beta \equiv \frac{p(\ell) - p(K)}{p(\ell) + p(K)}, \tag{5.5}$$

is investigated as a function of the invariant mass of the $K\ell$ system. Possible feedthrough backgrounds are due to pions or kaons identified as the ℓ or the kaon and can be determined by studying this distribution when a K or a π is identified as one of the D^0 daughters. For both lepton modes the following cases are considered:

- both D^0 daughters correctly identified $K^-\ell^+ \to K^-\ell^+$ (Figs. 5.2(a), 5.2(e), 5.3(a) and 5.3(e))
- a kaon identified as the lepton $K^-\ell^+ \to K^-K^+$ (Figs. 5.2(b), 5.2(f), 5.3(b) and 5.3(f))
- a pion identified as the lepton, $K^-\ell^+ \to K^-\pi^+$ (Figs. 5.2(c), 5.2(g), 5.3(c) and 5.3(g))
- a π^+ identified as the lepton and a π^- as the K^-, $K^-\ell^+ \to \pi^-\pi^+$ (Figs. 5.2(d), 5.2(h), 5.3(d) and 5.3(h))

The shapes of β as a function of $m(K\ell)$ are represented in Figs. 5.2 and 5.3 for electron and muon modes, respectively. The top row represents the β distributions before the offline selection, while the ones in the bottom row the β after applying the requirements of Tab. 5.6.

[1] DIRA is the cosine of the angle between the particle momentum and the direction extracted from the PV position.

[2] PID and ProbNN variables are defined in Sec. 4.3.2.

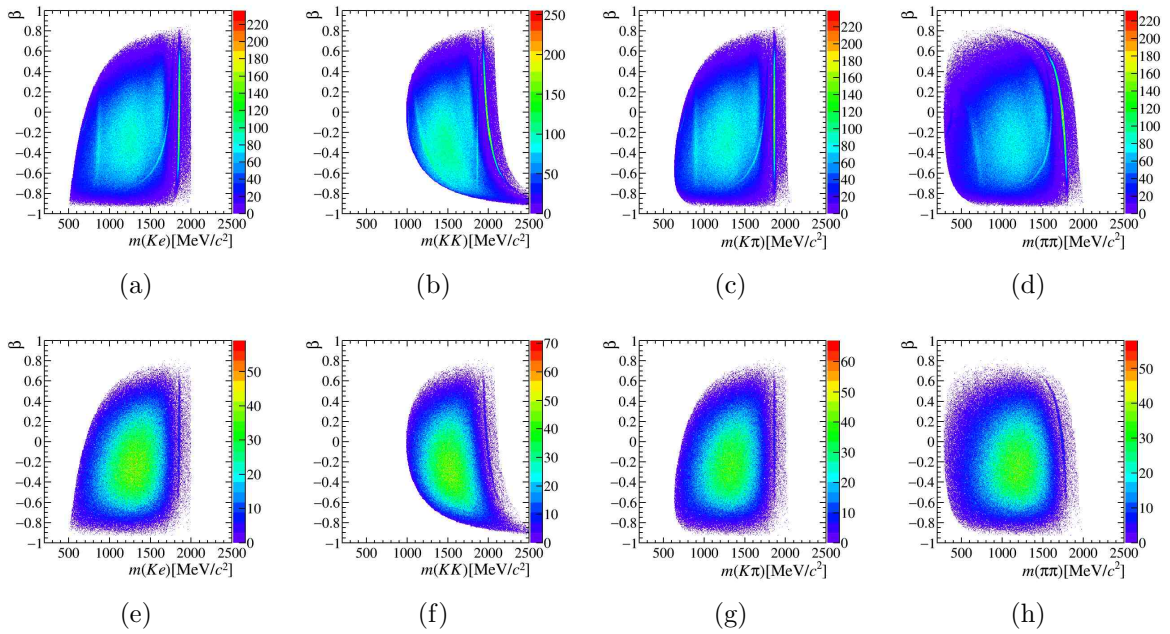

Figure 5.2: Momentum asymmetry β versus $m(Ke)$ for different mass hypotheses, from left to right: $\ell \to e$, $\ell \to K$, $\ell \to \pi$ and $\ell \to \pi$ and $K \to \pi$. Top row: plots before the application of PID cuts; bottom row: plots after PID requirements.

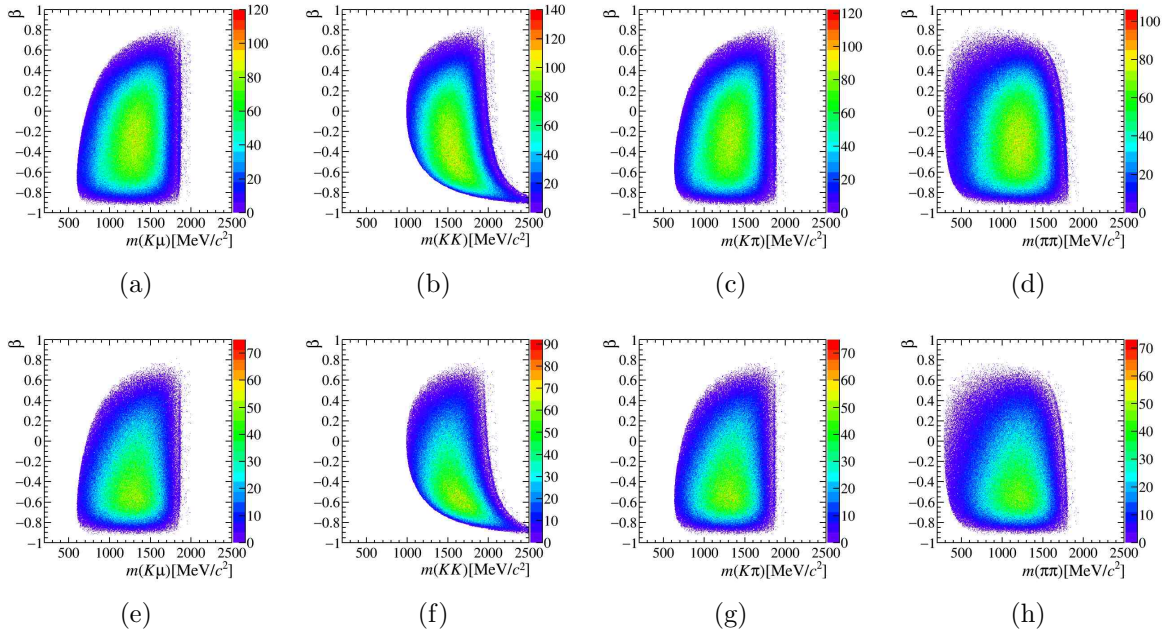

Figure 5.3: Momentum asymmetry β, versus $m(K\mu)$ for different mass hypotheses, from left to right: $\ell \to \mu$, $\ell \to K$, $\ell \to \pi$ and $\ell \to \pi$ and $K \to \pi$. Top row: plots before the application of PID cuts; bottom row: plots after PID requirements.

Cut	Value
e	
PIDe	> 7
PID$(K-e)$	< -10
η	$\in [1.9, 4.5]$
μ	
PID(μ)	> 7
PID$(K$-$\mu)$	< -10
π	
PID(e)	< 1

Table 5.6: Offline selection criteria of $D^0 \to K^-\ell^+\nu_\ell$ analysis.

The peaking structures in the left plots allow to identify relevant background contributions. As expected, these are more visible in the electron sample. The $D^0 \to K^-e^+\nu_e$ signal distribution in Fig. 5.2(a) shows a defined peak at the D^0 mass value, attributable to $D^0 \to K^-\pi^+$ decays. This contribution is also clearly visible in Fig. 5.2(c). In this plot other structures are recognisable, one is due to a pion coming from $K^{*0} \to K^-\pi^+$ decays. Besides, there is a blob for $D^0 \to K^-\pi^+\pi^0$ decays around 1610 MeV. In the $m(KK)$ plot of Fig. 5.2(b) clear contributions of $D^0 \to KK$ mediated by the $\phi(1020)$ resonance can be seen (Fig. 5.2(b)). Further searches for doubly-misidentified two body decays did not show any clear excesses other than the ones above considered.

After applying the selection of Tab. 5.6, the described structures reduce visibly. The PID(e) requirement on the pion is based on previous analyses [145, 146] and the other selection criteria on PID are tuned based on the disappearance of the peaking structures in the asymmetry plots. The efficiencies of these cuts are evaluated in Sec. 5.7.5. Regardless, possible residual feedthroughs are assessed by adding truth-matching requirements in the template making (see Sec. 5.6). In addition to the PID selection, the electron pseudorapidity is required to lie in the $[1.9, 4.5]$ interval, which corresponds to the fiducial acceptance of the LHCb detector.

5.3.3 Multiple Candidate Selection

Data samples may have multiple candidates in the same event. Since there is no *a priori* good reason to pick one candidate above another, candidates are chosen randomly. Both before and after the offline selection, the percentage of multiple candidates for both the right sign and wrong sign samples is about 11.5%. In Appendix A, Tab. A.1 collects the percentage of multiple candidates before and after applying the selection criteria.

5.4 Corrections to simulation

The LHCb simulation provides a very good description of the interactions in the detector. However, it has some limitations. Some can be corrected while the rest are accounted for as the systematic uncertainties (see Sec. 5.8). The first correction accounts for the event multiplicity. Due to the LHCb pile-up (see Sec. 4.2), more than one PV can be associated to an event, this is corrected by the method developed in Sec. 5.4.1. Secondly, the theoretical models used in the simulation could introduce biases in the modelling of the decays. In order to reduce this, a procedure is discussed in Sec. 5.4.2.

5.4.1 Event Multiplicity re-weighting

The LHCb original detector can not cope with particle multiplicities produced in bunch crossings with many more than one inelastic proton-proton interaction. Therefore, the LHC is configured to provide about an interaction per bunch crossing at the LHCb interaction point. Nevertheless, there is the possibility that more than one inelastic collision happens and more than one PV is associated to an event. Since the simulation sample is produced with a single interaction, in order to match the multiplicity of data, a re-weighting procedure is implemented. This is performed using the number of VELO clusters, which is strongly correlated to the number of PVs, the number of long tracks and the number of hits in the SPD detector. Fig. 5.4 represents the distributions of these variables for the 2016 muon and electron sample before the procedure.

The corrections are applied using Gradient Boosted Decision Trees (BDT). The BDTs are implemented in the `hep_ml` framework, relying on `scikit-learn` package [147]. One BDT is prepared for each of the 2015 and 2016 samples. In order to calculate weights that transform the original MC distributions into the target data one, in blue in Fig. 5.4, the data and MC samples are randomly split in two. Two BDTs are trained separately and one sample is used as a test for the other. After the weight application to the original MC data, these variables distributions take the form shown in Fig. 5.5.

As an additional check, the Receiver Operator Characteristic (ROC) curve of the BDT is considered. The area under the curve (AUC) can be interpreted as a measure of the robustness of the re-weighting procedure. If the area approaches 0.5, the test and training samples are drawing from the same distribution. For the 2016 (2015) muon sample, the area under the ROC curve has a value of 0.845 (0.817), becoming 0.527 (0.522) after re-weighting. Similarly, for the 2016 (2015) electron sample, the area is 0.841 (0.810) before and 0.526 (0.520) after.

5.4.2 Form Factor model

As introduced in Section 2.2.3, the decay rate of $D^0 \to K^+\ell\nu_\ell$, depends only on the vector form factor $f_+(q^2)$. It can be parametrised following different models. In this thesis, two parametrisations are considered: the Isgur-Nathan-Scora-Grinstein-Wisen

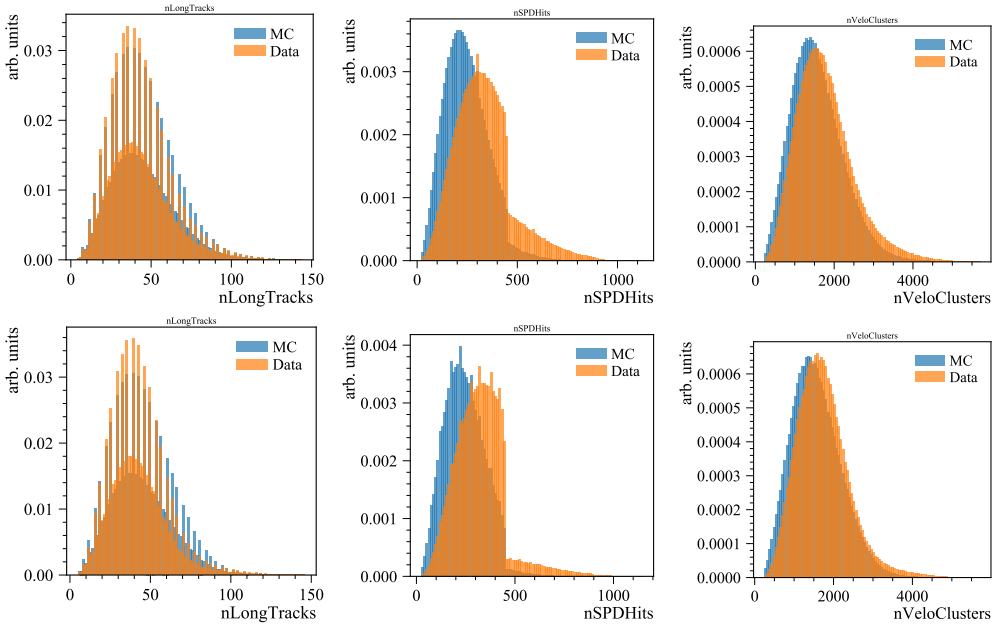

Figure 5.4: Event multiplicity variables for the muon mode (top) and electron mode (bottom) on 2016 data before the re-weighting procedure.

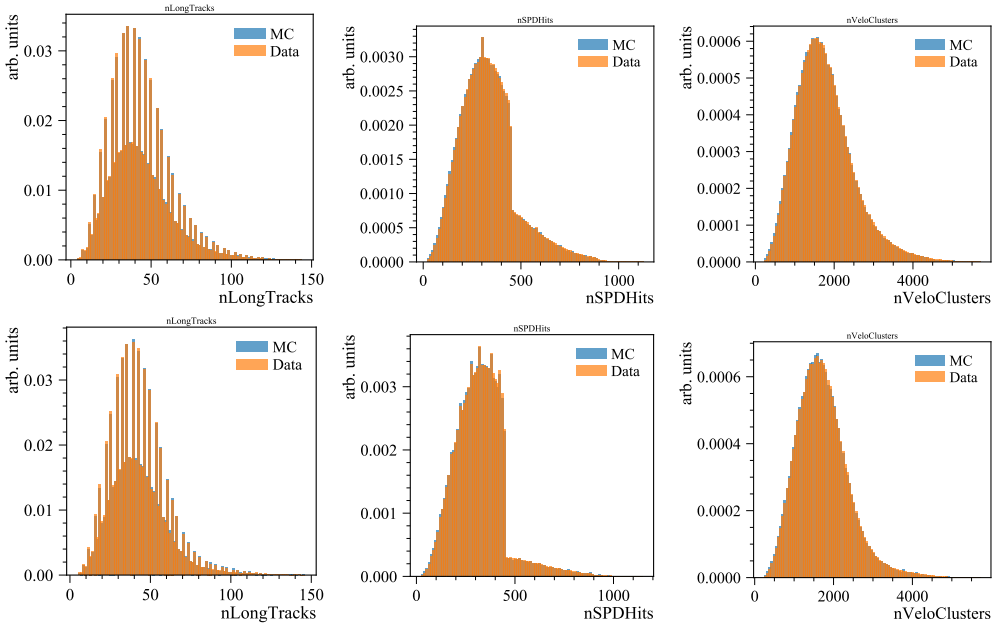

Figure 5.5: Event multiplicity variables for the muon mode (top) and electron mode (bottom) on 2016 data after the re-weighting procedure.

Channel	$f_+(0)$ [60]	$m_{\rm pole}$ (GeV/c^2) [43]	$\alpha_{\rm BK}$ [43]
$D^0 \to K^-\ell\nu_\ell$	0.760 ± 0.011	$1.921 \pm 0.010 \pm 0.007$	$0.309 \pm 0.020 \pm 0.013$
$D^0 \to \pi^-\ell\nu_\ell$	0.634 ± 0.015	$1.911 \pm 0.012 \pm 0.004$	$0.279 \pm 0.035 \pm 0.011$

Table 5.7: Input values of $f_+(0)$, $m_{\rm pole}$ and $\alpha_{\rm BK}$.

model (ISGW2) [30,31] and the modified pole parameterisation (BK) [32]. These are also included in the EvtGen package (see Sec. 4.3.3), allowing to simulate events using either one or the other.

The first MC productions for this analysis used the ISGW2 model. Once these simulation samples were ready, a new result was published [43], improving the knowledge on D^0 form factors and triggering better parameterisations, such as the BK one, defined in Eq. (2.75). To account for this, a FF re-weighting procedure with the BK parameterisation is implemented in the $D^0 \to K\ell\nu_\ell$ and $D^0 \to \pi\ell\nu_\ell$ decays of the aforementioned MC samples.

Samples of $\approx 10^8$ events for both the ISGW2 and the BK models are produced using RapidSim with EvtGen. In order to simulate the sample, the BK model parameters are required as inputs. These are the mass of the pole m_{pole}, the value of the form factor at $q^2 = 0$, $f_+(0)$, and the parameter α_{BK}. The values considered in the simulation are collected in Tab. 5.7 and are taken from both theoretical calculations and experimental measurements [43, 60].

Lookout tables are produced by comparing the true transferred momentum $q^2_{\rm true}$ obtained in the two simulation samples. The weight w, defined as

$$w = \frac{q^2_{\rm true}({\rm BK})}{q^2_{\rm true}({\rm ISGW2})}, \tag{5.6}$$

is then applied event by event to correct the templates and check the effect on the fit results. The visible D^0 mass, which is q^2-dependent, changes as in Fig. 5.6. This correction will be included in the systematic uncertainties evaluation.

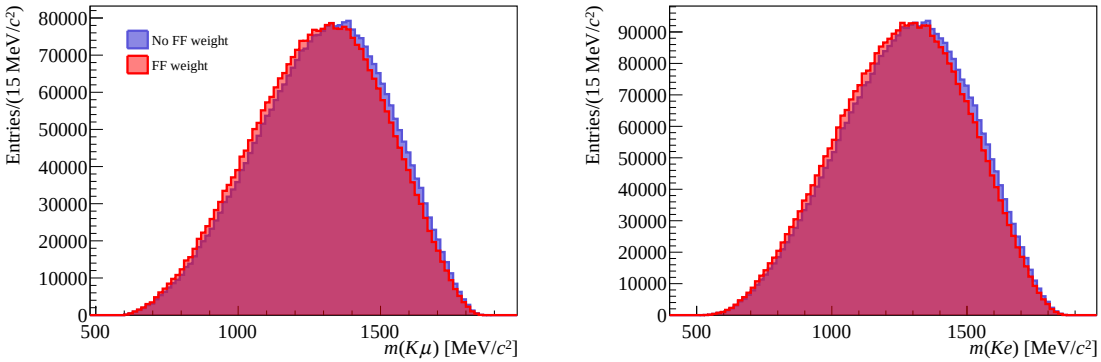

Figure 5.6: Toy distribution of the D^0 visible mass for $D^0 \to K^-\mu^+\nu_\mu$ (left) and $D^0 \to K^-e^+\nu_e$ (right). In blue before applying the FF weight, in red after the application.

5.5 Neutrino estimation and q^2 reconstruction

Studying $R_{e/\mu}$ as a function of q^2, the squared momentum transfer to the lepton-neutrino pair, is of high interest (Sec. 2.2.3). Therefore, it is fundamental to estimate the neutrino momentum. However, the LHCb design (see Chap. 4) does not allow the missing particle reconstruction techniques used by barrel spectrometers (see Sec. 3.2.1). Besides, algebraically solving for the neutrino momentum using reconstructed D^0 mesons and child kinematics produces a two-fold ambiguity in p_ν along the D^0 flight direction, as shown in Sec. 5.5.1. Two reconstruction methods are proposed to improve this. Both rely on the fact that adding an additional mass constraint from the $D^{*+} \to D^0\pi^+$ decay can resolve this ambiguity.

The first method, the cone-closure method, is described in Sec. 5.5.2. The second one is the "Global Fit" (GF) algorithm, first developed in Ref. [148] specifically for this study. As the name suggests, it aims to estimate the neutrino momentum by means of a kinematic fit to the complete decay chain. It is described in Sec. 5.5.3.

Both methods are developed in parallel and treated separately with a different fit procedure as shown in Sec. 5.6. Since they share the same original dataset, the final results cannot be combined, but rather be used for an internal consistency check. In order to decide which method is preferred, their resolutions are compared and presented in Sec. 5.5.4

5.5.1 Reconstruction of the neutrino momentum

In this section the neutrino information is treated algebraically. For instance, the invariant mass of the D^0 is defined as

$$m^2_{D^0} = (E_{K\ell} + E_\nu)^2 - (\vec{p}_{K\ell} + \vec{p}_\nu)^2, \tag{5.7}$$

where the charged daughter system momentum and energy are

$$\vec{p}_{K\ell} = \vec{p}_K + \vec{p}_\ell, \tag{5.8}$$
$$E_{K\ell} = E_K + E_\ell, \tag{5.9}$$

being $\vec{p}_K$ and $\vec{p}_\ell$ the momenta and E_K and E_ℓ the energies of the charged kaon and the lepton, respectively.

The slopes, A and B, of the conjugation line between the two decay vertices, as seen in Fig. 5.1 are defined as

$$A \equiv \frac{x_{D^0} - x_{D^*}}{z_{D^0} - z_{D^*}} = \frac{p_K^x + p_\ell^x + p_\nu^x}{p_K^z + p_\ell^z + p_\nu^z}, \tag{5.10}$$
$$B \equiv \frac{y_{D^0} - y_{D^*}}{z_{D^0} - z_{D^*}} = \frac{p_K^y + p_\ell^y + p_\nu^y}{p_K^z + p_\ell^z + p_\nu^z}. \tag{5.11}$$

Using Eq. (5.8) the two slopes become:

$$A = \frac{p_{K\ell}^x + p_\nu^x}{p_{K\ell}^z + p_\nu^z}, \tag{5.12}$$
$$B = \frac{p_{K\ell}^y + p_\nu^y}{p_{K\ell}^z + p_\nu^z}. \tag{5.13}$$

At this point, to compute the neutrino momentum, the following system of Eq. (5.14) must be solved:

$$\begin{cases} p_\nu^x = A(p_{K\ell}^z + p_\nu^z) - p_{K\ell}^x, \\ p_\nu^y = B(p_{K\ell}^z + p_\nu^z) - p_{K\ell}^y, \\ m_{D^0}^2 = (E_{K\ell} + |\vec{p}_\nu|)^2 - (\vec{p}_{K\ell} + \vec{p}_\nu)^2. \end{cases} \tag{5.14}$$

The neutrino mass is neglected, thus

$$E_\nu^2 = p_\nu^2 \,. \tag{5.15}$$

Parameterising the z coordinate of the momentum as

$$t = p_{K\ell}^z + p_\nu^z \,, \tag{5.16}$$

and substituting the first two lines into the third, one obtains

$$2E_{K\ell}p_\nu = m_{D^0}^2 - E_{K\ell}^2 - p_{K\ell}^2 + 2t(Ap_{K\ell}^x + Bp_{K\ell}^y + p_{K\ell}^z) \,. \tag{5.17}$$

If, after isolating p_ν, the quantity $u = Ap_{K\ell}^x + Bp_{K\ell}^y + p_{K\ell}^z$ is defined, squaring Eq. (5.17),

$$4E_{K\ell}^2[(A^2 + B^2 + 1)t^2 - 2tu + p_{K\ell}^2] = (m_{D^0}^2 - E_{K\ell}^2 - p_{K\ell}^2 + 2tu). \tag{5.18}$$

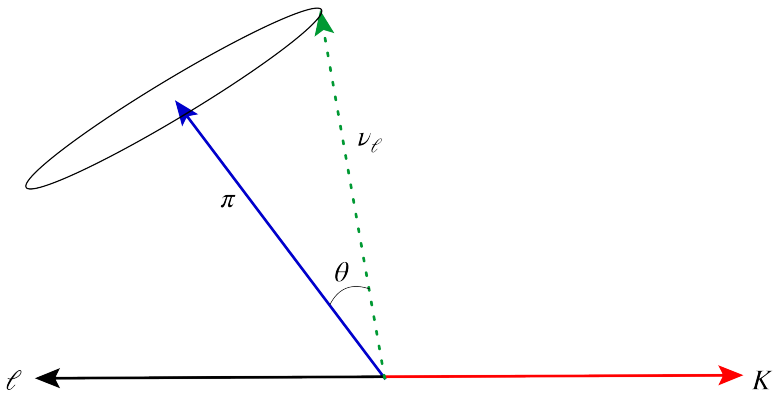

Figure 5.7: Decay topology of the $D^{*+} \to D^0(\to K^-\ell^+\nu_\ell)\pi^+$ decay in the $K\ell$ rest frame, θ is the angle formed by the pion and the neutrino momentum.

This way, only the variable t depends on p_ν^z. In order to obtain an equation at second order in t, another auxiliary variable, Z, is introduced: $Z^2 = m_{D^0}^2 + E_{K\ell}^2 - p_{K\ell}^2$. Substituting it in Eq. (5.18),

$$4\left[E_{K\ell}^2(A^2+B^2+1) - u^2\right]t^2 - 2\left[2sZ^2\right]t + \left[4E_{K\ell}^2 p_{K\ell}^2 - Z^4 - 4E_{K\ell}^4 + 4Z^2E_{K\ell}^2\right] = 0\,. \tag{5.19}$$

Finally, the two solutions for the z-coordinate of the neutrino momentum are obtained:

$$p_\nu^z = \frac{uZ^2 \pm \sqrt{(A^2+B^2+1)(Z^4 - 4m_{D^0}^2E_{K\ell}^2) + 4m_{D^0}^2u^2}}{2(E_{K\ell}^2(A^2+B^2+1) - u^2)} - p_{K\ell}^z. \tag{5.20}$$

Once p_ν^z is calculated it is possible to compute all the other coordinates and the invariant mass of the D^{*+}:

$$m_{D^{*+}} = \sqrt{(E_{K\ell} + E_\nu)^2 + (p_{K\ell} + p_\nu)^2}\,. \tag{5.21}$$

5.5.1.1 Reconstruction in the $K\ell$ rest frame

The cone closure method exploits the $K\ell$ rest frame for the decay reconstruction. In the $K\ell$ rest frame, $p_{K\ell} = 0$, the neutrino and the D^0 momenta are aligned, as visible in Fig. 5.7, so Eq. (5.8) becomes

$$p_{D^0} = p_\nu. \tag{5.22}$$

When substituting Eq. (5.22) into Eq. (5.9), one obtains

$$\begin{aligned} E_{D^0} &= E_{K\ell} + E_\nu, \\ &= \sqrt{p_{K\ell}^2 + m_{K\ell}^2} + \sqrt{p_\nu^2 + m_\nu^2}, \\ &= m_{K\ell} + p_{D^0}, \end{aligned} \tag{5.23}$$

where the neutrino mass is assumed to be zero. Then, the D^0 mass is constrained to its value to eliminate the true momentum of the D^0:

$$\begin{aligned} m_{D^0}^2 &= E_{D^0}^2 - p_{D^0}^2, \\ &= m_{K\ell}^2 + 2m_{K\ell}p_{D^0} + \cancelto{0}{p_{D^0}^2 - p_{D^0}^2}, \end{aligned}$$

obtaining

$$p_{D^0} = \frac{m_{D^0}^2 - m_{K\ell}^2}{2m_{K\ell}}. \tag{5.24}$$

Finally, the D^* mass constraint is introduced to eliminate the remaining variables in favor of angles in the $K\ell$ mass frame, such as θ, the angle between the π and ν_ℓ direction:

$$\begin{aligned} m_{D^*}^2 &= (E_{D^0} + E_\pi)^2 - (\vec{p}_{D^0} + \vec{p}_\pi)^2 \\ &= E_{D^0}^2 + E_\pi^2 + 2E_{D^0}E_\pi - p_{D^0}^2 - p_\pi^2 - 2p_{D^0}p_\pi\cos\theta \\ &= m_{D^0}^2 + m_\pi^2 + 2E_{D^0}E_\pi - 2p_{D^0}p_\pi\cos\theta \end{aligned} \tag{5.25}$$

Substituting Eqs. (5.23) and (5.24) into the D^* mass constraint (5.25), the angle θ between the pion and the neutrino momentum can be obtained as

$$\cos\theta = -\frac{m_{D^*}^2 - m_{D^0}^2 - m_\pi^2 - 2E_\pi\left(m_{K\ell} + \frac{m_{D^0}^2 - m_{K\ell}^2}{2m_{K\ell}}\right)}{\frac{m_{D^0}^2 - m_{K\ell}^2}{2m_{K\ell}p_\pi}}. \tag{5.26}$$

5.5.2 The cone closure method

The cone closure method was first introduced in Ref. [149] and it relies on the reconstruction of the $D^{*+} \to D^0(\to K^-\ell^+\nu_\ell)\pi^+$ decay in the $K\ell$ rest frame. The kinematic of the decay, introduced in the previous section, is schematised in Fig. 5.7. The neutrino momentum is restricted to lie on the cone of angle θ and centred in the pion momentum.

The angle θ can be obtained from the known quantities from Eq. (5.26), while the azimuthal angle ϕ, around the $\vec{p}_\pi$ direction, can not be calculated. This is numerically constrained by the D^0 flight direction in the laboratory frame by taking 5000 points inside the cone, corresponding to 0.5 mrad precision. Then, the ϕ and θ angles in the $K\ell$ rest frame are used to solve for the correspondent angles in the laboratory frame. Finally, the

value of ϕ is chosen by the solution for which the $K\ell$ momentum is closest to the D^0 flight direction.

Since the cone closure algorithm relies on kinematic constraints, the momentum resolution of the detector can influence the failure rate of the algorithm. The failure rate is assessed by considering candidates whose $\cos\theta$ is calculated to be beyond the physical range on simulated data. The calculation of q^2_{reco} using this method is found to always return physical values if $-1 \leq \cos\theta \leq 1$. Hence, this criterion is added to the selection.

5.5.3 The Global Fit method

The goal of the Global Fit algorithm (GF) is to obtain the D^{*+} invariant mass, m_{GF}, by constraining the kinematic of the decay in the laboratory system (Fig. 5.1). The D^{*+} decays as $D^{*+} \to D^0\pi^+$ mediated by the strong interaction. Therefore, its vertex is integrated in the pp interaction vertex. As a consequence, the π track must point to the PV of the event. The D^0 decay secondary vertex is displaced from the PV and is reconstructed with the two charged daughter tracks (K^- and ℓ^+).

In order to obtain the momentum of the missing neutrino, a global χ^2 fit is performed, using the momentum measurements of the reconstructed particles and the position of the primary and the secondary vertices. The χ^2 function is built following the least squares (LS) method (see Sec. 5.5.3.1), imposing kinematic constraints to the decay, and then it is minimised with respect to the free parameters.

Due to the presence of a nonlinear constraint, *i.e.* the D^0 mass constraint, the χ^2 can be calculated up to a two-fold ambiguity. The GF algorithm minimises both χ^2 functions and returns the values of the parameters corresponding to the χ^2 function with the lowest value.

5.5.3.1 The least square method

This algorithm is based on the least squares (LS) method. Therefore, before describing the details of the algorithm, the LS method is described. Consider a set of N variables y_i, Gaussian-distributed with a known covariance matrix V and unknown mean values. These are related x_i variables, assumed to be known with precision. Supposing that the true value is given by a function of x and a set of unknown parameters $\vec{\theta} = (\theta_1, ..., \theta_m)$, namely $\phi(\vec{x};\vec{\theta})$, it is possible to estimate these parameters given $\vec{x}$ as data. This is done by minimising the quantity

$$\chi^2(\vec{\theta}) = \sum_{i=1}^{N} \left(y_i - \phi(x_i;\vec{\theta})\right) (V^{-1})_{ij} \left(y_j - \phi(x_j;\vec{\theta})\right) . \tag{5.27}$$

Besides, if ϕ is a linear function of θ, such as

$$\phi(\vec{x};\vec{\theta}) = \sum_{j=1}^{m} a_j(\vec{x})\theta_j = \sum_{j=1}^{m} A_{ij}(\vec{x})\theta_j \, ,$$

it is possible to edit Eq. (5.27) accordingly. Being $A_{ij} = a_j(\vec{x})$, $\vec{y} = (y_1, ..., y_N)$ the vector of the measured values and $\vec{\phi} = (\phi_1, ..., \phi_N)$, Eq. (5.27) can be written as

$$\begin{aligned}\chi^2 &= (\vec{y} - \vec{\phi})^T V^{-1} (\vec{y} - \vec{\phi}) \\ &= (\vec{y} - A\vec{\theta})^T V^{-1} (\vec{y} - A\vec{\theta}) \,. \end{aligned} \tag{5.28}$$

The χ^2 is minimised by the set of estimators, $\hat{\vec{\theta}}$, which, providing that the matrix $A^T V^{-1} A$ is not singular, are found to be

$$\begin{aligned}\hat{\vec{\theta}} &= (A^T V^{-1} A)^{-1} A^T V^{-1} \vec{y} \\ &\equiv B\vec{y}, \end{aligned} \tag{5.29}$$

hence a linear function of the original measurements. The covariance matrix for the estimators C^{-1} can be obtained using the error propagation:

$$C = B^T V B = (A^T V^{-1} A)^{-1} \,. \tag{5.30}$$

Finally, by substituting this into Eq. (5.28), the χ^2 can be written as

$$\chi^2 = (\vec{y} - \hat{\vec{\theta}}) C^{-1} (\vec{y} - \hat{\vec{\theta}})^T \,. \tag{5.31}$$

5.5.3.2 The GF algorithm

The core of the GF algorithm is to obtain the neutrino momentum by minimising a single function containing all the information about the kinematics of the decay and the measured quantities. Thanks to the linearity of the χ^2, it is possible to write the function

$$\chi^2(\vec{\theta}, \hat{\vec{\theta}}) = \sum_{i \in \text{constraints}} \chi_i^2 \,, \tag{5.32}$$

where $\vec{\theta}$ are the measured quantities, $\hat{\vec{\theta}}$ the fit parameters, and χ_i^2 is the χ^2 computed for the i-th kinematic constraint of the decay. Each is obtained following different procedures.

For instance, to be able to implement the charged tracks constraints, it is useful to wrap the information of the reconstructed track in state vectors $\vec{\alpha}$. At a given z-position in the experiment $z = z_{\text{Ref}}$, they are defined as

$$\vec{\alpha} = \left(x,\, y,\, t_x,\, t_y,\, \frac{q}{p} \right)_{z_{\text{Ref}}} \,. \tag{5.33}$$

where q is the charge of the particle, $p = |\vec{p}|$ is the total particle momentum, p_i $(i = x, y, z)$ is the i-th coordinate of the momentum and $t_i = \frac{p_i}{p_z}$ is the i-th coordinate slope.

At this point each χ_i^2 in the algorithm can be implemented. Based on the decay topology, the following kinematic constraints are taken into account:

- The invariant mass of the D^0 is Gaussian constrained to the value from the PDG ($m(D^0) = 1864.83 \pm 0.05$ MeV/c^2 [1]), so the following χ^2 is written.

$$\chi^2(D^0) = \frac{(m(D^0) - \hat{m}(D^0))^2}{2\sigma^2_{m(D^0)}}, \tag{5.34}$$

  where $\sigma^2_{m(D^0)}$ is set at 1 MeV/c^2, greater than the PDG value, but small enough to constrain the D^0 invariant mass at the level of few MeV/c^2.

- The charged daughters of the D^0, ℓ^+ and K^-, have to come from the secondary vertex. In order to get a constraint from this, the first two coordinates of the track (x and y) must be reparameterised using the vertex coordinates as follows

$$\begin{cases} \hat{x}(K/\ell) = x(D^0) + (z_{\text{Ref}} - z(D^0))\hat{t}_x(K/\ell) \\ \hat{y}(K/\ell) = y(D^0) + (z_{\text{Ref}} - z(D^0))\hat{t}_y(K/\ell) \end{cases}, \tag{5.35}$$

  and then the χ^2 is obtained by substituting $\hat{\vec{\alpha}}$ into Eq. (5.33). Therefore the χ^2 of Eq. (5.31) for the two tracks can be written as

$$\chi^2(K) = (\vec{\alpha}_K - \hat{\vec{\alpha}}_K)^T C^{-1} (\vec{\alpha}_K - \hat{\vec{\alpha}}_K)\,, \tag{5.36}$$

$$\chi^2(\ell) = (\vec{\alpha}_\ell - \hat{\vec{\alpha}}_\ell)^T C^{-1} (\vec{\alpha}_\ell - \hat{\vec{\alpha}}_\ell)\,. \tag{5.37}$$

- The D^0 comes from the primary vertex, so a similar reparameterisation has been adopted:

$$\begin{cases} \hat{x}_{\text{PV}} = x(D^0) + (z_{\text{PV}} - z(D^0))\hat{t}_x(D^0) \\ \hat{y}_{\text{PV}} = y(D^0) + (z_{\text{PV}} - z(D^0))\hat{t}_y(D^0) \end{cases}, \tag{5.38}$$

  where the momentum of the D^0 is calculated as $\vec{p}(K) + \vec{p}(\ell) + \vec{p}(\nu_\ell)$. Being $\vec{x}_{\text{PV}}$ the position of the PV, $\chi^2(\text{PV})$ has the form

$$\chi^2(\text{PV}) = (\vec{x}_{\text{PV}} - \hat{\vec{x}}_{\text{PV}})^T C^{-1} (\vec{x}_{\text{PV}} - \hat{\vec{x}}_{\text{PV}})\,. \tag{5.39}$$

- The pion is constrained to the $D^{*+} \to D^0\pi^+$ decay. Similarly to the charged tracks of the kaon and the lepton, it is parameterised as

$$\begin{cases} \hat{x}(\pi) = x_{\text{PV}} + (z_{\text{Ref}} - z_{\text{PV}})\hat{t}_x(\pi) \\ \hat{y}(\pi) = y_{\text{PV}} + (z_{\text{Ref}} - z_{\text{PV}})\hat{t}_y(\pi) \end{cases} \tag{5.40}$$

  and $\chi^2(\pi)$ is obtained as

$$\chi^2(\pi) = (\vec{\alpha}_\pi - \hat{\vec{\alpha}}_\pi)^T C^{-1} (\vec{\alpha}_\pi - \hat{\vec{\alpha}}_\pi)\,. \tag{5.41}$$

Finally, the χ^2 of Eq. (5.32) can be written as the sum of all the above contributions:

$$\chi^2(\vec{\theta},\hat{\vec{\theta}}) = \chi^2(\mathrm{PV}) + \chi^2(\pi) + \chi^2(\ell) + \chi^2(K) + \chi^2(D^0)\,, \tag{5.42}$$

and it is the function that is minimised. The vector $\hat{\vec{\theta}}$ consist of the 16 parameters, including:

1. $\vec{p}(\nu_\ell)$, the coordinates of the neutrino momentum;
2. $\vec{p}(\ell)$, the coordinates of the lepton momentum;
3. $\vec{p}(K)$, the coordinates of the kaon momentum;
4. $\vec{p}(\pi)$, the coordinates of the soft pion momentum;
5. $\vec{x}(D^0)$, the coordinates of the D^0 decay vertex position;
6. z_{PV}, the third coordinate of the primary vertex.

All the parameters are initialised to the measured quantities, except for the neutrino momentum coordinates and the PV position. For instance, since generally in the LHCb detector the x and y coordinates of a track momentum are small as compared to the z one, for the neutrino $p_x(\nu)$ and $p_y(\nu)$ are initialised to 0 MeV/c. Therefore, the value of $p_z(\nu)$ is discriminatory and different values of $p_z(\nu)$ are investigated: 0, 5, 10, 15, 20, 35, 40, 60, 80 and 100 GeV/c. The fit is then performed with $p_z(\nu)$ initialised with all these values and the one with the lowest χ^2 is finally chosen for the next iterations. Once the "best" initial $p_z(\nu)$ is chosen, a similar procedure is followed for the PV position. For each event, more than one possible PV is saved, so the fit is performed with z_{PV} set to all these possible values and the one giving the lowest χ^2 is chosen as the initial value of z_{PV} in the final fit iteration.

The minimisation of Eq. (5.42) is performed using the `TMinuit` class [150] in the Root Data Analysis Framework [151]. In order to have the best performance, a set of iterations is implemented. Each time, the information on the value of the function, the precision of the fit, *i.e.* EDM, and the status (converged or not) are saved. If the minimisation does not fulfil these requirements, such as converged status and EDM $< 10^{-3}$, it is called again, until the fit converges with the desired EDM.

After applying the global fit, approximately 15% of candidates per signal channel have events which do not converge. This inefficiency is taken into account in the fit framework by requiring the convergence of the fit. The two `TMinuit` algorithms, `MIGRAD` and `HESSE` are used to obtain the central value of the parameters and to determine the parameters uncertainty, respectively. Hence, the convergence of the fit is required by selecting only events with a positive status for both algorithms.

One way to correct this inefficiency is to unfold the two possible solutions of the second-grade equation Eq. (5.20), $p_z(\nu)_+$ and $p_z(\nu)_-$. For both $p_z(\nu)_\pm$ the χ^2 is found to

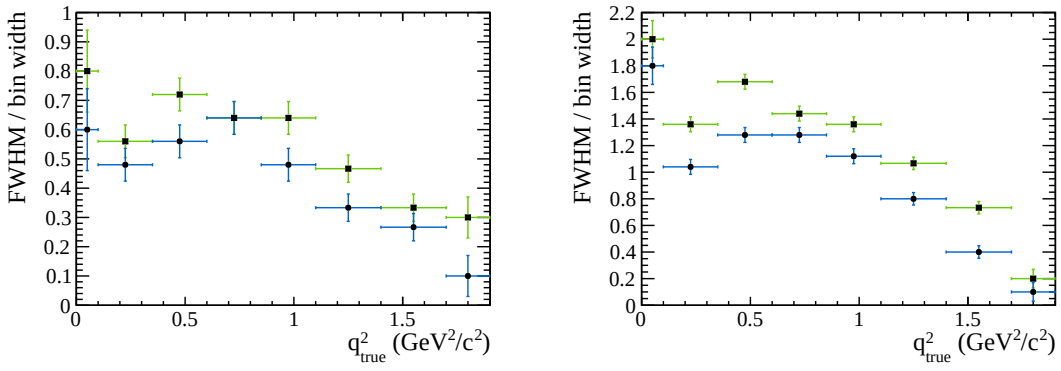

(a) (b)

Figure 5.8: Resolution estimated as the FWHM in bins of q^2_{true} for when the q^2 is reconstructed with cone closure method (left) and the GF (right). $D^0 \to K^-\mu^+\nu_\mu$ mode in blue and $D^0 \to K^-e^+\nu_e$ in green.

be the same, so the GF is performed again by initialising to one solution or the other. Then the D^0 mass is calculated following Eq. (5.7) and substituting the measured values and $p_z(\nu)_\pm$. Finally, this is compared to the D^0 invariant mass obtained with the true information stored in the MC, as it is done for the q^2 resolution (see 5.5.4). However, this procedure has not yet been implemented.

5.5.4 q^2 resolution

The q^2 is defined as

$$q^2 = (p(D^0) - p(K^-))^2 \,. \tag{5.43}$$

Its resolution is calculated by comparing the reconstructed q^2, to the simulated truth value, q^2_{true}, on an event-by-event basis. This is estimated as the full width at medium height (FWHM) of the $(q^2 - q^2_{\text{true}})$ distribution in bins of $q^2_{\text{true}} = 0.1$ GeV/c^2. This distribution is generally non-Gaussian and asymmetrical, especially in high and low q^2_{true} bins, and it is shown in Fig. 5.8(b) and 5.8(b) for both signal modes, using the cone closure and the global fit methods. As expected, the $D^0 \to K^-\mu^+\nu_\mu$ decay channel has a better resolution than the electron mode.

In order to choose which q^2 reconstruction should be used as the nominal one, a comparison between the resolution of the two methods is needed. In Fig. 5.9 the $q^2_{\text{reco}} - q^2_{\text{true}}$ distribution is plotted for q^2_{true} in the $(0.1, 0.35)$ GeV$^2/c^2$ interval (for demonstrative purposes). For both signal modes, it is evident that the q^2 reconstructed using the GF method has a worse resolution with respect to the one reconstructed using with the cone closure method. Therefore the cone closure method is chosen as the nominal method for the q^2 reconstruction.

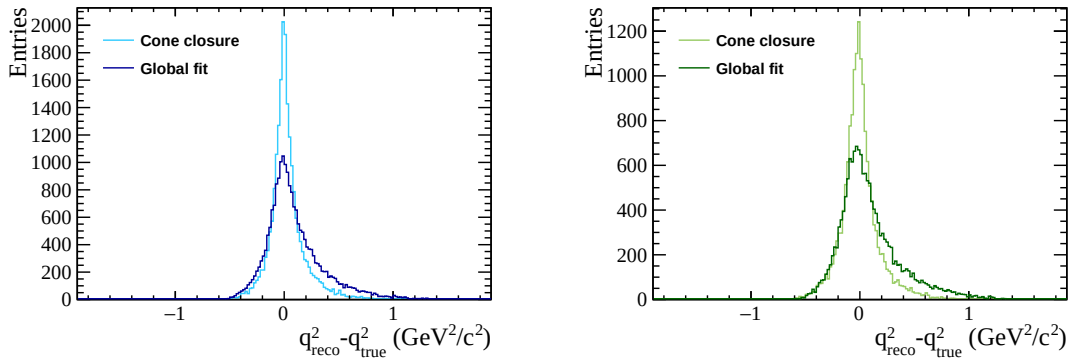

(a) Muon mode. (b) Electron mode.

Figure 5.9: Histograms of the $q^2_{\text{reco}} - q^2_{\text{true}}$ distribution in the $(0.1 \leq q^2_{\text{true}} < 0.35)\,\text{MeV}/c$ region for the two q^2 reconstruction methods. The magnitude distribution is shown for (left) $D^0 \to K^-\mu^+\nu_\mu$ and (right) $D^0 \to K^-e^+\nu_e$. The q^2 reconstructed with the global fit is represented in the darker colour.

5.6 Templates and fit frameworks

The yields for $D^0 \to K^-\mu^+\nu_\mu$ (N_μ) and $D^0 \to K^-e^+\nu_e$ (N_e) decays, and consequently $R_{e/\mu}$ (Eq. 5.3), are extracted with two different fit strategies. Two simultaneous bi-dimensional fits are performed to the same datasets using different variables. These two frameworks are referred to as *YATF* and *SAGF*, where the acronyms have been introduced to differentiate the fitter that uses the global fit output, the *SAGF* one, from the other. Afterwards, the signal yields extracted from both fits are compared to check for consistency.

Both fitters include $R_{e/\mu}$ as

$$N_e = N_\mu \cdot R_{e/\mu}. \tag{5.44}$$

This ensures that the uncertainties are correctly propagated. The value of $R_{e/\mu}$ is blinded using `RooBlindCategory` [151], which applies a random shift of the central result leaving the uncertainty unchanged and the seed of this shift is based on the same string of characters for both fitters. In this way, it is possible to compare the results in order to check the fitters consistency without revealing the true central value.

The *YATF* fit uses the difference between the D^{*+} and D^0 visible masses and the D^0 corrected mass as fitting variables:

$$\Delta m_{\text{visible}} = m(K^-\ell^+\pi_s^+) - m(K^-\ell^+), \tag{5.45}$$

$$m_{\text{corr}}(D^0) = \sqrt{m(K\ell)^2 + {p'_{\text{T}}}^2} + |p'_{\text{T}}|, \tag{5.46}$$

where $p'_{\rm T}$ is the transverse momentum of the $K\ell$ system with respect to the D^0 flight direction.

The signal and background shapes are taken from simulation using bi-dimensional templates, and for each template the only fit parameter is its yield. The fit implemented using the `HistFactory` framework. The incorporation of the statistical uncertainties on the templates is done using the Barlow-Beeston technique [152].

The *SAGF* fit, as the acronym suggests, relies on the outputs of the GF algorithm. The D^{*+} invariant mass, m_{GF}, is obtained using the neutrino momentum estimation of the GF. The D^0 visible mass, $m_{vis} = m(K\ell)$, is the other fit variable.

Initially, in order to have two independent methods, the idea was to perform an analytical fit; however, after some preliminary studies, a bi-dimensional template fit approach was adopted. The effect of the limited size of the MC samples in the fit result is estimated as a systematic uncertainty by repeating the fit with new templates obtained by modifying each bin of the template with a Poisson distributed fluctuation. This procedure is described in Sec. 5.8.

Both fitting methods rely on the fact that the variables provide good separation between the signal and background modes. To test the consistency between the two strategies, pseudoexperiment data are generated with given values of $R_{e/\mu}$. With these data, both fits are shown to give compatible results, validating the method. This is reported in Sec. 5.6.4.

The bi-dimensional templates are prepared using the same simulation datasets for both fits, aside from the small fraction of candidates for which the Global Fit algorithm fails to converge (see Sec. 5.5.3). The decay channels considered in the templates are listed in Table 5.8. They are selected using truth-matching selection, by applying requirements to the PID and to the MC truth of the complete decay chain. For example, to select the signal $D^0 \to K^-\mu^+\nu_\mu$, the μ and the K must originate from the same particle, the D^0, which has to originate from the same particle as the π^+, the D^{*+}.

The templates can be categorised in the following typologies:

i. **Signal channels.** $D^0 \to K^-\mu^+\nu_\mu$, muon mode and $D^0 \to K^-e^+\nu_e$, electron mode, where the D^0 comes from $D^{*+} \to D^0\pi^+$ decays.

ii. **Partially-reconstructed background channels** (Part-Reco), containing a kaon and a lepton in the final state and a neutral particle that is undetected. The considered channels are $D^{*+} \to D^0\pi^+$ decays, with $D^0 \to K^-\ell^+\nu_\ell\pi^0$, where the $K^-\pi^0$ pair can be non-resonant or from K^{*-} decays, $D^0 \to K^{*-}(\to K^-\gamma)\ell^+\nu_\ell$, $D^0 \to K^{*-}(\to K^-\pi^0)\ell^+\nu_\ell$ or $D^0 \to (K^{*-} \to \bar{K}^0\pi^-)\ell^+\nu_\ell$.

iii. **Mis-identified background channels** (misID) where a pion or a kaon is identified as the lepton or a pion is identified as the kaon. The D^{*+} decays as $D^{*+} \to D^0\pi^+$. Where the $D^0 \to \pi^-\ell^+\nu_\ell$ decay and the D^0 hadronic decays: $D^0 \to K^-K^+$, $D^0 \to K^-\pi^+\pi^0$, $D^0 \to K^-\pi^+\pi^+\pi^-$, $D^0 \to \pi^-\pi^+\pi^0$ and $D^0 \to K^-\pi^+$ are considered. Some of these decays are also partially reconstructed.

iv. **Random pion decays.** The slow pion coming from the $D^{*+} \to D^0\pi^+$ decay is chosen by truth-matching the D^0 decay and requiring that the D^{*+} decay is not truth-matched. These templates are a proxy of the D^{*+} combinatorial background.

v. **Same sign signal decay.** The $D^0 \to K^+\ell^+\nu_\ell$ decays are used as combinatorial proxy for the respective modes. These are obtained by the dedicated stripping lines described in Sec. 5.3.

It is worth noting that not all channels contribute to both muon and electron modes. This is checked by looking at the misidentification rates. For a number of these channels no candidates survive after the PID selection of either the muon or electron mode: all the channels where the lepton would be misidentified with the other lepton are not considered as template because their contribution is small. In the end, out of a total of possible 32 templates, only 21 for each mode are used in the fits, 11 of which are lepton-specific. These are identified in Table 5.8. Moreover, PID, Tracking and event multiplicity weights are added to all templates, irrespective of the fits.

In order to assess the quality of the fit, bi-dimensional pull plots (pull(i_x, i_y)) are produced for both modes. In order to include the errors of the total template, these are calculated by a custom method. Being $(i_x, i_y)_{\text{data}}$ and $(i_x, i_y)_{\text{model}}$ the population of the (i_x, i_y) bin of data and the model histograms, respectively, pull(i_x, i_y) is defined as

$$\text{pull}(i_x, i_y) = \frac{(i_x, i_y)_{\text{data}} - (i_x, i_y)_{\text{model}}}{\sqrt{\sigma^2_{\text{data}} + \sigma^2_{\text{model}}}}, \tag{5.47}$$

where the uncertainty, σ_{data}, is the square root of the (i_x, i_y) bin occupancy and σ_{model} is the error associated to the (i_x, i_y) bin of the histogram of the model.

5.6.1 Relative contributions fixes

Some of the branching fractions ($\mathcal{B}$) of the considered background modes have been measured with good precision, as shown in Tab. 5.9. The following procedure is implemented to take into account the branching fraction and the efficiencies of these channels. The PID and tracking efficiencies are considered in the templates by weighting the simulated events using lookup tables from PIDCalib [153].

The yield of the i-th mode can be rewritten as

$$N_i = \mathcal{L}_{int}\sigma_{(pp\to D)}\mathcal{B}_i\varepsilon_i, \tag{5.48}$$

where $\mathcal{L}_{int}$ is the integrated luminosity, ε_i is the i-th channel total efficiency and $\sigma_{(pp\to D)}$ is the D^{*+} production cross-section multiplied by the $D^{*+} \to D^0\pi^+$ branching fraction.

	Muon mode	**Electron mode**
Signal	$D^{*+} \to (D^0 \to K^-\mu^+\nu_\mu)\pi^+$	$D^{*+} \to (D^0 \to K^-e^+\nu_e)\pi^+$
Part-reco non-resonant $K^-\pi^0$	$D^{*+} \to (D^0 \to K^-\mu^+\nu_\mu\pi^0)\pi^+$	$D^{*+} \to (D^0 \to K^-e^+\nu_e\pi^0)\pi^+$
Part-reco $K^{*-} \to K^-\pi^0$ or $K^{*-} \to K^-\gamma$	$D^{*+} \to (D^0 \to K^{*-}\mu^+\nu_\mu)\pi^+$	$D^{*+} \to (D^0 \to K^{*-}e^+\nu_e)\pi^+$
Part-reco $K^{*-} \to \bar{K}^0\pi^-$	$D^{*+} \to (D^0 \to K^{*-}\mu^+\nu_\mu)\pi^+$	$D^{*+} \to (D^0 \to K^{*-}e^+\nu_e)\pi^+$
misID	$D^{*+} \to (D^0 \to \pi^-\mu^+\nu_\mu)\pi^+$	$D^{*+} \to (D^0 \to \pi^-e^+\nu_e)\pi^+$ $D^{*+} \to (D^0 \to K^-K^+)\pi^+$ $D^{*+} \to (D^0 \to K^-\pi^+\pi^0)\pi^+$ $D^{*+} \to (D^0 \to K^-\pi^+\pi^-\pi^+)\pi^+$ $D^{*+} \to (D^0 \to \pi^-\pi^+\pi^0)\pi^+$ $D^{*+} \to (D^0 \to K^-\pi^+)\pi^+$
Random π	$D^0 \to K^-\mu^+\nu_\mu$ $D^0 \to K^-\mu^+\nu_\mu\pi^0$ (non-res $K^-\pi^0$) $D^0 \to K^{*-}\mu^+\nu_\mu$ - $K^{*-} \to K^-(\pi^0/\gamma)$ $D^0 \to (K^{*-} \to \bar{K}^0\pi^-)\mu^+\nu_\mu$ $D^0 \to \pi^-\mu^+\nu_\mu$	$D^0 \to K^-e^+\nu_e$ $D^0 \to K^-e^+\nu_e\pi^0$ (non-res $K^-\pi^0$) $D^0 \to K^{*-}e^+\nu_e$ - $K^{*-} \to K^-(\pi^0/\gamma)$ $D^0 \to (K^{*-} \to \bar{K}^0\pi^-)e^+\nu_e$ $D^0 \to \pi^-e^+\nu_e$ $D^0 \to K^-K^+$ $D^0 \to K^-\pi^+\pi^0$ $D^0 \to K^-\pi^+\pi^-\pi^+$ $D^0 \to \pi^-\pi^+\pi^0$ $D^0 \to K^-\pi^+$
Same sign	$D^0 \to K^+\mu^+\nu_\mu$	$D^0 \to K^+e^+\nu_e$

Table 5.8: Decay channels considered in the templates in electron and muon modes. Misidentified hadronic channels are common to both modes.

Channel	$\mathcal{B}$ (%) [1]
$D^0 \to K^- e^+ \nu_e$	3.542 ± 0.0035
$D^0 \to K^- \mu^+ \nu_\mu$	3.41 ± 0.04
$D^0 \to K^{*-} \mu^+ \nu_\mu$	1.89 ± 0.24
$D^0 \to K^{*-} e^+ \nu_e$	2.15 ± 0.16
$D^0 \to K^- e^+ \nu_e \pi^0$	$1.6^{+1.3}_{-0.5}$
$D^0 \to K^- \pi^+$	3.950 ± 0.031
$D^0 \to K^- \pi^+ \pi^0$	14.4 ± 0.5
$D^0 \to K^- K^+$	0.408 ± 0.006
$D^0 \to K^- \pi^+ \pi^- \pi^+$	8.22 ± 0.14
$D^0 \to \pi^- e^+ \nu_e$	0.291 ± 0.004
$D^0 \to \pi^- \mu^+ \nu_\mu$	0.267 ± 0.012
$D^0 \to \pi^- \pi^+ \pi^0$	1.49 ± 0.06

Table 5.9: External branching fraction values for signal and background channels [1].

If one channel is chosen as reference, one can write, with self-explanatory labels,

$$N_{\rm ref} = \mathcal{L}_{int}\sigma_{(pp\to D)}\mathcal{B}_{\rm ref}\varepsilon_{\rm ref}, \tag{5.49}$$

$$\frac{N_i}{N_{\rm ref}} = \frac{\mathcal{L}_{int}\sigma_{(pp\to D)}\mathcal{B}_i\varepsilon_i}{\mathcal{L}_{int}\sigma_{(pp\to D)}\mathcal{B}_{\rm ref}\varepsilon_{\rm ref}}, \tag{5.50}$$

$$\frac{N_i}{N_{\rm ref}} = \frac{\mathcal{B}_i\varepsilon_i}{\mathcal{B}_{\rm ref}\varepsilon_{\rm ref}} = \frac{f_i}{\mathcal{B}_{\rm ref}}, \tag{5.51}$$

$$f_i = \left(\mathcal{B}_i \frac{\varepsilon_i}{\varepsilon_{\rm ref}}\right), \tag{5.52}$$

where f_i, defined in Eq. (5.52), can be calculated for each channel. This means that, for some selected channels, the background yields are not free parameters of the fit anymore, but that they are constrained to the reference channel through f_i. This fraction, f_i, is allowed to vary within 2σ from its central value. This procedure is implemented for both the muon and electron modes for selected channels, such as $D^0 \to K^- K^+$, $D^0 \to K^- \pi^+ \pi^0$, $D^0 \to K^- \pi^+ \pi^+ \pi^-$, $D^0 \to \pi^- \pi^+ \pi^0$ and $D^0 \to K^- \pi^+$ and the correspondent decays with a random pion. As a result, the yields of the other channels are obtained as

$$N_i = f_i \frac{N_{K\ell\nu}}{\mathcal{B}_{K\ell\nu}}. \tag{5.53}$$

The starting values of the background parameters of the two fits are obtained by calculating the expected number of events of the given background mode, using their relative branching fractions with respect to an estimate of what the expected yield of the signal mode, and corrected by the efficiencies. When such information is not available

(for instance, for the random slow pion templates or the same sign template), the starting value is chosen randomly within a given range. Varying the starting values has proven to have little to no effect on the fit results.

Moreover, in order to validate the fit, additional studies are performed with both frameworks. First, in order to reduce the complexity of the fit, fit components whose yields are consistent with zero within uncertainties are sequentially removed. As an additional check, in order to model the combinatorial contributions to the background and not relying only on the same sign $D^0 \to K^+\ell^+\nu_\ell$ channel, a BDT study is implemented. However, since this study is still ongoing and lies outside the scope of the thesis it is not included.

5.6.2 The *YATF* Fitter results

The templates of the 2D YATF fit are formed using a binning of 25×25 in both the corrected mass and the visible delta mass. The fit method relies on the `HistFactory` framework of `RooFit`, without modifying the code to use the "Lite" Beeston-Barlow method [152]. All the two-dimensional templates are reported in App. A.2.

In Figure 5.10, the fit to 2016 data is shown. In this Figure, the projections of the muon mode fit for the corrected mass (left) and Δm_{vis} (right) are shown at the top and the electron mode fit at the bottom. The individual components of the fit are given in the legend. In order to understand different background contributions, the same fit is shown on semi-logy scale in Figure A.3.

With this fit a blinded result of $R_{e/\mu} = x.xxx \pm 0.002$ is obtained and the muon signal yield is $N_\mu^{\text{YATF}} = 264700 \pm 510$. The two dimensional pulls of the fits are displayed in Figure 5.11. There is good coverage of the pulls over the majority of the phase space region. The area where the pulls are larger corresponds to the least populated part in the corrected mass distribution.

5.6.3 The *SAGF* Fitter results

The SAGF fitter employs a strategy similar to the one used for the YATF fitter, described in Section 5.6.2. This is a simultaneous bidimensional template fit to the mass of the $K\ell$ system and the D^{*+} mass reconstructed with the Global Fit algorithm, discussed in Section 5.5.3 (m_{GF}).

The templates use again a binning of 25×25 and are produced with the same procedure as for the YATF fitter, with the addition that the Global Fit algorithm has succeeded (see Sec. 5.5.3); therefore, there is a slightly lower signal efficiency due to this additional requirement, respectively for the two modes $\varepsilon_e^{\text{SAGF}}(82.052 \pm 0.015)$ % and $\varepsilon_\mu^{\text{SAGF}}(84.014 \pm 0.004)$ %. The two dimensional template shapes are represented in Figs. 5.12 and 5.13 for the muon and the electron mode, respectively.

In Fig. 5.14 the projections of the fit on the two variables, for both the muon and electron modes, are shown. The bidimensional pulls are shown in Figure 5.15. All the fit parameters after performing the fit are listed in Tab. 5.10. Considering background

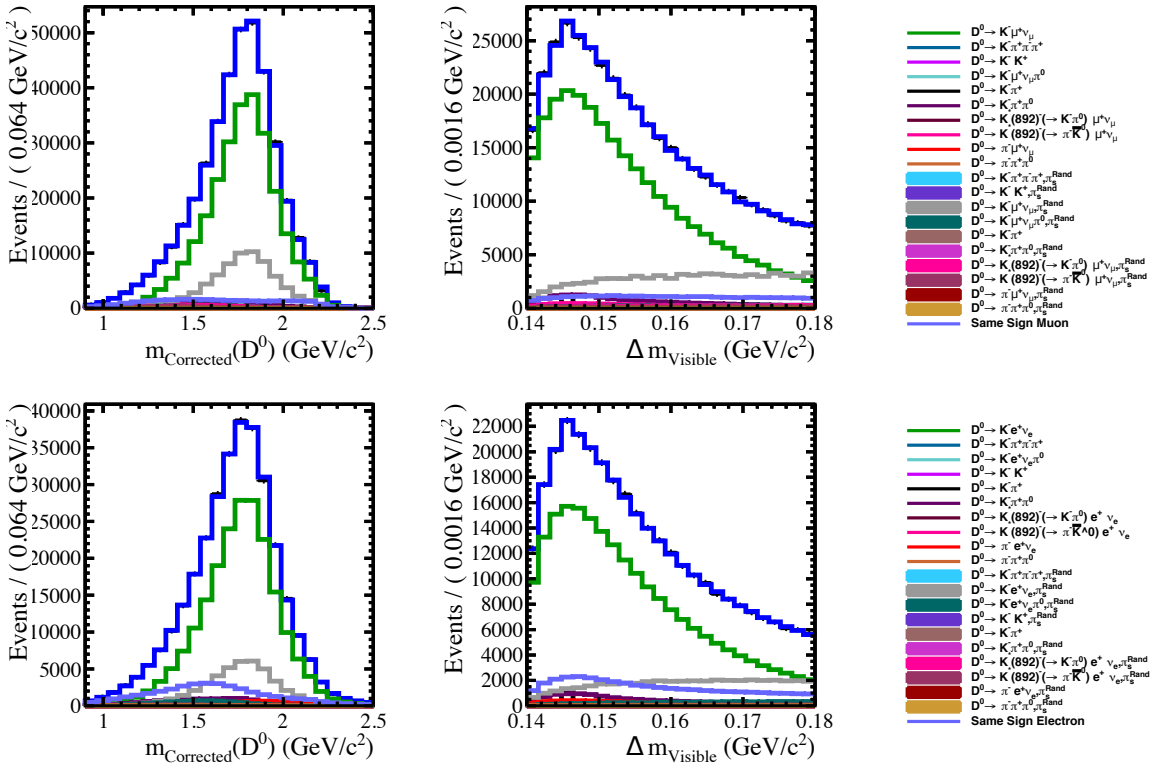

Figure 5.10: Fit to 2016 Data with the YATF method. In the top rows the projections of the muon modes and in the bottom rows the projection of the electron modes are shown. On the left the projection on the corrected D^0 mass and on the right the projection on the visible delta mass. The legends for the colours are given on the right. For each model, the total fit is displayed in blue and the data points are in black dots.

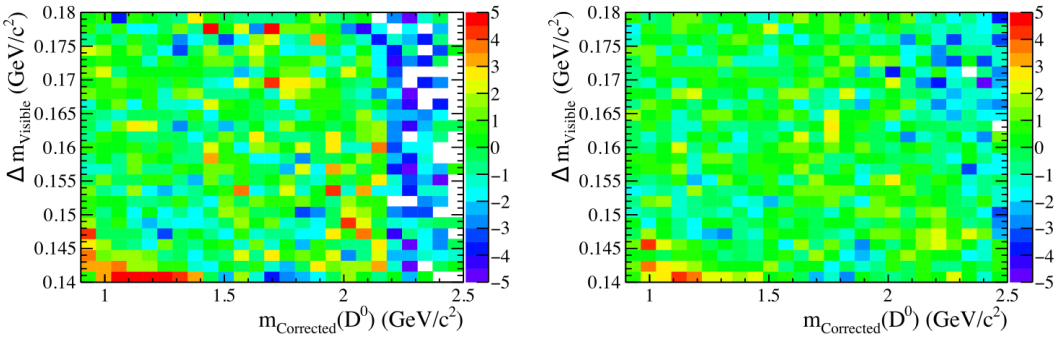

Figure 5.11: 2D pulls of the YATF method over the space of the fit. On the left the muon mode pull, and on the right, the electron mode pull.

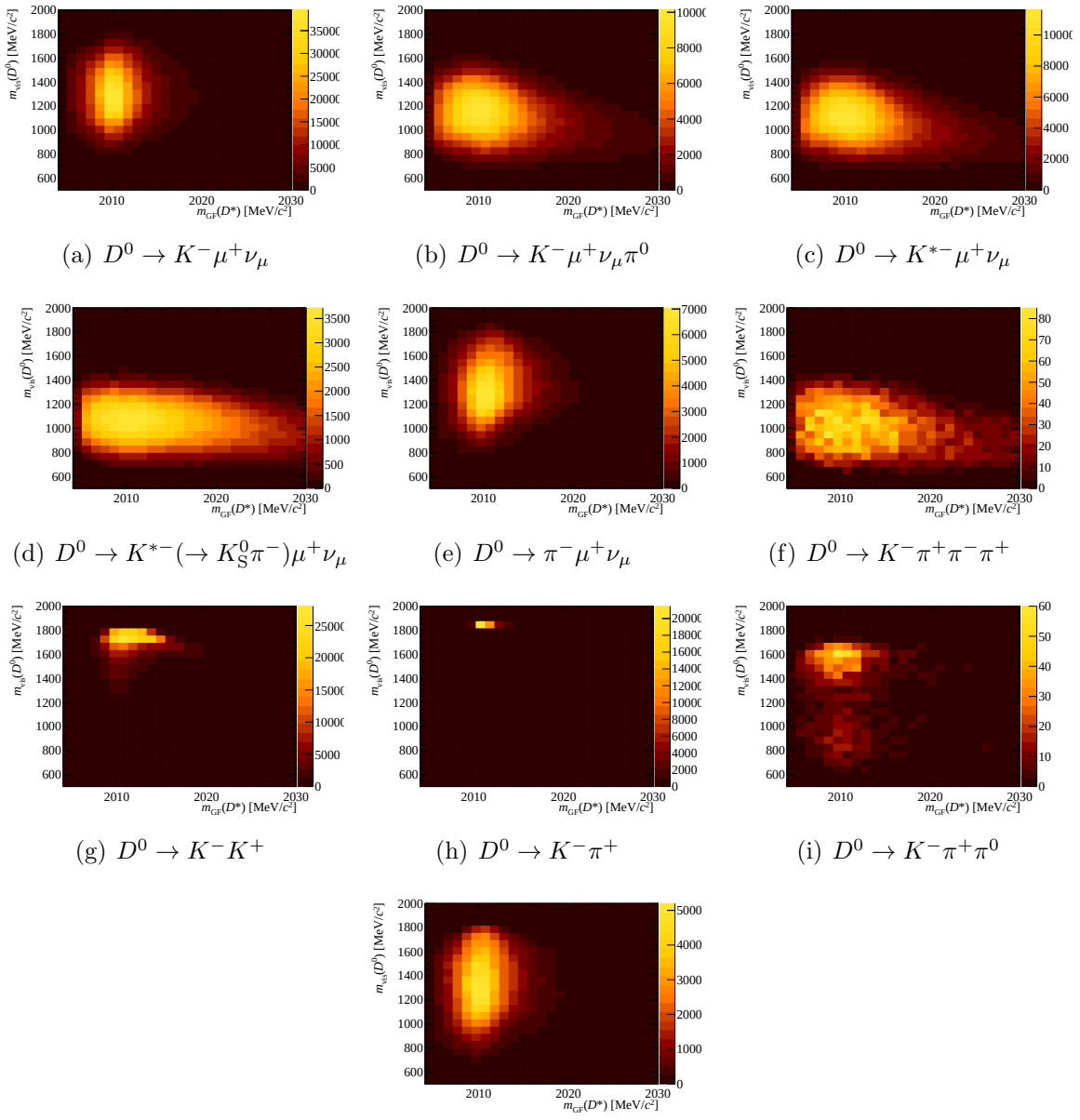

(a) $D^0 \to K^-\mu^+\nu_\mu$ (b) $D^0 \to K^-\mu^+\nu_\mu\pi^0$ (c) $D^0 \to K^{*-}\mu^+\nu_\mu$

(d) $D^0 \to K^{*-}(\to K^0_S\pi^-)\mu^+\nu_\mu$ (e) $D^0 \to \pi^-\mu^+\nu_\mu$ (f) $D^0 \to K^-\pi^+\pi^-\pi^+$

(g) $D^0 \to K^-K^+$ (h) $D^0 \to K^-\pi^+$ (i) $D^0 \to K^-\pi^+\pi^0$

(j) $D^0 \to \pi^+\pi^-\pi^0$

Figure 5.12: Two-dimensional template shapes for the muon mode $D^0 \to K^-\mu^+\nu_\mu$. From top left to bottom right, these include: Signal $D^0 \to K^-\mu^+\nu_\mu$, $D^0 \to K^-\mu^+\nu_\mu\pi^0$, $D^0 \to K^{*-}\mu^+\nu_\mu$ with $K^{*-} \to K^-\pi^0$ or $K^-\gamma$, $D^0 \to \pi^-\mu^+\nu_\mu$, $D^0 \to K^-\pi^+\pi^-\pi^+$, $D^0 \to K^-K^+$, $D^0 \to K^-\pi^+$, $D^0 \to K^-\pi^+\pi^0$, and $D^0 \to \pi^+\pi^-\pi^0$.

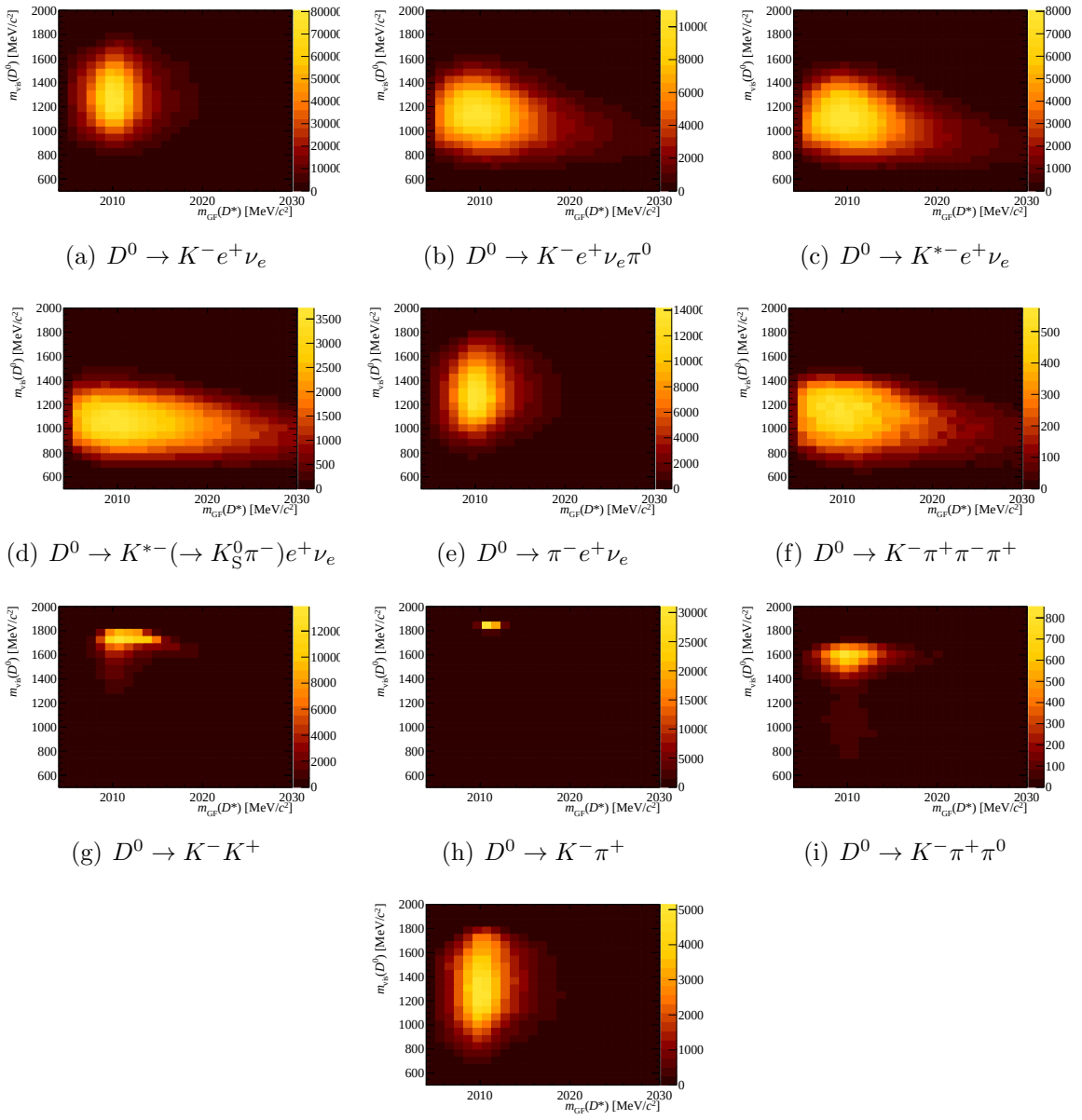

(a) $D^0 \to K^- e^+ \nu_e$ (b) $D^0 \to K^- e^+ \nu_e \pi^0$ (c) $D^0 \to K^{*-} e^+ \nu_e$

(d) $D^0 \to K^{*-} (\to K^0_S \pi^-) e^+ \nu_e$ (e) $D^0 \to \pi^- e^+ \nu_e$ (f) $D^0 \to K^- \pi^+ \pi^- \pi^+$

(g) $D^0 \to K^- K^+$ (h) $D^0 \to K^- \pi^+$ (i) $D^0 \to K^- \pi^+ \pi^0$

(j) $D^0 \to \pi^+ \pi^- \pi^0$

Figure 5.13: Two-dimensional template shapes for the electron mode $D^0 \to K^- e^+ \nu_e$. From top left to bottom right, these include: Signal $D^0 \to K^- e^+ \nu_e$, $D^0 \to K^- e^+ \nu_e \pi^0$, $D^0 \to K^{*-} e^+ \nu_e$ with $K^{*-} \to K^- \pi^0$ or $K^- \gamma$, $D^0 \to \pi^- e^+ \nu_e$, $D^0 \to K^- \pi^+ \pi^- \pi^+$, $D^0 \to K^- K^+$, $D^0 \to K^- \pi^+$, $D^0 \to K^- \pi^+ \pi^0$, and $D^0 \to \pi^+ \pi^- \pi^0$.

contributions, a large fraction of the modes with a random pion are compatible with zero, as visible in the fit projections and when comparing the yields. The yield of the signal muon mode is measured to be $N_\mu = 179400 \pm 3200$, with the uncertainties only due to statistics. In order to be able to compare it with the yield obtained by the YATF fitter, it is multiplied by the SAGF efficiency, obtaining 213500 ± 3800, which is in agreement with the value of $N_\mu^{\text{YATF}} = 264700 \pm 510$ within 2σ. Finally, we obtain $R_{e/\mu} = x.xxxx \pm 0.0027$, with an uncertainty in agreement with the YATF fitter result.

5.6.4 Fit consistency cross-checks

In order to take into account all the biases between the two different fitters and to evaluate the systematic uncertainties, the following studies have been performed. The consistency of the two fit frameworks is checked by a pseudoexperiment study. Toy datasets are produced from the simulated sample by requiring the muon yield to be 500000 events and with different $R_{e/\mu}$ values. Eleven values are chosen in the $R_{e/\mu}^{\text{gen}} \in (0.95, 1.05)$ range and for each $R_{e/\mu}^{\text{gen}}$, 200 datasets are created.

First, the two fits to the pseudodata are performed with all the templates and only one value of $R_{e/\mu}^{\text{gen}}$. This results in the same value for both fitters. Afterwards, the difference between $R_{e/\mu}$ obtained from the fit and $R_{e/\mu}^{\text{gen}}$ is calculated. They are all found to be compatible with zero at less than 0.5σ. This is visible in the three distributions shown in Fig 5.16 for the SAGF fitter.

Finally, for each of the 200 toy datasets with $R_{e/\mu}^{\text{gen}}$, the difference between the value obtained by the two fits, $R_{e/\mu}(\text{YATF}) - R_{e/\mu}(\text{SAGFF})$, is investigated. The distribution is narrow and peaked at a value different from zero (always negative) but within 1σ of the average error given by the SAGF fit; it is shown in Fig 5.17. Further studies have revealed that this small bias is due to a small difference in the signal efficiency coming from the different histograms boundaries of the two fit methods. The discrepancy disappears once this is fixed. In both fitters the variables are required to lay in the following ranges: $m_{\text{GF}}(D^*)$ in $(2005, 2030)$ MeV/c^2, $m(D^0)$ in $(500, 2000)$ MeV/c^2, $\Delta m_{\text{vis}} \in (140, 180)$ MeV/c^2 and $m_{\text{corr}}(D^0)$ in $(900, 2500)$ MeV/c^2.

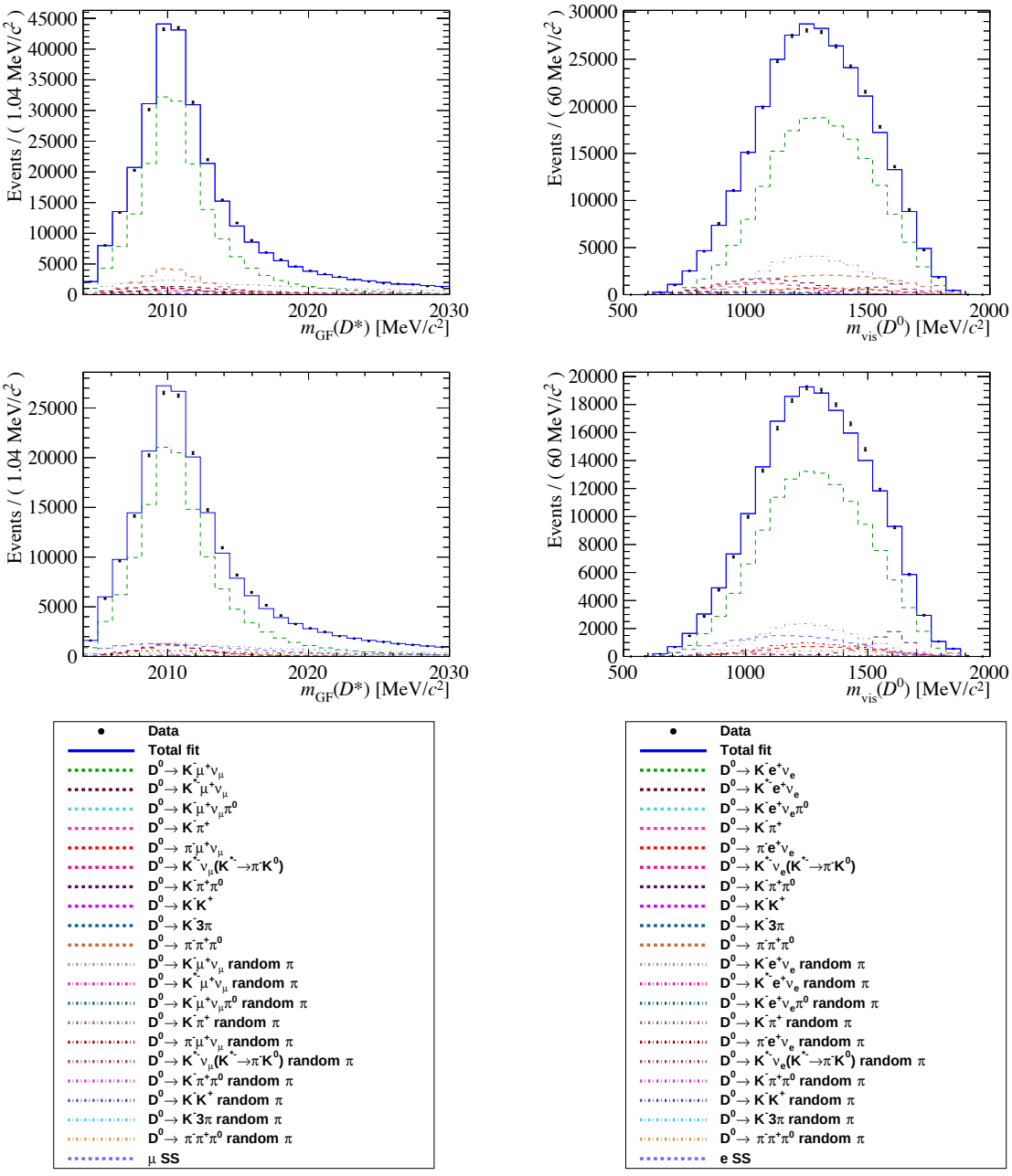

Figure 5.14: Projection of the SAGF fit results (m_{GF}-left, $m(K\ell)$-right). Top part muon mode, bottom electron mode.

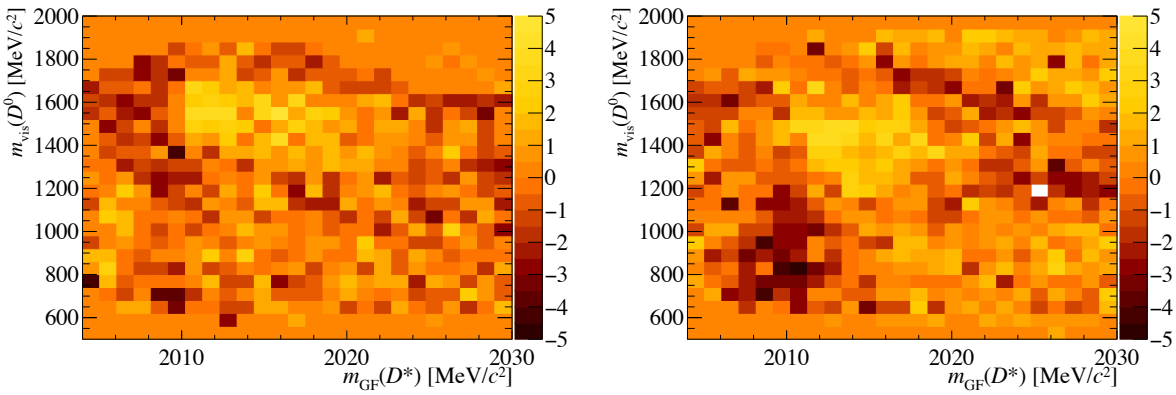

Figure 5.15: Bidimensional pulls of the SAGF fit. Muon mode on the left, electron mode on the right.

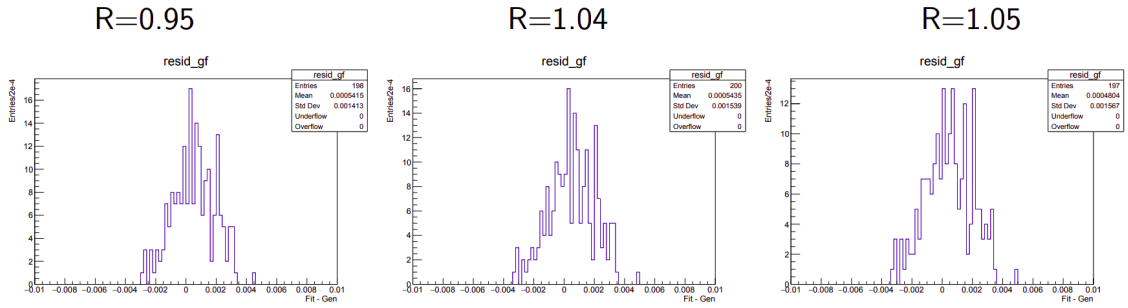

Figure 5.16: $R_{e/\mu}$ residual ($R^{\text{fit}}_{e/\mu} - R^{\text{gen}}_{e/\mu}$) distributions for different values of $R^{\text{gen}}_{e/\mu}$: 0.95, 1.04, 1.05 and SAGF fitter.

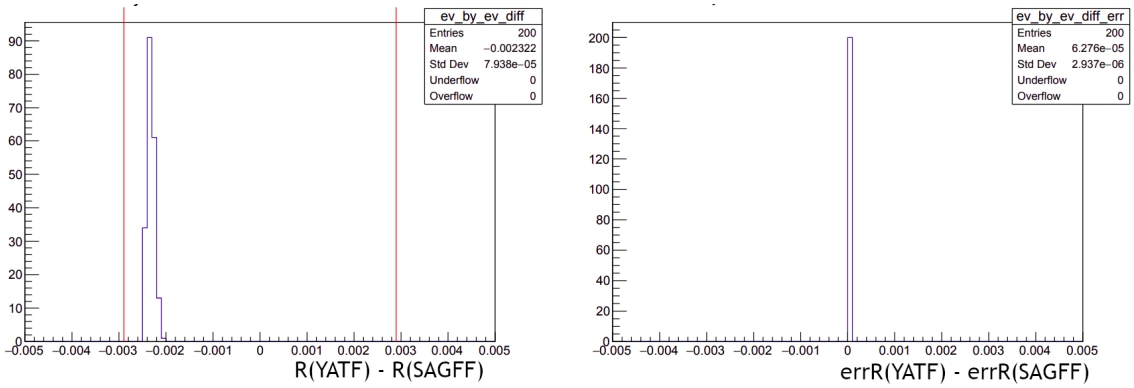

Figure 5.17: Difference between the values of $R_{e/\mu}$ obtained from the fits (left) and their errors (right). The red vertical lines indicate the average error on $R_{e/\mu}$ from the SAGF fit. Nominal $R_{e/\mu}$ is 1.00.

Parameter	**Fit result**
$\boldsymbol{R_{e/\mu}}$	$x.xxx \pm 0.013$
$\boldsymbol{N_\mu(D^0 \to K^-\mu^+\nu_\mu)}$	179400 ± 3200
$N_\mu(D^0 \to K^{*-}\mu^+\nu_\mu)$	14200 ± 2100
$N_\mu(D^0 \to K^{*-}(\to \pi^- K^0_S)\mu^+\nu_\mu\ )$	9700 ± 1400
$N_\mu(D^0 \to K^-\mu^+\nu_\mu\pi^0)$	0 ± 660
$N_\mu(D^0 \to \pi^-\mu^+\nu_\mu)$	6700 ± 2500
$N_\mu(D^0 \to \pi^-\pi^+\pi^0)$	24100 ± 3000
$N_\mu(D^0 \to K^-\pi^+)$	323 ± 29
$N_\mu(D^0 \to K^-\pi^+\pi^0)$	6860 ± 640
$N_\mu(D^0 \to K^-\pi^+\pi^-\pi^+)$	1800 ± 1700
$N_\mu(D^0 \to K^-K^+)$	1200 ± 200
$N_\mu(D^0 \to K^+\mu^+\nu_\mu)$ SS	2700 ± 3800
$N_e(D^0 \to K^+e^+\nu_e)$ SS	16000 ± 740
$N_e(D^0 \to K^-e^+\nu_e\pi^0)$	0 ± 73
$N_e(D^0 \to \pi^-e^+\nu_e)$	7000 ± 240
$N_e(D^0 \to \pi^-\pi^+\pi^0)$	0 ± 190
$N_e(D^0 \to K^-\pi^+)$	293 ± 46
$N_e(D^0 \to K^-\pi^+\pi^0)$	7400 ± 350
$N_e(D^0 \to K^-\pi^+\pi^-\pi^+)$	0 ± 110
$N_e(D^0 \to K^-K^+)$	539 ± 200
Random π:	
$N_e(D^0 \to K^-e^+\nu_e)$	20100 ± 1700
$N_e(D^0 \to K^-K^+)$	1200 ± 300
$N_e(D^0 \to K^-\pi^+)$	294 ± 55
$N_e(D^0 \to K^-\pi^+\pi^0)$	100 ± 17
$N_e(D^0 \to \pi^-e^+\nu_e)$	8800 ± 1400
$N_e(D^0 \to \pi^-\pi^+\pi^0)$	4400 ± 1300
$N_\mu(D^0 \to K^-\pi^+\pi^-\pi^+)$	0 ± 190
$N_\mu(D^0 \to K^-\mu^+\nu_\mu)$	34800 ± 1600
$N_\mu(D^0 \to K^-\pi^+\pi^0)$	200 ± 200
$N_\mu(D^0 \to K^{*-}\mu^+\nu_\mu)$	0 ± 210
$N_\mu(D^0 \to K^{*-}(\to \pi^- K^0_S)\mu^+\nu_\mu)$	0 ± 150
$N_\mu(D^0 \to \pi^-\pi^+\pi^0)$	7700 ± 1300

Table 5.10: Yields obtained by the SAGF fitter. In the bottom part the yields of the channels with a random pion are shown.

5.7 Efficiencies calculation

This section is dedicated to the calculation of efficiencies for this analysis, which is a cornerstone to obtain the final value of $R_{e/\mu}$. For each lepton, the total efficiency is defined as the product of the acceptance efficiency, the reconstruction efficiency, the selection efficiency and the PID efficiency, as defined in Eq. (5.4). In order to have the least biased results some efficiencies are only accounted for in the $\varepsilon_{\mu/e}$ ratio,

$$\varepsilon_{\mu/e} = \frac{\varepsilon_\mu}{\varepsilon_e}. \tag{5.54}$$

In Sec. 5.7.6 the efficiency ratios are reported.

5.7.1 Acceptance, reconstruction and selection efficiencies

The acceptance efficiency is calculated using MC simulation. It is given by the number of the final particles within the LHCb fiducial region over the generated ones. Afterwards, the reconstruction efficiency is calculated by running the DaVinci reconstruction application (Sec. 4.3) over the accepted sample, and counting the total number of reconstructed events. These efficiencies are summarised in Table 5.11.

5.7.2 Hardware trigger selection efficiencies (L0)

As stated in Sec. 5.3, the hardware trigger requirement is constructed as the logical `OR` between the TOS on the kaon in the signal decay and the TIS on the prompt D^*. This choice is made so that all biases in the estimation of the L0 efficiencies should cancel in the ratio when measuring $R_{e/\mu}$.

To assess possible systematic effects in the efficiency ratio determined with simulation two approaches based on data are used to provide independent estimations. The first one takes the efficiency values directly from the MC simulation as the ratio between the passing candidates over the truth-matched ones. This is done by using the so called TISTOS method. Events are separated in TIS, TOS and TISTOS categories (see Sec. 4.2.8). The TISTOS efficiencies, $\varepsilon_{\text{TISTOS}}$, are obtained as the sum of weights for candidates passing the TIS requirement over the number of truth-matched candidates. Assuming the TIS and TOS decisions are independent, ε_{TIS} are computed from the ratio of TISTOS and TOS corrected efficiencies. Finally, the overall TIS or TOS efficiency is obtained as

$$\varepsilon_{\text{TIS}\,||\,\text{TOS}} = \varepsilon_{\text{TOS}} + \varepsilon_{\text{TIS}} - \varepsilon_{\text{TISTOS}}. \tag{5.55}$$

The efficiency uncertainties, σ_ε, are computed using the binomial distribution with the number of passed (N_{passed}) and total (N_{tot}) candidates:

$$\sigma_\varepsilon = \sqrt{\frac{\varepsilon(1-\varepsilon)}{N_{\text{tot}}}} \tag{5.56}$$

Channel	Event Number	Acceptance Efficiency (%) MD	Acceptance Efficiency (%) MU	Reconstruction Efficiency
$D^0 \to K^- e^+ \nu_e$	27583002	21.909 ± 0.099	21.992 ± 0.075	0.843 ± 0.005
$D^0 \to K^- \mu^+ \nu_\mu$	27173001	22.437 ± 0.075	22.443 ± 0.076	1.135 ± 0.006
$D^0 \to K^{*-} \mu^+ \nu_\mu$,$K^{*-} \to K^- \pi^0$ or $K^- \gamma$	27572001	19.679 ± 0.068	19.686 ± 0.066	0.558 ± 0.004
$D^0 \to K^{*-} e^+ \nu_e$,$K^{*-} \to K^- \pi^0$ or $K^- \gamma$	27582401	18.930 ± 0.066	19.130 ± 0.064	0.249 ± 0.003
$D^0 \to K^- e^+ \nu_e \pi^0$	27583400	18.872 ± 0.064	18.794 ± 0.063	0.527 ± 0.004
$D^0 \to K^- \mu^+ \nu_\mu \pi^0$	27573400	19.320 ± 0.065	19.416 ± 0.065	0.782 ± 0.005
$D^0 \to K^- K^+$	27163002	22.881 ± 0.075	22.940 ± 0.077	1.438 ± 0.006
$D^0 \to K^- \pi^+ \pi^0$	27263400	19.258 ± 0.018	19.272 ± 0.066	0.874 ± 0.002
$D^0 \to K^- \pi^+ \pi^- \pi^+$	27265000	19.845 ± 0.065	19.968 ± 0.067	0.444 ± 0.003
$D^0 \to \pi^- \pi^+ \pi^0$	27163403	18.382 ± 0.0177	18.419 ± 0.018	0.505 ± 0.004
$D^0 \to \pi^- \mu^+ \nu_\mu$	27573001	21.296 ± 0.068	21.242 ± 0.072	1.219 ± 0.006
$D^0 \to \pi^- e^+ \nu_e$	27583000	20.752 ± 0.071	20.833 ± 0.070	0.917 ± 0.005
$D^0 \to K^- \pi^+$	27163003	21.644 ± 0.047	21.631 ± 0.048	0.986 ± 0.006

Table 5.11: Acceptance and reconstruction efficiencies $D^0 \to K^- \ell^+ \nu_\ell$ samples.

In the second method the calibration tables of Ref. [154] are used to correct the simulation event by event. Finally, the efficiencies are obtained as the sum of weights over the number of truth-matched candidates in all the trigger categories and their uncertainty is taken from the TISTOS method.

In Figure 5.18 the values obtained with the two methods are represented as a function of ${q^2}_{\text{true}}$ and for the integrated q^2. The two approaches lead to consistent results. The uncertainties using the data-weighted simulation are larger, since they depend on the TISTOS method.

5.7.3 Software trigger selection efficiencies (HLT1 and HLT2)

The software level trigger efficiencies are calculated using the TISTOS method on the truth-matched simulation sample. As the trigger candidates are associated offline, the HLT1 efficiencies and the HLT2 efficiencies, given HLT1, are computed as (5.57). The HLT2 efficiencies are computed given HLT1 requirements, accounting for the increase in precision.

$$\varepsilon_{\text{TISTOS}}(\text{HLT1}) = \frac{N_{truth}[K_{\text{track}}(\text{TIS AND TOS})]}{N_{truth}[K_{\text{track}}(\text{TIS})]} \tag{5.57}$$

$$\varepsilon_{\text{TISTOS}}(\text{HLT2} \mid \text{HLT1}) = \frac{N_{truth}[K_{\text{TOS}}(\text{HLT1}) \text{ AND } {D^{*+}}_{\text{TIS AND TOS}}(\text{HLT2})]}{N_{truth}[K_{\text{TOS}}(\text{HLT1}) \text{ AND } {D^{*+}}_{\text{TIS}}(\text{HLT2})]} \tag{5.58}$$

Table 5.12 reports the HLT efficiency for modes reconstructed as $D^0 \to K^- \mu^+ \nu_\mu$, while Table 5.13 for $D^0 \to K^- e^+ \nu_e$.

Decay mode	$\varepsilon_{\text{TISTOS}}$(HLT1) (%)	$\varepsilon_{\text{TISTOS}}$(HLT2) (%)
$\boldsymbol{D^0 \to K^-\mu^+\nu_\mu}$	71.56 ± 0.02	33.57 ± 0.15
$D^0 \to K^-\mu^+\nu_\mu\pi^0$	61.89 ± 0.03	36.05 ± 0.32
$D^0 \to K^{*-}\mu^+\nu_\mu$	61.50 ± 0.03	37.28 ± 0.29
$D^0 \to K^{*-}(\to \pi^-K^0)\mu^-\nu_\mu$	47.10 ± 0.03	28.74 ± 0.31
$D^0 \to \pi^-\mu^+\nu_\mu$	69.15 ± 0.03	27.50 ± 0.28
$D^0 \to K^-\pi^+\pi^-\pi^+$	57.57 ± 0.05	27.23 ± 0.37
$D^0 \to K^-K^+$	75.86 ± 0.04	36.07 ± 0.55
$D^0 \to K^-\pi^+\pi^0$	73.33 ± 0.77	27.6 ± 2.5
$D^0 \to \pi^-\pi^+\pi^0$	65.10 ± 0.05	27.26 ± 0.44
$D^0 \to K^-\pi^+$	76.83 ± 0.06	21.72 ± 0.59

Table 5.12: HLT1 and HLT2 efficiencies of the sample for the reconstructed $D^0 \to K^-\mu^+\nu_\mu$ mode.

Decay mode	$\varepsilon_{\text{TISTOS}}$(HLT1) (%)	$\varepsilon_{\text{TISTOS}}$(HLT2) (%)
$\boldsymbol{D^0 \to K^-e^+\nu_e}$	75.70 ± 0.02	31.41 ± 0.14
$D^0 \to K^-e^+\nu_e\pi^0$	67.71 ± 0.03	32.59 ± 0.27
$D^0 \to K^{*-}e^+\nu_e$	67.72 ± 0.04	33.72 ± 0.29
$D^0 \to K^{*-}(\to \pi^-K^0)e^-\nu_e$	52.97 ± 0.04	23.61 ± 0.27
$D^0 \to \pi^-e^+\nu_e$	72.90 ± 0.03	25.71 ± 0.25
$D^0 \to K^-\pi^+\pi^-\pi^+$	57.65 ± 0.05	26.97 ± 0.36
$D^0 \to K^-K^+$	75.89 ± 0.04	36.07 ± 0.56
$D^0 \to K^-\pi^+\pi^0$	73.61 ± 0.77	27.01 ± 0.52
$D^0 \to \pi^-\pi^+\pi^0$	65.10 ± 0.05	27.25 ± 0.44
$D^0 \to K^-\pi^+$	76.83 ± 0.05	21.88 ± 0.60

Table 5.13: HLT1 and HLT2 efficiencies of the sample for the reconstructed $D^0 \to K^-e^+\nu_e$ mode.

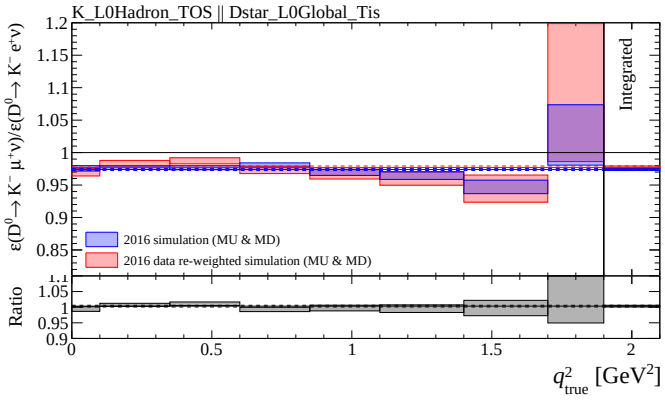

Figure 5.18: Comparison between the $D^0 \to K^-\mu^+\nu$ over $D^0 \to K^-e^+\nu$ efficiencies for L0 TOS directly from MC (blue) and after data-driven correction (red), as a function of $q^2_{\rm true}$.

5.7.4 Tracking efficiencies

The tracking efficiencies are applied as per event weights to each template. These values are obtained by using the standard LHCb methods which also provide the efficiencies. For muon and hadron tracking efficiencies, the LHCb standard tracking tables of Ref. [155] are used. For electrons tracks, the track reconstruction follows the method described in Sec. 4.3.1.1, which also provides the efficiencies see Figs 4.17 and 4.18.

5.7.5 PID efficiencies

The kaon and muon and pion PID efficiencies are obtained directly from the PIDCalib [153] calibration samples. The efficiencies are then applied event by event, and the associated error is then propagated.

The π^+ coming from the D^{*+} decays has as signature low momentum. The standard PIDCalib samples used for pions are simulated with high momentum. Hence, a to extract the efficiency a dedicated study is performed. This is not in the scope of this thesis, we refer to App. A.3 for further information. Electron efficiencies are calculated using the custom method described in Sec. 4.3.2.1.

The PID cuts on electrons that optimise the signal over background ratio are collected in Tab. 5.6. The electron must have PID(e) > 7 and PID($K - e$) < -10, so that the probability of the candidate being a K is way lower than the electron one (ΔLL($K - e$) < -10 by definition of PID). In Fig. 5.19 the η-$p_{\rm T}$ distribution of the probe tracks is represented. The binning chosen for the efficiency calculation is represented in blue. In Appendix A.3, the results for a given probe charge, added brem flag, magnet polarity and

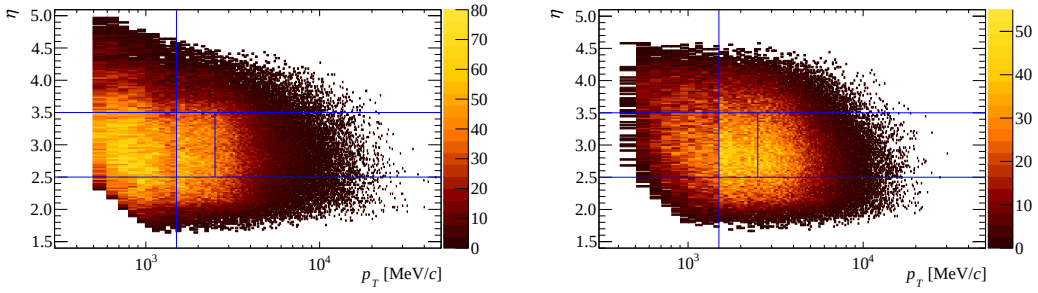

(a) (b)

Figure 5.19: Distribution of probe tracks in the $p_T - \eta$ plane, without (top) and with (bottom) added bremsstrahlung. The blue lines define the binning chosen to calculate binned PID efficiencies [123].

Probe	e with Brem	Efficiencies (%)			
		MU 2015	MD 2015	MU 2016	MD 2016
e^-	0	49.93 ± 0.77	48.29 ± 0.88	51.51 ± 0.30	50.67 ± 0.29
	1	81.63 ± 0.61	79.70 ± 0.74	82.87 ± 0.23	83.87 ± 0.22
e^+	0	50.07 ± 0.77	49.93 ± 0.90	51.37 ± 0.30	51.42 ± 0.29
	1	80.76 ± 0.61	81.09 ± 0.73	84.71 ± 0.23	82.16 ± 0.23

Table 5.14: Integrated efficiencies of e^- and e^+ separated by Bremsstrahlung categories (e with Brem) and data samples.

year are reported in Tables A.2 and A.3. These are extracted as

$$\varepsilon_{\text{PID}e} = \sum_{i \in B} \frac{N_i^{MC}}{N^{MC}} \varepsilon_i \tag{5.59}$$

where B is the set of bins used for the calculation. The efficiencies are weighted by the percentage of from fully simulated $D \to Ke\nu_e$ decays in the i-th bin. Finally, in Table 5.14 the efficiencies for $D^0 \to K^-e^+\nu_e$, integrated in p_{T} and η, are reported with their statistical error in the two bremsstrahlung categories.

5.7.5.1 Efficiencies on simulation samples

As previously introduced all the PID efficiencies are introduced as per-event weights. The PIDCalib procedure is replicated with two binnings for hadrons and muons, nevertheless for the moment only the nominal one is used. The lookout tables for the different decay channels are reported in Tables A.4 and A.5 for the electron and muon mode respectively.

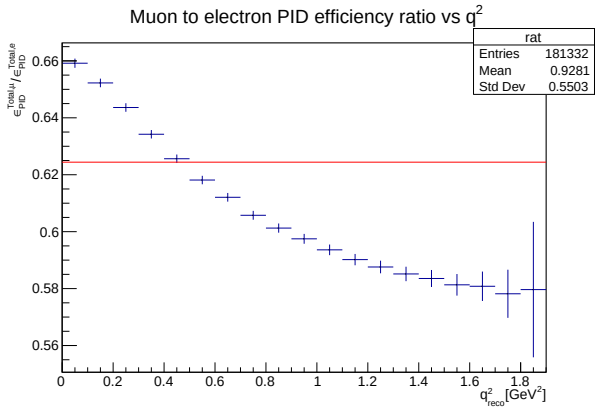

Figure 5.20: Efficiency PID ratio $\varepsilon_{\mathrm{PID}\mu/e}$ as a function of $q^2{}_{\mathrm{reco}}$ obtained with the cone closure method. The red line represent the integrated q^2 value.

The final column of these tables is not the simple multiplication of the individal preceeding columns, but rather the average of the per-event efficiency which is multiplied together. The preceeding columns are only included to help provide an understanding of the individual breakdowns of the efficiency.

It is important to note that the PID efficiencies are in agreement at the level of 0.05%, which will be varied to be accounted as a systematic uncertainty. Besides, the cross feed channels between muon and electron modes are reduced to negligible levels, ensuring that the statistical separation between muon and electron are achieved at the same level of precision as the systematic uncertainty will be propagated.

The ratio of efficiency is used in (5.4), foreseeing the analysis in bins of q^2, the total PID efficiency for both signal modes and the ratio as a function of q^2 is calculated. Figure 5.20 represents $\varepsilon_{\mathrm{PID}\mu/e} = \varepsilon(D^0 \to K^-\mu^+\nu_\mu)/\varepsilon(D^0 \to K^-e^+\nu_e)$. There is a significant q^2 dependence of the ratio.

5.7.6 Summary of Efficiencies

In Table 5.15 a summary of all efficiencies and their ratio is reported.

Each item, apart from the first one, reports the efficiency of a given source given the previous one. The total efficiency is the product of all the single efficiencies and the errors are added in quadrature.

Furthermore, the summary of the fitter-specific efficiencies is reported in the last rows of Tab. 5.15. These efficiencies depend on the histogram boundaries, the pseudorapidity cuts and, only for SAGF, the requirement of convergence of the Global Fit algorithm. Also in this case each item in the table, apart from the first one, reports the efficiency of a given source given the previous one.

Source	ε_e (%)	ε_μ (%)	$\varepsilon_e/\varepsilon_\mu$
Acceptance	21.95 ± 0.12	22.44 ± 0.11	1.0223 ± 0.0076
Reconstruction	0.843 ± 0.005	1.350 ± 0.006	1.601 ± 0.12
L0	-	-	0.9770 ± 0.020
HLT1	75.698 ± 0.015	71.560 ± 0.015	0.94534 ± 0.00027
HLT2	31.41 ± 0.14	33.57 ± 0.15	1.0686 ± 0.0068
K PID	78.27800 ± 0.00005	77.74700 ± 0.00005	0.9932165 ± 0.0000009
π PID	99.00 ± 0.38	99.02 ± 0.34	1.0001 ± 0.0052
ℓ PID	76.2206 ± 0.0001	47.40 ± 0.16	0.6218 ± 0.0022
Tracking	-	-	-
YATF cuts	98.273 ± 0.005	99.159 ± 0.004	1.00902 ± 0.00007
SAGF cuts	82.052 ± 0.015	84.014 ± 0.004	1.0239 ± 0.00019
Total	0.02599 ± 0.00026	0.02594 ± 0.00025	0.998 ± 0.014

Table 5.15: Summary of signal efficiencies for both the muon and electron channel and their electron-to-muon ratio.

5.8 Systematic uncertainties evaluation

Studying the branching fraction ratio $R_{e/\mu}$ allows to have many systematic uncertainties cancelles, such as the ones due to the tracking efficiencies of the hadrons. Nevertheless, there are several residual sources of systematic uncertainties. Some of these can be propagated directly from the efficiency calculations, such as the trigger selection ones, while for others the following study is implemented.

The simulation is corrected by considering the form factor parametrisation, tracking and PID efficiencies and the bremsstrahlung of the electrons. Besides, the simulation sample has a finite size. The uncertainties due to these are accounted for by performing a pseudoexperiment procedure.

In this study, 100 sets of templates are generated. For each event, the single-event weight is randomly obtained by sampling from a Gaussian distribution. This is centred in the actual value of the event weight and with a standard deviation equal to the value of its error. This ensures the correct propagation and combination of the individual weights errors with the statistical errors of the sample.

Therefore, individual weights include form factors weights, PID and tracking efficiencies for all charged final-state particles and bremsstrahlung correction for electrons. The spread of the distribution of the values of $R_{e/\mu}$ obtained by repeating the fit with these 100 sets of templates is a good estimate of the combined systematic due to the errors of all the weights applied to the events and the statistical errors of the templates.

Since this study has to be finalised, only an estimation is reported. The main contribution to the systematic uncertainties is expected to be due to PID efficiencies, estimated

to a value of about 1.1%.

Table 5.16 summarise all the contribution to the systematic uncertainties. First, the reconstruction efficiency (Tab. 5.11) is limited by the size of the simulation sample and the related systematic uncertainties corresponds to $\sigma_{\text{reco}} = 0.6\%$. The second contribution is due to the trigger selection. L0 efficiencies are directly propagated to the final result, which is about 0.2%, without considering the data-driven method and the statistical uncertainty of the calibration sample (see Sec. 5.7.2). For the HLT1 and HLT2 selection, an uncertainties of 0.6% is estimated.

Systematic source	σ_{syst} (%)
Recontruction	0.6
L0	0.2
HLT1&2	0.6
PID	~ 1.1
re-weighting	–

Table 5.16: Systematic uncertainties summary.

5.9 Blinded result and conclusions

Since the analysis is still blinded, the final result of $R_{e/\mu}$ is still unknown. However, it is possible to evaluate the uncertainties to compare the achieved precision with the other previous results of $R_{e/\mu}$. The final $R_{e/\mu}$ value obtained by this analysis is

$$R_{e/\mu} = x.xxx \pm 0.003 \text{ (stat.)} \pm 0.014 \text{ (syst.)}, \tag{5.60}$$

where the first uncertainty is statistical, while the second is the estimation of the systematic uncertainty obtained in Sec. 5.8.

To compare this result with $R_{\mu/e}$ from previous measurements, $R^{-1}_{e/\mu}$ is investigated. The central value is taken from the SM prediction [27] while the uncertainties are propagated from our measurement accordingly, obtaining

$$R_{\mu/e} = R^{-1}_{e/\mu} = x.xxx \pm 0.003 \text{ (stat.)} \pm 0.013 \text{ (syst.)}. \tag{5.61}$$

Fig. 5.21 represents the comparison of this measurement, centred in the SM prediction, the previous measurement by BESIII and the branching fraction ratios. This figure is an update of Fig. 3.2.

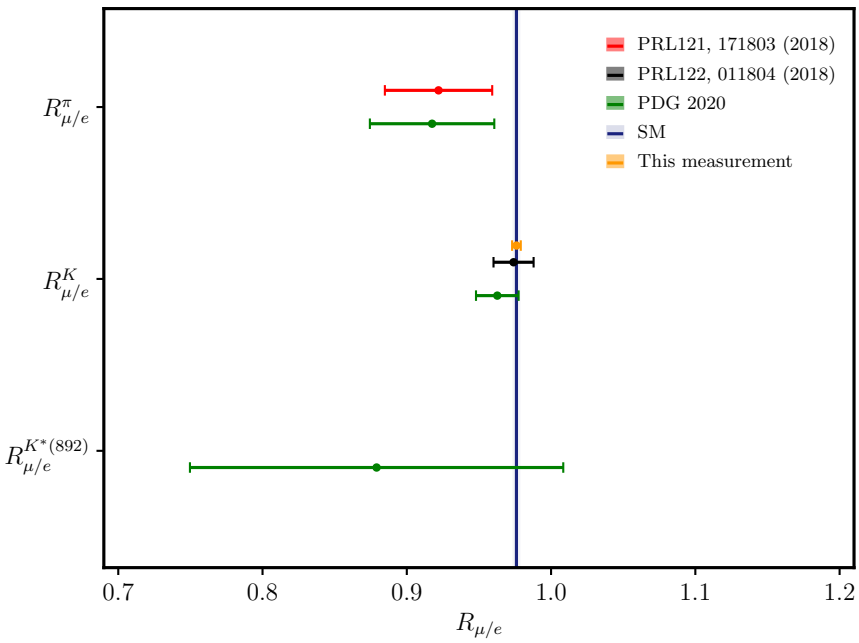

Figure 5.21: Comparison between $R_{\mu/e}$ measurements and $R^K_{\mu/e}$ SM predictions. This is to be compared with Fig. 3.2. The $R_{\mu/e}$ result of this thesis is centred in the SM prediction.

6

Test of Lepton Flavour Universality using $B^+ \to \overline{D}^{(*)0}\tau^+\nu_\tau$ decays

6.1 Introduction and strategy

This analysis aims to test LFU by measuring the branching fraction ratios $R(D^0)$ and $R(D^{*0})$, defined as

$$R(D^0) = \frac{\mathcal{B}(B^+ \to \overline{D}^0\tau^+\nu_\tau)}{\mathcal{B}(B^+ \to \overline{D}^0\ell^+\nu_\ell)}, \tag{6.1}$$

$$R(D^{*0}) = \frac{\mathcal{B}(B^+ \to \overline{D}^{*0}\tau^+\nu_\tau)}{\mathcal{B}(B^+ \to \overline{D}^{*0}\ell^+\nu_\ell)}, \tag{6.2}$$

where $\ell = \mu, e$. The topology of the signal decays is shown in Fig. 6.1. Some relevant features of the analysis strategy are:

- The τ lepton is reconstructed using the 3-prong $\tau^+ \to \pi^+\pi^-\pi^+\overline{\nu}_\tau$ and $\tau^+ \to \pi^+\pi^-\pi^+\pi^0\overline{\nu}_\tau$ decay modes.
- The $\overline{D}^0$ is reconstructed with the $\overline{D}^0 \to K^+\pi^-$ decay.
- The $\overline{D}^{*0}$ meson decays into a $\overline{D}^0$ and a neutral particle: $\overline{D}^0\pi^0$, with a branching fraction of $(64.7 \pm 0.9)\%$ [1] or $\overline{D}^{*0} \to \overline{D}^0\gamma$, with $\mathcal{B}$ of $(35.3 \pm 0.9)\%$ [1] where the additional neutral particle is not reconstructed.

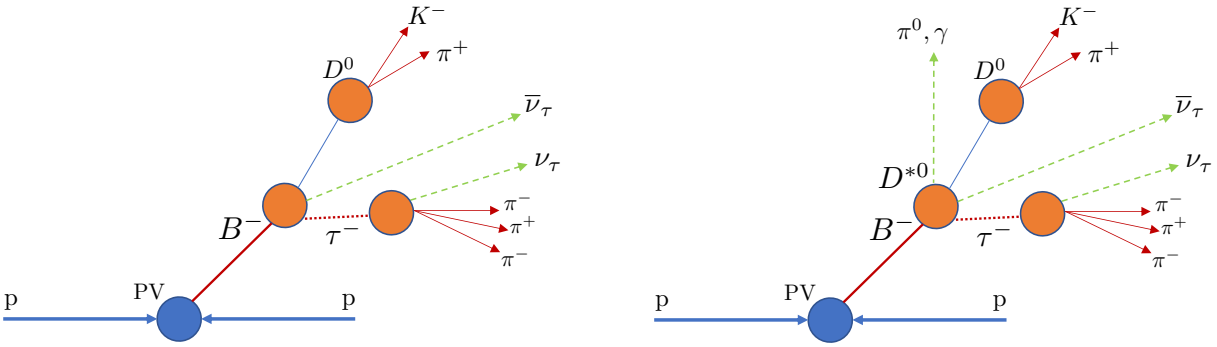

Figure 6.1: Topology of signal decays corresponding to the $B^+ \to \overline{D}^0 \tau^+ \nu_\tau$ decay chain (left) and $B^+ \to \overline{D}^{*0} \tau^+ \nu_\tau$ (right). In both configurations there are two neutrinos in the final state, one from the B vertex and one from the $\tau^+ \to \pi^+\pi^-\pi^+\overline{\nu}_\tau$ decay.

Similarly to the $R_{e/\mu}$ analysis of Ch. 5, there are neutrinos in the final state, which means that the only final state visible particles are four charged pions and a kaon. The use of ratio observables permits to investigate independently the numerator and the denominator. In this thesis, the denominators of Eqs. (6.1) and (6.2), $\mathcal{B}(B^+ \to \overline{D}^{(*)0} \ell^+ \nu_\ell)$, are taken from the HFLAV average [60] of the external measurements. This is reported in Tab. 6.1 together with branching fractions measurements performed by the CLEO, BaBar and Belle collaborations. For the $B^+ \to \overline{D}^{(*)0} \tau^+ \nu_\tau$ decay, a normalisation mode with the same final state as the signal decay is chosen. In this way, systematic uncertainties due to reconstruction, are partially cancelled in the ratio. In the previous hadronic $R(D^{*-})$ measurement [53, 54], the $B^0 \to D^{*-} 3\pi$ decay was used as normalisation channel. For this study the $B^+ \to \overline{D}^0 3\pi$, namely $B^+ \to \overline{D}^0 \pi^+\pi^-\pi^+$, decay was considered as a first choice. However, its branching fraction is measured with an uncertainty of almost 40% [1]. Therefore, the $B^+ \to \overline{D}^0 D_s^+$ decay, where $D_s^+ \to 3\pi$, is chosen instead. The measured branching ratio of the $B^+ \to \overline{D}^0 D_s^+$ mode is $(9.9 \pm 0.1) \times 10^{-3}$ [1] and that of the $D_s^+ \to 3\pi$ decay equals to $(1.08 \pm 0.04)\%$ [1].

Considering the normalisation channels, Eqs. (6.1) and (6.2) can be rewritten as

$$R(D^{(*)0}) = \mathcal{K}(D^{(*)0}) \left(\frac{\mathcal{B}(B^+ \to \overline{D}^0 D_s^+) \mathcal{B}(D_s^+ \to 3\pi)}{\mathcal{B}(B^+ \to \overline{D}^{(*)0} \ell^+ \nu_\ell)} \right)_{\text{ext.}} , \tag{6.3}$$

where, as discussed above, the branching fractions of the second factor are taken from external inputs [1, 60]. The ratio $\mathcal{K}(D^{(*)0})$ is defined as

$$\mathcal{K}(D^{(*)0}) = \frac{\mathcal{B}(B^+ \to \overline{D}^{*0} \tau^+ \nu_\tau)}{\mathcal{B}(B^+ \to \overline{D}^0 D_s^+) \mathcal{B}(D_s^+ \to \pi^+\pi^-\pi^+)} . \tag{6.4}$$

Thus, the goal of the analysis is to obtain $\mathcal{K}(D^{(*)0})$ as a function of the signal and nor-

Decay channel	$\mathcal{B}$ (%)	Experiment
$B^+ \to \overline{D}^0\ell^+\nu_\ell$	$2.13 \pm 0.13 \pm 0.17$	CLEO [156]
	$2.16 \pm 0.08 \pm 0.12$	BaBar [157]
	$2.46 \pm 0.04 \pm 0.12$	Belle [158]
	$2.30 \pm 0.03 \pm 0.08$	HFLAV average [60]
$B^+ \to \overline{D}^{*0}\ell^+\nu_\ell$	$6.20 \pm 0.20 \pm 0.26$	CLEO [159]
	$5.30 \pm 0.15 \pm 0.33$	BaBar tagged [160]
	$5.00 \pm 0.08 \pm 0.31$	BaBar untagged [161]
	$5.58 \pm 0.07 \pm 0.21$	HFLAV average [60]

Table 6.1: Branching fraction measurements for semileptonic $B \to \overline{D}^0\ell^+\nu_\ell$ and $B \to \overline{D}^{*0}\ell^+\nu_\ell$ decays. In all the measurements, the first contribution to the uncertainty is statistical, while the second one stands for the systematic effects.

malisation yields. By taking into account the signal and normalisation efficiencies,

$$\mathcal{K}(D^{(*)0}) = \frac{N(B^+ \to \overline{D}^{(*)0}\tau^+\nu_\tau)}{N(B^+ \to \overline{D}^0 D_s^+)} \cdot \frac{\varepsilon_{\text{norm}}}{\varepsilon_{\text{sig}}} \,. \tag{6.5}$$

The efficiency ratio $\varepsilon_{\text{norm}}/\varepsilon_{\text{sig}}$ is defined as

$$\frac{\varepsilon_{\text{norm}}}{\varepsilon_{\text{sig}}} = \frac{\varepsilon_{B^+\to\overline{D}^0 D_s^+}}{\varepsilon^{\tau^+\to 3\pi\overline{\nu}_\tau}_{B^+\to\overline{D}^{(*)0}\tau^+\nu_\tau}\mathcal{B}(\tau^+ \to 3\pi\overline{\nu}_\tau) + \varepsilon^{\tau^+\to 3\pi\pi^0\overline{\nu}_\tau}_{B^+\to\overline{D}^{(*)0}\tau^+\nu_\tau}\mathcal{B}(\tau^+ \to 3\pi\pi^0\overline{\nu}_\tau)} \,, \tag{6.6}$$

where $\varepsilon_{B^+\to\overline{D}^0 D_s^+}$ is the normalisation efficiency, $\varepsilon^{\tau^+\to 3\pi(\pi^0)\nu_\tau}_{B^+\to\overline{D}^{(*)0}\tau^+\nu_\tau}$ are the signal efficiencies relative to the τ decay modes, whose decays branching fractions, respectively, are $\mathcal{B}(\tau^+ \to \pi^+\pi^-\pi^+\overline{\nu}_\tau) = (9.02 \pm 0.05)\%$ and $\mathcal{B}(\tau^+ \to \pi^+\pi^-\pi^+\pi^0\overline{\nu}_\tau) = (4.49 \pm 0.05)\%$ [1].

The signal and normalisation yields in Eq. (6.5) are obtained with two different fit strategies. To measure $N(B^+ \to \overline{D}^{(*)0}\tau^+\nu_\tau)$, a three-dimensional template fit to the transferred momentum of the $\tau\nu$ system, q^2, the tau decay time, t_τ, and the output of a Boosted Decision Tree, BDT, is performed. On the other hand, a one-dimensional template fit to the invariant mass $m(D^0 D_s^+)$ is used to get the normalisation yield, $N(B^+ \to \overline{D}^0 D_s^+)$.

It is of paramount importance to model precisely all the background contributions. The largest ones are due to decays with the same charged final state of 4π and a K^+. Firstly, the main background component is due to *prompt* $B \to \overline{D}^0\pi^+\pi^-\pi^+(X)$ decays, where the three π are produced in the B decay vertex and X represents other possible additional particles in the final state. These are largely reduced after applying the selection requirements. At this point, the doubly charmed $B \to \overline{D}^0 D(X)$ decays, where

the D stands for a D_s^+, a D^0 or a D^+ meson decaying in the 3π vertex[1], represent the main physical background. Subsequently, the other main source of background is due to inclusive $D_s^+ \to \pi^+\pi^-\pi^+(X)$ decays with the D_s^+ decaying in the 3π vertex. Since these background channels are not fully suppressed by the selection requirements, control sample models have been developed to understand them. As schematised in Fig. 6.2, these control samples are used to correct the simulation in the preparation of the template for both the signal and the normalisation mode fits. The main contribution of this thesis to the $R(D^{(*)0})$ analysis is the model to control the inclusive $D_s^+ \to \pi^+\pi^-\pi^+(X)$ decays, which is described in Sec. 6.7.

6.1.1 Analysis workflow

This chapter is structured following the logic of the analysis workflow, displayed in Fig. 6.2. First of all, the data and simulation samples used in the analysis are presented in Sec. 6.2. The selection process and the specific algorithms deployed are described in Sec. 6.3. Then, the reconstruction method used for signal decays is described in Sec. 6.4. In Sec. 6.5 the different corrections applied to the simulation in order to describe the data as accurately as possible are described.

As already mentioned, after the selection, there are some residual contributions from background, so the simulation has to be optimised in order to model the data. The strategies used for the background contributions are reported in Secs. 6.6 and 6.7. Sec. 6.6, including the control samples to model the doubly charmed $B \to \overline{D}^0 D(X)$ decays and the procedure to account for excited $B \to D^{**}\tau^+\nu_\tau$ decays. In Sec. 6.7, the $D_s^+ \to \pi^+\pi^-\pi^+(X)$ decay model is described in detail.

Once the simulation is corrected for the background contributions, the efficiencies are computed in Sec. 6.8. The final fits to obtain the signal and the normalisation yields are reported in Sec. 6.9. At the time of the writing of this thesis the systematic uncertainties evaluation is not finalised. A description of some of the methods that are proposed is included in Sec. 6.10. Finally, the blinded results are reported in Sec. 6.11.

[1] Throughout this chapter, the τ daughters are conventionally called in this order: $\tau^+ \to \pi^+{}_0\pi^-{}_1\pi^+{}_2\overline{\nu}_\tau$ and the τ vertex is referred as both τ and 3π.

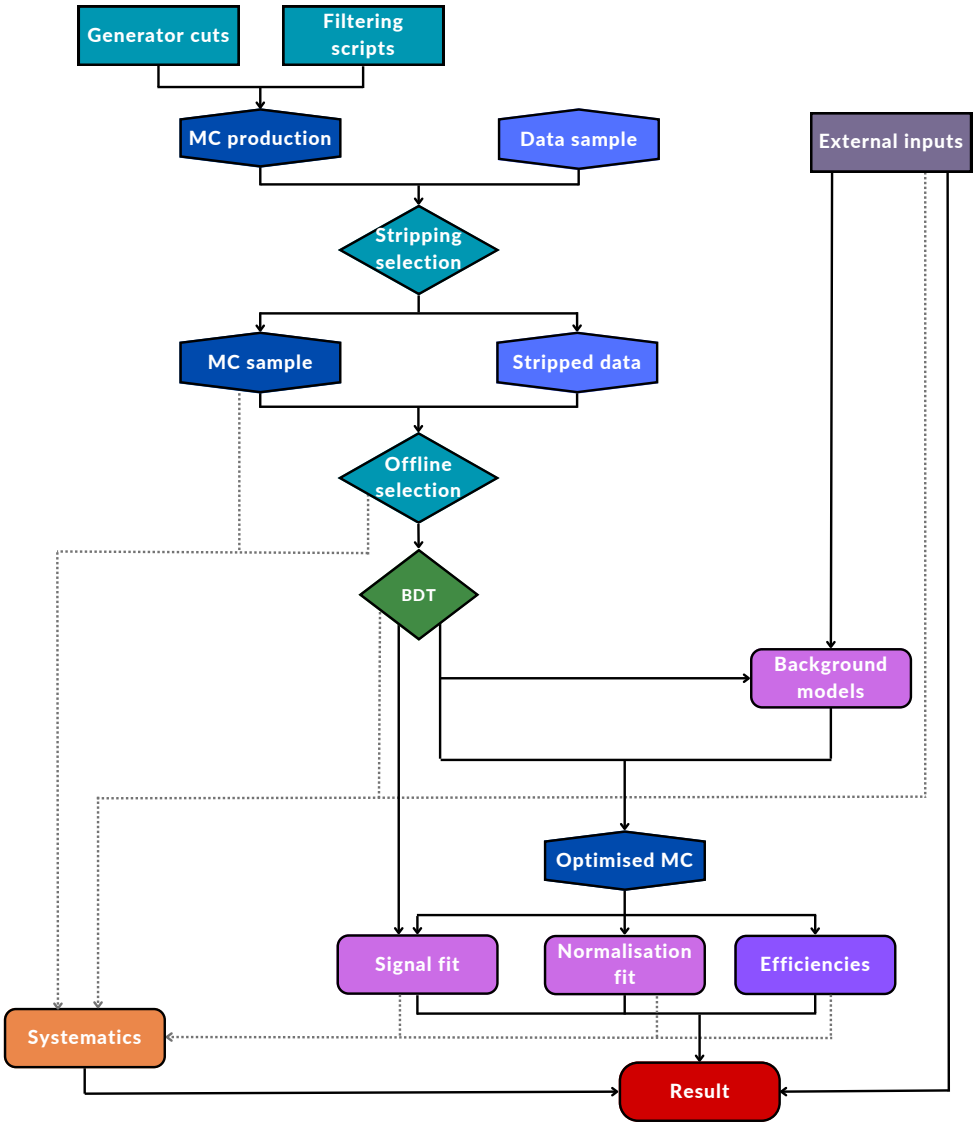

Figure 6.2: Workflow of the analysis.

6.2 Data and simulation samples

This measurement is performed using Run 2 ($\sqrt{s}$ =14 TeV) data taken by LHCb in 2016, 2017 and 2018, corresponding to an integrated luminosity of 5.4 fb^{-1}, while the simulation sample is produced using 2016 conditions.

Several samples containing the relevant decay modes have been produced for this analysis with different simulation options, differentiated by an alphanumeric string, *e.g.* Sim09h. Table 6.2 summarises the simulation conditions and the number of events produced. For instance, in order to model inclusive $D_s^+ \to \pi^+\pi^-\pi^+(X)$ decays, specific samples are produced. These include $B \to \overline{D}^0 H_c X'$ decays, where B is either B^+, B^0 or B_s^0, H_c a charm meson and X' any other posssible additional particle. These are produced using fast simulation, namely ReDecay [143] (see 4.3.3). Additionally, data samples with the nonphysical $B \to D^0\tau^+\nu_\tau$ decay, where instead of a $\overline{D}^0$ meson there is a D^0 one, are employed. These wrong-sign (WS) samples are used in the control sample studies to account for possible combinatorial contributions.

Event Number	**Decay Channel**	**Simulation option**	**Events on Disk** (MU/MD)
12562001	$B^+ \to \overline{D}^0\tau^+(\to \pi^+\pi^-\pi^+\overline{\nu}_\tau)\nu_\tau$	Sim09i filtered	1001755 / 10121572
12562011	$B^+ \to \overline{D}^0\tau^+(\to \pi^+\pi^-\pi^+\pi^0\overline{\nu}_\tau)\nu_\tau$	Sim09i filtered	754189 / 773537
12562411	$B^+ \to \overline{D}^{*0}\tau^+(\to \pi^+\pi^-\pi^+\overline{\nu}_\tau)\nu_\tau$	Sim09i filtered	1001245 / 1007497
12562421	$B^+ \to \overline{D}^{*0}\tau^+(\to \pi^+\pi^-\pi^+\pi^0\overline{\nu}_\tau)\nu_\tau$	Sim09i filtered	756863 / 759234
11160001	$B^0 \to D^{*-}\tau^+(\to \pi^+\pi^-\pi^+\nu_\tau)\overline{\nu}_\tau$	Sim09e ReDecay filtered	687279 / 687279
11563020	$B^0 \to D^{*-}\tau^+(\to \pi^+\pi^-\pi^+\pi^0\nu_\tau)\overline{\nu}_\tau$	Sim09c Redecay	20039288 /20039288
12863030	$B^+ \to D^{**}\tau\nu_\tau$	Sim09k Redecay filtered	286712 / 288831
11563400	$B^0 \to D^{**}\tau\nu_\tau$	Sim09k ReDecay filtered	255781 / 250003
13863000	$B_s^0 \to D^{**}\tau\nu_\tau$	Sim09k ReDecay filtered	288831 / 286712
12195049	$B^+ \to \overline{D}^0 D_s^+(\to \pi^+\pi^-\pi^+)$	Sim09i filtered	520804 / 520972
12265008	$B^+ \to \overline{D}^0\pi^+\pi^-\pi^+$	Sim09i filtered	284698 / 262503
12495410	$B^+ \to \overline{D}^0 H_c X'$	Sim09h ReDecay filtered	1288010 / 1853494
11496400	$B^0 \to \overline{D}^0 H_c X'$	Sim09h ReDecay filtered	10754686 / 11004407
13496400	$B_s^0 \to \overline{D}^0 H_c X'$	Sim09h ReDecay filtered	2429723 / 3501039
12465400	*prompt* $B^+ \to \overline{D}^0\pi^+\pi^-\pi^+ X$	Sim09i ReDecay filtered	14240203 / 14230745
11466400	*prompt* $B^0 \to \overline{D}^0\pi^+\pi^-\pi^+ X$	Sim09i ReDecay filtered	17818266 / 17890479
13466400	*prompt* $B_s^0 \to \overline{D}^0\pi^+\pi^-\pi^+ X$	Sim09i ReDecay filtered	1813758 / 1823421
22102000	$\overline{D}^0$ and 3π not from same B	Sim09i ReDecay filtered	12592113 / 12503618

Table 6.2: Simulation samples used in the analysis. The H_c symbol stands for a D_s^+, a D^+ or a D^0 meson and the D^{**} symbol for any of the following excited mesons: $D_2^*(2460)$, $D_1(2420)$, $D_1'(2430)$, $D_0^*(2300)$, $D_{s1}(2536)^+$ or $D_{s2}^*(2573)^+$. Decays listed as *prompt* are the ones where three pions are produced in the B vertex.

6.3 Selection

The analysis event selection is divided in several steps. The first set of requirements is applied by the the trigger and the stripping selections (see Sec. 4.3). Afterwards, in order to optimise the background suppression, some cleaning cuts, named *preselection*, are applied. These cuts are described in Sec. 6.3.1.

The reconstructed final state consists in three charged pions and the $\overline{D}^0$ daughters. Hence, inclusive B decays with a similar final state have a significant impact in the selection process. In order to suppress $B \to \overline{D}^0\pi^+\pi^-\pi^+(X)$ decays, a requirement is applied to the detachment between the B and τ vertices, reported in Sec. 6.3.2. In addition to this, specific algorithms modelling all possible particles coming from the same vertex have been deployed and are described in Sec. 6.3.3 and in Sec. 6.3.4, the BDT is described. Finally, a summary of all the selection cuts applied to the signal and normalisation channels is given in Sec. 6.3.5

6.3.1 Stripping, trigger and preselection requirements

The trigger selection requires specific lines to be fired at the three levels: L0, HLT1 and HLT2. The trigger requirements are summarised as follows:

- L0: the B is selected by a Trigger Independent of Signal (TIS) `OR` Trigger On Signal (TOS) logic (see Sec. 4.2.8) (`B_L0HadronDecision_TOS || B_L0Global_TIS`)
- HLT1: at least one track from the B triggered on signal, TOS (`B_Hlt1TrackMVA-Decision_TOS`)
- HLT2: the trigger fires if the event has two `OR` three `OR` four charged tracks by using topological trigger lines [162]: (`B_Hlt2Topo2BodyDecision_TOS || B_Hlt2-Topo3BodyDecision_TOS || B_Hlt2Topo4BodyDecision_TOS`).

Once passed the trigger, inclusive $B \to \overline{D}^0\pi^+\pi^-\pi^+(X)$ events, with $\overline{D}^0 \to K^+\pi^-$, are selected using the `Bu2D0TauNuForB2XTauNuAllLines` stripping line, whose requirements, summarised in Table 6.3, select three charged pions forming the τ candidate vertex and a good B vertex formed by the τ and the $\overline{D}^0$ candidates. In addition, for both B and D meson candidates, a requirement on the cosine of the angle formed between the particle momentum and the direction given by the position of the particle decay vertex and the PV (DIRA) is applied.

The *preselection* cuts are collected in Table 6.4. First, the B vertex is required to be be well separated from the PV. The three π must form a good vertex. Also, a requirement is applied to their impact parameter χ^2, ($\chi^2_{\rm IP}$). The $\overline{D}^0$ and τ candidates must point close to the same PV. Besides, the number of hits in the SPD detector must be below 450. Finally, loose requirements on the candidate momentum, pseudo-rapidity and PID are applied.

Cut	Value
B^+	
$m(D^0 3\pi)$	2.7-5.6 GeV/c^2
DOCA	< 0.15 mm
DIRA	> 0.995
D^0	
$\lvert m(K\pi) - m(D^0)_{\rm PDG}\rvert$	< 40 MeV/c^2
Vertex χ^2/DOF	< 10
DIRA	> 0.995
PV distance χ^2	> 36
p_T	> 1.2 GeV/c
$\chi^2_{\rm IP}$(PV)	> 10
DOCA$_{K\pi}$	< 0.5 mm
DOCA$_{K\pi}$ χ^2	< 15
τ	
DIRA	> 0.99
$m(3\pi)$	0.4-3.5 GeV/c^2
DOCA	< 0.15 mm
min$[m(\pi^+\pi^-)]$	< 1.67 GeV/c^2
Vertex χ^2	< 25
At least two pions with p_T	> 0.3 GeV/c^2
At least two pions with $\chi^2_{\rm IP}$(PV)	> 5
D^0 daughters	
Track p	> 2 GeV/c
Track ghost Probability	< 0.4
Track χ^2	$> 10^{-8}$
$\chi^2_{\rm IP}$(PV)	> 10
$p_T(K)$	> 1.5 GeV/c
$p_T(\pi)$	> 0.25 GeV/c
K track χ^2/DOF	< 30
π track χ^2/DOF	< 3
K: PID(K)	> 3
π: PID(K)	< 50
τ daughter pions	
p_T	> 0.25 GeV/c
$\chi^2_{\rm IP}$(PV)	> 4
Track χ^2/DOF	< 4
PID(K)	< 8
Ghost probability	< 0.4

Table 6.3: Selection requirements of the `Bu2D0TauNuForB2XTauNuAllLines` stripping line.

Cut	Value
3π vertex transverse distance to PV *	> 0.2 mm
χ^2_{IP}(PV) of pions from 3π vertex *	> 15
B vertex transverse distance to PV	> 0.6 mm
τ vertex χ^2	< 16
π from τ ProbNNpi	> 0.2
K^+ from D^0 ProbNNk	> 0.4
π from D^0 ProbNNpi	> 0.4
$\lvert z_{\text{PV}}(D^0) - z_{\text{PV}}(3\pi)\rvert$	< 0.0001 mm
All tracks momentum	$[2, 200]$ GeV/c
All tracks η	$[1.5, 5]$
nSPDHits	≤ 450

Table 6.4: *Preselection* requirements list. The cuts marked with * have been applied at the DaVinci stage in order to highly reduce the size of the output samples.

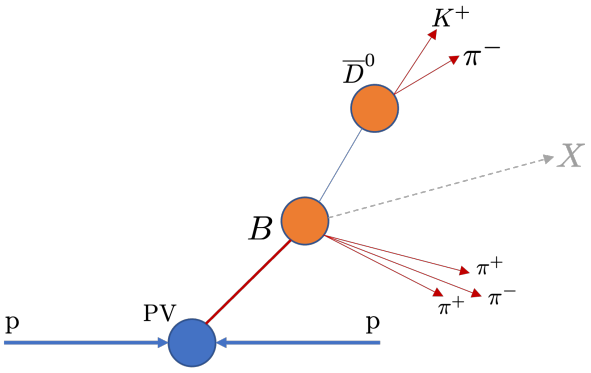

Figure 6.3: Topology of the prompt $B \to \overline{D}^0\pi^+\pi^-\pi^+(X)$ decays.

6.3.2 The distance detachment criterion

One of the largest background contributions in this analysis are $B \to \overline{D}^0\pi^+\pi^-\pi^+(X)$ decays, named *prompt* because the three pions are produced directly at the B vertex, as shown in Fig. 6.3. This topology differentiates from the signal, shown in Fig. 6.1, where the D^0 and 3π vertices are detached from the B one. In order to reduce this *prompt* contribution, a requirement on the distance along the beam direction (z) between the B and the τ vertices is applied. This strategy was first introduced in the Run 1 hadronic $R(D^*)$ measurement [53, 54].

Being $\sigma_{3\pi}$ and σ_B the uncertainties of the z-component of the two vertices, the $3\pi - B$

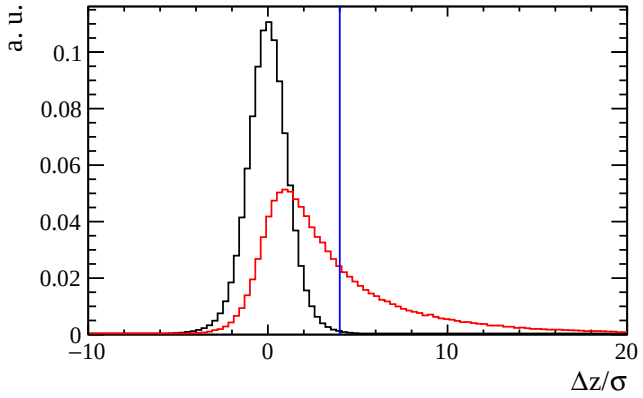

Figure 6.4: Distribution of $\Delta z/\sigma_z$, for inclusive *prompt* $B^+ \to \overline{D}^0\pi^+\pi^-\pi^+(X)$ (black) and signal $B^+ \to \overline{D}^0\tau^+\nu_\tau$, with $\tau^+ \to \pi^+\pi^-\pi^+\overline{\nu}_\tau$, (red) decays. The $\Delta z/\sigma_z > 4$ criterion applied in this study is indicated by the vertical blue line.

vertex distance divided by its uncertainty can be written as

$$\Delta z/\sigma_z = \frac{z_{3\pi} - z_B}{\sqrt{\sigma_z^2(3\pi) + \sigma_z^2(B)}} \equiv \frac{z_{3\pi} - z_B}{\sigma_z}. \tag{6.7}$$

The $\Delta z/\sigma_z$ distribution for prompt inclusive $B^+ \to \overline{D}^0\pi^+\pi^-\pi^+(X)$ and signal $B^+ \to \overline{D}^0\tau^+\nu_\tau$, with $\tau^+ \to \pi^+\pi^-\pi^+\overline{\nu}_\tau$ decays, is shown in Fig. 6.4. The same requirement as for the Run 1 analysis is applied, $\Delta z/\sigma_z > 4$, allowing to highly reduce the prompt contribution.

After the distance detachment requirement, the main background comes from doubly-charmed $B \to \overline{D}^0 D(X)$ decays, where D stands for a D_s^+, a D^+ or a $\overline{D}^0$ meson. Amongst these, the inclusive $B \to \overline{D}^0 D(X)$ decays, where the D_s^+ meson decays inclusively into 3 pions, is the main source of background in the analysis. For this reason, in addition to this requirement, control sample studies are fundamental to correct the simulation in order to precisely model these contributions.

6.3.3 Vertex Isolation

Charged and neutral particles other than those produced in the studied decays can be present in the event and can be used both to isolate the signal and normalisation candidates and to produce control samples for the background. This section focuses on the description of charged and neutral isolation algorithms, along with their impact in the signal and normalisation selection.

The isolation variables are exploited in the development of the D_s^+ decay model to produce control samples with additional neutral and/or charged particles coming from the τ vertex. These have the same topology as the decays represented in Fig. 6.19. For the detailed description of the D_s^+ control samples selections see Sec. 6.7.2.

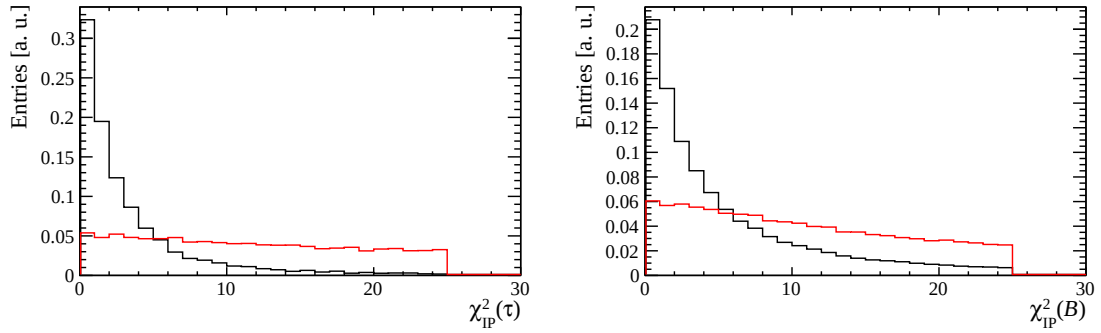

(a) (b)

Figure 6.5: $\chi^2_{\rm IP}$ distribution with respect to the τ (left) and B (right) vertices of extra tracks for signal $B \to \overline{D}^0\tau^+(\to 3\pi)\nu_\tau$ (red) and background $B^0 \to \overline{D}^0 D_s^+ X$ (black) decays. The extra tracks have $p_T > 250$ MeV/c and a $\chi^2_{\rm IP}(PV) > 4$. The distributions are normalised to the same area for comparison.

6.3.3.1 Charge isolation

In the Run 1 hadronic $R(D^{*-})$ analysis, a dedicated vertex isolation algorithm, called `TupleToolVtxIsolnPlus` tool [163], has been developed. This algorithm allows to reduce the contribution of inclusive decays with one or more extra track pointing to either the B or the τ decay vertices.

Background decays with extra tracks are mainly due to inclusive $B \to \overline{D}^0 D(X)$ decays. The D_s^+ or the D^+ mesons can decay into $D \to \pi^+\pi^-\pi^+\pi^+\pi^-(X)$ and the D^0 can decay into $K^-\pi^+\pi^-\pi^+(X)$ or $\pi^-\pi^+\pi^-\pi^+(X)$, with the extra tracks pointing to the τ decay vertex. Besides, other background events have the extra tracks pointing to the B vertex, such as $B \to \overline{D}^0 DK^\pm$ or $B \to \overline{D}^0 D\pi^\pm$.

Tracks pointing to the same vertex can be selected by considering the $\chi^2_{\rm IP}$. For a specific vertex, $\chi^2_{\rm IP}$ is defined as the difference between the vertex χ^2 built with and without the track. The $\chi^2_{\rm IP}$ distributions for signal $B \to \overline{D}^0\tau^+(\to 3\pi)\nu_\tau$ and inclusive $B \to \overline{D}^0 D_s^+(X)$ decays are visible in Fig. 6.5. For both τ (Fig. 6.5(a)) and B (Fig. 6.5(b)) vertices, the background peaks at low $\chi^2_{\rm IP}$ values, while the signal distribution is more uniform. In Fig. 6.5(a) the D_s^+ meson decays exclusively into 5π.

For the τ and the B vertices, the following variables are defined:

- $\boldsymbol{N^{\tau}_{\rm iso}(p_{\rm T} > 250; \chi^2_{\rm IP}(\rm PV) > 4; \chi^2_{\rm IP}(\tau) < 25)}$: number of additional tracks with $p_{\rm T} > 250$ MeV/c, an $\chi^2_{\rm IP}$ with respect to the PV larger than 4 and $\chi^2_{\rm IP}$ with respect to the τ vertex smaller than 25 (Fig. 6.6(a)).

- $\boldsymbol{N^{B}_{\rm iso}(p_{\rm T} > 250; \chi^2_{\rm IP}(\rm PV) > 4; \chi^2_{\rm IP}(B) < 25)}$: number of additional tracks with $p_{\rm T} > 250$ MeV/c, $\chi^2_{\rm IP}(\rm PV) > 4$ and $\chi^2_{\rm IP}(B) < 25$ (Fig. 6.6(b)).

$N^B_{iso}(p_T > 250; \chi^2_{\rm IP}(\rm PV) > 4; \chi^2_{\rm IP}(B) < 25)$ and $N^\tau_{iso}(p_T > 250; \chi^2_{\rm IP}(\rm PV) > 4; \chi^2_{\rm IP}(\tau) < 25)$

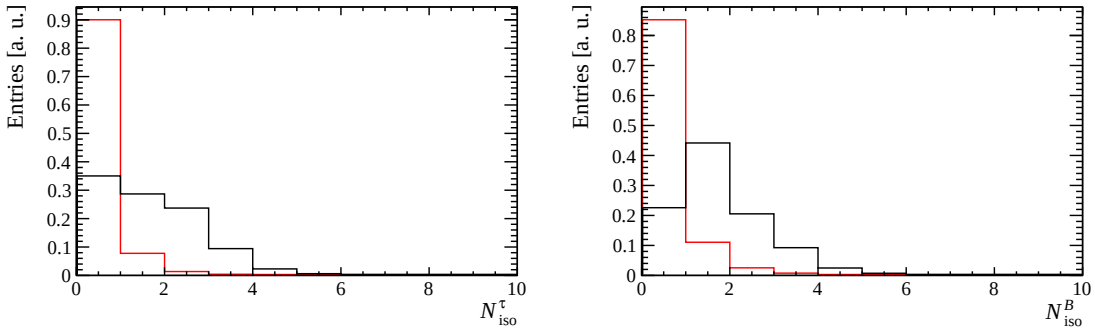

(a) (b)

Figure 6.6: Distributions of $N^{\tau}_{iso}(p_T > 250; \chi^2_{\rm IP}({\rm PV}) > 4; \chi^2_{\rm IP}(\tau) < 25)$ (left) and $N^{B}_{iso}(p_T > 250; \chi^2_{\rm IP}({\rm PV}) > 4; \chi^2_{\rm IP}(B) < 25)$ (right) for signal $B^+ \to \overline{D}^0\tau^+\nu_\tau$, with $\tau^+ \to \pi^+\pi^-\pi^+\overline{\nu}_\tau$, (red) and background $B \to \overline{D}^0 D^+_s(X)$ (black) decays.

distributions for inclusive $B \to \overline{D}^0 D(X)$ and signal $B^+ \to \overline{D}^0\tau^+\nu_\tau$ decays are represented in Fig. 6.6.

As a result, the requirements for isolated events are

$$N^{\tau}_{iso}(p_T > 250; \chi^2_{\rm IP}({\rm PV}) > 4; \chi^2_{\rm IP}(\tau) < 25) = n, \tag{6.8}$$

$$N^{B}_{iso}(p_T > 250; \chi^2_{\rm IP}({\rm PV}) > 4; \chi^2_{\rm IP}(B) < 25) = m, \tag{6.9}$$

where m and n are integers representing the number of extra tracks coming the respective vertices. These charged isolation variables are largely used to optimise the $D^+_s \to \pi^+\pi^-\pi^+(X)$ model by requiring the B vertex to be isolated ($m = 0$ in Eq. (6.9)) and producing control samples with additional charged tracks pointing to the τ vertex ($n = 1,\ 2$ in Eq. (6.8)). Nevertheless, the $\overline{D}^0$ meson can be produced also from a $D^{*+} \to D^0\pi^+$ decay, producing a slow pion, with a $p_{\rm T}$ lower than 250 MeV/c. In this case, the requirements on $N_{\rm iso}$ are not sufficient. The distribution of $m(D^0\pi^+) - m(D^0)$ is investigated when the extra track passes the requirement of Eq. (6.9), shown in Fig. 6.7. The vertical blue lines represent the range out of which the D^0 candidate is accepted, *i.e.* the D^{*+} veto: $[143, 148]$ MeV/c^2. This requirement is also used in the control sample study of inclusive $B \to \overline{D}^0 D^+_s(X)$ decays to split the sample in $B \to \overline{D}^0 D^+_s(X)$ and $B \to D^{*-} D^+_s(X)$ decays (Sec. 6.6).

6.3.3.2 Neutral isolation

When considering inclusive decays, such as $B \to \overline{D}^0 D^+_s(X)$ or $D^+_s \to \pi^+\pi^-\pi^+(X)$, neutral particles, such as photons from $\pi^0 \to \gamma\gamma$, $\eta \to \gamma\gamma$ and $\eta' \to \rho^0\gamma$ decays are another important contribution to the background. The strategy used to select neutral particles is based on the algorithm `TupleToolEWTrackIsolation` applied to the τ (3π) decay vertex.

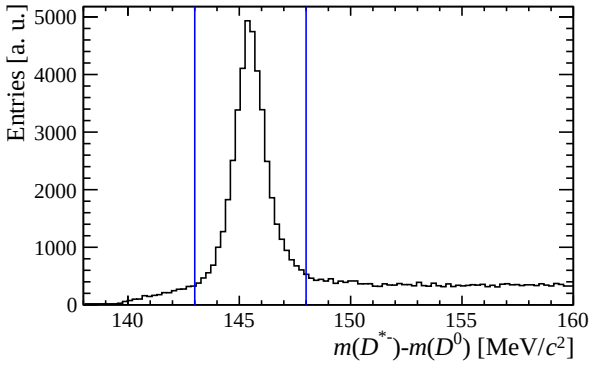

Figure 6.7: $m(D^0\pi^+) - m(D^0)$ distribution from data, obtained by adding a track passing the requirement of (6.9). The vertical blue lines represent D^{*+} veto.

First of all, in the ECAL, a set of cones centred on the 3π direction and with different radius is chosen. Each radius is defined as $\sqrt{\Delta\eta^2 + \Delta\phi^2}$, where $\Delta\eta$ and $\Delta\phi$ are intervals of pseudo-rapidity and the azimuth angle, respectively. The cone with radius 0.00 corresponds to the one with no requirement on $\sqrt{\Delta\eta^2 + \Delta\phi^2}$. For each cone, photons are searched for and recorded. Only the three photons with the largest p_T are considered in order to save space and computing time.

In addition to photons, this procedure is applied also to neutral particles compatible with $\pi^0 \to \gamma\gamma$ and $\eta \to \gamma\gamma$, with the additional requirement of the di-photon invariant mass. For example, `tau_0.40_nc_maxPt_mult` is the number of photons (`mult`) in the cone `0.40` around the 3π vertex; while `tau_0.00_pi0_maxPt_PT` is the p_{T} of the π^0 without requirement on $\sqrt{\Delta\eta^2 + \Delta\phi^2}$.

6.3.4 The BDT

In order to reduce the contribution of the largest background, i.e. the doubly-charmed $B \to \overline{D}^0 D_s^+(X)$ decays, a Boosted Decision Tree (BDT) algorithm is implemented with the TMVA toolkit [164]. The BDT output is then used as a variable in the three-dimensional fit to obtain the signal yields (Sec. 6.9).

Aiming to obtain the less biased result, the input variables are chosen to be as uncorrelated as possible with the other two fit variables, q^2 and t_τ. When identifying the pions from the τ decay as $\tau^+ \to \pi_0^+\pi_1^-\pi_2^+\overline{\nu}_\tau$, the BDT input variables are:

- the minimum mass of oppositely-charged pions: $\min[m(\pi_0^+\pi_1^-), m(\pi_2^+\pi_1^-)]$
- the maximum mass of oppositely-charged pions: $\max[m(\pi_0^+\pi_1^-), m(\pi_2^+\pi_1^-)]$
- the mass of the same-sign pions: $m(\pi_0^+\pi_2^+)$
- $\dfrac{\texttt{tau\_0.40\_nc\_vPT}}{\texttt{tau\_PT} + \texttt{tau\_0.40\_nc\_vPT}}$, where `tau_PT` is the transverse momentum of the 3π

Variable	Signal cuts	Normalisation cuts
trigger	true	true
$\Delta z/\sigma$	> 4	> 4
$\chi^2_{\rm IP}(\tau)$ D^0 daughters	> 5	> 5
D^{*+} veto: $\left(m(\overline{D}^0\pi^+) - m(\overline{D}^0)\right)$	$\notin [143, 148]$ MeV/c^2	$\notin [143, 148]$ MeV/c^2
$N^\tau_{iso}(p_T > 250; \chi^2_{\rm IP}({\rm PV}) > 4; \chi^2_{\rm IP}(\tau) < 25)$	$= 0$	$= 0$
$N^B_{iso}(p_T > 250; \chi^2_{\rm IP}({\rm PV}) > 4; \chi^2_{\rm IP}(B) < 25)$	$= 0$	$= 0$
q^2	> 0 GeV/c^2	> 0 GeV/c^2
t_τ	< 2 ns	< 2 ns
$\lvert m(\overline{D}^0) - m(\overline{D}^0)_{\rm PDG}\rvert$	< 20 MeV/c^2	< 20 MeV/c^2
$m(3\pi)$	< 1600 MeV/c^2	± 30 MeV/c^2 around D_s^+ mass
$m(\overline{D}^0 3\pi)$	—	± 60 MeV/c^2 around B^+ mass
BDT	> -0.4	—
K from $\overline{D}^0$ PID	DLLK$>$ 3 and ProbNNk$>$ 0.4	
π from $\overline{D}^0$ PID	DLLK$<$ 50 and ProbNNpi$>$ 0.4	
π_0^+ from $\tau^+ \to \pi_0^+\pi_1^-\pi_2^+\overline{\nu}_\tau$	DLLK$<$ 8 and ProbNNpi$>$ 0.2	
π_1^- from $\tau^+ \to \pi_0^+\pi_1^-\pi_2^+\overline{\nu}_\tau$	DLLK$<$ 8 and ProbNNpi$>$ 0.2 and ProbNNk$<$ 0.1	
π_2^+ from $\tau^+ \to \pi_0^+\pi_1^-\pi_2^+\overline{\nu}_\tau$	DLLK$<$ 8 and ProbNNpi$>$ 0.2	

Table 6.5: Signal and nosmalisation mode selections. Note that all the PID cuts are also applied to the control samples used in the background models of Sec. 6.6 when not specified.

system and `tau_0.40_nc_vPT` is the sum of the p_T of the photons in a cone of 0.40 around the 3π direction.

- `tau_0.40_nc_mult`: the number of photons detected in the cone of `0.40` around the 3π direction.

The maximisation of the figure of merit proposed in Ref. [165] yields a BDT cut of -0.4 with a signal efficiency of 90% and a background rejection of 65%.

6.3.5 Signal and normalisation selection summary

In Table 6.5, all the requirements for the signal and the normalisation modes are reported. For the signal fit variables, the q^2 is required to be greater than zero, the tau decay time $t_\tau < 2$ ns and the BDT> -0.4.

Additional requirements are applied to the $\overline{D}^0$. The invariant mass is required to be in a window of ± 20 MeV/c^2 around the known $\overline{D}^0$ mass and finally $D^+ \to \pi^+K^-\pi^+$ decays are suppressed by a PID cut. Besides, an additional requirement is needed to suppress events where one of the D^0 daughters belongs to the 3π vertex.

Finally, in order to select pions and kaons in the final state, the PID requirements listed at the bottom of Tab 6.5, are applied. Differently from the $R_{e/\mu}$ analysis, both DLL and ProbNN variables are used. PID efficiencies are obtained using PIDCalib [135]. In

particular, for the calibration samples, a larger momentum range was used, allowing to include particles with momentum in the range of $[2, 200]$ MeV/c.

6.4 Reconstruction of signal events

In both signal decays the final state presents two neutrinos, as shown in Fig. 6.1. One neutrino comes from the B meson decay and the other from the $\tau^+ \to \pi^+\pi^-\pi^+\overline{\nu}_\tau$ decay. Since the B and the τ vertices and the flight direction are measured, it is possible to infer the neutrino momentum up to a two fold ambiguity in the laboratory frame.

In the reconstruction of $B^+ \to \overline{D}^0\tau^+\nu_\tau$ decays, the B^+ line of flight is obtained by connecting the PV to the B^+ vertex. Subsequently, the τ lepton line of flight is given by the line joining the 3π and the B^+ vertices. The left diagram of Fig. 6.8 illustrates the angle θ between the τ flight direction and the 3π system, while the diagram on the right shows the angle θ' between the B^+ flight direction and the $\overline{D}^0\tau^+$ system. All this considered, the τ momentum in the laboratory frame is[2]

$$|\vec{p}_\tau| = \frac{(m_{3\pi}^2 + m_\tau^2)|\vec{p}_{3\pi}|\cos\theta \pm E_{3\pi}\sqrt{(m_\tau^2 - m_{3\pi}^2)^2 - 4m_\tau^2|\vec{p}_{3\pi}|^2\sin^2\theta}}{2(E_{3\pi}^2 - |\vec{p}_{3\pi}|^2\cos^2\theta)}\,, \tag{6.10}$$

where $m_{3\pi}$, $|\vec{p}_{3\pi}|$ and $E_{3\pi}$ are the invariant mass, 3-momentum and energy of the 3π system, respectively; and m_τ is the known τ mass. The quadratic ambiguity disappears when the square root in Eq. (6.10) argument vanishes. Hence, the θ angle reaches its maximum allowed value, given by

$$\theta_{max} = \arcsin\left(\frac{m_\tau^2 - m_{3\pi}^2}{2m_\tau|\vec{p}_{3\pi}|}\right). \tag{6.11}$$

Therefore the τ momentum is estimated as $|\vec{p}_\tau| = |\vec{p}_\tau(\theta_{max})|$, leading to

$$|\vec{p}_\tau| \approx \frac{(m_{3\pi}^2 + m_\tau^2)|\vec{p}_{3\pi}|\cos\theta_{max}}{2(E_{3\pi}^2 - |\vec{p}_{3\pi}|^2\cos^2\theta_{max})}. \tag{6.12}$$

With the $|\vec{p}_\tau|$ value it is possible to repeat the procedure to estimate the B^+ momentum, obtaining

$$|\vec{p}_B| = \frac{(m_{\overline{D}^0\tau}^2 + m_B^2)|\vec{p}_{\overline{D}^0\tau}|\cos\theta' \pm E_{\overline{D}^0\tau}\sqrt{(m_B^2 - m_{\overline{D}^0\tau}^2)^2 - 4m_B^2|\vec{p}_{\overline{D}^0\tau}|^2\sin^2\theta'}}{2(E_{\overline{D}^0\tau}^2 - |\vec{p}_{\overline{D}^0\tau}|^2\cos^2\theta')}\,, \tag{6.13}$$

where $m_{\overline{D}^0\tau}$, $|\vec{p}_{\overline{D}^0\tau}|$ and $E_{\overline{D}^0\tau}$ are the invariant mass, 3-momentum and energy of the $\overline{D}^0\tau$ system, respectively; and m_B is the known B^+ mass.

[2] All these calculations are made in units where $c = 1$. For a particle x the unit vector is defined as $\hat{u}_x = \vec{p}_x/|\vec{p}_x|$ where p_x is the module of the vector.

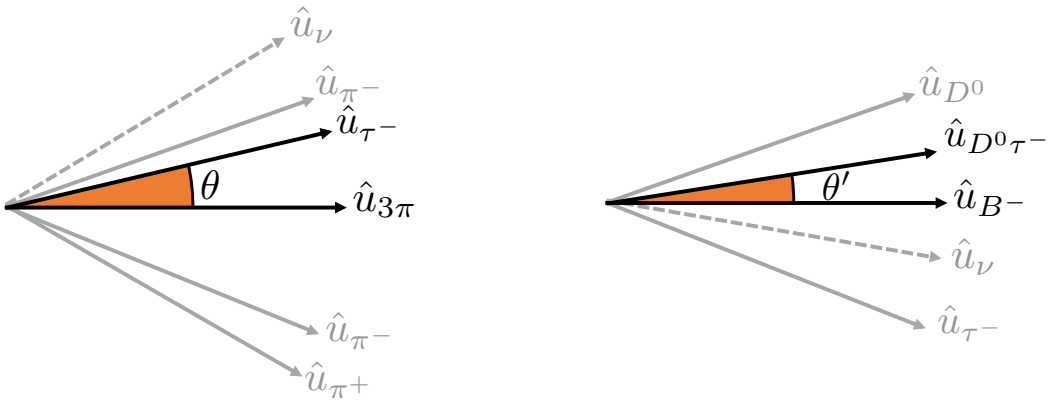

Figure 6.8: Left: angle between the τ and the 3π system directions. Right: angle between the $\overline{D}^0\tau$ system and the B^+ directions. The vectors represent the direction of the momenta of the considered particles.

When the 4-momentum of the $\overline{D}^0$ meson and the τ lepton are respectively denoted by $p_{\overline{D}^0}$ and $p_\tau(\theta_{\max})$, the momentum of the $\overline{D}^0\tau$ combination is

$$p_{\overline{D}^0\tau} = p_{\overline{D}^0} + p_\tau(\theta_{\max})\,. \tag{6.14}$$

Similarly to the τ^+ case, the quadratic ambiguity disappears by setting the square root in Eq. (6.13) to zero and the θ' angle reaches its maximum allowed value, given by

$$\theta'_{max} = \arcsin\left(\frac{m_B^2 - m_{\overline{D}^0\tau}^2}{2m_B|\vec{p}_{\overline{D}^0\tau}|}\right), \tag{6.15}$$

so the B^+ momentum is estimated as $|\vec{p}_B| = |\vec{p}_B(\theta'_{\max})|$, leading to

$$|\vec{p}_B| \approx \frac{(m_{\overline{D}^0\tau}^2 + m_B^2)|\vec{p}_{\overline{D}^0\tau}|\cos\theta'_{\max}}{2(E_{\overline{D}^0\tau}^2 - |\vec{p}_{\overline{D}^0\tau}|^2\cos^2\theta'_{\max})}. \tag{6.16}$$

Finally, following these two approximations it is possible to obtain the B^+ and τ 4-momenta as:

$$p_\tau = (m_\tau, |\vec{p}_\tau|\hat{u}_\tau) \quad \text{and} \tag{6.17}$$
$$p_B = (m_B, |\vec{p}_B|\hat{u}_B). \tag{6.18}$$

where $\hat{u}_\tau$ ($\hat{u}_B$) is the unit vector pointing to the τ (B) vertex from the reconstructed B vertex (PV). With the τ 4-momentum of Eq. (6.17) it is possible to estimate the τ decay time, t_τ, and the squared momentum transfer to the $\tau^+\nu_\tau$ system, using also the measured 4-momentum of the $\overline{D}^0$ $p_{\overline{D}^0} = (m_{\overline{D}^0}, \vec{p}_{\overline{D}^0})$. The q^2 is defined as

$$q^2 = (p_B - p_{\overline{D}^0})^2, \tag{6.19}$$

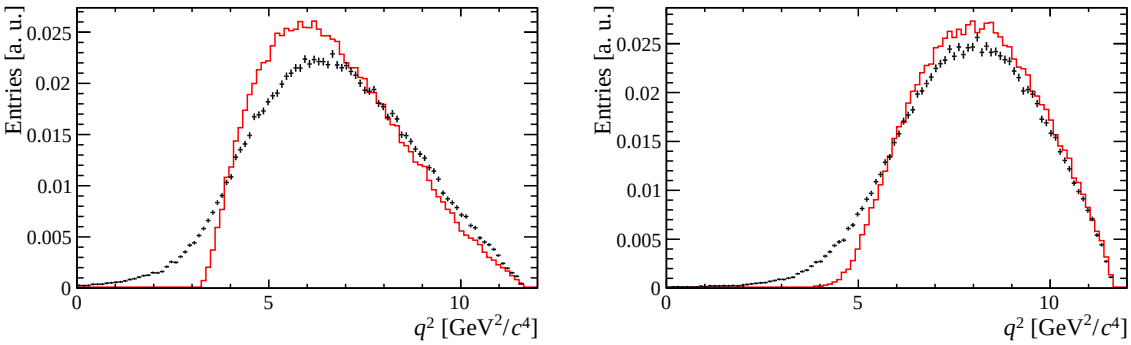

(a) $B^+ \to \overline{D}^0\tau^+\nu_\tau$ (b) $B^+ \to \overline{D}^{*0}\tau^+\nu_\tau$

Figure 6.9: Distribution of the q^2 estimated (black) and generated (red) for signal $B^+ \to \overline{D}^0\tau^+\nu_\tau$ (left) and $B^+ \to \overline{D}^{*0}\tau^+\nu_\tau$ (right) decays, with $\tau^+ \to \pi^+\pi^-\pi^+\overline{\nu}_\tau$.

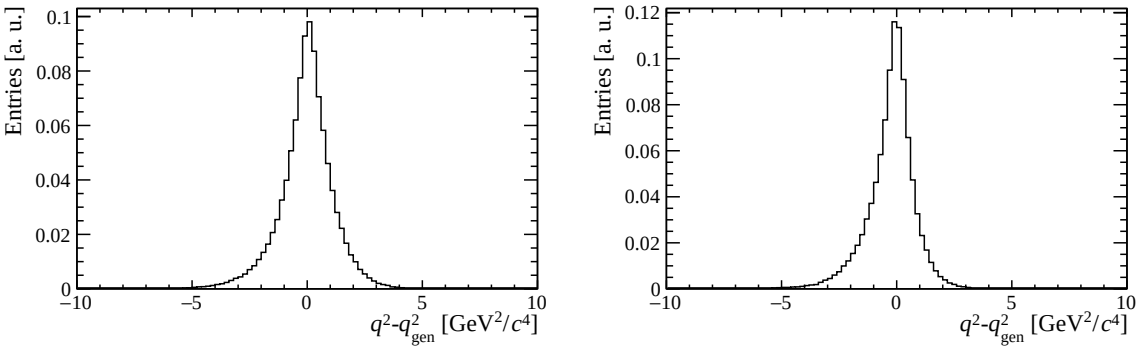

(a) $B^+ \to \overline{D}^0\tau^+\nu_\tau$ (b) $B^+ \to \overline{D}^{*0}\tau^+\nu_\tau$

Figure 6.10: q^2 resolution $q^2 - q^2_{\text{gen}}$ for signal $B^+ \to \overline{D}^0\tau^+\nu_\tau$ (left) and $B^+ \to \overline{D}^{*0}\tau^+\nu_\tau$ (right) decays, with $\tau^+ \to \pi^+\pi^-\pi^+\overline{\nu}_\tau$.

for both $B^+ \to \overline{D}^0\tau^+\nu_\tau$ and $B^+ \to \overline{D}^{*0}\tau^+\nu_\tau$ decays. In Figs. 6.9(a) and 6.9(b) the q^2 distribution is shown for $B^+ \to \overline{D}^0\tau^+\nu_\tau$ and $B^+ \to \overline{D}^{*0}\tau^+\nu_\tau$ decays respectively. The q^2 resolution is obtained by comparing the reconstructed q^2 with the MC truth $q^2{}_{\text{gen}}$: $q^2 - q^2_{\text{gen}}$. This resolution is represented in Figs. 6.10(a) and 6.10(b) for the two signal decays. The τ decay time distribution is represented in Figs. 6.11(a) and 6.11(b) together with the respective resolution $t_\tau - t_\tau^{\text{gen}}$ in Figs. 6.12(a) and 6.12(b).

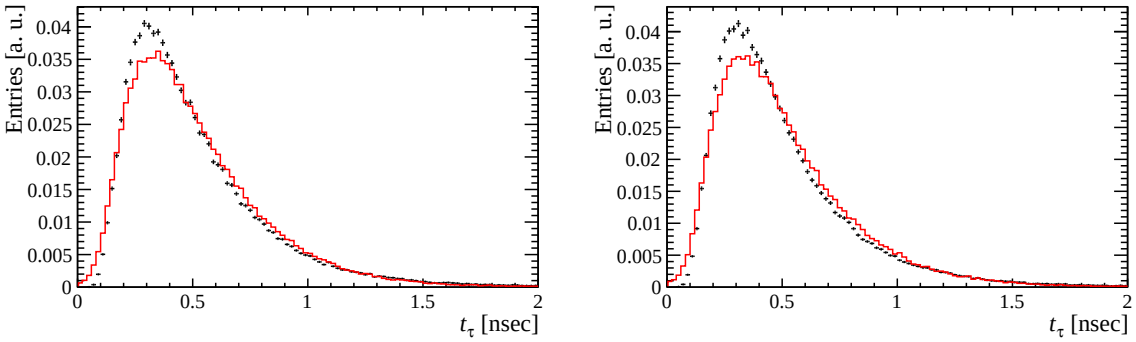

(a) $B^+ \to \overline{D}^0\tau^+\nu_\tau$ (b) $B^+ \to \overline{D}^{*0}\tau^+\nu_\tau$

Figure 6.11: Reconstructed τ decay time (black) and generated t_τ^{gen} (red) distributions for signal $B^+ \to \overline{D}^0\tau^+\nu_\tau$ (left) and $B^+ \to \overline{D}^{*0}\tau^+\nu_\tau$ (right) decays, with $\tau^+ \to \pi^+\pi^-\pi^+\overline{\nu}_\tau$.

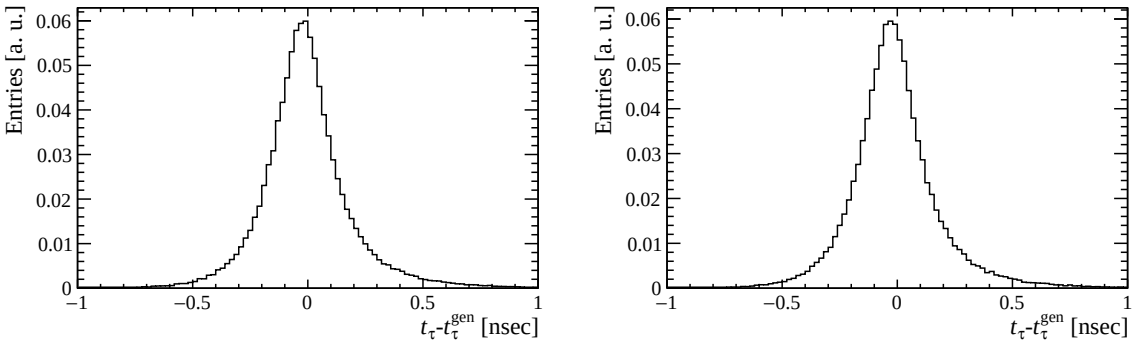

(a) $B^+ \to \overline{D}^0\tau^+\nu_\tau$ (b) $B^+ \to \overline{D}^{*0}\tau^+\nu_\tau$

Figure 6.12: τ decay time resolution $t_\tau - t_\tau^{\text{gen}}$ for $B^+ \to \overline{D}^0\tau^+\nu_\tau$ (left) and $B^+ \to \overline{D}^{*0}\tau^+\nu_\tau$ (right) decays, with $\tau^+ \to \pi^+\pi^-\pi^+\overline{\nu}_\tau$.

6.5 Corrections to simulation

In this section, the corrections applied to the simulation in order to describe the data as accurately as possible, are presented.

6.5.1 Vertex resolution

Before applying the vertex detachment cut $\Delta z/\sigma_z > 4$ (Sec. 6.3.2), the dominant contribution in the data sample are $B \to \overline{D}^0\pi^+\pi^-\pi^+(X)$ events, where three pions are produced at the B vertex. In this sample, the Δz and the $\Delta z/\sigma_z$ distributions depend on vertex resolution effects. The $\Delta z/\sigma_z$ distribution depends also on the $\sigma_z(3\pi)$ and $\sigma_z(B)$ uncertainties. This is evident in Fig. 6.13, where the the Δz (6.13(a)) and the $\Delta z/\sigma_z$ (6.13(b)) distributions of exclusive $B \to \overline{D}^0\pi^+\pi^-\pi^+$ decays are shown for the three years of data taking (2016, 2017, 2018) and the simulation (2016 only). The 2016 data sample has a worse resolution than those of 2017 and 2018, and the simulation does not reproduce the change of resolution between 2016 and the other years.

In order to take into account these differences, a correction procedure is developed. This can be divided in two steps: scaling and smearing.

- $\sigma_z(3\pi)$ and $\sigma_z(B)$, the vertex uncertainties on the z position of τ and B, respectively, are scaled by exploiting the dependence on the $m(3\pi)$ and $m(D^0 3\pi)$ invariant mass distributions.
- the $\Delta z/\sigma_z$ distribution is not in agreement with 2016 data after the scaling, so a smearing factor is applied.

These corrections are obtained from the inclusive $B \to \overline{D}^0\pi^+\pi^-\pi^+(X)$ decays *prompt* control sample, and tested in the exclusive $B \to \overline{D}^0\pi^+\pi^-\pi^+$ peak. Before the correction procedure, the $\sigma_z(3\pi)$ and $\sigma_z(B)$ distributions as a function of $m(3\pi)$ and $m(D^0 3\pi)$ for data and simulation are represented in Fig. 6.14(a) and Fig. 6.14(b), respectively. The corresponding ratios of 2016 data over 2017, 2018 and (2016) simulation are represented in Fig. 6.14(c) and 6.14(d) for the τ and B vertex, respectively.

The uncertainties $\sigma_z(3\pi)$ and $\sigma_z(B)$ are corrected by applying the following first-order polynomials separately for the 2016, 2017 and 2018 samples:

$$\sigma_z(3\pi)' = (\alpha_0^{3\pi} + \alpha_1^{3\pi} \times m(3\pi)) \times \sigma_z(3\pi), \quad (6.20)$$

$$\sigma_z(B)' = (\alpha_0^{B} + \alpha_1^{B} \times m(D^0 3\pi)) \times \sigma_z(B). \quad (6.21)$$

After this procedure, the agreement is observed only in the 2017 and 2018 samples. As a consequence, a smearing factor is applied to the vertex resolution distribution to reproduce the 2016 data sample. This is modelled following a Gaussian distribution. Afterwards, a simultaneous fit to the simulation and 2016 data in the Δ/σ_z variable is performed. For the years 2016/2017/2018 the simulation is corrected using the relative proportions 31%/32%/37% respectively.

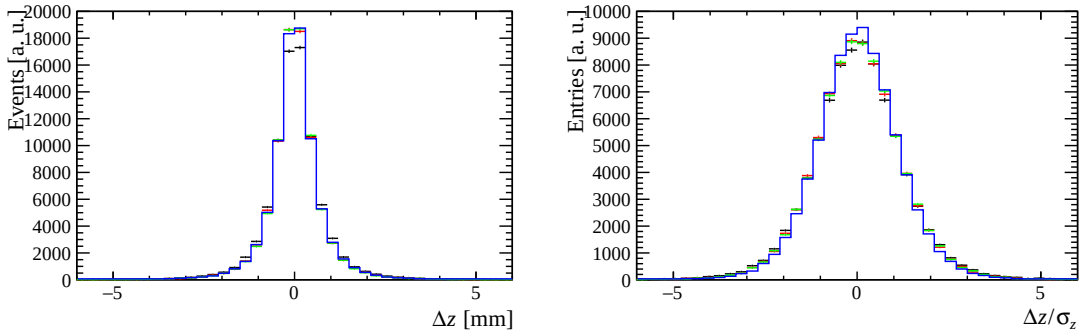

(a) (b)

Figure 6.13: Δz (left) and $\Delta z/\sigma_z$ (right) distributions for exclusive $B \to \overline{D}^0\pi^+\pi^-\pi^+$ events, for 2016 (black), 2017 (red), 2018 (green) data and simulation (blue).

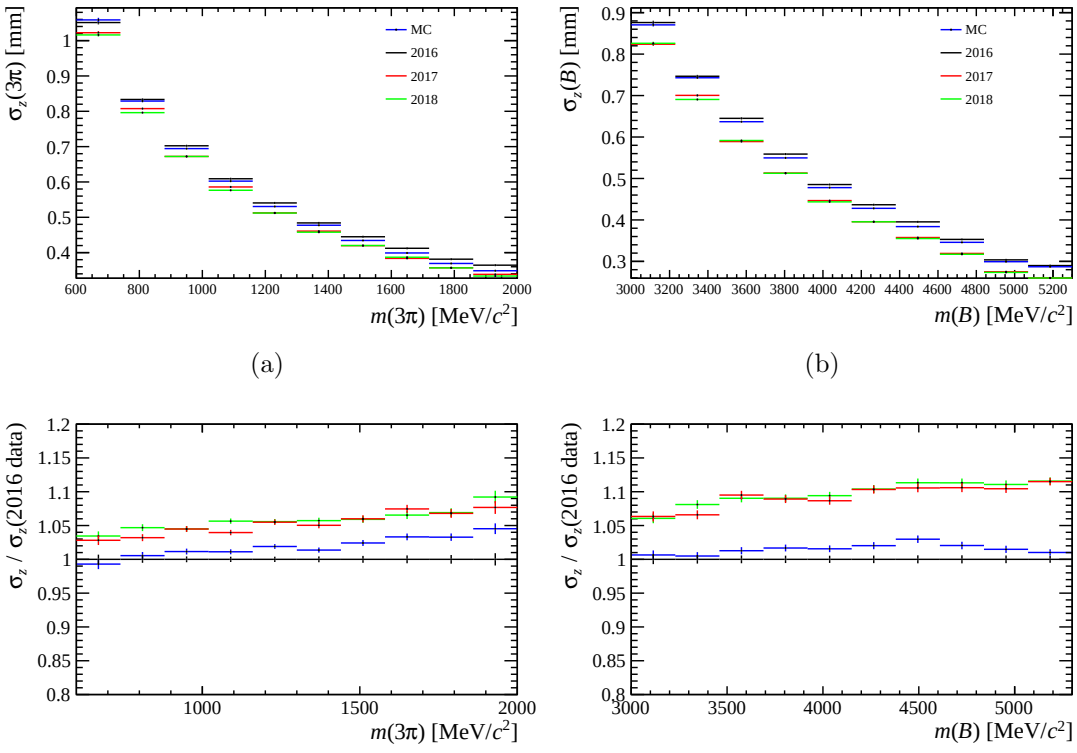

(a) (b)

(c) (d)

Figure 6.14: Top: mean of the $\sigma_{3\pi}$ (left) and σ_B (right) distributions. Simulation is shown in blue, 2016, 2017 and 2018 data in black, red and green, respectively. Bottom: the corresponding ratios 2016/2017, 2016/2018 and 2016/simulation.

After the corrections, the Δz and $\Delta z/\sigma_z$ distributions of Fig. 6.13 agree with data. This is represented in Fig. 6.15(a), 6.15(b) and 6.15(c) for 2016, 2017 and 2018, respectively.

6.5.2 B meson kinematics, event multiplicity and trigger category

The distributions of kinematic variables of B mesons and the event multiplicity in simulation are corrected with a two dimensional re-weighting procedure, similar to the one implemented in Ref. [51]. The weights are obtained by comparing the $B \to \overline{D}^0\pi^+\pi^-\pi^+$ peak in the data and the simulation samples. In order to maximise the statistics for the exclusive 3π peak, both $B \to \overline{D}^0\pi^+\pi^-\pi^+$ and $B \to \overline{D}^0 3\pi(X)$ simulation samples are used.

The first weight is obtained considering the $B \to \overline{D}^0\pi^+\pi^-\pi^+$ peak in the distributions of the number of degrees of freedom of the PV, $N^{\text{PV}}_{\text{DoF}}$, and the number of tracks in the event, N_{tracks}. The second one is obtained from the data-simulation comparison in the p_{T} and the pseudorapidity of the B meson, $p_{\text{T}}(B)$ and $\eta(B)$ distributions respectively. This two steps procedure is repeated for the three exclusive trigger categories, `!B_L0Global_TIS`, `!B_L0HadronDecision_TOS` and `B_L0Global_TIS & B_L0HadronDecision_TOS`. Then an additional weight is applied in order to match the TISTOS efficiency (see Sec. 5.7.2 and 4.2.8) between data and simulation. In Fig. 6.16 the comparison between the distributions before and after the re-weighting procedure is represented. Thanks to this procedure, the agreement between data and simulation increases in all the distributions considered.

6.5.3 Form Factors model

The form factor parameterisation chosen in the production of simulation samples can introduce biases in the modelling of signal decays. A different strategy from the $R_{e/\mu}$ analysis is chosen to reduce these effects since for B decays, which is implemented with the HAMMER (Helicity Amplitude Module for Matrix Element Re-weighting) [166] tool. This software is dedicated to fast and efficient transformations of large MC samples and was primarily developed for $b \to c\tau\nu_\tau$ processes. It can be used to the change the FF parameterisation of a MC sample or in NP studies.

The form factors of the hadronic transitions of the signal $B^+ \to \overline{D}^{(*)0}\tau^+\nu_\tau$ decays are introduced in Sec. 2.2.4.1. The MC sample is produced following the ISGW2 model [30, 31]. For this analysis, the Boyd-Grinstein-Lebed (BGL) parameterisation is chosen to re-weight the MC. For the two signals, the series expansion from which the parameters are obtained, is truncated at different points, as justified in Ref. [38, 67, 167]. For the detailed HAMMER re-weighting procedure, see Ref. [166].

The BGL parameters used for $B^+ \to \overline{D}^0\tau^+\nu_\tau$ decays are given in Ref. [38]. These are obtained by means of a global fit to lattice QCD calculations (HPQCD and FNAL/MILC) and experimental measurements (Belle and BaBar). The model is constructed truncating

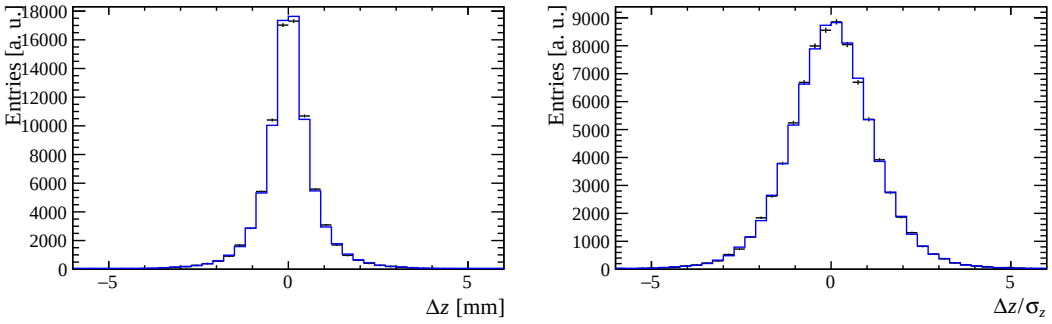

(a) 2016 data sample

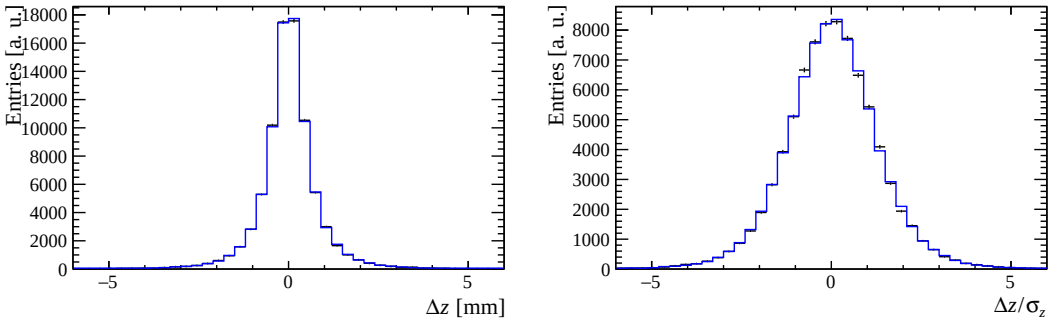

(b) 2017 data sample

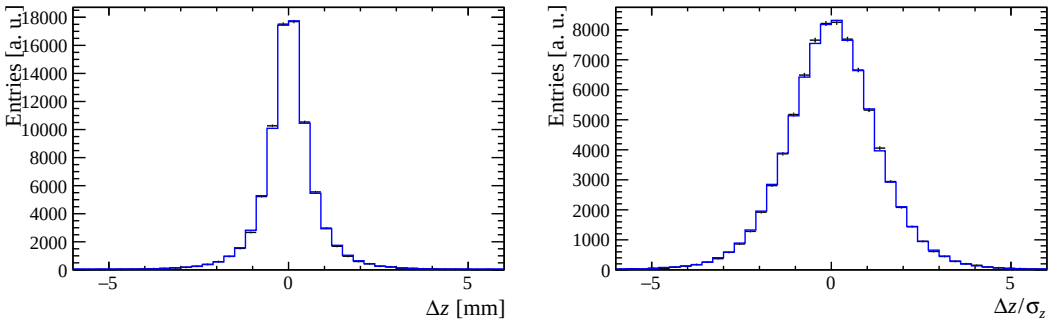

(c) 2018 data sample

Figure 6.15: Distributions of Δz (left) and $\Delta z/\sigma_z$ (right) after the uncertainties scaling correction and vertex smearing (2016 only) for the different data-taking years. Black points correspond to data and the blue histogram to simulation.

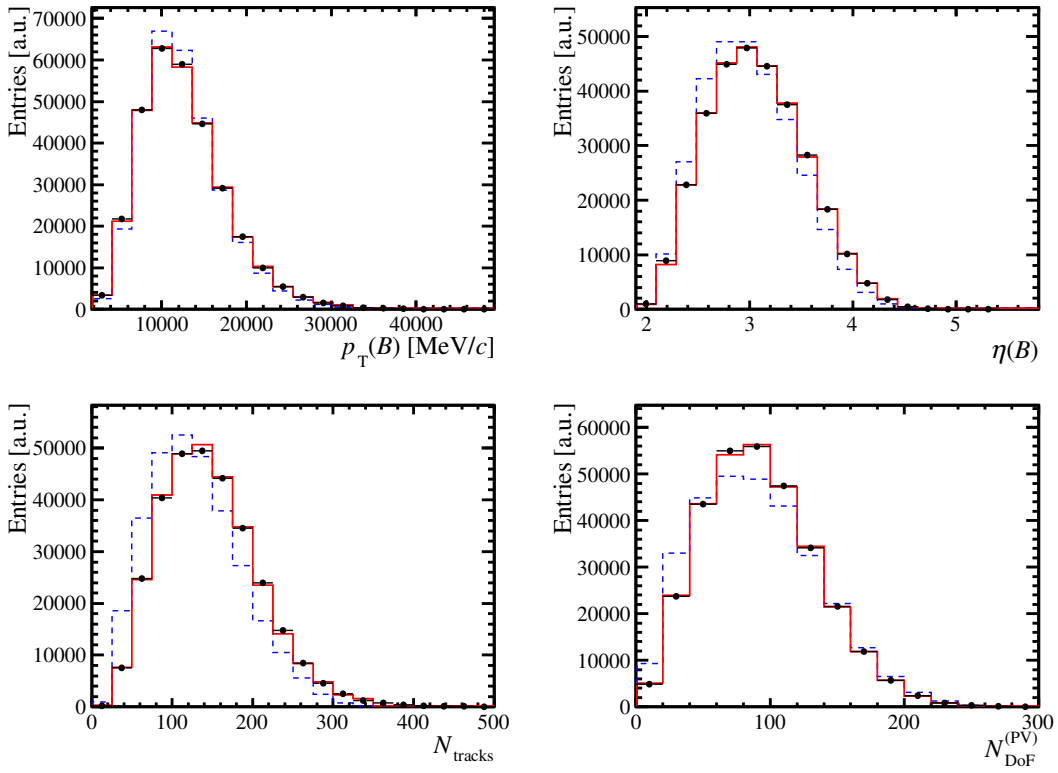

Figure 6.16: Comparison of the kinematic and occupancy variables before (dashed blue line) and after (red) the re-weighting procedure for the trigger integrated sample. From left-top to bottom right:$p_{\mathrm{T}}(B)$, $\eta(B)$, N_{tracks} and $N_{\mathrm{DoF}}^{\mathrm{PV}}$.

$B \to D\tau^+\nu_\tau$ [38]		$B \to D^*\tau^+\nu_\tau$ [67, 167]	
Parameter	Value	Parameter	Value
a_0^0	0.07932 ± 0.00058	a_0^g	$0.0299^{+0.0053}_{-0.0035}$
a_1^0	$-0.214^{+0.015}_{-0.014}$	a_1^g	$0.04^{+0.07}_{-0.20}$
a_2^0	$0.17^{+0.10}_{-0.24}$	a_2^g	$-0.9^{+1.8}_{-0.0}$
a_3^0	$-0.958^{+1.060}_{-2.000}$	–	–
a_0^+	0.01565 ± 0.00011	a_0^f	0.01218 ± 0.00016
a_1^+	-0.0353 ± 0.0031	a_1^f	$-0.029^{+0.021}_{-0.013}$
a_2^+	$-0.043^{+0.021}_{-0.035}$	a_2^f	$0.5^{+0.0}_{-0.3}$
a_3^0	$0.194^{+0.019}_{-0.016}$	–	–
–	–	$a_0^{\mathcal{F}_1}$	$0.1675 a_0^f$
–	–	$a_1^{\mathcal{F}_1}$	$-0.0051^{+0.0049}_{-0.0013}$
–	–	$a_2^{\mathcal{F}_1}$	$0.065^{+0.009}_{-0.089}$
–	–	$a_0^{\mathcal{F}_2}$	0.0595 ± 0.0093
–	–	$a_1^{\mathcal{F}_2}$	-0.318 ± 0.170
–	–	$a_2^{\mathcal{F}_2}$	$\lvert a_2^{\mathcal{F}_2}\rvert < 1$

Table 6.6: Form Factor BGL parameters employed in the analysis. Left: $B \to D\tau^+\nu_\tau$ FF values and uncertainties taken from Ref. [38]. Right: $B \to D^*\tau^+\nu_\tau$ FF parameters values from Ref. [67], estimated using the LCSR constraint [167].

the series expansions of Eqs.(2.95)-(2.98) at $N = 3$, resulting in 8 free parameters. Besides, for $N = 3$, Ref. [38] provides lookout tables for the systematic evaluation. The parameter values are collected in the left part of Tab. 6.6.

For the $B \to D^*\tau^+\nu_\tau$ decay, the FF parameters are estimated by Ref. [67], including the Light Cone Sum Rules (LCSR) constraints, described in Ref. [167]. The right part of Tab. 6.6 shows the parameter values used in the re-weighting procedure.

6.6 Background contributions studies

When aiming to isolate the signal and normalisation decay modes, understanding all the background contributions is of fundamental importance. Despite the selection requirements suppressing a large part of the background, there is still a large contribution from doubly-charmed $B \to \overline{D}^0 D_s^+(X)$ decays, where the D_s^+ decays inclusively as $D_s^+ \to \pi^+\pi^-\pi^+(X)$ in the signal sample. In order to control this background, two independent studies are performed, which are used to improve the simulation.

Another important contribution to the background is due to semitauonic $B \to D^{**}\tau^+\nu_\tau$

decays, where D^{**} is an excited D meson different from a D^*. These have not been measured, so an estimation procedure is done to account for them.

This section is structured as follows. In Sec. 6.6.1, the main features of the doubly-charmed $B \to \overline{D}^0 D_s^+(X)$ decay model is reported. The study of the feed down from excited D^{**} mesons is reported in Sec. 6.6.2. The $D_s^+ \to \pi^+\pi^-\pi^+(X)$ model is described in detail in next section, Sec. 6.7.

6.6.1 The $B \to \overline{D}^0 D_s^+(X)$ decay model

In order to improve the description of $B \to \overline{D}^0 D_s^+(X)$ decays, a control sample is produced, obtained by selecting exclusive $D_s^+ \to \pi^+\pi^-\pi^+$ decays in a window of ± 30 MeV/c^2 around the D_s^+ mass. Afterwards, this sample is split into two: the $\overline{D}^0 D_s^+$ and $D^{*-} D_s^+$ sub-samples. The last one is produced by requiring the presence of a soft pion compatible with a $D^{*+} \to D^0\pi^+$ decay by means of the isolation algorithm. Then, a simultaneous fit to the $m'_{\overline{D}^0 D_s^+}$ and $m'_{D^{*-} D_s^+}$ distributions from the $\overline{D}^0 D_s^+$ and $D^{*-} D_s^+$ sub-samples, respectively, is performed. These variables are defined as

$$m'_{\overline{D}^0 D_s^+} \equiv m(\overline{D}^0 D_s^+) - m(\overline{D}^0) - m(D_s^+) + m_{\rm PDG}(\overline{D}^0) + m_{\rm PDG}(D_s^+), \tag{6.22}$$

$$m'_{D^{*-} D_s^+} \equiv m(D^{*-} D_s^+) - m(D^{*-}) - m(D_s^+) + m_{\rm PDG}(D^{*-}) + m_{\rm PDG}(D_s^+), \tag{6.23}$$

where m is the reconstructed mass and $m_{\rm PDG}(\overline{D}^0)$ and $m_{\rm PDG}(D_s^+)$ are the known masses [1].

The components used in the fit are:

- B^+ decays: $B^+ \to \overline{D}^0 D_s^+$, $B^+ \to \overline{D}^{*0} D_s^+$, $B^+ \to \overline{D}^0 D_s^{*+}$, $B^+ \to \overline{D}^{*0} D_s^{*+}$, $B^+ \to \overline{D}^0 D_{s1}(2460)^+$ and $B^+ \to \overline{D}^{*0} D_{s1}(2460)^+$.

- B^0 decays: $B^0 \to D^{*-} D_s^+$, $B^0 \to D^{*-} D_s^{*+}$, $B^0 \to D^{*-} D_{s0}^*(2317)^+$, $B^0 \to D^{*-} D_{s1}(2460)^+$ and $B^0 \to \overline{D}^0 D_s^+(X)$.

- Decays coming from a B^+ or a B_s^0 which are not included in the other categories: $B^+|B_s^0 \to \overline{D}^0 D_s^+(X)$.

- Background that includes contributions due to wrong-sign (WS) $D^0 D_s^+$.

For the i-th component, the number of events is denoted $N_i^{\rm sub-sample}$, depending on the sub-sample from which it is obtained. The fit parameters include the relative yields, F_i and F_i^*, and the relative efficiencies ε_i.

For the i-th component, F_i is its relative yield with respect to the $B^+ \to \overline{D}^0 D_s^+$ component in the $\overline{D}^0 D_s^+$ sub-sample:

$$F_i = \frac{N_i^{(\overline{D}^0 D_s^+)}}{N_{B^+ \to \overline{D}^0 D_s^+}^{(\overline{D}^0 D_s^+)}}, \tag{6.24}$$

and F_i^* are obtained with respect the $B^0 \to D^{*-}D_s^+$ component as

$$F_i^* = \frac{N_i^{(\bar{D}^0 D_s^+)}}{N_{B^0\to D^{*-}D_s^+}^{(\bar{D}^0 D_s^+)}}, \tag{6.25}$$

resulting in $F_i = F_{B^0\to D^{*-}D_s^+} F_i^*$. These factors are shared by the simultaneous fit to the two control samples. The relative efficiencies, ε_i, are

$$\varepsilon_i = \frac{N_i^{(D^{*-}D_s^+)}}{N_i^{(\bar{D}^0 D_s^+)}}, \tag{6.26}$$

and the sum of the F_i parameters $\sum_i F_i$ is

$$\begin{aligned}\sum_i F_i = {} & F_{B^+\to\bar{D}^0 D_s^+} + F_{B^+\to\bar{D}^{*0} D_s^+} + F_{B^+\to\bar{D}^0 D_s^{*+}} + F_{B^+\to\bar{D}^{*0} D_s^{*+}} \\ & + F_{B^+\to\bar{D}^0 D_{s1}(2460)^+} + F_{B^+\to\bar{D}^{*0} D_{s1}(2460)^+} + F_{B^+|B_s^0\to\bar{D}^0 D_s^+ X} \\ & + F_{B^0\to\bar{D}^0 D_s^+ X} + F_{B^0\to D^{*-}D_s^+} + F_{B^0\to D^{*-}D_s^+} \times F^*_{B^0\to D^{*-}D_s^{*+}} \\ & + F_{B^0\to D^{*-}D_s^+} \times F^*_{B^0\to D^{*-}D^*_{s0}(2317)^+} \\ & + F_{B^0\to D^{*-}D_s^+} \times F^*_{B^0\to D^{*-}D_{s1}(2460)^+},\end{aligned}$$

where $F^{(\bar{D}^0 D_s^+)}_{B^+\to\bar{D}^0 D_s^+} = 1$ by definition.

The models for the $\overline{D}^0 D_s^+$ and the $D^{*-}D_s^+$ subsamples, respectively: $f^{(\bar{D}^0 D_s^+)}(m'_{\bar{D}^0 D_s^+})$ and $f^{(D^{*-}D_s^+)}(m'_{D^{*-}D_s^+})$, are defined as

$$f^{(\bar{D}^0 D_s^+)}(m'_{\bar{D}^0 D_s^+}) = N_{\rm WS}^{(\bar{D}^0 D_s^+)} f_{\rm WS}^{(\bar{D}^0 D_s^+)}(m'_{\bar{D}^0 D_s^+}) + \sum_i N_i^{(\bar{D}^0 D_s^+)} f_i^{(\bar{D}^0 D_s^+)}(m'_{\bar{D}^0 D_s^+}), \tag{6.27}$$

$$f^{(D^{*-}D_s^+)}(m'_{D^{*-}D_s^+}) = N_{\rm WS}^{(D^{*-}D_s^+)} f_{\rm WS}^{(D^{*-}D_s^+)}(m'_{D^{*-}D_s^+}) + \sum_i N_i^{(D^{*-}D_s^+)} f_i^{(D^{*-}D_s^+)}(m'_{D^{*-}D_s^+}), \tag{6.28}$$

where f_i and WS_i are the mass distributions of the i^{th} and the wrong-sign component, respectively. The yields can be expressed in terms of the free parameters of the fit and the relative efficiencies as

$$N_i^{(\bar{D}^0 D_s^+)} = N_{\rm D_s^+}^{(\bar{D}^0 D_s^+)} \frac{F_i}{\sum_j F_j}, \tag{6.29}$$

$$N_i^{(D^{*-}D_s^+)} = N_{\rm D_s^+}^{(\bar{D}^0 D_s^+)} \times \varepsilon_i \times \frac{F_i}{\sum_j F_j}. \tag{6.30}$$

The fit results are collected in Fig. 6.17 and Tab. 6.7. These values are then used in the three-dimensional fit to obtain the signal yields as an input.

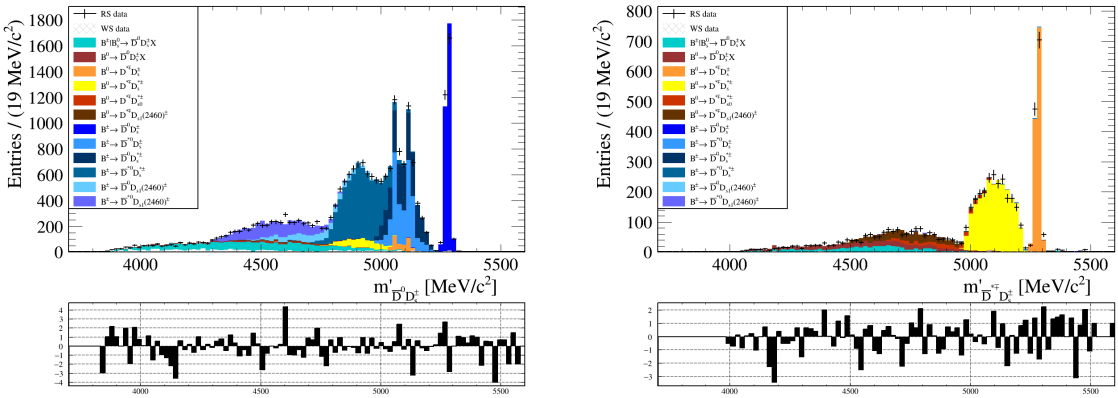

(a) (b)

Figure 6.17: $m(\overline{D}^0 D_s^+)$ and $m(D^{*-} D_s^+)$ distributions after fit.

Free parameter	Values after fit
$N_{D_s^+}^{(\overline{D}^0 D_s^+)}$	21520 ± 150
$F_{B^+ \to \overline{D}^{*0} D_s^+}$	0.915 ± 0.054
$F_{B^+ \to \overline{D}^0 D_s^{*+}}$	0.935 ± 0.056
$F_{B^+ \to \overline{D}^{*0} D_s^{*+}}$	1.829 ± 0.047
$F_{B^+ \to \overline{D}^0 D_{s1}(2460)^+}$	0.332 ± 0.038
$F_{B^+ \to \overline{D}^{*0} D_{s1}(2460)^+}$	0.710 ± 0.040
$F_{B^+ \mid B_s^0 \to \overline{D}^0 D_s^+ X}$	0.817 ± 0.037
$F_{B^0 \to \overline{D}^0 D_s^+ X}$	0.0990 ± 0.0092
$F_{B^0 \to D^{*-} D_s^+}$	0.1205 ± 0.0041
$F^*_{B^0 \to D^{*-} D_s^{*+}}$	1.705 ± 0.062
$F^*_{B^0 \to D^{*-} D_{s0}^*(2317)^+}$	0.146 ± 0.036
$F^*_{B^0 \to D^{*-} D_{s1}(2460)^+}$	0.398 ± 0.048

Table 6.7: Fit results. The top part is obtained from the $\overline{D}^0 D_s^+$ sub-sample (Fig. 6.17(a)) and the bottom from the $D^{*-} D_s^+$ one (Fig. 6.17(b)).

B decay	D^{**} decay mode	$\mathcal{B}$ from [1] (%)	Estimated $\mathcal{B}(\overline{B} \to D^{**}\ell^-\overline{\nu}_\ell)$ (%)	Estimated $\mathcal{B}(\overline{B} \to D^{**}\ell^-\overline{\nu}_\ell)$ [168] (%)	Estimated $\mathcal{B}(\overline{B} \to D^{**}\ell^-\overline{\nu}_\ell) \times \mathcal{B}(D^{**} \to D^0X)$ (%)	$R(D^{**})$ [168]	Estimated $\mathcal{B}(\overline{B} \to D^{**}\tau^-\overline{\nu}_\tau) \times \mathcal{B}(D^{**} \to D^0X)$ (%)
$B^- \to D_1^0\ell^-\overline{\nu}_\ell$	$D_1^0 \to D^{*+}\pi^-$	0.303 ± 0.020	0.721 ± 0.048	0.67 ± 0.05	0.55 ± 0.04	0.10 ± 0.01	0.055 ± 0.007
$B^- \to D_2^{*0}\ell^-\overline{\nu}_\ell$	$D_2^{*0} \to D^{*+}\pi^-$	0.101 ± 0.024	0.385 ± 0.044	0.30 ± 0.04	0.194 ± 0.022	0.07 ± 0.01	0.014 ± 0.002
$B^- \to D_2^{*0}\ell^-\overline{\nu}_\ell$	$D_2^{*0} \to D^+\pi^-$	0.153 ± 0.016					
$B^- \to D_1^0\ell^-\overline{\nu}_\ell$	$D_1^0 \to D^{*+}\pi^-$	0.27 ± 0.06	0.403 ± 0.090	0.20 ± 0.05	0.313 ± 0.070	0.06 ± 0.02	0.019 ± 0.008
$B^- \to D_0^{*0}\ell^-\overline{\nu}_\ell$	$D_0^{*0} \to D^+\pi^-$	0.25 ± 0.05	0.373 ± 0.075	0.44 ± 0.08	0.123 ± 0.025	0.08 ± 0.03	0.010 ± 0.004
$\overline{B}^0 \to D_1^+\ell^-\overline{\nu}_\ell$	$D_1^+ \to D^{*0}\pi^+$	0.280 ± 0.028	0.667 ± 0.067	—	0.525 ± 0.052	0.10 ± 0.01	0.052 ± 0.007
$\overline{B}^0 \to D_2^{*+}\ell^-\overline{\nu}_\ell$	$D_2^{*+} \to D^{*0}\pi^+$	0.068 ± 0.012	0.286 ± 0.053	—	0.214 ± 0.040	0.07 ± 0.01	0.015 ± 0.004
$\overline{B}^0 \to D_2^{*+}\ell^-\overline{\nu}_\ell$	$D_2^{*+} \to D^0\pi^+$	0.121 ± 0.033		—			
$\overline{B}^0 \to D_1'^+\ell^-\overline{\nu}_\ell$	$D_1'^+ \to D^{*0}\pi^+$	0.31 ± 0.09	0.463 ± 0.134	—	0.412 ± 0.120	0.06 ± 0.02	0.025 ± 0.011
$\overline{B}^0 \to D_0^{*+}\ell^-\overline{\nu}_\ell$	$D_0^{*+} \to D^0\pi^+$	0.30 ± 0.12	0.448 ± 0.179	—	0.30 ± 0.12	0.08 ± 0.03	0.024 ± 0.013
$\overline{B}_s^0 \to D_{s1}'^+\ell^-\overline{\nu}_\ell X$	$D_{s1}'^+ \to D^{*0}K^+$	0.44 ± 0.13	0.88 ± 0.26	—	0.73 ± 0.22	$0.09 \pm 0.02^*$	0.066 ± 0.024
$\overline{B}_s^0 \to D_{s2}^+\ell^-\overline{\nu}_\ell X$	$D_{s2}^+ \to D^0K^+$	0.27 ± 0.10	0.54 ± 0.20	—	0.27 ± 0.10	$0.07 \pm 0.01^*$	0.019 ± 0.008

Table 6.8: Measured branching fractions measurements of $\overline{B} \to D^{**}(\to D^{(*)}X)\ell^-\overline{\nu}_\ell$ decays and all other inputs needed to estimate $\mathcal{B}(\overline{B} \to D^{**}\tau^-\overline{\nu}_\tau) \times \mathcal{B}(D^{**} \to D^0X)$ in this work. The estimated $\mathcal{B}(B^- \to D^{**}\tau^-\overline{\nu}_\tau)$ are compared with the results from Ref. [168].

6.6.2 Excited $B \to D^{**}\tau^+\nu_\tau$ decays

Semitauonic B meson decays into highly excited charm mesons ($B \to D^{**}\tau^-\overline{\nu}_\tau$), are an important contribution to the signal sample. Hence, understanding them is a critical point of the analysis. The D^{**} meson decays strongly into a charm meson and pions or kaons, having the same topology as the signal. The branching fractions of such decays are not well known. These background contributions are estimated by taking into account previous measurements on semileptonic $B \to D^{**}\ell^-\overline{\nu}_\ell$ decays and the theoretical predictions of the LFU ratios [168]

$$R(D^{**}) = \frac{\mathcal{B}(\overline{B} \to D^{**}\tau^-\overline{\nu}_\tau)}{\mathcal{B}(\overline{B} \to D^{**}\ell^-\overline{\nu}_\ell)}. \tag{6.31}$$

The D^{**} symbol represents the D_1, D_2^*, D_0^*, D_1', D_{s1}' and D_{s2}^* mesons, where each of these refers to $D_1(2420)^+/D_1(2420)^0$, $D_2^*(2460)^+/D_2^*(2460)^0$, $D_0^*(2300)^+/D_0^*(2300)^0$, $D_1'(2430)^+/D_1'(2430)^0$, $D_{s1}'(2536)^+$ and $D_{s2}^*(2573)^+$, respectively.

The D_2^*, D_1, D_1' and D_0^* mesons decay strongly into a charm meson and pions. These decay branching fractions have been estimated using experimental measurements and isospin relations in Ref. [169]. Besides, The D_1 meson can decay through non-D^*-resonant three-body decays into $D\pi^+\pi^-$, $D\pi^0\pi^0$ and $D\pi^0\pi^+$. All this considered, the branching fractions of $B \to D^{**}\tau^-\overline{\nu}_\tau$ decays can be estimated. These results, together with the inputs considered to estimate them, are collected in Tab. 6.8.

As a crosscheck of this procedure, the total branching fractions $\mathcal{B}(B \to D^{**}\ell^-\overline{\nu}_\ell)$ are compared to the experimental measurements published in Ref. [1]. For $B^- \to D^{(*)}n\pi\ell\nu$ when $(n \geq 1)$, $\mathcal{B}_{\text{PDG}} = (1.88 \pm 0.25)$ % and the estimated value is equal to $\mathcal{B} = (1.88 \pm 0.13)$ %, both figures being in agreement. Likewise, for the $\overline{B}^0$ decay, $\mathcal{B}_{\text{PDG}} = (2.3 \pm 0.5)$ % and its estimated value $\mathcal{B} = (1.86 \pm 0.24)$ %, also in agreement within uncertainties. Once the branching fractions are estimated, the parameter $f_{D^{**}/\overline{D}^{*0}}$ which is considered in the

signal fit is defined as

$$f_{D^{**}/\overline{D}^{*0}} = \frac{\mathcal{B}(B^+\to D^{**}\tau^+\nu_\tau)\times\frac{\varepsilon_{B^+\to D^{**}}}{\varepsilon_{B^+\to\overline{D}^{*0}}}+\mathcal{B}(B^0\to D^{**}\tau^+\nu_\tau)\times\frac{f_d}{f_u}\times\frac{\varepsilon_{B^0\to D^{**}}}{\varepsilon_{B^+\to\overline{D}^{*0}}}+\mathcal{B}(B_s^0\to D^{**}\tau^+\nu_\tau)\times\frac{f_s}{f_u}\times\frac{\varepsilon_{B_s^0\to D^{**}}}{\varepsilon_{B^+\to\overline{D}^{*0}}}}{\mathcal{B}(B^+\to\overline{D}^{*0}\tau^+\nu_\tau)\times\mathcal{B}(\overline{D}^{*0}\to\overline{D}^0X)}, \tag{6.32}$$

where $\varepsilon_{B^+\to D^{**}}/\varepsilon_{B^+\to\overline{D}^{*0}}$, $\varepsilon_{B^0\to D^{**}}/\varepsilon_{B^+\to\overline{D}^{*0}}$ and $\varepsilon_{B_s^0\to D^{**}}/\varepsilon_{B^+\to\overline{D}^{*0}}$ are the relative efficiencies for $B^+\to D^{**}\tau^+\nu_\tau$, $B^0\to D^{**}\tau^+\nu_\tau$ and $B_s^0\to D^{**}\tau^+\nu_\tau$ decays with respect to signal $B^+\to\overline{D}^{*0}\tau^+\nu_\tau$ decays; f_d/f_u and f_s/f_u are the ratios of the fragmentation fractions, taken from Ref. [170], and $\mathcal{B}(\overline{D}^{*0}\to\overline{D}^0X)$ is considered to be 100%. Taking all of the above into account, a fraction of $f_{D^{**}/\overline{D}^{*0}} = 0.043$ is obtained and set as a fixed parameter in the signal fit.

6.7 The $D_s^+\to\pi^+\pi^-\pi^+(X)$ decay model

Since inclusive $B\to\overline{D}^0D_s^+(X)$ with $D_s^+\to\pi^+\pi^-\pi^+(X)$ decays are the largest background contribution to the signal sample, their description is of paramount importance. Inclusive $D_s^+\to\pi^+\pi^-\pi^+(X)$ decays have a larger branching ratio than the exclusive $D_s^+\to\pi^+\pi^-\pi^+$ decay. This difference is due to the contribution from decays involving intermediate states as η, η', K_S^0, ϕ and ω.

In the hadronic $R(D^{*-})$ analysis [53,54], the $D_s^+\to\pi^+\pi^-\pi^+(X)$ model is determined using the following method. First, a sample enriched in $B\to D^{*-}D_s^+(X)$ decays is selected by requiring the output of the BDT to be below a certain threshold. Afterwards, a simultaneous template fit to four distributions sensitive to $D_s^+\to\pi^+\pi^-\pi^+(X)$ decays is performed, namely, the minimum and the maximum of the opposite charged pions invariant mass ($m(\pi_0^+\pi_1^-)$ and $m(\pi_1^-\pi_2^+)$), the mass of the same-sign charged pions, $m(\pi_0^+\pi_2^+)$, and the mass of the 3π system, $m(3\pi)$. This model includes the D_s^+ decays contributions with an η or an η' in the final state, other D_s^+ decays and backgrounds originating from decays not involving the D_s^+. This background model was estimated to contribute to the systematic uncertainty on $R(D^{*-})$ about 2.5%. [53,54].

An innovative strategy proposed in this thesis to estimate the contribution of these modes. This is a re-weighting procedure to correct the description of D_s^+ decays exploiting the isolation algorithms (see Sec. 6.3.3) and then is validated with data. An exhaustive description of the considered D_s^+ decays is reported in Sec. 6.7.1 together with the details of the simulated sample employed in the model. A total of 9 control samples are produced following Sec. 6.7.2 and then a simultaneous fit to data is performed to obtain the said weights. The fit model is reported in Sec. 6.7.3 and the results are shown in Sec. 6.7.4.

6.7.1 The D_s^+ decay modes

The considered D_s^+ decays contributing to the $D_s^+\to\pi^+\pi^-\pi^+(X)$ background are listed in Table 6.9, together with their known branching fractions [1,171] and the values of these branching fractions used as input to the simulation. It is important to notice

that the $D_s^+ \to \eta'\pi^+\pi^-\pi^+$ and non-resonant $D_s^+ \to \pi^+\pi^-\pi^+\pi^0$ decays are not reported in the PDG [1], but have been included in the simulation production, anticipating their presence in the data.

The D_s^+ decays can be classified in different categories depending on the final state and the presence of a light intermediate state. In the following, R represents either a η, ϕ or ω meson. Taking that into account, the following final states are considered:

- **Exclusive $D_s^+ \to \pi^+\pi^-\pi^+$ decays.**

- **3-prong final states with additional neutral pions.** These decays include $D_s^+ \to R\pi^+(\pi^0)$ with $R \to \pi^+\pi^-\pi^0$, and non-resonant $D_s^+ \to \pi^+\pi^-\pi^+\pi^0$ decays.

- **5-pions final states.** These have the topology represented in Fig. 6.19 and include $D_s^+ \to R\pi^+\pi^-\pi^+(\pi^0)$ decays: $D_s^+ \to \eta'(\to \eta(\to \pi^+\pi^-\pi^0)\pi^+\pi^-)\pi^+$, $D_s^+ \to \eta'(\to \rho^0(\to \pi^+\pi^-)\gamma)\pi^+\pi^-\pi^+$, $D_s^+ \to \omega(\to \pi^+\pi^-\pi^0)\pi^+\pi^-\pi^+$, $D_s^+ \to \eta(\to \pi^+\pi^-\pi^0)$-$\pi^+\pi^-\pi^+$, $D_s^+ \to \phi(\to \pi^+\pi^-\pi^0)\pi^+\pi^-\pi^+$ and the non-resonant $D_s^+ \to \pi^+\pi^-\pi^+\pi^-\pi^+$. For the $D_s^+ \to \eta\pi^+\pi^-\pi^+$ decay, the branching fraction measurement from Ref. [171] is considered.

- **5-prong decays with kaons.** These include $D_s^+ \to \phi\pi^+\pi^-\pi^+$ decays, where $\phi \to K^+K^-$. This decay mode is modelled as phase-space in the simulation but it is known to be dominated by $D_s^+ \to \phi a_1(1260)^+$ decays, where $a_1(1260)^+ \to \rho^0\pi^+$ and $\phi \to K^+K^-$, with a branching fraction of $(0.74 \pm 0.12)\%$ [1].

- **Final states with $\eta \to \gamma\gamma$.** These include all the final states with an η decaying into two photons: $D_s^+ \to \eta'(\to \eta\pi^+\pi^-)\pi^+(\pi^0)$, $D_s^+ \to \eta'(\to \eta\pi^0\pi^0)\pi^+\pi^-\pi^+$ and $D_s^+ \to \eta\pi^+\pi^-\pi^+$.

- **Tauonic $D_s^+ \to \tau^+\nu_\tau$ decays**, with 3-prong τ decays.

- **Other D_s^+ decays.** Decays with lower branching fractions that are included in the MC simulation: $D_s^+ \to K_S^0K_S^0\pi^+\pi^-\pi^+$, $D_s^+ \to K_L^0\pi^+\pi^-\pi^-$, $D_s^+ \to K_L^0K_L^0\pi^+\pi^-\pi^-$, $D_s^+ \to K^-\pi^+\pi^-$, $D_s^+ \to \phi e^+\nu_e$, $D_s^+ \to \phi\mu^+\nu_\mu$, $D_s^+ \to \eta e^+\nu_e$, $D_s^+ \to \eta\mu^+\nu_\mu$, $D_s^+ \to \eta' e^+\nu_e$, $D_s^+ \to \eta'\mu^+\nu_\mu$, $D_s^+ \to f_0(980)e^+\nu_e$, $D_s^+ \to f_0(980)\mu^+\nu_\mu$. These decay channels are not listed in the summary of Tab. 6.9.

- **"Not D_s^+ " decays.** These are residual decays passing the selection requirements, including D^0 or D^+ decays, signal decays, prompt decays and combinatorial background.

These D_s^+ decay modes are represented in Fig. 6.18, which shows the components used in the fit model.

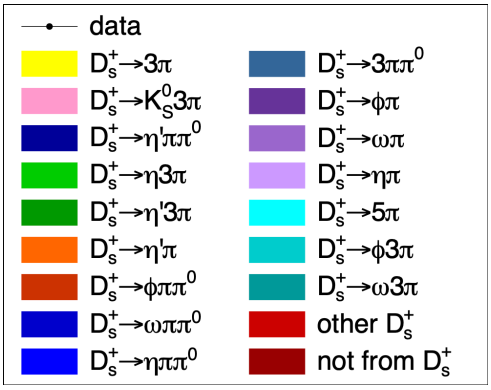

Figure 6.18: Components used in the $D_s^+ \to \pi^+\pi^-\pi^+(X)$ decay model.

D_s^+ **decay channels**	**Measured** $\mathcal{B}$ **[1]** (%)	$\mathcal{B}$ **simulation sample** (%)
$D_s^+ \to \pi^+\pi^-\pi^+$	1.09 ± 0.05	1.09
$D_s^+ \to \pi^+\pi^-\pi^+\pi^0$ non resonant	-	1.5
$D_s^+ \to \eta\pi^+$	1.70 ± 0.09	1.70
$D_s^+ \to \omega\pi^+$	0.24 ± 0.06	0.24
$D_s^+ \to \phi\pi^+$	4.5 ± 0.4	4.5
$D_s^+ \to \eta'\pi^+$	3.94 ± 0.25	3.94
$D_s^+ \to \eta\pi^+\pi^0$	9.2 ± 1.2	11.7
$D_s^+ \to \omega\pi^+\pi^0$	2.8 ± 0.7	2.8
$D_s^+ \to \phi\pi^+\pi^0$	$8.4^{+1.9}_{-2.3}$	9.2
$D_s^+ \to \eta'\pi^+\pi^0$	5.6 ± 0.8	6.9
$D_s^+ \to \pi^+\pi^-\pi^+\pi^-\pi^+$	0.80 ± 0.08	0.8
$D_s^+ \to \omega\pi^+\pi^-\pi^+$	1.6 ± 0.5	1.6
$D_s^+ \to \phi\pi^+\pi^-\pi^+$	1.21 ± 0.16	1.21
$D_s^+ \to K_S^0\pi^+\pi^-\pi^+$	0.30 ± 0.11	0.3
$D_s^+ \to \eta\pi^+\pi^-\pi^+$	$3.12 \pm 0.16^{\dagger}$	3.0
$D_s^+ \to \eta'\pi^+\pi^-\pi^+$	-	2.0
$D_s^+ \to \tau^+\nu_\tau$	5.48 ± 0.23	5.48

Table 6.9: Main D_s^+ decay modes with their corresponding branching fractions, as in the PDG [1], used in the MC simulation. The branching fraction for the $D_s^+ \to \eta\pi^+\pi^-\pi^+$ decay, noted with †, is not reported by the PDG, so the measured branching fraction was taken from the BESIII measurement in Ref. [171].

6.7.2 $D_s^+ \to \pi^+\pi^-\pi^+(X)$ control samples

In order to obtain a reliable decay model for inclusive $D_s^+ \to \pi^+\pi^-\pi^+(X)$ decays, nine samples are produced applying dedicated selections. Each sample is expected to be sensitive to, at least, one of the decay modes shown in Tab. 6.9. To produce these samples, the requirements of the signal selection are applied, with the exception of the vertex isolation and $m(\pi^+\pi^-\pi^+)$ requirements. Besides, in order to enrich the sample with D_s^+ decays, only events in the q^2 range $[3, 6.5]$ GeV$^2/c^4$ are considered. This requirement suppresses $B \to \overline{D}^0 D^0(X)$ and $B \to \overline{D}^0 D^+(X)$ decays, which are located in the high q^2 region. Regarding the simulation, this is produced with the branching fractions shown in Tab. 6.9.

To produce control samples with additional charged tracks, the isolation tools described in Sec. 6.3.3.1 are employed. Only tracks with $\chi^2_{\rm IP}({\rm PV}) > 4$ and $p_{\rm T} > 250$ GeV/c are considered. As an example, the topology of a D_s^+ decay with two additional charged tracks is shown in Fig. 6.19(a). In addition to the `TupleToolVtxIsolnPlus` tool [163], the output of the `TupleToolIsoKS` algorithm, specially developed for this study, is used to include additional $K^0_{\rm S}$ mesons, reconstructed using the $K^0_{\rm S} \to \pi^+\pi^-$ mode.

Neutral particles in the final state are accounted for with the tools introduced in Sec. 6.3.3.2. Neutral pions and η mesons are reconstructed using the $\gamma\gamma$ final state. Since the highly-energetic proton-proton collision produce many of these mesons, at least that otherwise stated, the π^0 and η candidates with the highest p_T in the event are selected. Also, the π^0 mass is required to lie in the $|m(\gamma\gamma) - m(\pi^0)_{\rm PDG}| < 15$ GeV/c^2 range with a confidence level CL > 0.2. The η invariant mass is required to lie in the $|m(\gamma\gamma) - m(\eta)_{\rm PDG}| < 30$ GeV/c^2 range with a confidence level CL > 0.2. The topology of a D_s^+ meson decay with an additional π^0 is shown in Fig. 6.19(b).

The nine control samples produced for the D_s^+ model fit are the following:

I. **Exclusive $\boldsymbol{D_s^+ \to \pi^+\pi^-\pi^-}$ decays**. These are selected by applying the same isolation requirements as in the signal selection. The $m(\pi^+\pi^-\pi^+)$ distribution in the $[1.9, 2.0]$ GeV/c^2 range is used.

II. **$\boldsymbol{D_s^+ \to \pi^+\pi^-\pi^+\pi^-\pi^+(X)}$ decays**. A control sample with two extra opposite-sign charged pions pointing to the 3π vertex is produced (see Fig. 6.19(a)). The $m(\pi^+\pi^-\pi^+\pi^-\pi^+)$ mass distribution is used in the $[1.6, 2.1]$ GeV/c^2 range. This control sample is most sensitive to $D_s^+ \to \pi^+\pi^-\pi^+\pi^-\pi^+$, $D_s^+ \to \eta(\to \pi^+\pi^-\pi^0)\pi^+\pi^-\pi^+$, $D_s^+ \to \eta'(\to \eta(\to \pi^+\pi^-\pi^0)\pi^+\pi^-)\pi^+$ and $D_s^+ \to \omega(\to \pi^+\pi^-\pi^0)\pi^+\pi^-\pi^+$ decays.

III. **$\boldsymbol{D_s^+ \to K^+K^-\pi^+\pi^-\pi^+}$ decays**. To control these decays, two opposite-sign charged kaons are added to the 3π vertex. The characteristic variable of this sample is the $m(K^+K^-\pi^+\pi^-\pi^+)$ mass in the $[1.9, 2.0]$ GeV/c^2 range. This samples selects pure $D_s^+ \to \phi(\to K^+K^-)\pi^+\pi^-\pi^+$ decays.

IV. **$\boldsymbol{D_s^+ \to \eta'\pi^+\pi^-\pi^+}$ decays**. This control sample is produced by adding to the 3π vertex, two opposite-sign charged pions and a η meson decaying into two photons.

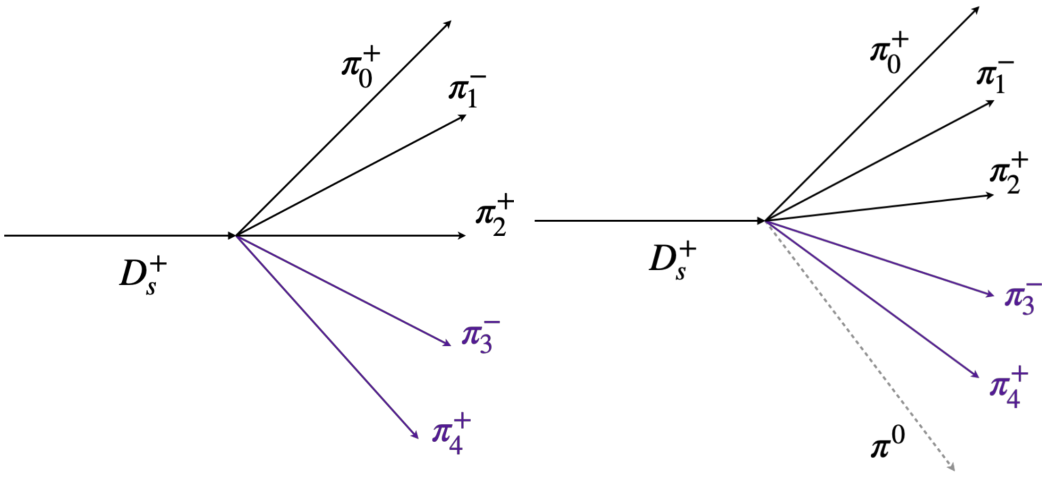

(a) (b)

Figure 6.19: Topology of the $D_s^+ \to \pi^+\pi^-\pi^+\pi^-\pi^+$ (left) and $D_s^+ \to \pi^+\pi^-\pi^+\pi^-\pi^+\pi^0$ (right) decays.

The $m(5\pi\eta)$ distribution in the $[1.6, 2.2]$ GeV/c^2 range is used. The $\eta \to \gamma\gamma$ candidate is selected in a 0.50 cone around the 3π direction. In order to enrich the sample in $D_s^+ \to \eta'(\to \eta\pi^+\pi^-)\pi^+\pi^-\pi^+$ decays, which have never been observed, the minimum of the opposite charged pion mass $\min[m(\pi^+\pi^-)]$ is required to be around the η' known mass.

V. $\boldsymbol{D_s^+ \to K_S^0\pi^+\pi^-\pi^+}$ **decays**. A sample is produced by attaching a $K_S^0 \to \pi^+\pi^-$ to the 3π vertex. The $m(K_S^0\pi^+\pi^-\pi^+)$ mass is used and must be in the $[1.92, 2.0]$ GeV/c^2 range. The two pions from the K_S^0 decay must have an invariant mass in the range $|m(\pi^+\pi^-) - m_{\rm PDG}(K_S^0)| < 30$ MeV/c^2. This sample is sensitive to $D_s^+ \to K_S^0\pi^+\pi^-\pi^+$ decays.

VI. $\boldsymbol{D_s^+ \to \eta\pi^+(\pi^0)}$ **decays**. The η meson is reconstructed in its $\pi^+\pi^-\pi^0$ mode by attaching a π^0 to the 3π vertex. Its invariant mass is required to be in a window around the η known mass. The variable used is $m((\pi^+\pi^-\pi^0)_\eta\pi^+)$, where the sub-index η indicates the reconstructed η decay. This sample is sensitive to $D_s^+ \to \eta(\to \pi^+\pi^-\pi^0)\pi^+$ and $D_s^+ \to \eta(\to \pi^+\pi^-\pi^0)\pi^+\pi^0$ decays.

VII. **Exclusive** $\boldsymbol{D_s^+ \to \pi^+\pi^-\pi^+\pi^0}$ **decays**. This sample is created attaching a π^0 to the 3π vertex. The invariant mass $m(\pi^+\pi^-\pi^+\pi^0)$ is required to lie in a ± 30 MeV/c^2 window around the D_s^+ known mass, such that only exclusive $D_s^+ \to \pi^+\pi^-\pi^+\pi^0$ decays are selected. The variable used for this sample is the minimum of the $m(\pi_0^+\pi_1^-\pi^0)$ and $m(\pi_2^+\pi_1^-\pi^0)$ masses, represented as $\min[m(\pi_p^+ i^-\pi^0)]$. This control sample is sensitive to $D_s^+ \to \eta(\to \pi^+\pi^-\pi^0)\pi^+$, $D_s^+ \to \omega(\to \pi^+\pi^-\pi^0)\pi^+$,

$D_s^+ \to \phi(\to \pi^+\pi^-\pi^0)\pi^+$ and non-resonant $D_s^+ \to \pi^+\pi^-\pi^+\pi^0$ decays. Here, non-resonant indicates that the $\pi^+\pi^-\pi^0$ system does not form any intermediate state.

VIII. $\boldsymbol{D_s^+ \to \eta\pi^+\pi^-\pi^+}$ **decays**. The sample is produced attaching a $\eta \to \gamma\gamma$ to the 3π vertex. In order to select exclusive $D_s^+ \to \eta\pi^+\pi^-\pi^+$ decays, a veto on $\min[m(\eta\pi^+\pi^-)]$ is applied such that $\eta' \to \eta\pi^+\pi^-$ decays are suppressed. The variable used for this sample is $m(\eta\pi^+\pi^-\pi^+)$, in the range $[1.9, 2.05]$ GeV/c^2. Therefore, this sample is sensitive to $D_s^+ \to \eta(\to \gamma\gamma)\pi^+\pi^-\pi^+$ decays.

IX. $\boldsymbol{D_s^+ \to \eta'\pi^+(\pi^0)}$ **decays**. A $\eta \to \gamma\gamma$ candidate is attached to the 3π vertex. Contrarily to the previous sample, $\min[m(\eta\pi^+\pi^-)]$ is required to lie around the η' known mass, specifically in $[0.9, 1.01]$ GeV/c^2 range. The variable used is $m((\eta\pi^+\pi^-)_{\eta'}\pi^+)$. This control sample is sensitive to $D_s^+ \to \eta'(\to \eta(\to \gamma\gamma)\pi^+\pi^-)\pi^+$ and $D_s^+ \to \eta'(\to \eta(\to \gamma\gamma)\pi^+\pi^-)\pi^+\pi^0$ decays.

All this considered, this model is sensitive to most of the $D_s^+ \to \pi^+\pi^-\pi^+(X)$ decay modes, except the $D_s^+ \to \tau^+\nu_\tau$, $D_s^+ \to \omega\pi^+\pi^0$ and $D_s^+ \to \phi\pi^+\pi^0$ channels. In Tab. 6.10 the selection for all control samples and the decay modes which they are sensitive to are summarised.

6.7.2.1 Resonant structure corrections to phase-space simulation

For the $D_s^+ \to \eta 3\pi$ and $D_s^+ \to \phi 3\pi$ decays, some variables, known to be sensitive to resonant contributions, are investigated and a correction procedure is implemented. These are $m(3\pi)$, $\min[m(\pi^+\pi^-)]$, $\max[m(\pi^+\pi^-)]$ and $m(K^+K^-)$ (the latter only for the $\phi \to K^+K^-$ decay). Hence, it is possible to account for the presence of resonant contributions in these decays, which are originally simulated as pure phase-space. The $D_s^+ \to \eta 3\pi$ and $D_s^+ \to \phi 3\pi$ decays are re-weighted to account for $D_s^+ \to \eta\rho^0\pi^+$ and $D_s^+ \to \phi a_1^+(\to \rho^0\pi^+)$, respectively.

In Fig. 6.20, the mass of the 3π system is represented when selecting $D_s^+ \to \phi 3\pi$ events (control sample III). Before the correction (Fig. 6.20(a)) a peaking structure not included by the simulation is visible. This is due to $D_s^+ \to a_1(1260)^+\phi$ decays. After the re-weighting, in the right side of Fig. 6.20, the simulation describes better the data. Similar results are observed also in Fig. 6.21. The distributions for $\min[m(\pi^+\pi^-)]$, $\max[m(\pi^+\pi^-)]$ and $m(K^+K^-)$ before and after the correction are shown in Figs. 6.21(a), 6.21(b) and 6.21(c), respectively.

An analogous procedure is applied to $D_s^+ \to \eta 3\pi$ decays to account for resonant contributions. In Fig. 6.22, the $m(\pi^+\pi^-)$ distribution is shown. A peaking structure centred around around the ρ^0 known mass (~ 770 MeV/c^2) is visible in data, and not reproduced by the simulation before the correction (left). After the re-weighting to $D_s^+ \to \eta\rho^0\pi^+$, the agreement between simulation and data improves, as seen in Fig. 6.22(b).

Control sample	D_s^+ decay modes	Selection requirements and discriminating variable
I. $\boldsymbol{D_s^+ \to \pi^+\pi^-\pi^+}$	$D_s^+ \to \pi^+\pi^-\pi^+$	$\lvert m(\pi^+\pi^-\pi^+) - m_{\rm PDG}(D_s^+)\rvert < 30$ MeV/c^2. No additional tracks pointing to the 3π or B vertices. Variable used: m($\pi^+\pi^-\pi^+$).
II. $\boldsymbol{D_s^+ \to \pi^+\pi^-\pi^+\pi^-\pi^+(X)}$	$D_s^+ \to \pi^+\pi^-\pi^+\pi^-\pi^+$ $D_s^+ \to \omega(\to \pi^+\pi^-\pi^0)\pi^+\pi^-\pi^+$ $D_s^+ \to \eta\pi^+\pi^-\pi^+$ $\hookrightarrow (\pi^+\pi^-\pi^0)$ $D_s^+ \to \eta'\pi^+$ $\hookrightarrow \eta(\to \pi^+\pi^-\pi^0)\pi^+\pi^-$	$1.6 < m(\pi^+\pi^-\pi^+\pi^-\pi^+) < 2.1$ GeV/c^2. Two additional opposite-charged pions pointing to the 3π vertex. Variable used: $m(\pi^+\pi^-\pi^+\pi^-\pi^+)$.
III. $\boldsymbol{D_s^+ \to K^+K^-\pi^+\pi^-\pi^+}$	$D_s^+ \to \phi(\to K^+K^-)\pi^+\pi^-\pi^+$	PIDK extra tracks > 5. Two additional opposite-charged kaons pointing to the 3π vertex. Variable used: $m(K^+K^-\pi^+\pi^-\pi)$.
IV. $\boldsymbol{D_s^+ \to \eta'\pi^+\pi^-\pi^+}$	$D_s^+ \to \eta'\pi^+\pi^-\pi^+$ $\hookrightarrow \eta(\to \gamma\gamma)\pi^+\pi^-$	$\lvert\min[m(\eta\pi^+\pi^-)] - m_{\rm PDG}(\eta')\rvert < 50$ MeV/c^2. Two additional opposite-charge pions pointing to the 3π vertex. One $\eta \to \gamma\gamma$ in a cone of 0.5 around the 3π direction. Variable used: $m(\pi^+\pi^-\pi^+\pi^-\pi^+\eta)$.
V. $\boldsymbol{D_s^+ \to K_S^0\pi^+\pi^-\pi^+}$	$D_s^+ \to K_S^0\pi^+\pi^-\pi^+$	$\lvert m(\pi^+\pi^-) - m_{\rm PDG}(K_S^0)\rvert < 30$ MeV/c^2; $1.92 < m(K_S^0\pi^+\pi^-\pi^+) < 2.0$ GeV/c^2; An additional $K_S^0 \to \pi^+\pi^-$ pointing to the 3π vertex. Variable used: $m(K_S^0\pi^+\pi^-\pi^+)$.
VI. $\boldsymbol{D_s^+ \to \eta\pi^+(\pi^0)}$	$D_s^+ \to \eta(\to \pi^+\pi^-\pi^0)\pi^+$ $D_s^+ \to \eta(\to \pi^+\pi^-\pi^0)\pi^+\pi^0$	$\lvert\min[m(\pi^+\pi^-\pi^0)] - m_{\rm PDG}(\eta)\rvert < 50$ MeV/c^2; No additional tracks pointing to the 3π or B vertices. Additional π^0 with the highest $p_{\rm T}$ in the event. Variable used: $m((\pi^+\pi^-\pi^0)_\eta\pi^0)$.
VII. $\boldsymbol{D_s^+ \to \pi^+\pi^-\pi^+\pi^0}$	$D_s^+ \to \pi^+\pi^-\pi^+\pi^0$ $D_s^+ \to \eta(\to \pi^+\pi^-\pi^0)\pi^+$ $D_s^+ \to \omega(\to \pi^+\pi^-\pi^0)\pi^+$ $D_s^+ \to \phi(\to \pi^+\pi^-\pi^0)\pi^+$	$\lvert m(\pi^+\pi^-\pi^+\pi^0) - m_{\rm PDG}(D_s^+)\rvert < 30$ MeV/c^2. No additional tracks pointing to the 3π or B vertices. Additional π^0 with the highest $p_{\rm T}$ in the event. Variable used: $\min[m(\pi^+\pi^-\pi^0)]$.
VIII. $\boldsymbol{D_s^+ \to \eta\pi^+\pi^-\pi^+}$	$D_s^+ \to \eta(\to \gamma\gamma)\pi^+\pi^-\pi^+$	$\lvert m(\eta\pi^+\pi^-) - m(\eta')\rvert > 50$ MeV/c^2; $1.9 < m(\eta 3\pi) < 2.05$ GeV/c^2; An additional $\eta \to \gamma\gamma$ is included using the two photons with highest $p_{\rm T}$ with $\lvert m(\gamma\gamma) - m_{\rm PDG}(\eta)\rvert < 30$ MeV/c^2. No additional tracks pointing to the 3π or B vertices. Variable used: $m(\eta\pi^+\pi^-\pi^+)$.
IX. $\boldsymbol{D_s^+ \to \eta'\pi^+(\pi^0)}$	$D_s^+ \to \eta'\pi^+$ $\hookrightarrow \eta(\to \gamma\gamma)\pi^+\pi^-$ $D_s^+ \to \eta'\pi^+\pi^0$ $\hookrightarrow \eta(\to \gamma\gamma)\pi^+\pi^-$	$\lvert m(\eta\pi^+\pi^-) - m_{\rm PDG}(\eta')\rvert < 30$ MeV/c^2. An additional $\eta \to \gamma\gamma$ is included using the two photons with $\lvert m(\gamma\gamma) - m_{\rm PDG}(\eta)\rvert < 30$ MeV/c^2. No additional tracks pointing to the 3π or B vertices. Variable used: $m((\eta\pi^+\pi^-)_{\eta'}\pi^+)$.

Table 6.10: D_s^+ control samples selection requirements.

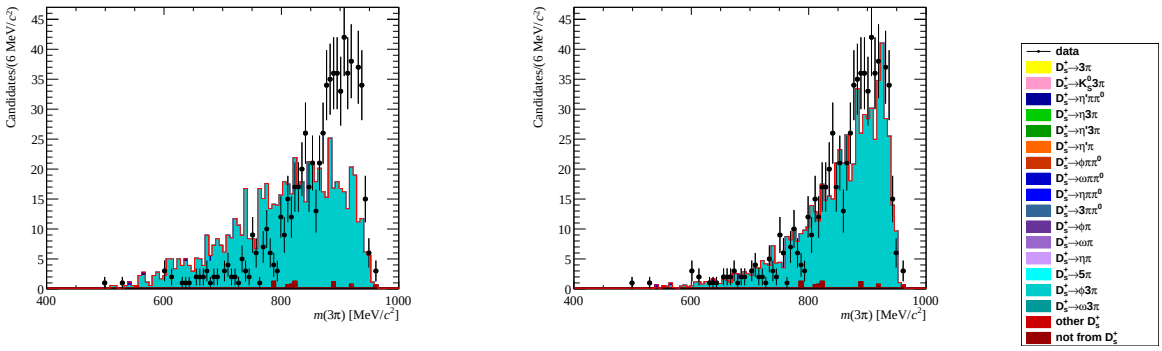

(a) (b)

Figure 6.20: $m(3\pi)$ distribution selecting two kaons in the final state (control sample **III**) before (left) and after (right) the correction procedure. Black points represent the data and $D_s^+ \to \phi(\to K^+K^-)3\pi$ mode is shown light blue.

6.7.3 Fit model

Each D_s^+ control sample can be described by the product of the probability density function for a D_s^+ decay and its yield summed over the considered decays:

$$\sum_{j \in D_s^+ \text{ decays}} N_j^{(K)} \times \mathcal{P}_j^{(K)}(x^{(K)}) \,, \tag{6.33}$$

where the super-index K indicates the control sample, the sub-index j indicates the D_s^+ decay mode and $x^{(K)}$ is the variable used to describe each sample.

The yields can be parameterised as a function of the $D_s^+ \to \pi^+\pi^-\pi^+$ yield observed in the $D_s^+ \to \pi^+\pi^-\pi^+$ control sample (sample I) corrected by the relative efficiencies:

$$N_j^{(K)} = \left(\frac{\varepsilon_j^{(K)}}{\varepsilon_{D_s^+ \to 3\pi}^{(\mathrm{I})}} \right) \times \left(\frac{\mathcal{B}_j}{\mathcal{B}(D_s^+ \to 3\pi)_{\mathrm{PDG}}} \right) \times N_{D_s^+ \to 3\pi}^{(\mathrm{I})}, \tag{6.34}$$

being $\mathcal{B}(D_s^+ \to 3\pi)_{\mathrm{PDG}}$ the $D_s^+ \to \pi^+\pi^-\pi^+$ known branching fraction and $\mathcal{B}_j$ the branching fraction of the decay j to be determined in this study. This branching fraction can be further parameterised as a function of the branching fraction used to generate the simulation, $\mathcal{B}_j^{(\mathrm{sim})}$,

$$\mathcal{B}_j = w_j \times \mathcal{B}_j^{(\mathrm{sim})}, \tag{6.35}$$

such that, finally, for the control sample (K), the model is given by

$$f^{(K)} = \sum_{j \in D_s^+ \text{ decays}} w_j \times \left(\frac{\varepsilon_j^{(K)}}{\varepsilon_{D_s^+ \to 3\pi}^{(\mathrm{I})}} \right) \times \left(\frac{\mathcal{B}_j^{(\mathrm{sim})}}{\mathcal{B}(D_s^+ \to 3\pi)_{\mathrm{PDG}}} \right) \times N_{D_s^+ \to 3\pi}^{(\mathrm{I})} \times \mathcal{P}_j^{(K)}(x^{(K)}) \,. \tag{6.36}$$

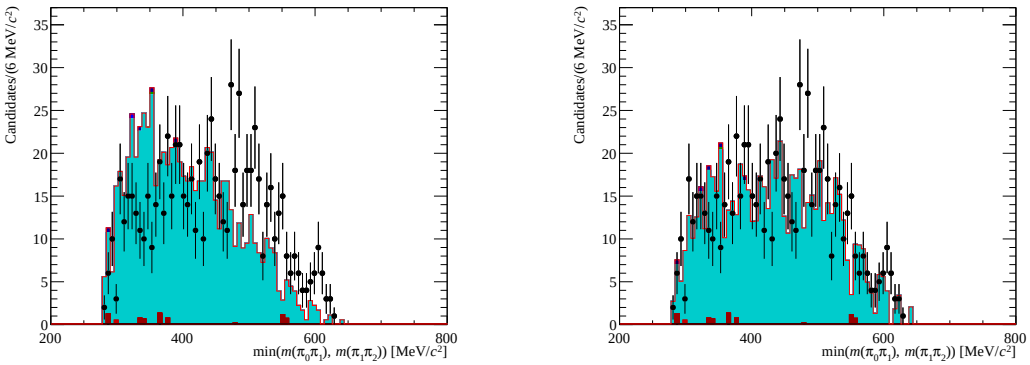

(a) min$[m(\pi^+\pi^-)]$ distribution

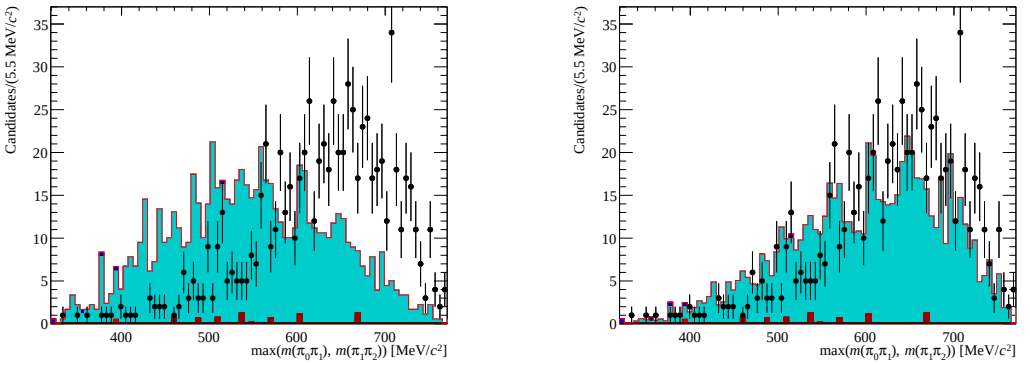

(b) max$[m(\pi^+\pi^-)]$ distribution

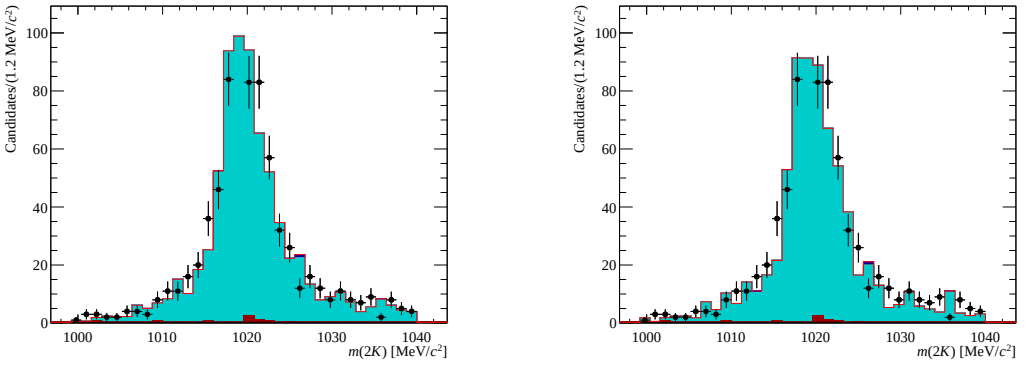

(c) $m(K^+K^-)$ distribution

Figure 6.21: Distributions of min$[m(\pi^+\pi^-)]$ (top) max$[m(\pi^+\pi^-)]$ (middle) and $m(K^+K^-)$ (bottom) when selecting two additional kaons in the final state before (left) and after (right) the re-weighting procedure. Black points represent the data and $D_s^+ \to \phi(\to K^+K^-)3\pi$ mode is shown light blue.

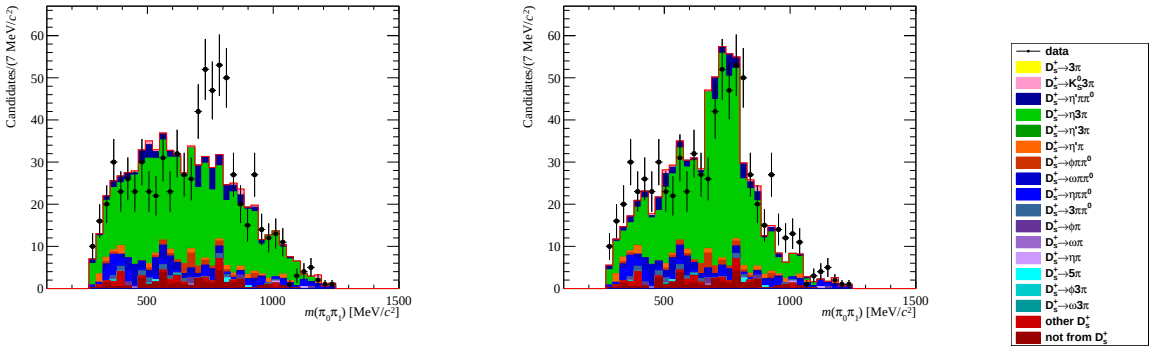

(a) (b)

Figure 6.22: $m(\pi^+\pi^-)$ distribution selecting η outside the η' mass range before (left) and after (right) the re-weighting procedure. Black points are the data and the $D_s^+ \to \eta(\to \gamma\gamma)3\pi$ contribution is shown in green.

At this point, a simultaneous fit to the nine control samples is performed. The weights w_j are the free parameters, with the exception of the modes to which the model is not sensitive: $D_s^+ \to \tau^+\nu_\tau$, $D_s^+ \to \omega\pi^+\pi^0$ and $D_s^+ \to \phi\pi^+\pi^0$. These decays weights are fixed in the fit taking into account their known branching fractions as

$$w_j^{\text{fixed}} = \frac{\mathcal{B}_j^{(\text{PDG})}}{\mathcal{B}_j^{(\text{sim})}} \,. \tag{6.37}$$

The D_s^+ decays accounted for the fit are the ones previously described in Sec. 6.7.1 and collected in Fig. 6.18. The "other D_s^+ " channel includes $D_s^+ \to K^+\pi^-\pi^+$ and other possible D_s^+ decays not included in the previous categories. Finally, the "not from D_s^+ " component accounts for all the contributions due to residual D^+, D^0, signal decays, prompt decays (decays where the pions are produced at the B vertex) and combinatorial background that passed the control samples selection. The weight of the "not from D_s^+ " component is also fixed in the fit.

6.7.4 D_s^+ decay model results

The weights returned by the fit are collected in Tab. 6.11 and Fig. 6.23. The fit projections for each sample are represented in Figs. 6.24 and 6.25.

Using the weights returned by the fit it is possible to provide a measurement of the branching fractions with respect to a reference mode, the exclusive $D_s^+ \to \pi^+\pi^-\pi^+$ decay. Following Eq. (6.35), the relative branching fractions are

$$\frac{\mathcal{B}_j}{\mathcal{B}(D_s^+ \to 3\pi^+)} = \frac{w_j \times \mathcal{B}_j^{(\text{sim})}}{w_{D_s^+\to 3\pi} \times \mathcal{B}_{D_s^+\to 3\pi}^{(\text{sim})}}, \tag{6.38}$$

D_s^+ **decay mode**	**Weight value**
$D_s^+ \to \pi^+\pi^-\pi^+$	1.004 ± 0.008
$D_s^+ \to \pi^+\pi^-\pi^+\pi^0$ non resonant	0.99 ± 0.07
$D_s^+ \to \eta\pi^+$	0.78 ± 0.04
$D_s^+ \to \omega\pi^+$	0.7 ± 0.1
$D_s^+ \to \phi\pi^+$	0.73 ± 0.06
$D_s^+ \to \eta'\pi^+$	0.86 ± 0.05
$D_s^+ \to \eta\pi^+\pi^0$	0.96 ± 0.05
$D_s^+ \to \eta'\pi^+\pi^0$	0.93 ± 0.06
$D_s^+ \to 5\pi$	0.90 ± 0.02
$D_s^+ \to \omega 3\pi$	0.66 ± 0.04
$D_s^+ \to \phi 3\pi$	0.95 ± 0.04
$D_s^+ \to \eta 3\pi$	1.06 ± 0.04
$D_s^+ \to K_S^0 3\pi$	0.79 ± 0.05
$D_s^+ \to \eta' 3\pi$	0.25 ± 0.04
$D_s^+ \to \omega\pi^+\pi^0$	1
$D_s^+ \to \phi\pi^+\pi^0$	0.9
$D_s^+ \to \tau^+\nu_\tau$	1

Table 6.11: Weights obtained from the $D_s^+ \to \pi^+\pi^-\pi^+(X)$ decay model fit. The constant parameters of the fit, the weights for $D_s^+ \to \omega\pi^+\pi^0$, $D_s^+ \to \phi\pi^+\pi^0$ and $D_s^+ \to \tau^+\nu_\tau$ modes, are set to the ratio of the $\mathcal{B}$ used in the simulation and the value from the PDG.

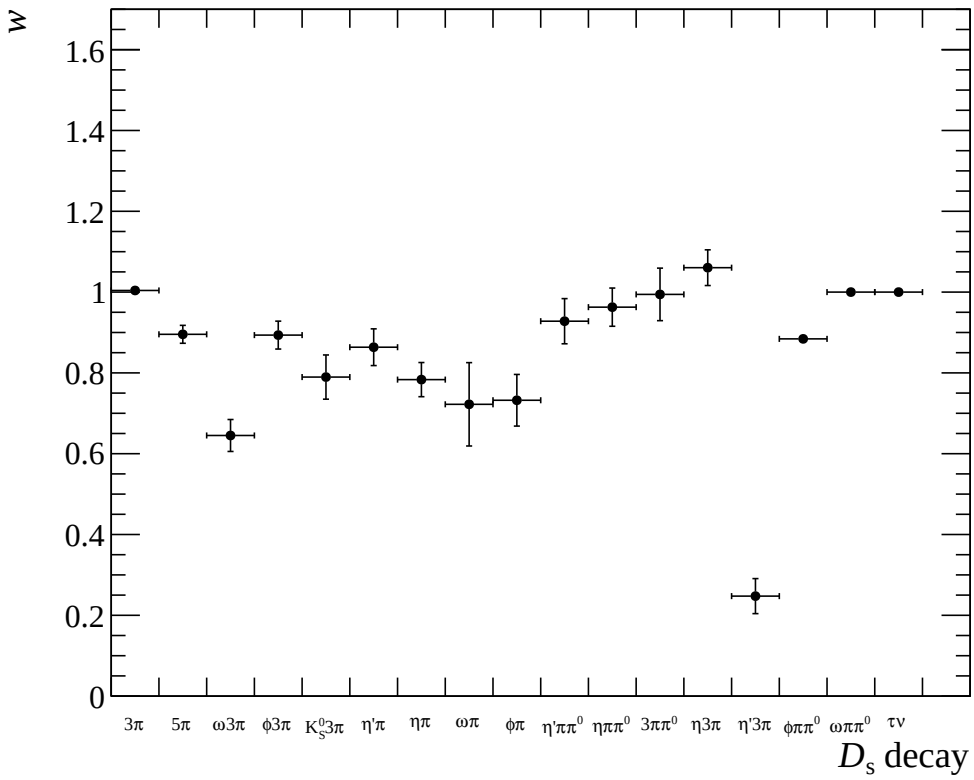

Figure 6.23: Values of the weights for each component in the D_s^+ decay model returned by a simultaneous fit to the control samples. Note that the values of $w_{D_s^+\to\tau^+\nu_\tau}$, $w_{D_s^+\to\omega\pi^+\pi^0}$, $w_{D_s^+\to\phi\pi^+\pi^0}$ and $w_{D_s^+\to\ell^+\nu_\ell}$ are fixed in the fit according to their known branching fractions.

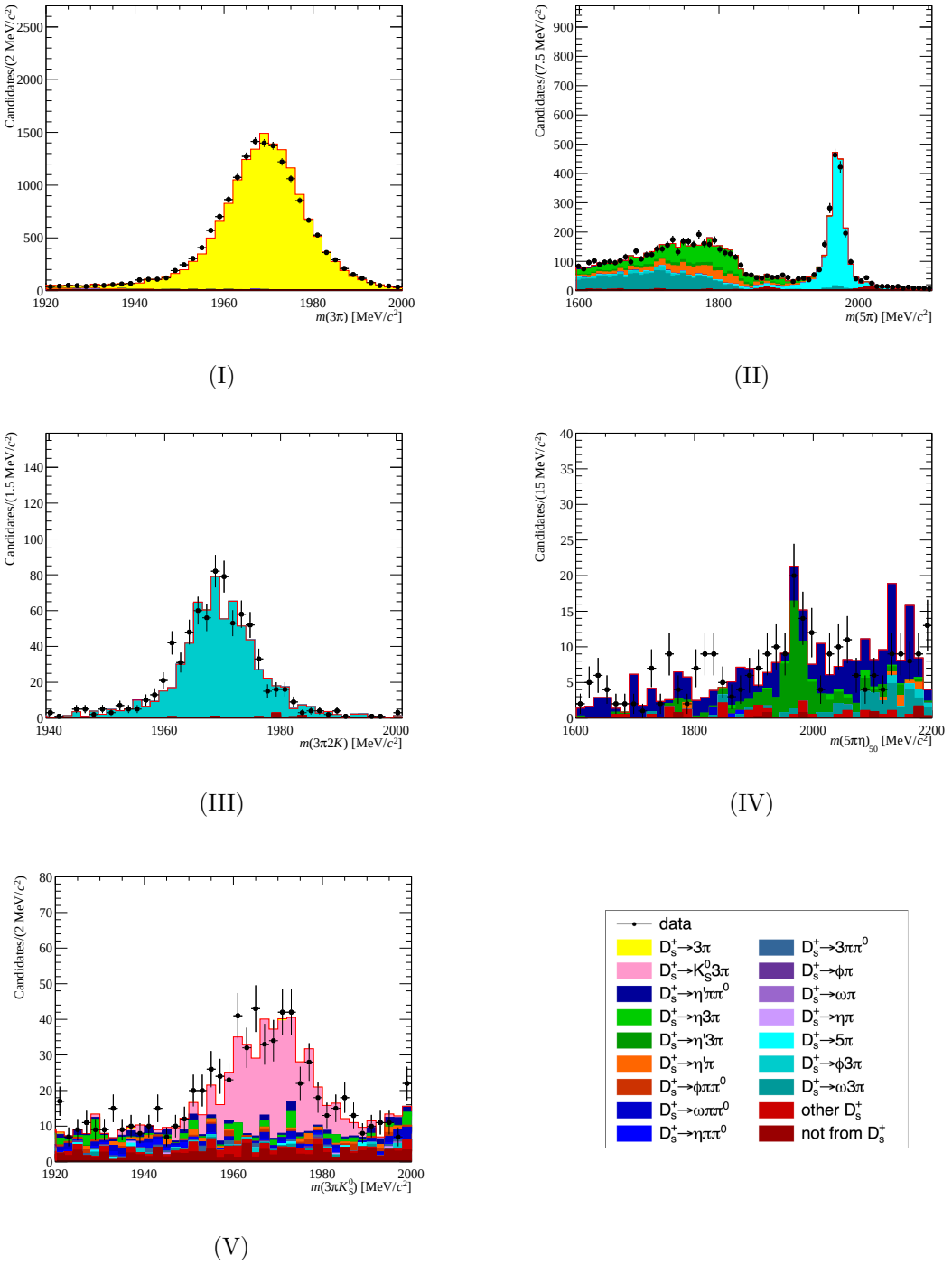

Figure 6.24: Control samples projections after the $D_s^+ \to \pi^+\pi^-\pi^+(X)$ fit. Top row (from left to right): $m(\pi^+\pi^-\pi^+)$, for exclusive $D_s^+ \to \pi^+\pi^-\pi^+$ events, and $m(\pi^+\pi^-\pi^+\pi^-\pi^-)$ distributions, Middle row: $m(K^+K^-\pi^+\pi^-\pi^-)$ distribution (left) and $m(5\pi\eta)$ distribution, with $\eta \to \gamma\gamma$. Bottom row $m(K^0_S(\to \pi^+\pi^-)\pi^+\pi^-\pi^+)$ distribution and legend.

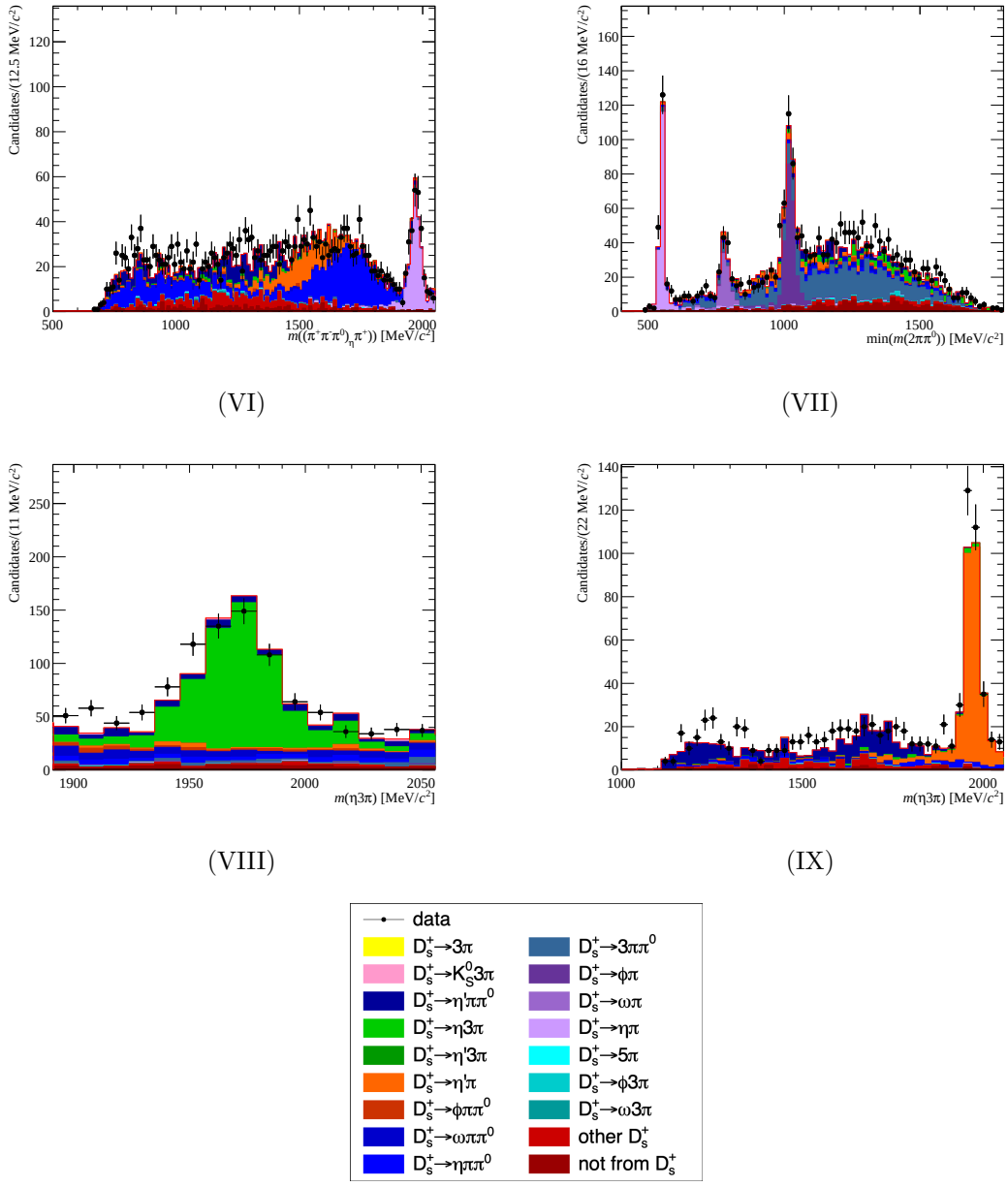

Figure 6.25: Top row: $m\left((\pi^+\pi^-\pi^0)_\eta\pi^+(\pi^0)\right)$ for inclusive $D_s^+ \to \eta\pi^+(X)$ decays; and $\min[m(\pi^+\pi^-\pi^0)]$ for $D_s^+ \to \pi^+\pi^-\pi^+\pi^0$ decays control samples after the D_s^+ decay model fit. Middle row : $m(\eta\pi^+\pi^-\pi^+)$ distribution after fit when selecting events outside (left) and inside (right) the η' mass range.

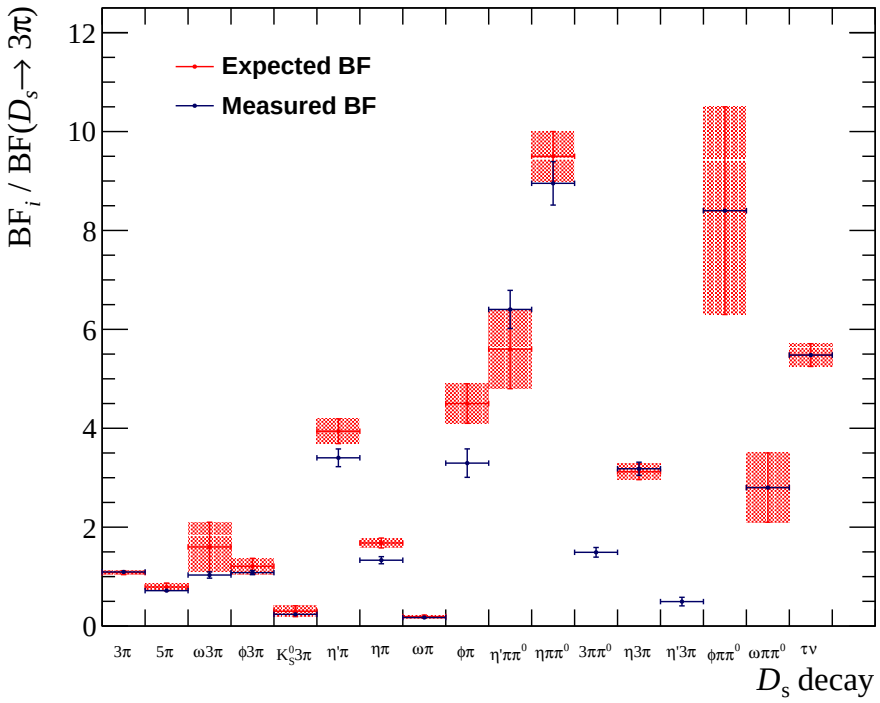

Figure 6.26: Branching fractions measured relative to the $D_s^+ \to \pi^+\pi^-\pi^+$ mode as obtained by the D_s^+ model (blue) and from Refs. [1, 171] (red).

where the branching fractions with the super-index (sim) correspond to the values used to generate the simulated events (see Tab. 6.9). The branching fractions relative to the exclusive $D_s^+ \to \pi^+\pi^-\pi^+$ mode are shown in Tab. 6.12. Figure 6.26 shows the comparison between the measured relative branching fractions and the same values from previous measurements, shown in Tab. 6.9 [1, 171]. Note that the branching fractions of $D_s^+ \to \eta'\pi^+\pi^-\pi^+$ and the non-resonant $D_s^+ \to \pi^+\pi^-\pi^+\pi^0$ decays are not reported since they have not been observed before.

It can be concluded that, in general, the relative branching fractions obtained in this study are in agreement with the PDG values within uncertainties. Moreover, using the relative branching fractions, this model can be used also to produce new simulation samples and for other semitauonic decays studies using 3-prong τ decays.

Employing the results from the $D_s^+ \to \pi^+\pi^-\pi^+(X)$ model and the other background models described in Sec. 6.6, the simulation is corrected. Therefore it is possible to obtain the signal and normalisation yields, their efficiencies and, eventually, the $\mathcal{K}(D^{(*)0})$ result.

D_s^+ decay mode	$\frac{\mathcal{B}_j}{\mathcal{B}(D_s^+\to\pi^+\pi^-\pi^+)}$	$\frac{\mathcal{B}_{\rm PDG,j}}{\mathcal{B}_{\rm PDG}(D_s^+\to\pi^+\pi^-\pi^+)}$	Pull
$D_s^+ \to \pi^+\pi^-\pi^+$	1	1	–
$D_s^+ \to \pi^+\pi^-\pi^+\pi^0$ non resonant	1.4 ± 0.09	–	–
$D_s^+ \to \eta\pi^+$	1.22 ± 0.07	1.54 ± 0.12	-2.3
$D_s^+ \to \omega\pi^+$	0.16 ± 0.02	0.18 ± 0.03	-0.55
$D_s^+ \to \phi\pi^+$	3.0 ± 0.3	4.13 ± 0.41	-2.2
$D_s^+ \to \eta'\pi^+$	3.1 ± 0.2	3.6 ± 0.3	-1.4
$D_s^+ \to \eta\pi^+\pi^0$	8.2 ± 0.4	8.7 ± 0.6	-0.7
$D_s^+ \to \eta'\pi^+\pi^0$	5.9 ± 0.4	5.1 ± 0.8	0.89
$D_s^+ \to 5\pi$	0.65 ± 0.02	0.72 ± 0.08	-0.9
$D_s^+ \to \omega 3\pi$	0.94 ± 0.06	1.5 ± 0.5	-1.1
$D_s^+ \to \phi 3\pi$	0.99 ± 0.04	1.10 ± 0.16	-0.67
$D_s^+ \to \eta 3\pi$	2.9 ± 0.1	2.8 ± 0.2	0.4
$D_s^+ \to K_S^0 3\pi$	0.22 ± 0.02	0.28 ± 0.10	-0.58
$D_s^+ \to \eta' 3\pi$	0.45 ± 0.08	–	–

Table 6.12: Relative branching fractions from the $D_s^+ \to \pi^+\pi^-\pi^+(X)$ model relative to the $D_s^+ \to \pi^+\pi^-\pi^+$ mode determined by the fit and compared with the values from the PDG. The pulls are also indicated.

Decay mode	Generation MU/MD	Filtering (%)	Selection (%)	Total ($\times 10^{-5}$)
$B^+ \to \overline{D}^0\tau^+\nu_\tau$, $\tau^+ \to \pi^+\pi^-\pi^+\overline{\nu}_\tau$	$0.04178 \pm 0.00011/0.04186 \pm 0.00011$	5.0063 ± 0.0034	4.648 ± 0.015	9.73 ± 0.04
$B^+ \to \overline{D}^0\tau^+\nu_\tau$, $\tau^+ \to \pi^+\pi^-\pi^+\pi^0\overline{\nu}_\tau$	$0.037156 \pm 0.000099/0.037107 \pm 0.000097$	4.936 ± 0.004	2.093 ± 0.012	3.837 ± 0.023
$B^+ \to \overline{D}^{*0}\tau^+\nu_\tau$, $\tau^+ \to \pi^+\pi^-\pi^+\overline{\nu}_\tau$	$0.04004 \pm 0.00010/0.04032 \pm 0.00011$	4.9301 ± 0.0034	4.240 ± 0.014	8.398 ± 0.033
$B^+ \to \overline{D}^{*0}\tau^+\nu_\tau$, $\tau^+ \to \pi^+\pi^-\pi^+\pi^0\overline{\nu}_\tau$	$0.036045 \pm 0.000096/0.036071 \pm 0.000096$	4.881 ± 0.004	1.775 ± 0.011	3.123 ± 0.020
$B^0 \to D^{*-}\tau^+\nu_\tau$, $\tau^+ \to \pi^+\pi^-\pi^+\overline{\nu}_\tau$	$0.1601 \pm 0.0022/0.1592 \pm 0.0022$	2.2727 ± 0.0019	0.490 ± 0.006	1.778 ± 0.028
$B^0 \to D^{*-}\tau^+\nu_\tau$, $\tau^+ \to \pi^+\pi^-\pi^+\pi^0\overline{\nu}_\tau$	$0.1559 \pm 0.0021/0.1578 \pm 0.0022$	1 ± 0	3.93 ± 0.10	0.616 ± 0.017
$B^+ \to \overline{D}^0 D_s^+$, $D_s^+ \to \pi^+\pi^-\pi^+$	$0.05980 \pm 0.00015/0.05992 \pm 0.00015$	6.137 ± 0.006	10.37 ± 0.03	38.09 ± 0.13

Table 6.13: Efficiency table for the all signal and normalisation modes. The generation efficiency is divided by magnet polarity.

6.8 Efficiencies calculation

Signal and normalisation efficiencies are needed as an input to determine the signal branching fractions. These are computed using simulation by applying the corresponding selection criteria. They are collected in Tab. 6.13 for all the signals and the normalisation mode. In addition to the efficiencies, a few parameters depending on signal the branching fractions and efficiencies are needed as an input for the final fit:

- $f_{3\pi}^{D^0}$: fraction of $B^+ \to \overline{D}^0\tau^+\nu_\tau$ events with $\tau^+ \to \pi^+\pi^-\pi^+\overline{\nu}_\tau$ with respect to the total number of $B^+ \to \overline{D}^0\tau^+\nu_\tau$ candidates (the sum of the $\tau^+ \to \pi^+\pi^-\pi^+\overline{\nu}_\tau$ and $\tau^+ \to \pi^+\pi^-\pi^+\pi^0\overline{\nu}_\tau$ events).
- $f_{3\pi}^{D^{*0}}$: fraction of $B^+ \to \overline{D}^{*0}\tau^+\nu_\tau$ events with $\tau^+ \to \pi^+\pi^-\pi^+\overline{\nu}_\tau$ with respect to the total number of $B^+ \to \overline{D}^{*0}\tau^+\nu_\tau$ events.
- $f_{3\pi}^{D^{*-}}$: fraction of $B^0 \to D^{*-}\tau^+\nu_\tau$ events with $\tau^+ \to \pi^+\pi^-\pi^+\overline{\nu}_\tau$ with respect to the total number of $B^0 \to D^{*-}\tau^+\nu_\tau$ candidates.
- $f_{D^{*-}/D^{*0}}$: ratio of $B^0 \to D^{*-}\tau^+\nu_\tau$ events with respect to $B^+ \to \overline{D}^{*0}\tau^+\nu_\tau$ candidates.

The B^+ and B^0 mesons production rates are assumed to be the same, $f_u = f_d$. Furthermore, the values of $\mathcal{B}(B^+ \to \overline{D}^{*0}\tau^+\nu_\tau)$ and $\mathcal{B}(B^0 \to D^{*-}\tau^+\nu_\tau)$ are also considered to be equal, based on isospin assumptions. The ratio $\mathcal{B}(D^{*-} \to \overline{D}^0 X)/\mathcal{B}(D^{*0} \to \overline{D}^0 X)$ is set to 0.677 from [172]. The values for these parameters are collected in Eq. (6.39).

$$\begin{aligned} f_{3\pi}^{D^0} &= 0.836, \\ f_{3\pi}^{D^{*0}} &= 0.844, \\ f_{3\pi}^{D^{*-}} &= 0.853, \\ f_{D^{*-}/D^{*0}} &= 0.142. \end{aligned} \tag{6.39}$$

6.9 Measurement of signal and normalisation yields

6.9.1 Determination of the normalisation yield

The $B^+ \to \overline{D}^0 D_s^+$ candidates selected as normalisation channel must pass the selection requirements of Tab. 6.5. A fit to data considering the deconvoluted invariant mass of the $\overline{D}^0 D_s^+$ system in a window of ± 60 MeV/c^2 around the B^+ nominal mass is performed to obtain the normalisation yield. This mass distribution is defined as

$$m'_{\overline{D}^0 D_s^+} = m_{\text{meas.}}(\overline{D}^0 D_s^+) - m_{\text{meas.}}(\overline{D}^0) - m_{\text{meas.}}(D_s^+) + m_{\text{PDG}}(\overline{D}^0) + m_{\text{PDG}}(D_s^+). \tag{6.40}$$

The model used to describe it is made of two distributions. The signal is modelled by a Crystal Ball (CB) function [173], with the parameters m_{mean}, σ, $\alpha_{R,L}$ and $n_{R,L}$. Using

Parameter	Fit to MC result	Fit to data result
N_{norm}	162650 ± 400	3047 ± 56
m_{mean}	5279.455 ± 0.026	5278.87 ± 0.17
σ	8.288 ± 0.030	8.66 ± 0.14
α_R	-1.674 ± 0.031	-1.674 (fixed)
α_L	1.510 ± 0.023	1.510 (fixed)
n_R	44 ± 17	44 (fixed)
n_L	15.7 ± 2.0	15.7 (fixed)
N_{bkg}	-	27 ± 10
r_{bkg}	-	-0.0043 ± 0.0068

Table 6.14: Results of the normalisation fit to MC (second column) and data (third column). The parameters of the Crystal Ball function are m_{mean}, σ, $\alpha_{R,L}$ and $n_{R,L}$, while N_{bkg} and r_{bkg} are the parameters of the exponential background model.

$\beta(m) = (m - m_{mean})/\sigma$, the distribution has the following form:

$$\text{CB}(m) = \begin{cases} -\frac{\alpha_L}{2} \cdot \left[\frac{\alpha_L}{n_L} \cdot \left(\frac{n_L - \alpha_L^2}{\alpha_L} - \beta(m)\right)\right]^{-n_L} & \text{for } \beta \leq -\alpha_L\,, \\ e^{\alpha_R^2/2} & \text{for } \beta < -\alpha_R\,, \\ e^{\alpha_R^2/2} \cdot \left[\frac{\alpha_R}{n_R} \cdot \left(\frac{\alpha_R^2 - n_R}{\alpha_R} + \beta(m)\right)\right]^{n_L} & \text{every other case}\,. \end{cases} \tag{6.41}$$

For the background, an exponential function is used, with the parameters N_{bkg} (yield) and r_{bkg} (slope). As a first step, a fit to the $B^+ \to \overline{D}^0 D_s^+$ simulation sample is performed using only the CB function. Its result is used to extract the tail parameters of the CB function, which are fixed in the second fit to the data sample. This second fit is performed using the complete model, with all parameters floating except those of the CB tail. Table 6.14 shows all the parameters after the fit.

The normalisation yield determined by the fit to the data is 3047 ± 56, and the fit projection is shown in Fig. 6.27. This will be used as an input for the measurement of the signal branching fractions.

6.9.2 Determination of the signal yields

In order to determine the $B^+ \to \overline{D}^0\tau^+\nu_\tau$ and $B^+ \to \overline{D}^{*0}\tau^+\nu_\tau$ decays signal yields, a 3-dimensional template fit to the τ decay time (t_τ), the squared di-lepton mass q^2 and the output of the BDT is performed. The template is chosen to have 3 bins of the BDT output and 8 bins, each, for the q^2 and the τ decay time. This fit framework uses the

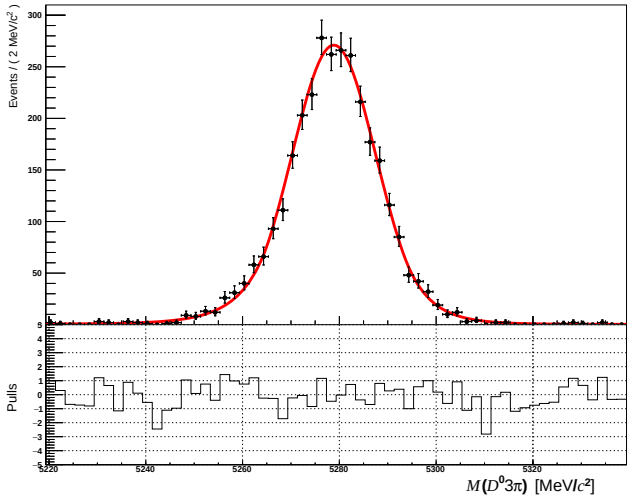

Figure 6.27: $m'_{\overline{D}^0 D_s^+}$ distribution after the normalisation fit. The red line represent the fit model (Crystal Ball and exponential functions), and data are represented by black dots.

"Lite" Beeston-Barlow technique [152] to account for the limited statistics of the model templates.

The 3-dimensional templates are obtained from the simulation and corrected by using the dedicated control samples or from the data. The model components considered in the fit, together with their parameters are listed in Tab. 6.15. The parameters are defined as follows:

- $N(B^+ \to \overline{D}^0 \tau^+ \nu_\tau)$ is the number of signal $B^+ \to \overline{D}^0 \tau^+ \nu_\tau$ events. It is a free parameter blinded by adding a Gaussian shift, x_{D^0}.
- $N(B^+ \to \overline{D}^{*0} \tau^+ \nu_\tau)$ is the number of signal $B^+ \to \overline{D}^{*0} \tau^+ \nu_\tau$ events. It is a free parameter blinded by adding a Gaussian shift, $x_{D^{*0}}$.
- The parameters $f_{3\pi}^{D^0}$, $f_{3\pi}^{D^{*0}}$, $f_{3\pi}^{D^{*-}}$ and $f_{D^{*-}/D^{*0}}$, defined in Sec. 6.8, are fixed to the values of Eq. 6.39.
- $f_{D^{**}/D^{*0}}$ is the amount of $B \to D^{**} \tau^+ \nu_\tau$ events relative to $B^+ \to \overline{D}^{*0} \tau^+ \nu_\tau$ decays (see Sec. 6.6.2). It is fixed to 0.043.
- $N(B \to \overline{D}^0 D^0(X))$ is the number of $B \to \overline{D}^0 D^0(X)$ events. A Gaussian constraint of 15% is added to it, based on the measurement of the $\overline{D}^0 \to K^+ 3\pi$ yield.
- $N(B \to \overline{D}^0 D^+(X))$ is the number of $B \to \overline{D}^0 D^+(X)$ events. This is a free parameter.

- $N(B \to \overline{D}^0 3\pi(X)) = N_{\text{prompt}}$ is the number of prompt events $B \to \overline{D}^0 3\pi(X)$. This is a free parameter.

- $N_{\text{comb-bkg}}$ is the number of combinatorial events where the D^0 and the 3π originate in different decays. This is fixed based on the number of events with the invariant mass of the $\overline{D}^0 3\pi$ system above the B^+ best-known mass.

- $N_{\text{not } \overline{D}^0}$ is the number of events with a fake $\overline{D}^0$. It is fixed to the number of the events measured in the $\overline{D}^0$ sidebands.

- $N_{D_s^+}$ is the number of events involving a D_s^+ meson and it is a free parameter (see Sec. 6.6.1).

- The parameters obtained from the $B^+ \to \overline{D}^0 D_s^+(X)$ decay model of Sec. 6.6.1 are the following:

  - ε_i is the relative efficiency of the i-th component between the $B \to \overline{D}^0 D_s^+(X)$ control sample and the signal sample.
  - F_i is the relative yield of the i-th component with respect to the $B^+ \to \overline{D}^0 D_s^+$ decays. F_i fractions are constrained based on the study of the $B \to \overline{D}^0 D_s^+(X)$ control sample.
  - F_i^* is the relative yield of the i-th component with respect to the $B^0 \to D^{*-} D_s^+$ decays. Similarly to F_i these are also constrained.

Note that, with $F^{(\overline{D}^0 D_s^+)}_{B^+ \to \overline{D}^0 D_s^+} = 1$ and $\varepsilon_{B^+ \to \overline{D}^0 D_s^+} = 1$, $\sum_i \varepsilon_i F_i$ is defined by

$$
\begin{aligned}
\sum_i \varepsilon_i F_i = {} & \varepsilon_{B^+ \to \overline{D}^0 D_s^+} \times F^{(\overline{D}^0 D_s^+)}_{B^+ \to \overline{D}^0 D_s^+} + \varepsilon_{B^+ \to \overline{D}^{*0} D_s^+} \times F^{(\overline{D}^0 D_s^+)}_{B^+ \to \overline{D}^{*0} D_s^+} \\
& + \varepsilon_{B^+ \to \overline{D}^0 D_s^{*+}} \times F^{(\overline{D}^0 D_s^+)}_{B^+ \to \overline{D}^0 D_s^{*+}} + \varepsilon_{B^+ \to \overline{D}^{*0} D_s^{*+}} \times F^{(\overline{D}^0 D_s^+)}_{B^+ \to \overline{D}^{*0} D_s^{*+}} \\
& + \varepsilon_{B^+ \to \overline{D}^0 D_{s1}(2460)^+} \times F^{(\overline{D}^0 D_s^+)}_{B^+ \to \overline{D}^0 D_{s1}(2460)^+} \\
& + \varepsilon_{B^+ \to \overline{D}^{*0} D_{s1}(2460)^+} \times F^{(\overline{D}^0 D_s^+)}_{B^+ \to \overline{D}^{*0} D_{s1}(2460)^+} \\
& + \varepsilon_{B^+ | B_s^0 \to \overline{D}^0 D_s^+(X)} \times F^{(\overline{D}^0 D_s^+)}_{B^+ | B_s^0 \to \overline{D}^0 D_s^+(X)} + \varepsilon_{B^0 \to \overline{D}^0 D_s^+ X} \times F^{(\overline{D}^0 D_s^+)}_{B^0 \to \overline{D}^0 D_s^+ X} \\
& + \varepsilon_{B^0 \to D^{*-} D_s^+} \times F^{(\overline{D}^0 D_s^+)}_{B^0 \to D^{*-} D_s^+} \\
& + \varepsilon_{B^0 \to D^{*-} D_s^{*+}} \times F^{(\overline{D}^0 D_s^+)}_{B^0 \to D^{*-} D_s^+} \times F^{*(D^{*-} D_s^+)}_{B^0 \to D^{*-} D_s^{*+}} \\
& + \varepsilon_{B^0 \to D^{*-} D_s^+} \times F^{(\overline{D}^0 D_s^+)}_{B^0 \to D^{*-} D_s^+} \times F^{*(D^{*-} D_s^+)}_{B^0 \to D^{*-} D_{s0}^*(2317)^+} \\
& + \varepsilon_{B^0 \to D^{*-} D_{s1}(2460)^+} \times F^{(\overline{D}^0 D_s^+)}_{B^0 \to D^{*-} D_s^+} \times F^{*(D^{*-} D_s^+)}_{B^0 \to D^{*-} D_{s1}(2460)^+} .
\end{aligned}
\tag{6.42}
$$

Fit component	**Yield**
$B^+ \to \overline{D}^0 \tau^+ \nu_\tau$, $\tau^+ \to 3\pi\overline{\nu}_\tau$	$N(B^+ \to \overline{D}^0 \tau^+ \nu_\tau) \times f_{3\pi}^{D^0}$
$B^+ \to \overline{D}^0 \tau^+ \nu_\tau$, $\tau^+ \to 3\pi\pi^0\overline{\nu}_\tau$	$N(B^+ \to \overline{D}^0 \tau^+ \nu_\tau) \times (1 - f_{3\pi}^{D^0})$
$B^+ \to \overline{D}^{*0} \tau^+ \nu_\tau$, $\tau^+ \to 3\pi\overline{\nu}_\tau$	$N(B^+ \to \overline{D}^{*0} \tau^+ \nu_\tau) \times f_{3\pi}^{D^{*0}}$
$B^+ \to \overline{D}^{*0} \tau^+ \nu_\tau$, $\tau^+ \to 3\pi\pi^0\overline{\nu}_\tau$	$N(B^+ \to \overline{D}^{*0} \tau^+ \nu_\tau) \times (1 - f_{3\pi}^{D^{*0}})$
$B^0 \to D^{*-} \tau^+ \nu_\tau$, $\tau^+ \to 3\pi\overline{\nu}_\tau$	$N(B^0 \to D^{*-} \tau^+ \nu_\tau) \times f_{D^{*-}/D^{*0}} \times f_{3\pi}^{D^{*-}}$
$B^0 \to D^{*-} \tau^+ \nu_\tau$, $\tau^+ \to 3\pi\pi^0\overline{\nu}_\tau$	$N(B^+ \to \overline{D}^{*0} \tau^+ \nu_\tau) \times f_{D^{*-}/D^{*0}} \times (1 - f_{3\pi}^{D^{*-}})$
$B \to D^{**} \tau^+ \nu_\tau$	$N(B^+ \to \overline{D}^{*0} \tau^+ \nu_\tau) \times f_{D^{**}/D^{*0}}$
$B \to \overline{D}^0 D^0(X)$	$N(B \to \overline{D}^0 D^0(X))$
$B \to \overline{D}^0 D^+(X)$	$N(B \to \overline{D}^0 D^+(X))$
$B \to \overline{D}^0 3\pi(X)$	$N(B \to \overline{D}^0 3\pi(X))$
Comb. background $\overline{D}^0/3\pi$	$N_{\text{comb-bkg}}$
not $\overline{D}^0$	$N_{\text{not } \overline{D}^0}$ ($\overline{D}^0$ sideband)
$B^+ \to \overline{D}^0 D_s^+$	$N_{D_s^+} \times \varepsilon_{B^+ \to \overline{D}^0 D_s^+} \times F^{(\overline{D}^0 D_s^+)}_{B^+ \to \overline{D}^0 D_s^+} / \sum_i \varepsilon_i F_i$
$B^+ \to \overline{D}^{*0} D_s^+$	$N_{D_s^+} \times \varepsilon_{B^+ \to \overline{D}^{*0} D_s^+} \times F^{(\overline{D}^0 D_s^+)}_{B^+ \to \overline{D}^{*0} D_s^+} / \sum_i \varepsilon_i F_i$
$B^+ \to \overline{D}^0 D_s^{*+}$	$N_{D_s^+} \times \varepsilon_{B^+ \to \overline{D}^0 D_s^{*+}} \times F^{(\overline{D}^0 D_s^+)}_{B^+ \to \overline{D}^0 D_s^{*+}} / \sum_i \varepsilon_i F_i$
$B^+ \to \overline{D}^{*0} D_s^{*+}$	$N_{D_s^+} \times \varepsilon_{B^+ \to \overline{D}^{*0} D_s^{*+}} \times F^{(\overline{D}^0 D_s^+)}_{B^+ \to \overline{D}^{*0} D_s^{*+}} / \sum_i \varepsilon_i F_i$
$B^+ \to \overline{D}^0 D_{s1}(2460)^+$	$N_{D_s^+} \times \varepsilon_{B^+ \to \overline{D}^0 D_{s1}(2460)^+} \times F^{(\overline{D}^0 D_s^+)}_{B^+ \to \overline{D}^0 D_{s1}(2460)^+} / \sum_i \varepsilon_i F_i$
$B^+ \to \overline{D}^{*0} D_{s1}(2460)^+$	$N_{D_s^+} \times \varepsilon_{B^+ \to \overline{D}^{*0} D_{s1}(2460)^+} \times F^{(\overline{D}^0 D_s^+)}_{B^+ \to \overline{D}^{*0} D_{s1}(2460)^+} / \sum_i \varepsilon_i F_i$
$B^+ \vert B_s^0 \to \overline{D}^0 D_s^+(X)$	$N_{D_s^+} \times \varepsilon_{B^+ \vert B_s^0 \to \overline{D}^0 D_s^+(X)} \times F^{(\overline{D}^0 D_s^+)}_{B^+ \vert B_s^0 \to \overline{D}^0 D_s^+(X)} / \sum_i \varepsilon_i F_i$
$B^0 \to \overline{D}^0 D_s^+(X)$	$N_{D_s^+} \times \varepsilon_{B^0 \to \overline{D}^0 D_s^+(X)} \times F^{(\overline{D}^0 D_s^+)}_{B^0 \to \overline{D}^0 D_s^+(X)} / \sum_i \varepsilon_i F_i$
$B^0 \to D^{*-} D_s^+$	$N_{D_s^+} \times \varepsilon_{B^0 \to D^{*-} D_s^+} \times F^{(\overline{D}^0 D_s^+)}_{B^0 \to D^{*-} D_s^+} / \sum_i \varepsilon_i F_i$
$B^0 \to D^{*-} D_s^{*+}$	$N_{D_s^+} \times \varepsilon_{B^0 \to D^{*-} D_s^{*+}} \times F^{(\overline{D}^0 D_s^+)}_{B^0 \to D^{*-} D_s^+} \times F^{*(D^{*-} D_s^+)}_{B^0 \to D^{*-} D_s^{*+}} / \sum_i \varepsilon_i F_i$
$B^0 \to D^{*-} D_{s0}^*(2317)^+$	$N_{D_s^+} \times \varepsilon_{B^0 \to D^{*-} D_{s0}^*(2317)^+} \times F^{(\overline{D}^0 D_s^+)}_{B^0 \to D^{*-} D_s^+} \times F^{*(D^{*-} D_s^+)}_{B^0 \to D^{*-} D_{s0}^*(2317)^+} / \sum_i \varepsilon_i F_i$
$B^0 \to D^{*-} D_{s1}(2460)^+$	$N_{D_s^+} \times \varepsilon_{B^0 \to D^{*-} D_{s1}(2460)^+} \times F^{(\overline{D}^0 D_s^+)}_{B^0 \to D^{*-} D_s^+} \times F^{*(D^{*-} D_s^+)}_{B^0 \to D^{*-} D_{s1}(2460)^+} / \sum_i \varepsilon_i F_i$

Table 6.15: Signal fit components list together with their yield parameterisation.

Parameter	Fit result	Constraint
$N(B^+ \to \overline{D}^0\tau^+\nu_\tau)$	xxx $\pm$1844	—
$N(B^+ \to \overline{D}^{*0}\tau^+\nu_\tau)$	xxx $\pm$1096	—
$N(D_s^+)$	xxx $\pm$1068	—
$N(D^0)$	7978 ± 613	6655 ± 998
$N(D^+)$	8606 ± 554	—
N_{prompt}	6223 ± 306	—
$N_{\text{not } \bar{\text{D}}^0}$	10902	10902
$N_{\text{comb. bkg.}}$	3286	3286
$F^{\overline{D}^0 D_s^+}_{B^+ \to \overline{D}^{*0} D_s^+}$	0.944 ± 0.037	0.915 ± 0.054
$F^{\overline{D}^0 D_s^+}_{B^+ \to \overline{D}^0 D_s^{*+}}$	0.870 ± 0.043	0.935 ± 0.056
$F^{\overline{D}^0 D_s^+}_{B^+ \to \overline{D}^{*0} D_s^{*+}}$	1.847 ± 0.041	1.828 ± 0.046
$F^{\overline{D}^0 D_s^+}_{B^+ \to \overline{D}^0 D_{s1}(2460)^+}$	0.266 ± 0.033	0.332 ± 0.038
$F^{\overline{D}^0 D_s^+}_{B^+ \to \overline{D}^{*0} D_{s1}(2460)^+}$	0.805 ± 0.030	0.710 ± 0.040
$F^{\overline{D}^0 D_s^+}_{B^+ \mid B_s^0 \to \overline{D}^0 D_s^+(X)}$	0.791 ± 0.034	0.817 ± 0.037
$F_{B \to D^{**}\tau\nu}$	0.043	0.043

Table 6.16: Three-dimensional signal fit results.

The fit is performed blinded in order to minimise biases. Hence, two random quantities, x_{D^0} and $x_{D^{*0}}$, are added to the number of signal events $N(B^+ \to \overline{D}^0\tau^+\nu_\tau)$ and $N(B^+ \to \overline{D}^{*0}\tau^+\nu_\tau)$, respectively. These values are extracted from Gaussian distributions with the mean centred in 0 ($\mu = 0$) and a width of $\sigma = 20000$, so that

$$\begin{aligned} N(B^+ \to \overline{D}^0\tau^+\nu_\tau) &= N(B^+ \to \overline{D}^0\tau^+\nu_\tau)_{\text{blind}} + x_{D^0}\,, \\ N(B^+ \to \overline{D}^{*0}\tau^+\nu_\tau) &= N(B^+ \to \overline{D}^{*0}\tau^+\nu_\tau)_{\text{blind}} + x_{D^{*0}}. \end{aligned} \tag{6.43}$$

This way it is possible to control only the uncertainties of the signal yields, while the relative uncertainties and the yield values are unknown. To further blind the result, also the yield of the dominant background, due to $B \to \overline{D}^0 D_s^+(X)$ decays, is hidden to the analysts following the same procedure. The additional parameter, x', is Gaussian distributed, with mean $\mu' = 0$ and width $\sigma' = 40000$. In addition, to not bias the results and still be able to control the fit projections, a third blinding is performed. The PDF of the $B^+ \to \overline{D}^0\tau^+\nu_\tau$ and $B^+ \to \overline{D}^{*0}\tau^+\nu_\tau$ signals are normalised to 9000 and 11000, respectively and the PDF of the $B \to \overline{D}^0 D_s^+(X)$ decays is normalised to 100000.

The Beeston-Barlow Lite method [174] is implemented to take into account the limited size of the MC sample. It consists in introducing a nuisance parameter per bin to account for the statistical uncertainty. Table 6.16 shows the fit results and the fit projections are shown in Fig. 6.28. The correlation between the $B^+ \to \overline{D}^0\tau^+\nu_\tau$ and $B^+ \to \overline{D}^{*0}\tau^+\nu_\tau$ yields is -0.94.

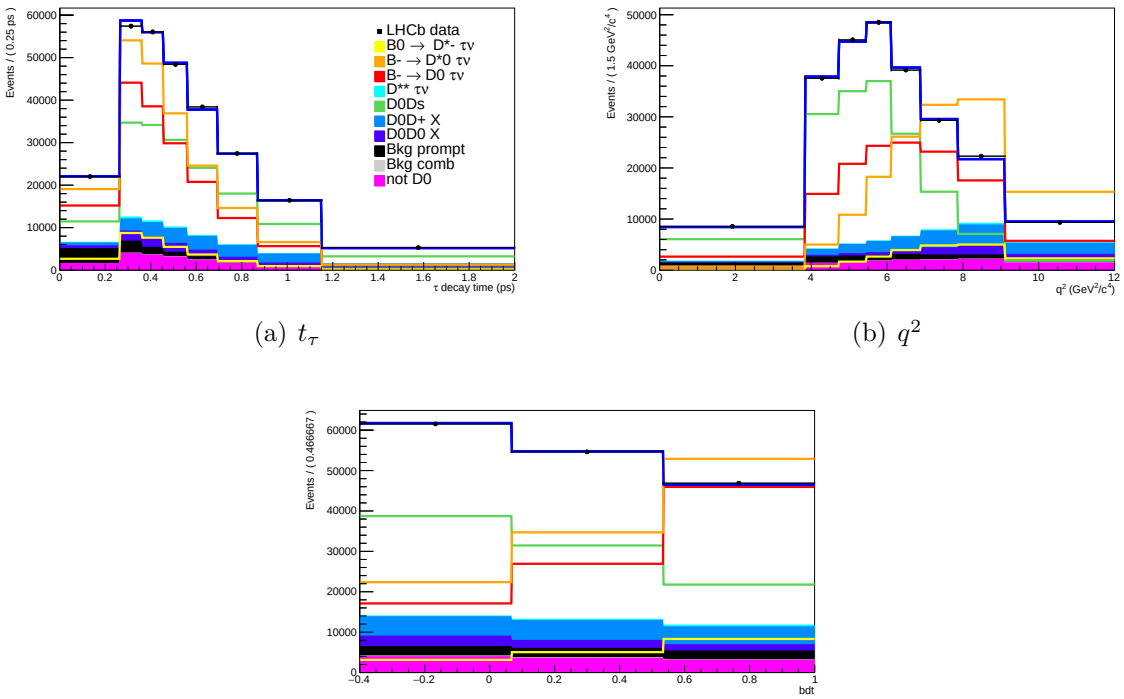

(a) t_τ

(b) q^2

(c) BDT output

Figure 6.28: Projections of the three-dimensional fit, from left to right: τ decay time, q^2 and BDT distributions. The $B^+ \to \overline{D}^0\tau^+\nu_\tau$ (red) and $B^+ \to \overline{D}^{*0}\tau^+\nu_\tau$ (orange) signal components and the D_s^+ background (green) are blind in the fit. The excited $B \to D^{**}\tau^+\nu_\tau$ mode is represented in cyan and the inclusive $B \to \overline{D}^0 D^+(X)$ and $B \to \overline{D}^0 D^0(X)$ modes are in blue.

6.10 Systematic uncertainties evaluation

At the time in which this thesis is written, the systematic uncertainties of the analysis are being evaluated. In this section the strategy adopted for some of the dominant systematic effects is described.

The systematic uncertainties are studied following a procedure similar to the one used in the $R_{e/\mu}$ analysis. First of all, the uncertainties are divided into categories: the ones due to the signal model and the one due to the background models.

In the signal fit (see 6.9.2), the Lite Beeston Barlow method was used in order to take into account the limited statistic of the model templates. The systematic uncertainty linked to this is obtained by performing the signal fit multiple times fluctuating the bin contents of the templates following a Poisson distribution.

The systematic uncertainties due to the background models are determined in a similar way. This is done for the inclusive $B \to \overline{D}^0 D_s^+(X)$, $B \to \overline{D}^0 D^0(X)$ and $B \to \overline{D}^0 D^+(X)$ components, and for the $D_s^+ \to \pi^+\pi^-\pi^-(X)$ decay model. The different sets of parameters for each model will be varied according to Gaussian distributions taking into account their uncertainties, and the resulting difference in signal yields is taken as the systematic uncertainty. The systematic uncertainty due to the prompt $B \to \overline{D}^0\pi^+\pi^-\pi^-(X)$ component is studied in an analogue way and the uncertainty is taken as the standard deviation of the resulting yield parameters. Finally, the contribution due to excited $B \to D^{**}\tau^+\nu_\tau$ decays (Sec. 6.6.2) is obtained by changing its yield and repeating the fit many times. Again, the change in the signal yields is taken as the systematic uncertainty.

6.11 Blinded results

Using the signal and normalisation yields obtained in Sec. 6.9 and the efficiencies obtained in Sec. 6.8, it is possible to obtain the yield ratio $\mathcal{K}(D^{(*)0})$ for the two signal channels. This, defined in Eq. (6.4), is calculated as

$$\begin{aligned}\mathcal{K}(D^{(*)0}) &= \frac{N(B^+ \to \overline{D}^{(*)0}\tau^+\nu_\tau)}{N(B^+ \to \overline{D}^0 D_s^+)} \times \\ &\times \frac{\varepsilon_{B^+\to\overline{D}^0 D_s^+}}{\varepsilon^{\tau^+\to 3\pi\overline{\nu}_\tau}_{B^+\to\overline{D}^{(*)0}\tau^+\nu_\tau}\mathcal{B}(\tau^+ \to 3\pi\overline{\nu}_\tau) + \varepsilon^{\tau^+\to 3\pi\overline{\nu}_\tau\pi^0}_{B^+\to\overline{D}^{(*)0}\tau^+\nu_\tau}\mathcal{B}(\tau^+ \to 3\pi\pi^0\overline{\nu}_\tau)}\,, \quad (6.44)\end{aligned}$$

where the τ branching fractions are $\mathcal{B}(\tau^+ \to \pi^+\pi^-\pi^+\overline{\nu}_\tau) = (9.02 \pm 0.05)\%$ and $\mathcal{B}(\tau^+ \to \pi^+\pi^-\pi^+\pi^0\overline{\nu}_\tau) = (4.49 \pm 0.05)\%$ [1], obtaining

$$\mathcal{K}(D^0) = xx \pm 22\ (\text{stat.}) \pm 0.35\ (\text{ext.})\,, \quad (6.45)$$

$$\mathcal{K}(D^{*0}) = xx \pm 16\ (\text{stat.}) \pm 0.74\ (\text{ext.})\,. \quad (6.46)$$

Here the first uncertainty contribution is due to statistics and the second one to the external branching fractions, which is considered negligible with respect to the statistical

one. The correlation between the statistical uncertainties is -0.91 and the one between the external ones is $+1$.

Then, using $\mathcal{K}(D^{(*)0})$ and the external measurements $\mathcal{B}(B^+ \to \overline{D}^0 D_s^+) = (9.0 \pm 0.9) \times 10^{-3}$ and $\mathcal{B}(D_s^+ \to \pi^+\pi^-\pi^+) = (1.08 \pm 0.04)\%$, the branching fractions of $B^+ \to \overline{D}^{*0}\tau^+\nu_\tau$ and $B^+ \to \overline{D}^0\tau^+\nu_\tau$ is calculated as

$$\mathcal{B}(B^+ \to \overline{D}^{(*)0}\tau^+\nu_\tau) = \mathcal{K}(D^{(*)0}) \times \mathcal{B}(B^+ \to \overline{D}^0 D_s^+) \times \mathcal{B}(D_s^+ \to \pi^+\pi^-\pi^+)\,, \tag{6.47}$$

obtaining

$$\mathcal{B}(B^+ \to \overline{D}^0\tau^+\nu_\tau) = xx \pm 0.21\ (\text{stat.}) \pm 0.07\ (\text{ext.})\%\,, \tag{6.48}$$
$$\mathcal{B}(B^+ \to \overline{D}^{*0}\tau^+\nu_\tau) = xx \pm 0.15\ (\text{stat.}) \pm 0.15\ (\text{ext.})\%\,. \tag{6.49}$$

The correlation between the determined branching fractions is the same as in the case of $\mathcal{K}(D^{(*)0})$, -0.91 and $+1$ for the statistical and the external uncertainties, respectively.

Being the state-of-the-art measurement of the branching fractions, [1]

$$\mathcal{B}(B^+ \to \overline{D}^0\tau^+\nu_\tau) = 0.77 \pm 0.25\%\,, \tag{6.50}$$
$$\mathcal{B}(B^+ \to \overline{D}^{*0}\tau^+\nu_\tau) = 1.88 \pm 0.20\%\,, \tag{6.51}$$

it is possible to add together the uncertainties of our result in order to be able to compare them. Hence,

$$\mathcal{B}(B^+ \to \overline{D}^0\tau^+\nu_\tau) = xx \pm 0.23\ (\text{stat.} + \text{ext.})\%\,, \tag{6.52}$$
$$\mathcal{B}(B^+ \to \overline{D}^{*0}\tau^+\nu_\tau) = xx \pm 0.22\ (\text{stat.} + \text{ext.})\%\,, \tag{6.53}$$

with a correlation of -0.37, resulting in a competitive measurement with the world average.

Taking all of this into account, the LFU ratios $R(D)$ and $R(D^*)$ can be determined as

$$R(D^{(*)0}) = \frac{\mathcal{B}(B^+ \to \overline{D}^{*0}\tau^+\nu_\tau)}{\mathcal{B}(B^+ \to \overline{D}^0 D_s^+)\mathcal{B}(D_s^+ \to \pi^+\pi^-\pi^+)} \times \left(\frac{\mathcal{B}(B^+ \to \overline{D}^0 D_s^+)\mathcal{B}(D_s^+ \to 3\pi)}{\mathcal{B}(B^+ \to \overline{D}^{(*)0}\ell^+\nu_\ell)}\right)_{\text{ext.}}, \tag{6.54}$$

and substituting the external measurements [60] of $\mathcal{B}(B \to \overline{D}^0\ell^+\nu_\ell) = 2.30 \pm 0.06 \pm 0.08$ and $\mathcal{B}(B \to \overline{D}^{*0}\ell^+\nu_\ell) = 5.58 \pm 0.07 \pm 0.21$, where the first is the statistical uncertainty and the second is due to statistics, the following values are obtained:

$$R(D^0) = xx \pm 0.093\ (\text{stat.}) \pm 0.034\ (\text{ext.})\ \%\,, \tag{6.55}$$
$$R(D^{*0}) = xx \pm 0.026\ (\text{stat.}) \pm 0.029\ (\text{ext.})\ \%\,. \tag{6.56}$$

with a correlation of -0.91 and $+1$ for the statistical and external uncertainties respectively. This result is included in Fig. 6.29 in magenta, together with the previous $R(D)$

and $R(D^*)$ measurements. Since the central value is blinded, the ellipse is centred in the SM prediction value. The continuous line represents the statistical uncertainty. The total uncertainty, including also external uncertainties is represented by the dashed line. The systematic uncertainty is not shown since it has not been evaluated at the time or writing this thesis.

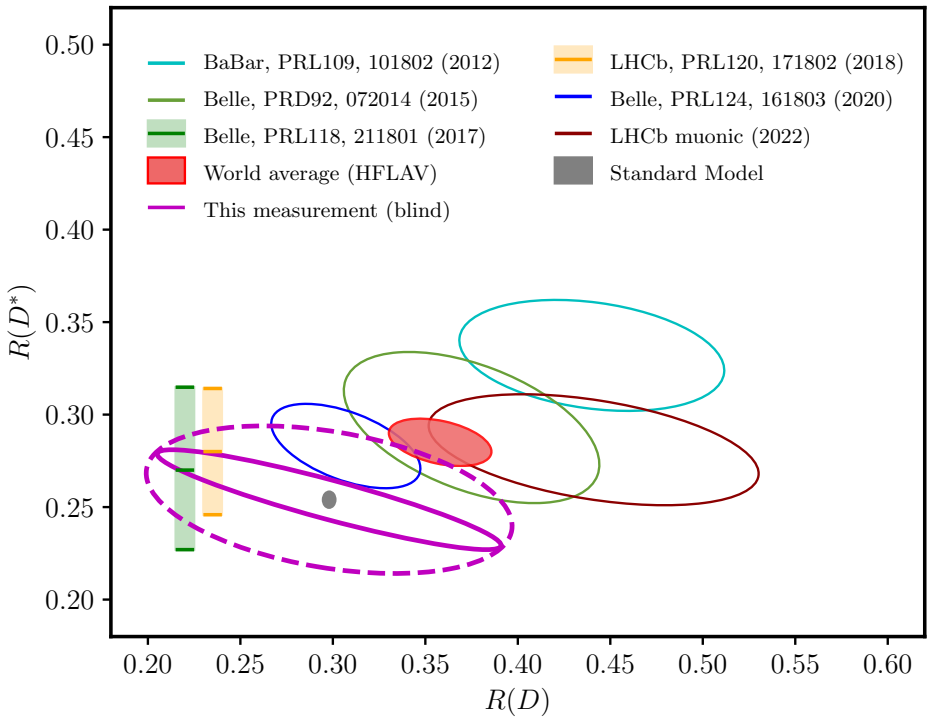

Figure 6.29: $R(D)$ and $R(D^*)$ result from this analysis (magenta) compared with the SM predictions and published measurements [44–51, 53, 54, 60]. The statistical uncertainty is reported as the continuous ellipse while an estimation of the total uncertainty (including the external uncertainty) as the dashed ellipse. The systematic uncertainty is not included. The correlation is represented by the slope of the ellipse. The SM prediction is represented by the grey point, whose width stands for the uncertainty. The world average is represented by the red ellipse and previous measurements are specified in the plot legend (see Sec. 3.2.2 for more details).

7

Run 3 trigger selections for 3-prong $H_b \to H_c\tau^+\nu_\tau$ decays

After the end of Run 2, in December 2018, the Second Long Shutdown of the LHC started (LS2). LS2 was planned as a three years period aiming to the upgrade of the LHC and its main experiments. Because of the impact of the COVID pandemic, it was prolonged until the beginning of 2022. As a result, the first collisions of Run 3 were recorded on July the 5^{th} 2022.

In order to continue studying $H_b \to H_c\tau^+\nu_\tau$ decays, with the 3-prong τ decay in Run 3, where H_b and H_c are b- and c-hadrons, respectively, HLT2 trigger lines have been developed. In this chapter, the main steps of this trigger algorithm are described. The chapter is structured as follows. First, the specifics of the LHCb Upgrade I detector are reported in Sec. 7.1. Then, in Sec. 7.2 the selection for the semileptonic decays of $H_b \to H_c\tau^+\nu_\tau$, with 3-prong τ decays is described.

7.1 The LHCb Upgrade I detector

Even though Run 2 was very successful, the majority of the analyses were limited by statistical uncertainties. Therefore, one of the main goals of both the LHC and the LHCb detector is the increase in the instantaneous luminosity and that implies changes in both the detector and the data acquisition system. In fact, the instant luminosity is expected to increase by a factor 5, up to $2 \times 10^{33}\,\text{cm}^2\,\text{s}^{-1}$, as shown in Fig. 7.1, leading to an integrated luminosity of 50 fb^{-1} at the end of the Upgrade I phase. For the next Upgrade phase, Upgrade II, the integrated luminosity is expected to reach 300 fb^{-1}.

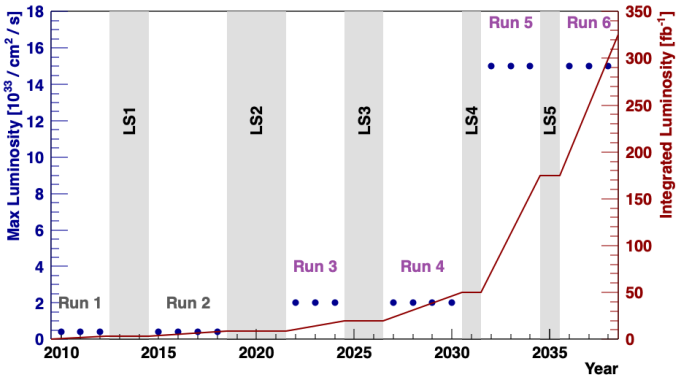

Figure 7.1: Time projection for the luminosity of LHCb, LHCb Upgrade I (Run 3 and 4) and Upgrade II (Run 5 and 6) [177]. Blue: peak luminosity

In order to monitor luminosity in the upgraded detector, the dedicated subsystem PLUME has been installed [175]. Besides, to continue the fixed target physics program, already active during Run 2, the gas injection system, called System for Measuring the Overlap with Gas (SMOG) has been upgraded [176]. SMOG is used to inject gas of different nuclei (He, Ne and Ar) , which will be fixed laboratory targets to proton and lead beams producing collisions up to a centre of mass energy of 115 GeV.

Fig. 7.2 represents the lateral section of the Upgrade I detector, to be compared with the one of Fig. 4.4. In order to have the same detector performance of Run 1 and 2, some of the sub-detectors have been replaced. The main changes to the detector subsystems are the following:

- **Tracking systems** [178]. Due to the higher multiplicity, all the tracking systems have been upgraded. From the interaction point to the right, the LHCb Upgrade I tracking system is composed by: the VELO, the Upstream Tracker (UT) and the Scintillating Fibre tracker (SciFi). The upgraded VELO [116] is based on silicon pixel detector modules with a geometry similar to the previous one with an aperture of 3.5 mm, in order to improve the IP resolution (see Sec. 4.2.1). The TT detector is replaced by the UT, based on silicon strips and a reduced thickness. After the magnet, the tracking stations are replaced by the SciFi, which is composed by scintillating fibres.

- **Particle identification** [179]. The upgraded PID systems RICH1, RICH2, ECAL and HCAL have been upgraded to maintain their performances in the new conditions. For instance, in the two RICH detectors, HPDs (see Sec. 4.2.2) have been replaced by multi-anode photomultipliers. In the calorimeter system, the PS and the SPD subdetectors have been removed in order to adapt to the new trigger strategy. In addition, the first muon station (M1) has been removed.

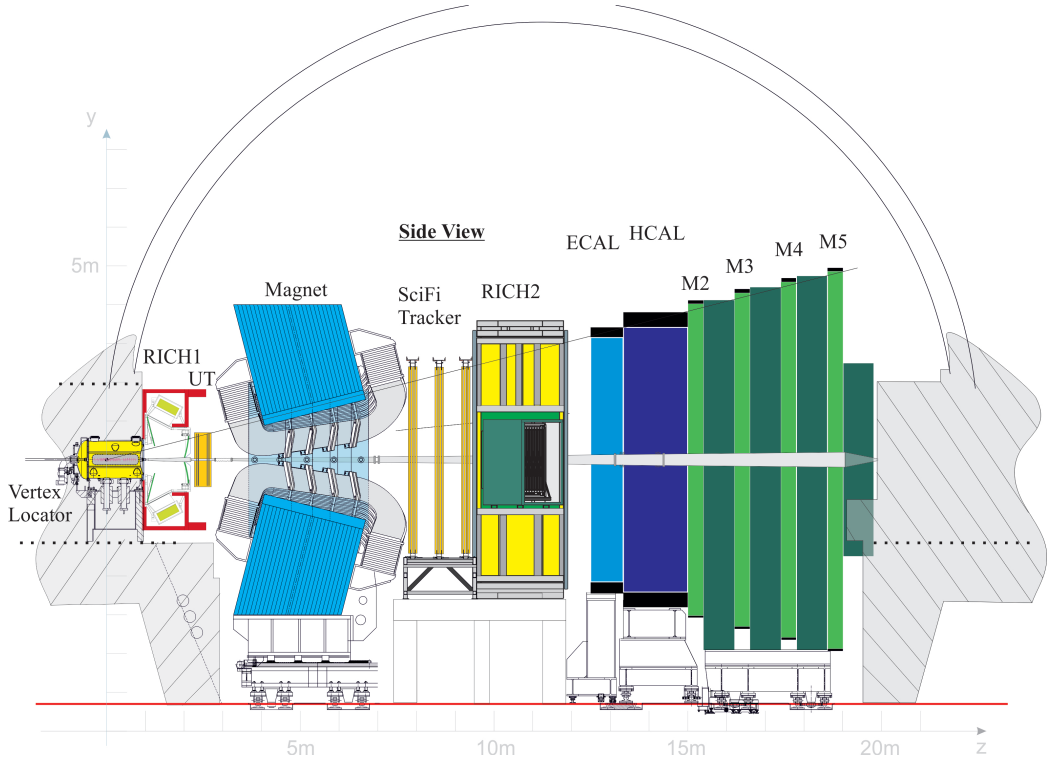

Figure 7.2: Overview of the LHCb Upgrade I detector [178]. From left to right: Vertex Locator (VELO), RICH1, UT, Magnet, the SciFi tracker, RICH2, ECAL, HCAL, and the five muon stations.

7.1.1 LHCb Upgrade I trigger and workflow

The main changes of the LHCb Upgrade I detector concern the trigger systems and the data workflow [180, 181]. In Run 1 and 2, the trigger operates with three different levels: the hardware L0 level and the software HLT1 and 2 (see Sec. 4.2.8). One of the limits in Run 2 physics analyses is due to the hardware based L0 trigger. For instance, for many studies, the high p_{T} and E_{T} signatures of this trigger stage are highly inefficient. Besides, its design does not allow to customise and adapt the trigger to new necessities. For these reasons, the L0 trigger is not present in the upgraded strategy and only the software trigger is maintained.

The main challenge of the trigger is to reduce the rate from the incoming bunch-crossing of 30 MHz to the readout rate of 1.1 MHz, so that only 10 GB/ s are written to permanent storage [180]. A real-time analysis (RTA) approach is adopted. This strategy was already used in Run 2 with the so-called *Turbo* streams [182] (see Sec. 4.2.8). With the RTA approach, the reconstruction is performed by the HLT trigger in real time. The software trigger is structured as follows:

1. **HLT1.** Similarly to Run 2 (see Sec. 4.2.8.2), a full reconstruction of the event is done at this level and some selections based on the decay topology are included. Regarding the PID, since the timing constraints do not allow to process the full information from the RICH detectors, their information is not available at this step. The software framework used at this stage is called Allen, implemented in GPU farms [181].

2. **HLT2.** Once passed the HLT1 filtering, a second selection is performed in CPU farms. At this stage all the information on particle identification and track quality are available. This will substitute the stripping selection, introduced in Sec. 4.3.3. The application in which the HLT2 is implemented is called Moore [180].

Therefore, the workflow of data and simulation changes from the one of Fig. 4.21 to the one in Fig. 7.4. After the trigger, there is another offline selection step the events can pass through. These are called *Sprucing lines*, also implemented in Moore.

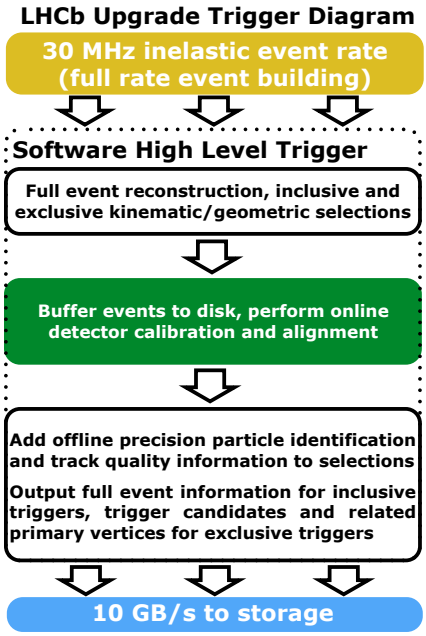

Figure 7.3: The LHCb trigger scheme for Run 3 [131].

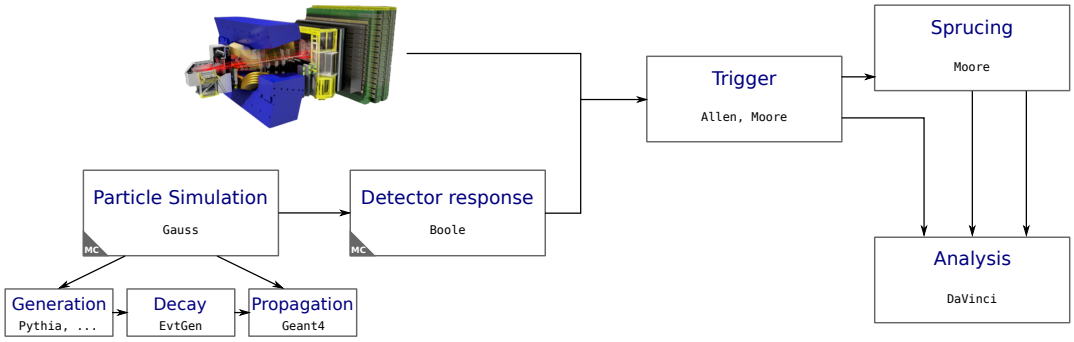

Figure 7.4: Run 3 data and MC workflow [183]. The steps with the label "MC" are relative only to simulation.

7.2 Selection for semitauonic 3-prong decays

As mentioned in both Sec. 3.2.2 and more in detail in Ch. 6, semitauonic $H_b \to H_c\tau^+\nu_\tau$ decays can be reconstructed using both the leptonic and the 3-prong τ decays. For example, tests of LFU of $H_b \to H_c\tau^+\nu_\tau$ decays with the τ reconstructed using the 3-prong decays have been studied for different charm hadrons by LHCb. The first measurement of $R(D^*)$ was published in Ref. [53, 54]. A generalisation in the baryon sector has been investigated by measuring the $\Lambda_b^0 \to \Lambda_c^+\tau^-\overline{\nu}_\tau$ decay and the LFU observable $R(\Lambda_c^+)$ [55]. Finally, this thesis (see Ch. 6) presents a simultaneous measurement of the LFU observables $R(D^{*0})$ and $R(D^0)$.

Other than the $B^+ \to D^{(*)0}\tau^+\nu_\tau$ decays analysis, more channels are investigated by different groups in the LHCb collaboration. These channels are planned to be studied also with the upgraded detector, so the HLT2 selection has to be implemented. In this thesis, the selection of the following 3-prong semitauonic decays is reported:

- $B^0 \to D^{*-}\tau^+\nu_\tau$, where $D^{*-} \to \overline{D}^0(\to K^+\pi^-)\pi^-$
- $B^+ \to \overline{D}^0\tau^+\nu_\tau$, where $\overline{D}^0 \to K^+\pi^-$
- $B^0 \to D^-\tau^+\nu_\tau$, where $D^- \to K^+\pi^-\pi^-$
- $B_c^+ \to J/\psi\tau^+\nu_\tau$, where $J/\psi \to \mu^+\mu^-$
- $B_s^0 \to D_s^-\tau^+\nu_\tau$, where $D_s^- \to K^-K^+\pi^-$
- $\Lambda_b^0 \to \Lambda_c^+\tau^-\overline{\nu}_\tau$, where $\Lambda_c^+ \to pK^-\pi^+$
- $\Lambda_b^0 \to p\tau^-\overline{\nu}_\tau$

These decays can be reconstructed by selecting the τ with both $\tau^+ \to \mu^+\nu_\mu\overline{\nu}_\tau$ and $\tau^+ \to \pi^+\pi^-\pi^+\nu_\tau$ decays. In order to have the same code structure for both τ reconstruction methods, the trigger selection for the charm hadrons is shared by the two groups, with proper tuning.

Because of the nature of HLT2 in the upgraded software, the Run 2 stripping selection is chosen as a starting point. For example, in Run 2 $B^+ \to \overline{D}^0\tau^+\nu_\tau$ decays, where $\overline{D}^0 \to K^+\pi^-$, are selected by applying the stripping requirements of Tab. 6.3. A similar selection is required to Run 3 data and reported in Tab. 7.1.

In order to pass the software requirements, for each line the efficiency and the rates have to be calculated. These are obtained both by applying the selection to a minimum bias data sample or to a simulated sample containing only the signal decay. In particular, the efficiencies are defined as

$$\varepsilon = \frac{N_{\text{Triggered}}}{N_{\text{events you might expect to trigger on}}}, \tag{7.1}$$

$$\varepsilon_{\text{TrueSim}} = \frac{N_{\text{Triggered \& Matched}}}{N_{\text{events you might expect to trigger on}}}, \tag{7.2}$$

Cut	Value
D^0	
$\lvert m(K\pi) - m(D^0)_{\text{PDG}} \rvert$	< 150 MeV/c^2
Vertex χ^2/DOF	< 6
DIRA	> 0.99
PV distance χ^2	> 25
χ^2_{IP}(PV)	> 10
DOCA$_{K\pi}$ χ^2	< 20
D^0 daughters	
Track ghost Probability	< 0.3
Track χ^2	$> 10^{-8}$
χ^2_{IP}(PV)	> 10
p_T	> 150 MeV/c
K: PID(K)	> 3
π: PID(K)	< 20
τ	
DIRA	> 0.99
$m(3\pi)$	0.4-3.5 GeV/c^2
$m(\pi^+\pi^-)$	< 1670 MeV/c^2
DOCA	< 0.15 mm
Vertex χ^2	< 16
At least two pions with p_T	> 300 MeV/c
At least two pions with χ^2_{IP}(PV)	> 15
τ daughter pions	
p_T	> 350 MeV/c
χ^2_{IP}(PV)	> 10
Track χ^2/DOF	< 4
Ghost probability	< 0.4

Table 7.1: Run 3 HLT2 trigger selection for the $B^+ \to \overline{D}^0 \tau^+ \nu_\tau$ decay, where $\overline{D}^0 \to K^+\pi^-$ and $\tau^+ \to \pi^+\pi^-\pi^+\overline{\nu}_\tau$.

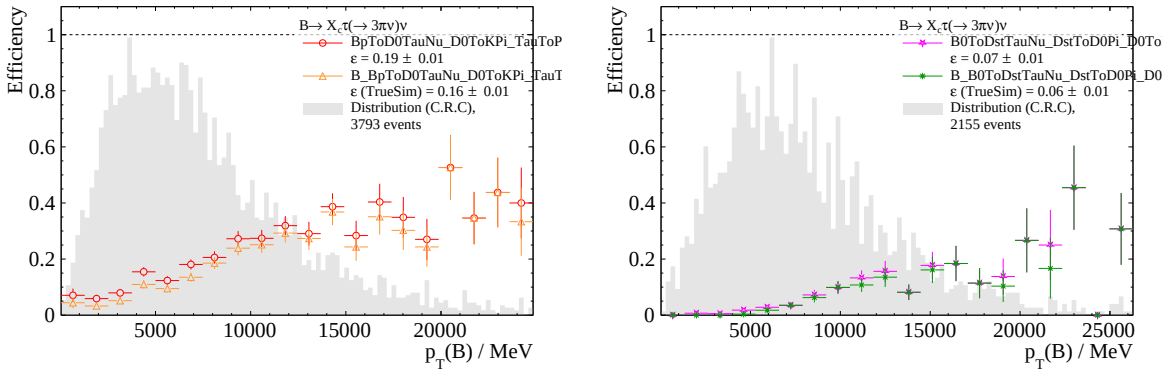

(a) $B^+ \to \overline{D}^0 \tau^+ \nu_\tau$ (b) $B^0 \to D^{*-} \tau^+ \nu_\tau$

Figure 7.5: Efficiency plots for $B \to \overline{D}^0 \tau^+ \nu_\tau$ (left) and $B^0 \to D^{*-} \tau^+ \nu_\tau$ (right) HLT2 trigger lines. The points points represent the events passing the trigger selection For $B \to \overline{D}^0 \tau^+ \nu_\tau$ ($B^0 \to D^{*-} \tau^+ \nu_\tau$) the red (magenta) points represent the efficiency calculated with the simulation and the orange (green) ones when considering the MC truth.

where the events are required to be in the LHCb fiducial acceptance. Fig. 7.5 represents the efficiencies of the HLT2 lines for $B^+ \to \overline{D}^0 \tau^+ \nu_\tau$ and $B^0 \to D^{*-} \tau^+ \nu_\tau$ decays tested on MC samples. The $B^+ \to \overline{D}^0 \tau^+ \nu_\tau$ decay is expected to be selected with an efficiency of 19% (Fig. 7.5(a)) while $B^0 \to D^{*-} \tau^+ \nu_\tau$ decays (Fig. 7.5(b)) with 7%.

The HLT2 line rates are obtained as

$$\text{Rate}_{\text{HLT2 line}} = 30 \text{ MHz} \times \frac{N_{\text{accepted}}}{N_{\text{processed}}}, \tag{7.3}$$

where $N_{\text{Triggered}}$ is the number of events that have passed the trigger and $N_{\text{processed}}$ the total number of events processed in the rate calculation. For all these lines the rates obtained from a test on a sample with a minimum bias trigger are reported in Tab. 7.2. Here, for each line, the exclusive rate is defined by events that only fire that trigger.

All this considered, the semitauonic trigger lines are working well and when more data will be available, they will be tested on data. These tests will be of paramount importance also in the migration to the upgraded software of the isolation algorithms, used in the selection of semitauonic decays, as seen in Sec. 6.3.3, by several analyses.

H_b decay	H_c decay	Rate (kHz)	
		Inclusive	Exclusive
$B^0 \to D^{*-}\tau^+\nu_\tau$	$D^{*-} \to \overline{D}^0(\to K^-\pi^+)\pi^-$	1.3 ± 0.2	0.14 ± 0.05
$B^+ \to \overline{D}^0\tau^+\nu_\tau$	$\overline{D}^0 \to K^-\pi^+$	34.8 ± 0.8	32.3 ± 0.8
$B^0 \to D^-\tau^+\nu_\tau$	$D^+ \to K^-\pi^+\pi^-$	0.21 ± 0.06	0.5 ± 0.03
$B_c^+ \to J/\psi\tau^+\nu_\tau$	$J/\psi \to \mu^+\mu^-$	2.6 ± 0.2	1.7 ± 0.2
$B_s^0 \to D_s^-\tau^+\nu_\tau$	$D_s^- \to K^-K^+\pi^-$	0.48 ± 0.10	0.23 ± 0.07
$\Lambda_b^0 \to \Lambda_c^+\tau^-\overline{\nu}_\tau$	$\Lambda_c^+ \to K^-\pi^+\pi^+$	0.36 ± 0.09	0.18 ± 0.06
$\Lambda_b^0 \to p\tau^+\nu_\tau$	-	3.4 ± 0.3	2.7 ± 0.2

Table 7.2: Preliminary results of Run 3 HLT2 trigger selection rates. For each line, the exclusive rate is defined as the ones where the events only fire that trigger.

8

Conclusions and prospects

In the SM, the coupling between the leptons and the gauge bosons is independent of the lepton generation. This feature is named Lepton Flavour Universality. Many new physics scenarios foresee LFU-violating processes, involving mostly the third generation [33]. Therefore, LFU tests are one of the best probes of the SM.

The LHCb experiment has proven to be an excellent tool to search for NP, in particular for LFU tests. The latest LHCb measurements in both neutral and charged currents processes are the most precise at present. In the first two LHC data taking periods LHCb collected data corresponding to an integrated luminosity of 9 fb^{-1}. The statistics will significantly increase with the upgraded detector, which started its operation in 2022. The LHCb Upgrade I, operating at a luminosity up to $2 \times 10^{33}\,\text{cm}^2\,\text{s}^{-1}$ and $\sqrt{s} = 14$ TeV, is planned to reach an integrated luminosity of 50 fb^{-1} (300 fb^{-1}) at the end of Run 3 (Run 4) in 2025 (2030).

This thesis is based on two LHCb data analyses, concerning semileptonic B and D meson decays. Both analyses are performed blinded. The main studies missed by the two are the systematic uncertainties evaluation.

The objective of the first analysis is to test LFU by measuring the ratio

$$R_{e/\mu} = \frac{\mathcal{B}(D^0 \to K^- e^+ \nu_e)}{\mathcal{B}(D^0 \to K^- \mu^+ \nu_\mu)}, \tag{8.1}$$

This is the first measurement of LFU in the charm sector at a hadron collider. The $D^0 \to K^- \ell^+ \nu_\ell$ candidates are selected from prompt $D^{*+} \to D^0 \pi^+$ decays and the value of $R_{e/\mu}$ is obtained by the ratio of the signal yields and the ratio of efficiencies between

the two modes. The obtained result is

$$R_{e/\mu} = x.xxx \pm 0.003 \text{ (stat.)} \pm 0.014 \text{ (syst.)}, \tag{8.2}$$

where the first contribution to the uncertainties is statistical, and the second is an estimation of the systematic uncertainty. In order to compare it with theoretical predictions and the BESIII collaboration measurement, the inverse, $R_{\mu/e}$, is calculated, propagating accordingly the errors, obtaining

$$R_{\mu/e} = R_{e/\mu}^{-1} = x.xxx \pm 0.003 \text{ (stat.)} \pm 0.013 \text{ (syst.)}, \tag{8.3}$$

This result is shown in Fig. 5.21 centred in the value of the SM predictions. Compared to the BESIII result, the LHCb one is more precise.

The second analysis aims to measure the LFU observables $R(D^0)$ and $R(D^{*0})$, defined in Eq. (6.3). This is the first simultaneous measurement at a hadron collider using the hadronic $\tau^+ \to \pi^+\pi^-\pi^+\overline{\nu}_\tau$ decay of the τ lepton. The blinded result of $R(D^0)$ and $R(D^{*0})$, also reported in Fig. 6.29, is:

$$R(D^0) = xx \pm 0.093 \text{ (stat.)} \pm 0.034 \text{ (ext.)}\%\,, \tag{8.4}$$

$$R(D^{*0}) = xx \pm 0.024 \text{ (stat.)} \pm 0.029 \text{ (ext.)}\%\,, \tag{8.5}$$

where the first contribution to the uncertainty is statistical and the second is due to the external measurements of $\mathcal{B}(B \to D^{(*)0}\ell^{'+}\nu_\ell)$, $\mathcal{B}(B \to D^0 D_s^+)$ and $\mathcal{B}(D_s^+ \to \pi^+\pi^-\pi^+)$. A correlation of -0.91 and $+1$ for the statistical and external uncertainties, respectively, is determined between the two measurements.

The main contribution of this thesis to the $R(D^{(*)0})$ analysis is a model to control the contributions to the irreducible background of inclusive $D_s^+ \to \pi^+\pi^-\pi^+(X)$ decays. The main sources of this background are doubly charmed $B^+ \to \overline{D}^0 D_s^+(X)$ decays. Knowing the relative contributions of the inclusive decays of the D_s^+ into three pions is of fundamental importance in the measurement of $R(D^{(*)0})$ and will also be a cornerstone for other $R(H_c)$ analyses. These results are reported in Fig. 6.26 and show an agreement with the current measurements. Besides, it is important to notice that the $D_s^+ \to \eta'\pi^+\pi^-\pi^+$ and the $D_s^+ \to \pi^+\pi^-\pi^+\pi^0$ decays, undiscovered to the date, have been measured.

Another contribution of this thesis is the development of specific trigger lines for the LHCb Upgrade I data taking. These include the majority of the $H_b \to H_c\tau^+(\to 3\pi\overline{\nu}_\tau)\nu_\tau$ decay channels measured (or currently studied) in the LHCb experiment. The specific charm hadrons are D^*, D^0, D^-, J/ψ, D_s^- and Λ_c^+ and the respective rates are listed in Tab. 7.2. This allows to continue the $R(H_c)$ measurements with 3-prong τ decays with the upgraded detector.

As of today, the experimental results on the combination of $R(D)$ and $R(D^*)$ show a discrepancy with respect to the SM of ~ 3.2 standard deviations. The uncertainties in ratio measurements are expected to improve as shown in Fig. 8.1. This is due to different reasons: the higher statistics, the complementary studies on the form factor parameters and the branching fractions of background decay channels that are being carried out, providing fundamental inputs to future measurements.

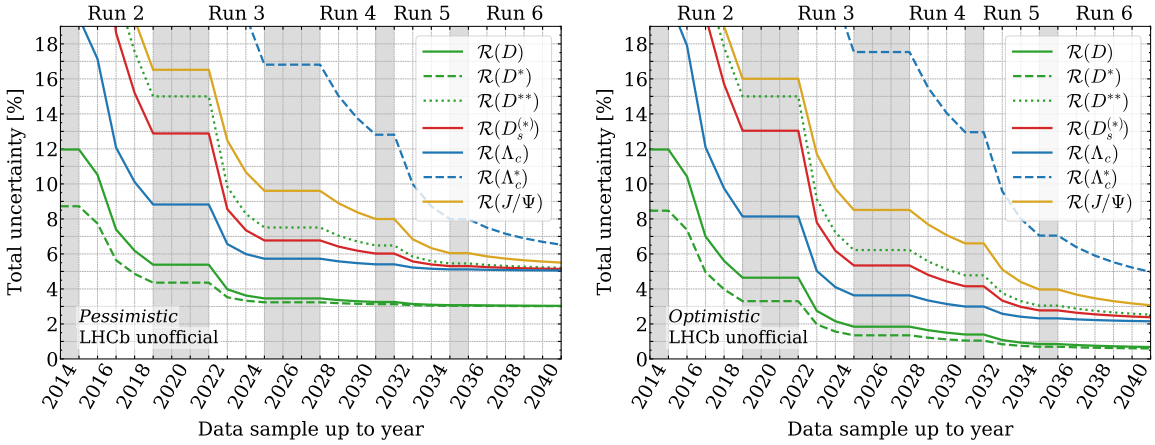

(a) $\sigma^{R(D^*)}_{\text{syst.}} \sim 3\%$ and $\sigma^{R(H_c')}_{\text{syst.}} \sim 5\%$

(b) $\sigma^{R(D^*)}_{\text{syst.}} \sim 0.5\%$ and $\sigma^{R(H_c')}_{\text{syst.}} \sim 2\%$

Figure 8.1: Prospects of the uncertainties of LFU ratios using $H_b \to H_c \tau^+ \nu_\tau$ decays by LHCb as a function of the year [169]. The different colours stand for $H_c = D, D^*, D^{**}, D_s^{(*)}, J/\psi, \Lambda_c^+$ and the grey areas represent the long shutdowns between the different LHC data taking periods.

A

Additional information for the $R_{e/\mu}$ analysis

A.1 Multiple Candidate selection

Year	2015(MU/MD)	2016(MU/MD)
No Selection		
$D^0 \to K^- e^+ \nu_e$	(14.40/14.39)%	(13.18/12.79)%
$D^0 \to K^- \mu^+ \nu_\mu$	(14.37/14.37)%	(12.78/12.56)%
$D^0 \to K^+ e^+ \nu_e$(Same-Sign)	(13.56/13.49)%	(12.37/12.22)%
$D^0 \to K^+ \mu^+ \nu_\mu$(Same-sign)	(12.35/12.47)%	(11.00/10.78)%
Offline Selection Applied		
$D^0 \to K^- e^+ \nu_e$	(12.99/12.90)%	(12.17/11.79)%
$D^0 \to K^- \mu^+ \nu_\mu$	(13.73/13.77)%	(12.66/12.23)%
$D^0 \to K^+ e^+ \nu_e$(Same-Sign)	(11.69/11.47)%	(10.81/10.50)%
$D^0 \to K^+ \mu^+ \nu_\mu$(Same-sign)	(11.88/11.71)%	(10.56/10.23)%

Table A.1: Percentage of multiple candidates in 2015 and 2016 both before and after offline selection. Candidates are chosen randomly.

A.2 YATF templates

The templates used in the YATF fit are represented in Fig. A.1 and A.2 for the muon and electron mode respectively.

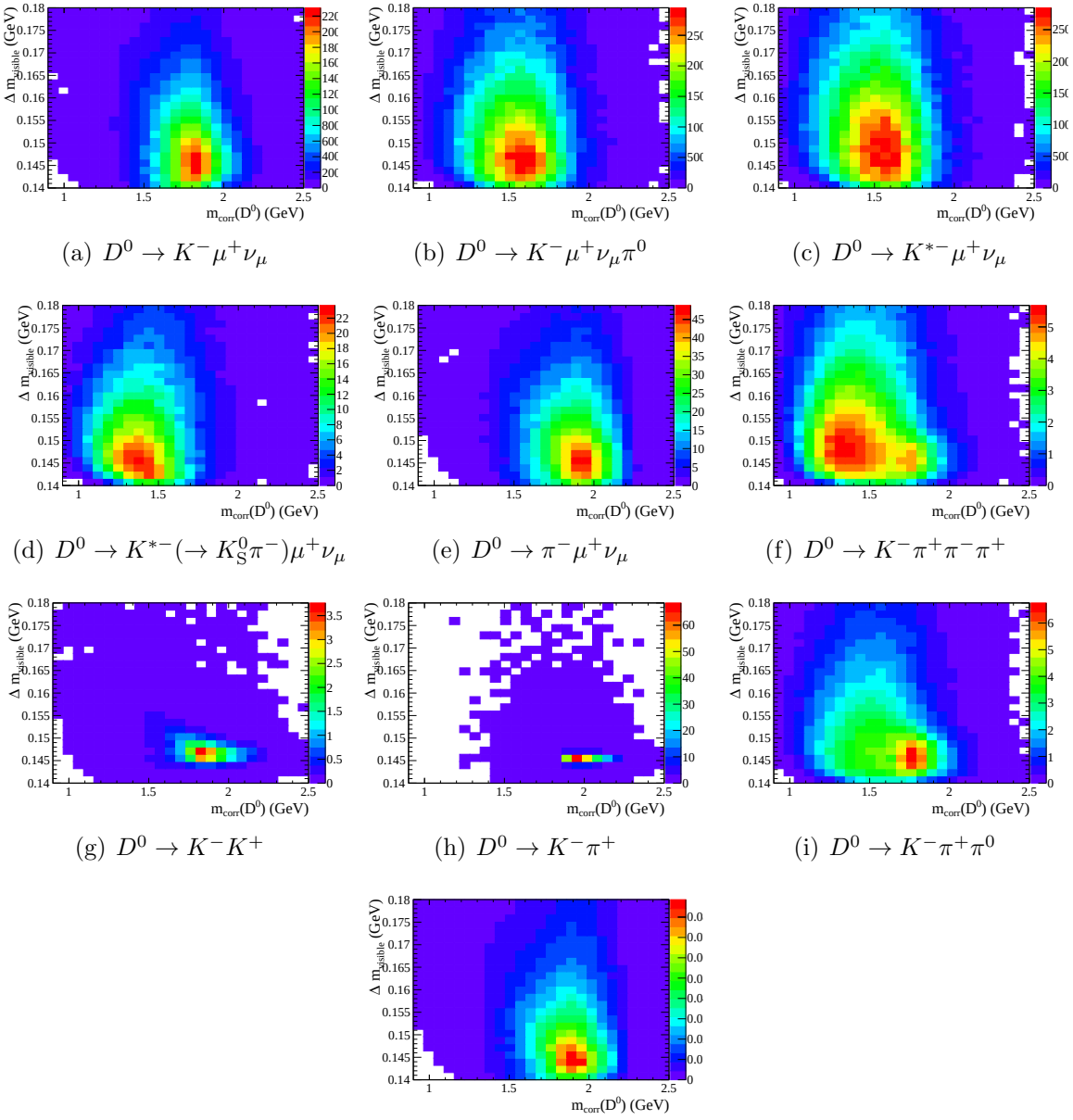

(a) $D^0 \to K^-\mu^+\nu_\mu$ (b) $D^0 \to K^-\mu^+\nu_\mu\pi^0$ (c) $D^0 \to K^{*-}\mu^+\nu_\mu$

(d) $D^0 \to K^{*-}(\to K^0_S\pi^-)\mu^+\nu_\mu$ (e) $D^0 \to \pi^-\mu^+\nu_\mu$ (f) $D^0 \to K^-\pi^+\pi^-\pi^+$

(g) $D^0 \to K^-K^+$ (h) $D^0 \to K^-\pi^+$ (i) $D^0 \to K^-\pi^+\pi^0$

(j) $D^0 \to \pi^+\pi^-\pi^0$

Figure A.1: Two-dimensional template shapes for the muon mode $D^0 \to K^-\mu^+\nu_\mu$. Included are from top left to bottom right, Signal $D^0 \to K^-\mu^+\nu_\mu$, $D^0 \to K^-\mu^+\nu_\mu\pi^0$, $D^0 \to K^{*-}\mu^+\nu_\mu$ with $K^{*-} \to K^-\pi^0$ or $K^-\gamma$, $D^0 \to K^{*-}(\to K^0_S\pi^-)\mu^+\nu_\mu$, $D^0 \to \pi^-\mu^+\nu_\mu$, $D^0 \to K^-\pi^+\pi^-\pi^+$, $D^0 \to K^-K^+$, $D^0 \to K^-\pi^+$, $D^0 \to K^-\pi^+\pi^0$, and $D^0 \to \pi^+\pi^-\pi^0$.

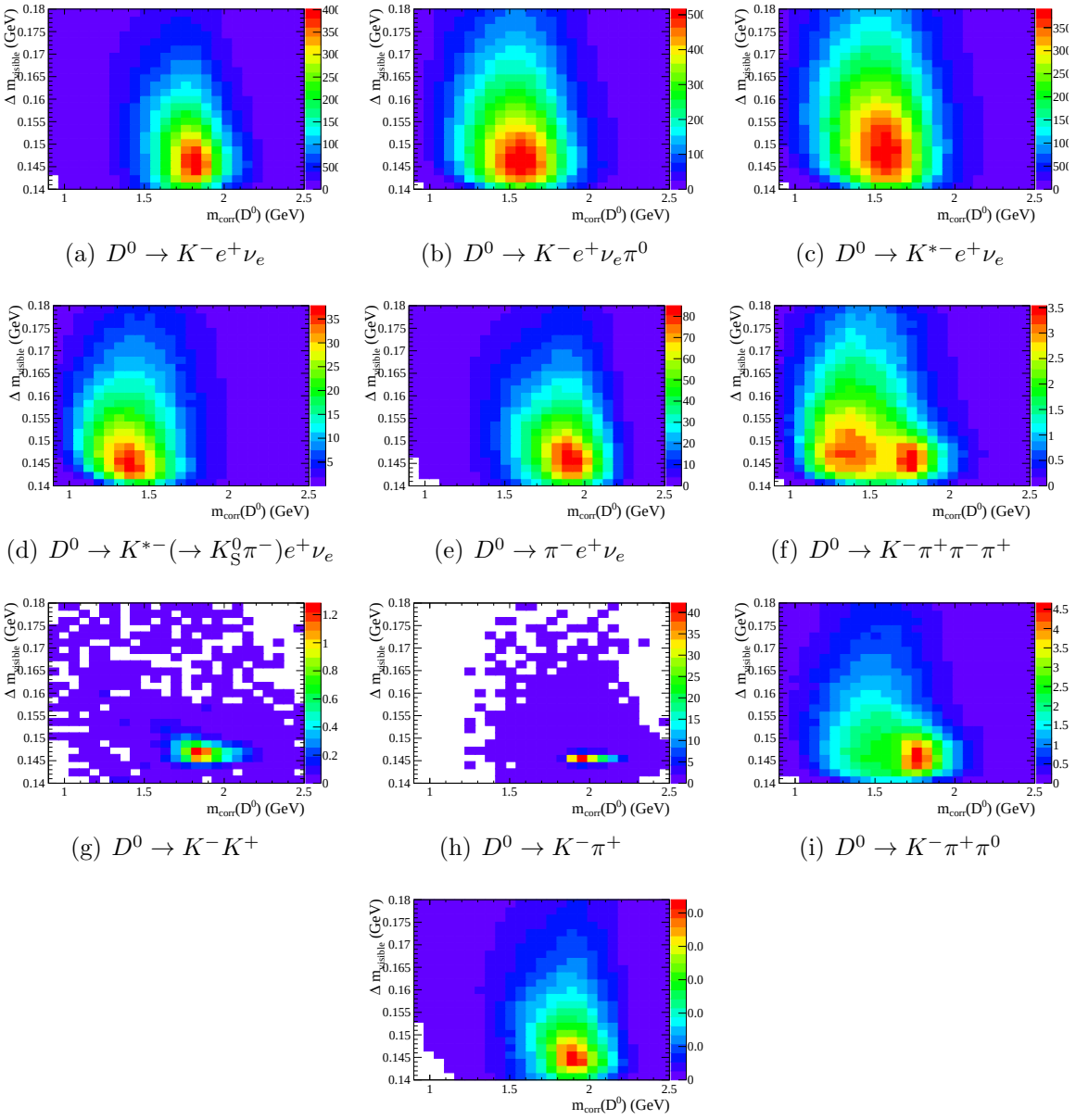

(a) $D^0 \to K^- e^+ \nu_e$ (b) $D^0 \to K^- e^+ \nu_e \pi^0$ (c) $D^0 \to K^{*-} e^+ \nu_e$

(d) $D^0 \to K^{*-}(\to K^0_S \pi^-) e^+ \nu_e$ (e) $D^0 \to \pi^- e^+ \nu_e$ (f) $D^0 \to K^- \pi^+ \pi^- \pi^+$

(g) $D^0 \to K^- K^+$ (h) $D^0 \to K^- \pi^+$ (i) $D^0 \to K^- \pi^+ \pi^0$

(j) $D^0 \to \pi^+ \pi^- \pi^0$

Figure A.2: Two-dimensional template shapes for the electron mode $D^0 \to K^- e^+ \nu_e$. Included are from top left to bottom right, Signal $D^0 \to K^- e^+ \nu_e$, $D^0 \to K^- e^+ \nu_e \pi^0$, $D^0 \to K^{*-} e^+ \nu_e$ with $K^{*-} \to K^- \pi^0$ or $K^- \gamma$,$D^0 \to K^{*-}(\to K^0_S \pi^-) e^+ \nu_e$, $D^0 \to \pi^- e^+ \nu_e$, $D^0 \to K^- \pi^+ \pi^- \pi^+$, $D^0 \to K^- K^+$, $D^0 \to K^- \pi^+$, $D^0 \to K^- \pi^+ \pi^0$, and $D^0 \to \pi^+ \pi^- \pi^0$.

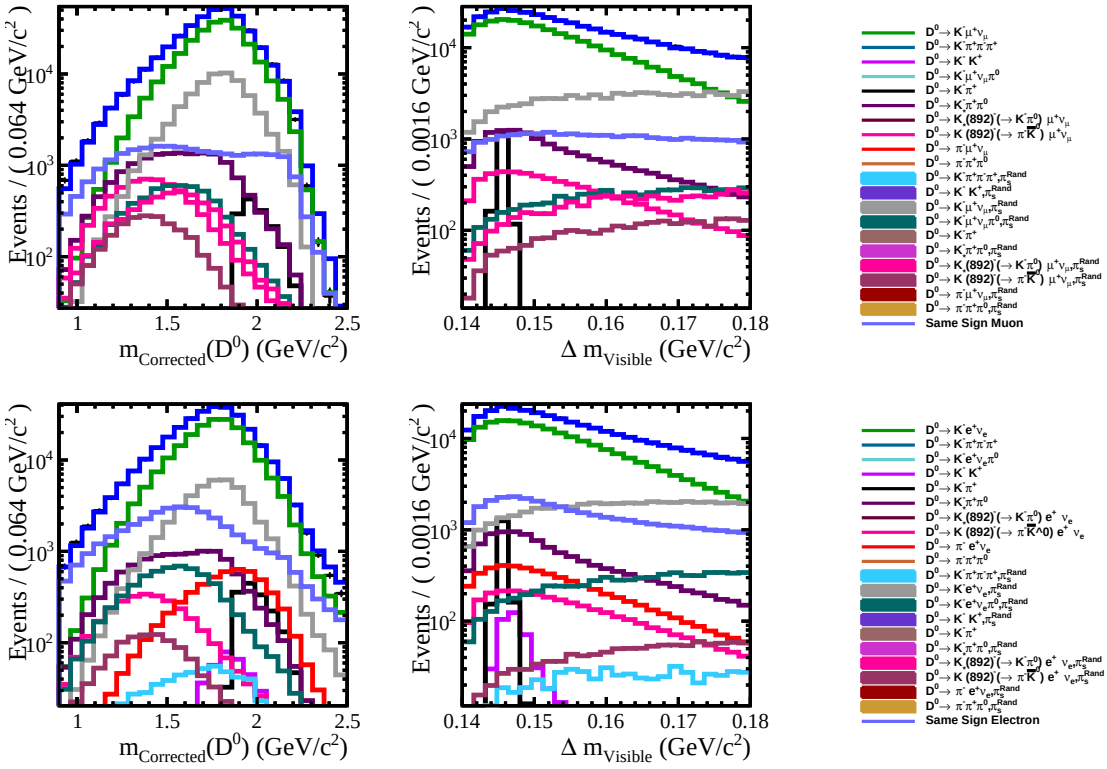

Figure A.3: Fit to 2016 Data for the YATF method in semi-log y scale. The top rows show the projections of the muon modes, the bottom with the projection on the electron modes. On the left is the projection onto the corrected D^0 mass and on the right the projection onto the visible delta mass. The legends for the colors are given on the right. For each model, the total fit is displayed in blue and the data points are in black dots.

A.3 Additional plots and tables for efficiencies calculation

In this section the tables resulting in the efficiency calculation are collected. Tables A.2 and A.3 list the efficiencies calculated for the electrons and the positron respectively divided for the different bremsstrahlung categories, η, p_{T}, year and magnet polarity. Tables A.4 and A.5 represent the summary of the PID efficiencies calculated for the electron and muon mode respectively.

A.3.1 Pion PID efficiency

While the momentum range of pions is covered using π from K^0_{S} decays in PIDCalib, χ^2_{IP} cuts on these pions do not allow for their use. In order to have a similar sample to the selection, the decay $D^{*+} \to D^0(\to K^-\pi^+)\pi^+$ is chosen as a calibration sample and it is obtained from PIDCalib. This requires then a dedicated analysis to extract the efficiency.

First, a minimal selection criterion is applied to the sample. The probe particle is required to be a kaon, by requiring that PID$K > 8$. Afterwards a binned maximum likelihood fit to the delta mass of the D^* and D^0 candidates, Δm is performed to the total sample simultaneously, by comparing the events with the π with PID$e < 1$, *pass*, and *fail*, with PIDe> 1. Ad this point, the efficiency is defined as the ration of the number of the *pass* events over the total number of events:

$$\varepsilon_{\mathrm{PID}\pi} = \frac{N_{\mathrm{pass}}}{(N_{\mathrm{pass}} + N_{\mathrm{fail}})} \tag{A.1}$$

Afterwards, the signal components are fixed, allowing a variation of the width and mean value of the signal shape fit. Fits in bins of $p_T(\pi)$, η, and nSPDHits are then performed separately for magnet polarisations.

Brem category	η	p_T [GeV/c]	MU 2015	MD 2015	MU 2016	MD 2016
No brem added	$1.4-2.5$	$0-2$	$0.650^{+0.025}_{-0.025}$	$0.673^{+0.029}_{-0.030}$	$0.682^{+0.010}_{-0.011}$	$0.698^{+0.009}_{-0.010}$
		$2-50$	$0.650^{+0.017}_{-0.018}$	$0.681^{+0.020}_{-0.021}$	$0.655^{+0.007}_{-0.007}$	$0.646^{+0.007}_{-0.007}$
	$2.5-3.5$	$0-2$	$0.509^{+0.015}_{-0.015}$	$0.498^{+0.017}_{-0.017}$	$0.593^{+0.006}_{-0.006}$	$0.550^{+0.006}_{-0.006}$
		$2-3.5$	$0.560^{+0.020}_{-0.020}$	$0.531^{+0.023}_{-0.023}$	$0.500^{+0.008}_{-0.008}$	$0.494^{+0.008}_{-0.008}$
		$3.5-50$	$0.486^{+0.016}_{-0.016}$	$0.447^{+0.018}_{-0.018}$	$0.497^{+0.005}_{-0.005}$	$0.498^{+0.006}_{-0.006}$
	$3.5-5.1$	$0-2$	$0.219^{+0.018}_{-0.017}$	$0.213^{+0.019}_{-0.018}$	$0.273^{+0.009}_{-0.008}$	$0.269^{+0.009}_{-0.008}$
		$2-50$	$0.259^{+0.023}_{-0.021}$	$0.188^{+0.025}_{-0.023}$	$0.249^{+0.009}_{-0.009}$	$0.268^{+0.009}_{-0.009}$
With brem added	$1.4-2.5$	$0-2$	$0.781^{+0.030}_{-0.033}$	$0.869^{+0.030}_{-0.038}$	$0.865^{+0.012}_{-0.013}$	$0.829^{+0.012}_{-0.013}$
		$2-50$	$0.903^{+0.010}_{-0.011}$	$0.868^{+0.013}_{-0.014}$	$0.906^{+0.004}_{-0.004}$	$0.904^{+0.004}_{-0.004}$
	$2.5-3.5$	$0-2$	$0.807^{+0.016}_{-0.017}$	$0.835^{+0.017}_{-0.018}$	$0.862^{+0.006}_{-0.006}$	$0.863^{+0.006}_{-0.006}$
		$2-3.5$	$0.871^{+0.013}_{-0.014}$	$0.812^{+0.018}_{-0.019}$	$0.864^{+0.005}_{-0.006}$	$0.863^{+0.005}_{-0.006}$
		$3.5-50$	$0.848^{+0.010}_{-0.010}$	$0.817^{+0.012}_{-0.013}$	$0.851^{+0.004}_{-0.004}$	$0.857^{+0.003}_{-0.004}$
	$3.5-5.1$	$0-2$	$0.632^{+0.028}_{-0.029}$	$0.654^{+0.033}_{-0.035}$	$0.631^{+0.012}_{-0.012}$	$0.691^{+0.011}_{-0.011}$
		$2-50$	$0.587^{+0.025}_{-0.026}$	$0.574^{+0.029}_{-0.029}$	$0.578^{+0.009}_{-0.009}$	$0.652^{+0.009}_{-0.009}$

Table A.2: Efficiency table for electrons (e^-) for the two bremsstrahlung categories: top without and bottom with bremsstrahlung, split by year and magnet polarity.

Brem category	η	p_T [GeV/c]	MU 2015	MD 2015	MU 2016	MD 2016
No brem added	$1.4-2.5$	$0-2$	$0.747^{+0.024}_{-0.026}$	$0.671^{+0.029}_{-0.030}$	$0.688^{+0.010}_{-0.010}$	$0.657^{+0.010}_{-0.010}$
		$2-50$	$0.684^{+0.018}_{-0.018}$	$0.679^{+0.021}_{-0.021}$	$0.652^{+0.007}_{-0.007}$	$0.653^{+0.007}_{-0.007}$
	$2.5-3.5$	$0-2$	$0.495^{+0.016}_{-0.017}$	$0.493^{+0.017}_{-0.017}$	$0.587^{+0.006}_{-0.006}$	$0.608^{+0.006}_{-0.006}$
		$2-3.5$	$0.545^{+0.019}_{-0.019}$	$0.497^{+0.023}_{-0.023}$	$0.483^{+0.008}_{-0.008}$	$0.513^{+0.008}_{-0.008}$
		$3.5-50$	$0.527^{+0.016}_{-0.016}$	$0.521^{+0.019}_{-0.019}$	$0.493^{+0.006}_{-0.006}$	$0.482^{+0.006}_{-0.006}$
	$3.5-5.1$	$0-2$	$0.156^{+0.014}_{-0.013}$	$0.210^{+0.020}_{-0.019}$	$0.294^{+0.009}_{-0.009}$	$0.263^{+0.008}_{-0.008}$
		$2-50$	$0.233^{+0.023}_{-0.021}$	$0.218^{+0.020}_{-0.019}$	$0.281^{+0.009}_{-0.009}$	$0.240^{+0.009}_{-0.008}$
With brem added	$1.4-2.5$	$0-2$	$0.780^{+0.030}_{-0.034}$	$0.791^{+0.033}_{-0.038}$	$0.862^{+0.012}_{-0.013}$	$0.816^{+0.012}_{-0.013}$
		$2-50$	$0.904^{+0.010}_{-0.011}$	$0.875^{+0.013}_{-0.014}$	$0.906^{+0.004}_{-0.004}$	$0.904^{+0.004}_{-0.004}$
	$2.5-3.5$	$0-2$	$0.824^{+0.015}_{-0.016}$	$0.789^{+0.018}_{-0.019}$	$0.873^{+0.006}_{-0.006}$	$0.867^{+0.005}_{-0.006}$
		$2-3.5$	$0.853^{+0.013}_{-0.014}$	$0.859^{+0.016}_{-0.018}$	$0.881^{+0.005}_{-0.005}$	$0.852^{+0.006}_{-0.006}$
		$3.5-50$	$0.838^{+0.010}_{-0.011}$	$0.837^{+0.012}_{-0.012}$	$0.851^{+0.004}_{-0.004}$	$0.842^{+0.004}_{-0.004}$
	$3.5-5.1$	$0-2$	$0.569^{+0.028}_{-0.029}$	$0.731^{+0.031}_{-0.034}$	$0.728^{+0.011}_{-0.011}$	$0.651^{+0.011}_{-0.011}$
		$2-50$	$0.561^{+0.026}_{-0.026}$	$0.523^{+0.028}_{-0.028}$	$0.668^{+0.009}_{-0.009}$	$0.553^{+0.009}_{-0.009}$

Table A.3: Efficiency table for positrons (e^+) for the two bremsstrahlung categories: top without and bottom with bremsstrahlung, split by year and magnet polarity.

Channel	$\epsilon_{PID}(K)(\%)$	$\epsilon_{PID}(\pi_s)(\%)$	Lepton $\epsilon_{PID}(\%)$	Total Efficiency (%)
$D^0 \to K^-\mu^+\nu_\mu$	78.3955 ± 0.0002	99.0222 ± 0.0030	0.0275 ± 0.0052	0.0212 ± 0.0040
$\boldsymbol{D^0 \to K^-e^+\nu_e}$	79.0514 ± 0.0000	99.0624 ± 0.0002	76.2040 ± 0.0001	59.2810 ± 0.0001
$D^0 \to K^-\mu^+\nu_\mu\pi^0$	79.0753 ± 0.0019	99.0582 ± 0.0604	0.0020 ± 0.0046	0.0014 ± 0.0037
$D^0 \to K^-e^+\nu_e\pi^0$	79.3955 ± 0.0000	99.0443 ± 0.0005	75.2433 ± 0.0002	58.7273 ± 0.0003
$D^0 \to K^{*-}\mu^+\nu_\mu$	79.0872 ± 0.0005	99.0159 ± 0.0089	0.0391 ± 0.0202	0.0254 ± 0.0131
$D^0 \to K^{*-}e^+\nu_e$	79.5914 ± 0.0000	99.0430 ± 0.0005	75.2074 ± 0.0002	58.8600 ± 0.0003
$D^0 \to K^{*-}(\to \pi^-K^0)\mu^+\nu_\mu$	0.8660 ± 0.0001	98.9470 ± 0.0096	0.0457 ± 0.0214	0.0004 ± 0.0002
$D^0 \to K^{*-}(\to \pi^-K^0)e^+\nu_e$	0.8650 ± 0.0000	98.9902 ± 0.0006	77.0005 ± 0.0003	0.6474 ± 0.0000
$D^0 \to \pi^-\mu^+\nu_\mu$	0.9101 ± 0.0002	99.0127 ± 0.0125	0.0579 ± 0.0320	0.0004 ± 0.0002
$D^0 \to \pi^-e^+\nu_\mu$	0.9052 ± 0.0000	99.0565 ± 0.0005	76.8579 ± 0.0002	0.6764 ± 0.0000
$D^0 \to K^-3\pi$	78.8924 ± 0.0000	99.0251 ± 0.0005	0.1004 ± 0.0000	0.0790 ± 0.0000
$D^0 \to K^-K^+$	77.9784 ± 0.0000	99.0833 ± 0.0007	0.0040 ± 0.0000	0.0032 ± 0.0000
$D^0 \to K^-\pi^+\pi^0$	78.7622 ± 0.0000	99.0258 ± 0.0006	0.1039 ± 0.0000	0.0817 ± 0.0000
$D^0 \to \pi^+\pi^-\pi^0$	0.9013 ± 0.0000	99.0456 ± 0.0007	0.1146 ± 0.0000	0.0010 ± 0.0000
$D^0 \to K^-\pi^+$	77.8523 ± 0.0001	99.0628 ± 0.0010	0.1156 ± 0.0000	0.0909 ± 0.0000

Table A.4: Summary of PID efficiencies for the nominal binning for modes reconstructed as $D^0 \to K^-e^+\nu_e$. Highlighted in bold is the signal mode $D^0 \to K^-e^+\nu_e$

.

Channel	$\epsilon_{PID}(K)(\%)$	$\epsilon_{PID}(\pi_s)(\%)$	Lepton $\epsilon_{PID}(\%)$	Total Efficiency (%)
$\boldsymbol{D^0 \to K^-\mu^+\nu_\mu}$	78.5503 ± 0.0000	99.0754 ± 0.0002	46.0656 ± 2.5428	36.3660 ± 2.0639
$D^0 \to K^-e^+\nu_e$	78.7531 ± 0.0002	98.9842 ± 0.0044	0.0654 ± 0.0200	0.0495 ± 0.0147
$D^0 \to K^-\mu^+\nu_\mu\pi^0$	78.9078 ± 0.0000	99.0699 ± 0.0005	46.9611 ± 5.4248	37.1728 ± 4.2722
$D^0 \to K^-e^+\nu_e\pi^0$	79.6866 ± 0.0033	98.9354 ± 0.0532	0.0248 ± 0.1923	0.0167 ± 0.1489
$D^0 \to K^{*-}\mu^+\nu_\mu$	79.1700 ± 0.0000	99.0713 ± 0.0004	46.8640 ± 5.2864	37.1784 ± 4.2173
$D^0 \to K^{*-}e^+\nu_e$	79.0697 ± 0.0007	98.9635 ± 0.0143	0.0786 ± 0.0141	0.0619 ± 0.0102
$D^0 \to K^{*-}(\to \pi^-K^0)\mu^+\nu_\mu$	0.8629 ± 0.0000	99.0275 ± 0.0006	47.7302 ± 4.4793	0.3974 ± 0.0419
$D^0 \to K^{*-}(\to \pi^-K^0)e^+\nu_e$	0.8692 ± 0.0002	98.9134 ± 0.0164	0.0687 ± 0.1106	0.0008 ± 0.0013
$D^0 \to \pi^-\mu^+\nu_\mu$	0.9076 ± 0.0000	99.0655 ± 0.0005	46.1306 ± 4.4828	0.4014 ± 0.0397
$D^0 \to \pi^-e^+\nu_\mu$	0.9099 ± 0.0002	98.9884 ± 0.0164	0.0634 ± 0.0141	0.0006 ± 0.0001
$D^0 \to K^-3\pi$	78.7757 ± 0.0000	99.0171 ± 0.0006	0.1871 ± 0.0000	0.1469 ± 0.0000
$D^0 \to K^-K^+$	77.8480 ± 0.0000	99.0705 ± 0.0008	0.0118 ± 0.0000	0.0092 ± 0.0000
$D^0 \to K^-\pi^+\pi^0$	78.6350 ± 0.0000	99.0173 ± 0.0007	0.1850 ± 0.0000	0.1451 ± 0.0000
$D^0 \to \pi^+\pi^-\pi^0$	0.9027 ± 0.0000	99.0327 ± 0.0008	0.1811 ± 0.0000	0.0015 ± 0.0000
$D^0 \to K^-\pi^+$	77.7016 ± 0.0001	99.0510 ± 0.0011	0.1739 ± 0.0000	0.1360 ± 0.0000

Table A.5: Summary of PID efficiencies for the nominal binning for modes reconstructed as $D^0 \to K^-\mu^+\nu_\mu$. Highlighted in bold is the signal mode $D^0 \to K^-\mu^+\nu_\mu$

.

A.4 Additional plots for q^2 studies

The alignment between q^2_{reco} and q^2_{true} can be seen from the folding matrix of Figure A.4. This matrix is used to unfold the true q^2 from the reconstructed. This is done first for cone closure method then for the GF one. Fig. A.5 and A.6 represents the q^2 resolution plots for the cone closure and the GF methods respectively. The candle plots in the bottom row are produced from the one on the top one. The circles represent the mean, while the central solid line in the boxes represents the median value of the distribution. The left and right edges of the box show the lower and upper quartiles, respectively. Finally, the range of values is represented by the dashed lines.

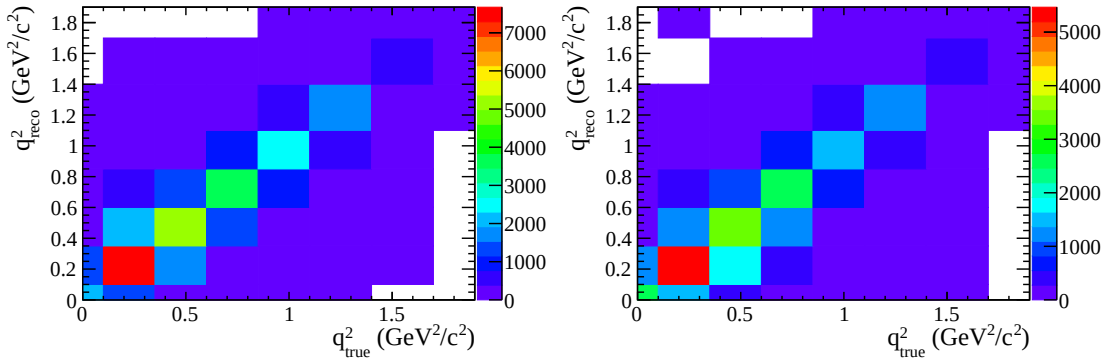

Figure A.4: Folding matrices of q^2_{reco} versus q^2_{true} for the $D^0 \to K^-\mu^+\nu_\mu$ (left) and $D^0 \to K^-e^+\nu_e$ channel (right).

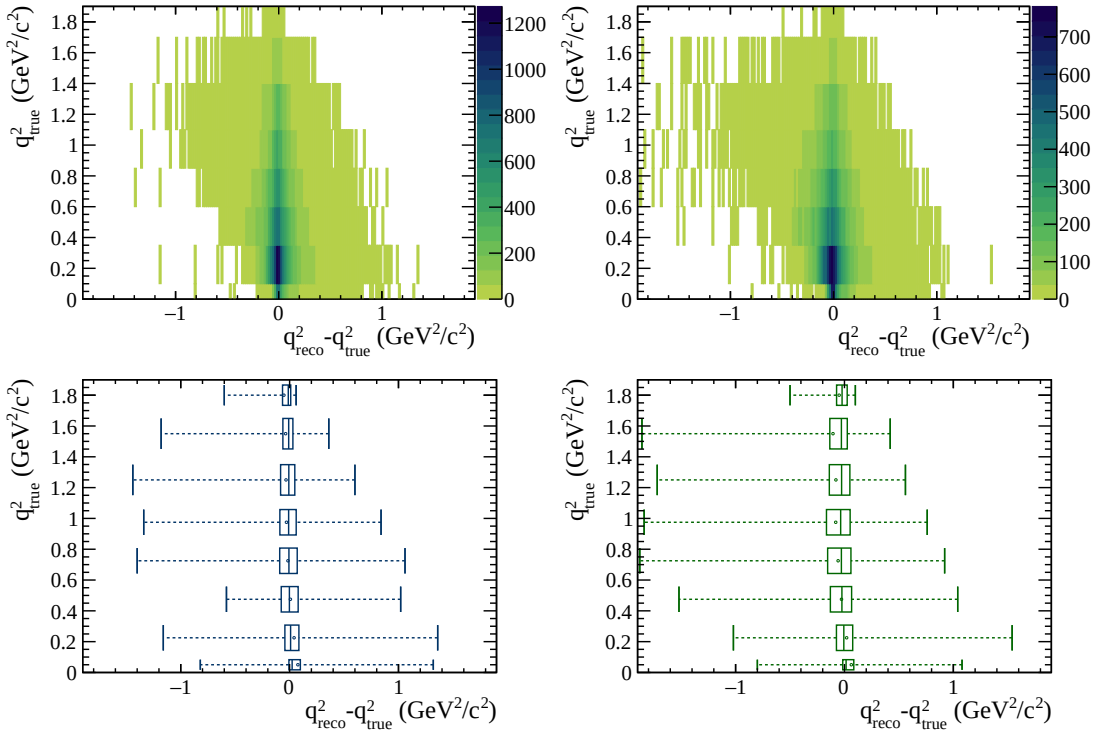

Figure A.5: Resolution plots for q^2_{reco} obtained using the cone closure method. Top: $q^2_{\text{reco}} - q^2_{\text{true}}$ with the nominal q^2_{true} binning for the $D^0 \to K^-\mu^+\nu_\mu$ (left) and $D^0 \to K^-e^+\nu_e$ (right) channel. Bottom: Candle plots produced of the top 2D plots.

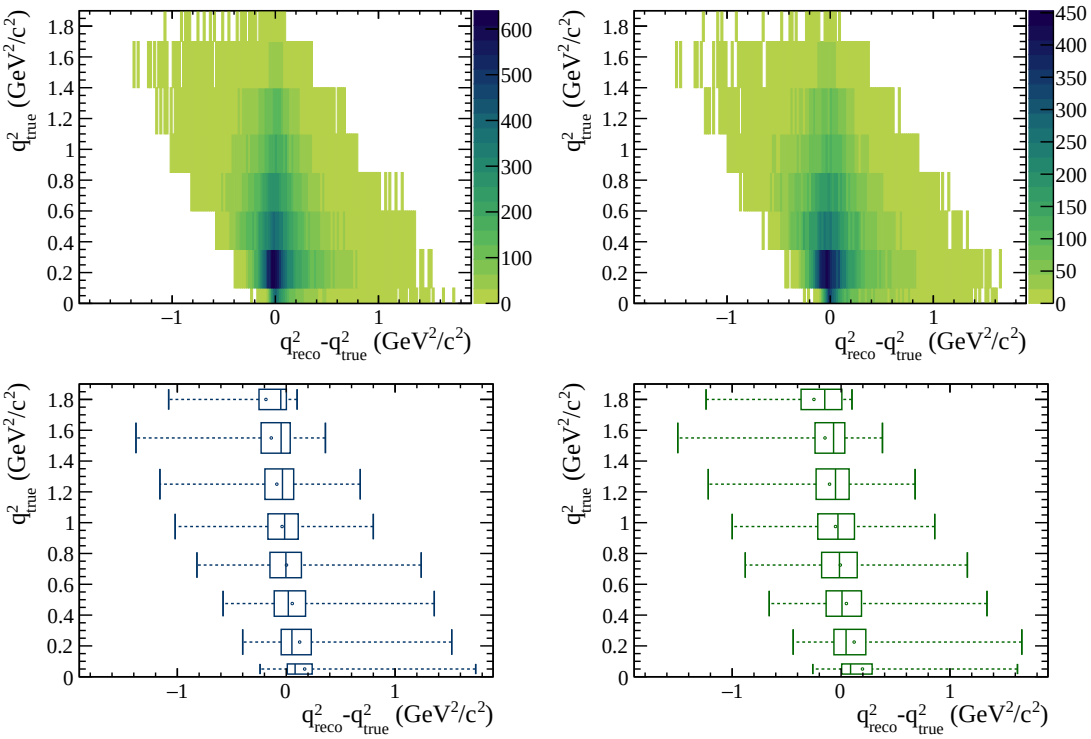

Figure A.6: Resolution plots for q^2_{reco} obtained using the GF algorithm. Top: $q^2_{\text{reco}} - q^2_{\text{true}}$ with the nominal q^2_{true} binning for the $D^0 \to K^-\mu^+\nu_\mu$ (left) and $D^0 \to K^-e^+\nu_e$ (right) channel. Bottom: Candle plots produced of the top 2D plots.

B

Additional plots for the $R(D^{(*)0})$ analysis

B.1 Signal events reconstruction

In this section, the distributions of the reconstructed τ and B momentum of the $B^+ \to \overline{D}^0 \tau^+ \nu_\tau$ and $B^+ \to \overline{D}^{*0} \tau^+ \nu_\tau$ decays are presented, together with the respective resolutions: in Fig. B.1, the τ, and in Fig. B.2, the B meson distributions.

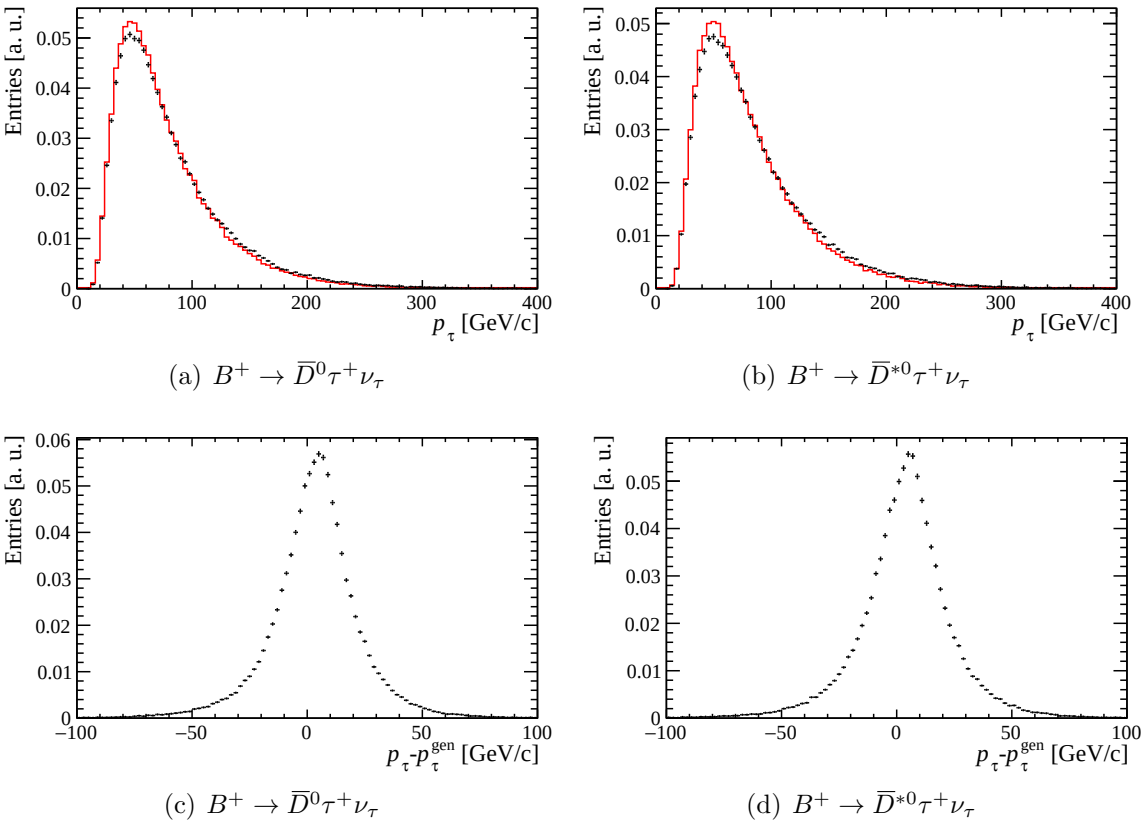

(a) $B^+ \to \overline{D}^0\tau^+\nu_\tau$ (b) $B^+ \to \overline{D}^{*0}\tau^+\nu_\tau$

(c) $B^+ \to \overline{D}^0\tau^+\nu_\tau$ (d) $B^+ \to \overline{D}^{*0}\tau^+\nu_\tau$

Figure B.1: Estimated (black) and generated (red) τ momentum distributions (top row) together with the respective resolution $p_\tau - p_\tau^{gen}$ (bottom row) for $B^+ \to \overline{D}^0\tau^+\nu_\tau$ decays on the left and $B^+ \to \overline{D}^{*0}\tau^+\nu_\tau$ decays on the right, with $\tau^+ \to \pi^+\pi^-\pi^+\overline{\nu}_\tau$.

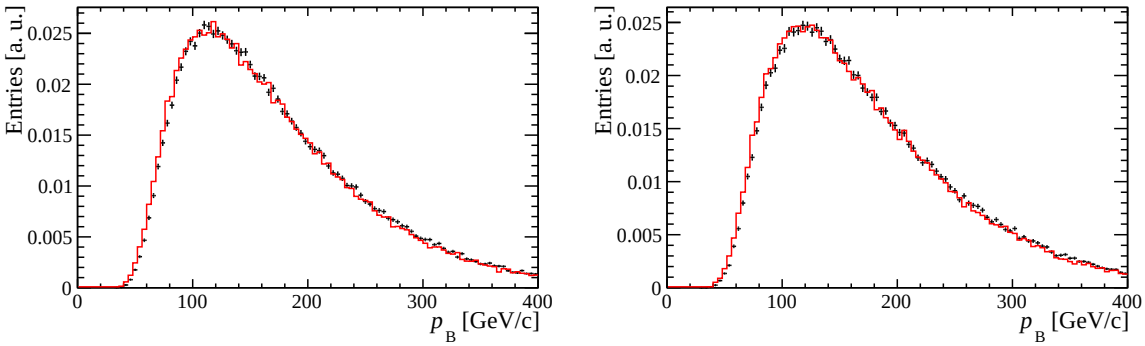

(a) $B^+ \to \overline{D}^0\tau^+\nu_\tau$

(b) $B^+ \to \overline{D}^{*0}\tau^+\nu_\tau$

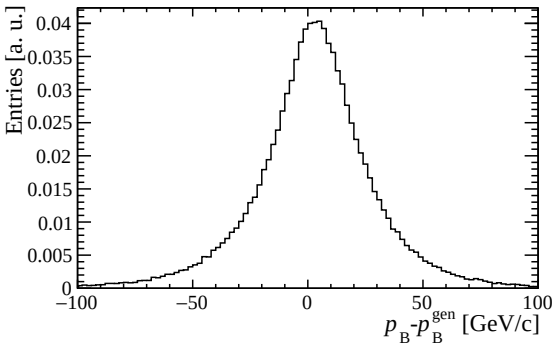

(c) $B^+ \to \overline{D}^0\tau^+\nu_\tau$

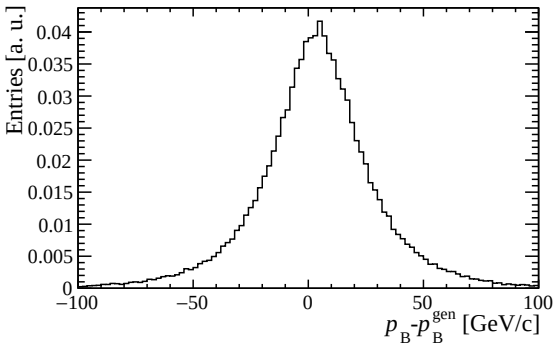

(d) $B^+ \to \overline{D}^{*0}\tau^+\nu_\tau$

Figure B.2: Estimated (black) and generated (red) B momentum ditributions (top row) and the respective resolution $p_B - p_B^{gen}$ (bottom row) for $B^+ \to \overline{D}^0\tau^+\nu_\tau$ (left) and $B^+ \to \overline{D}^{*0}\tau^+\nu_\tau$ (right) decays, with $\tau^+ \to \pi^+\pi^-\pi^+\overline{\nu}_\tau$.

B.2 Additional plots for the $D_s^+ \to \pi^+\pi^-\pi^+(X)$ decay model

As a cross-check, the output of the BDT is represented using the same selection of the control samples.

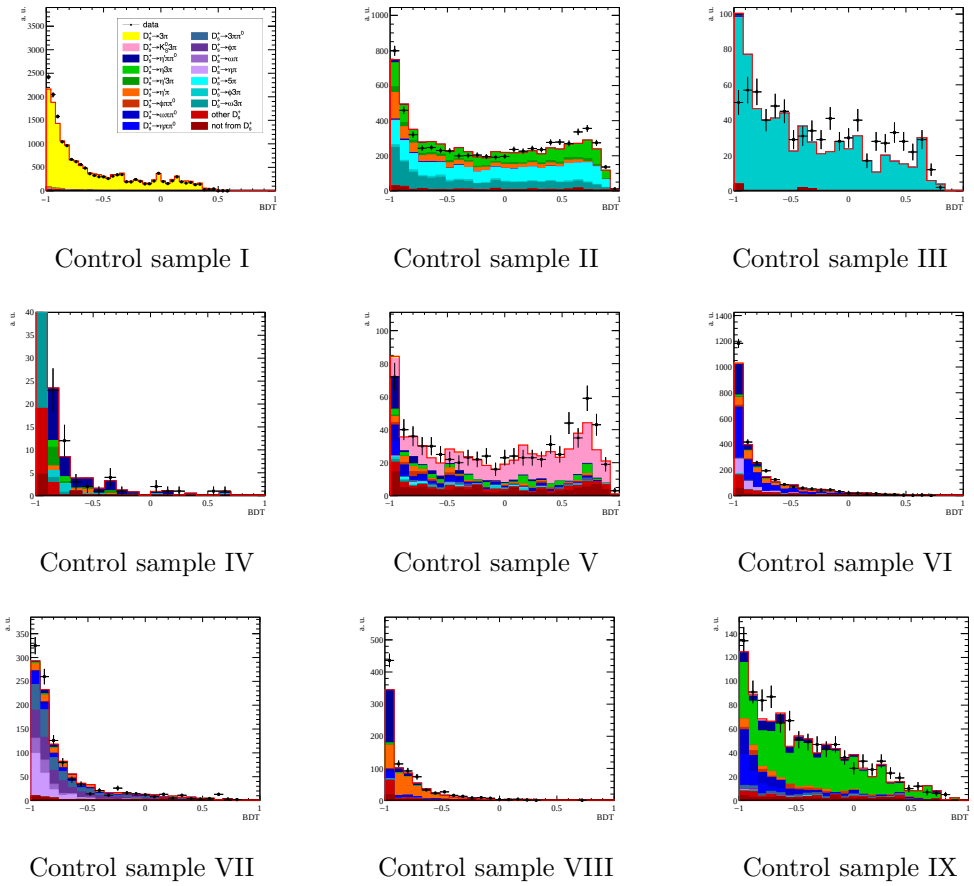

Control sample I | Control sample II | Control sample III

Control sample IV | Control sample V | Control sample VI

Control sample VII | Control sample VIII | Control sample IX

Figure B.3: BDT distribution for the control samples. The control samples are specified in each caption.

C

Resumo da tese

C.1 Motivación teórica e fenomenolóxica

O Modelo Estándar (SM) é a teoría que describe a dinámica dos constituíntes fundamentais do Universo, as partículas elementais e as súas interaccións, con excepción da gravidade. No SM, as tres xeracións de leptóns cargados son idénticas excepto polas súas masas. Os bosóns de *gauge* electrofeble γ, $W^{\pm}$ e Z acóplanse do mesmo xeito coas tres xeracións de leptóns (e, μ e τ). Esta peculiaridade coñécese como Universalidade Leptónica de Sabor (LFU) e está relacionada coa estrutura do SM, polo que é un moi bo laboratorio de pescudas de nova física.

Os resultados recentes das probas de LFU en transicións semileptónicas $b \to c\ell\nu$ e decaementos raros de $b \to s\ell\ell$ apuntan a unha violación da LFU. Pódese probar a Universalidade Leptónica de Sabor comparando o acoplamento nas desintegracións semileptonicas dos hadróns con sabor pesado, que conteñen un c-quark ou un b-quark.

Os observables experimentais preferidos para probar LFU son as fracións das taxas de desintegración con diferentes sabores de leptón nos estados finais (ℓ, ℓ'), como

$$R(q^2) = \frac{\mathrm{d}\Gamma^{(\ell')}}{\mathrm{d}q^2} \Big/ \frac{\mathrm{d}\Gamma^{(\ell)}}{\mathrm{d}q^2}. \tag{C.1}$$

Unha das principais vantaxes destes observables é que as incertezas de parametrización do factor de forma se anulan parcialmente na relación. Ademais, se hai neutrinos no estado final, só se consideran neutrinos dunha xeración, facendo irrelevante calquera contribución da mestura de neutrinos.

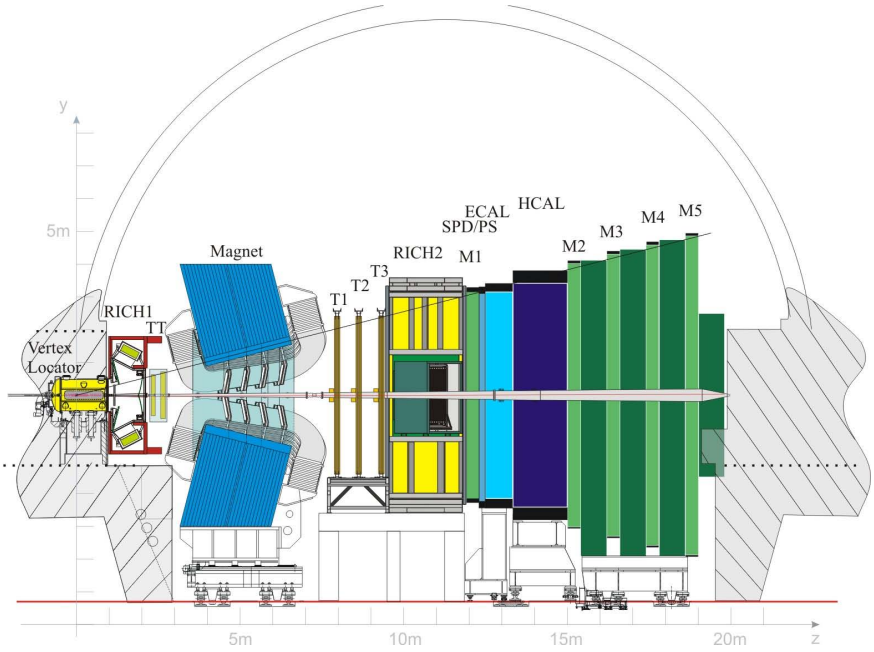

Figura C.1: Representación esquematica do detector LHCb e dos seus subdetectores. De esquerda a dereita: VELO, RICH1, TT, imán, as tres estacións de traza, RICH2, SPD, PS, calorímetro electromagnético (ECAL), calorímetro de hadróns (HCAL) e os detectores de muóns [102].

C.2 O experimento LHCb

O experimento LHCb [102] está dedicado a realizar medidas de física de sabores pesados e é un lugar excelente para buscar evidencias indirectas de NP. O experimento LHCb recolleu datos de colisións protón-protón en dous períodos, con diferentes condicións: Run 1 (2010-2012), cunha enerxía de centro de masa, $\sqrt{s}$, de 7 e 8 TeV e Run 2 (2015-2018) con $\sqrt{s} = 13$ TeV. A combinación das dúas mostras de datos corresponde a unha luminosidade integrada de 9 fb^{-1}, 3 e 6 fb^{-1}, respectivamente. Na Figura C.1 represéntase unha vista esquemática do detector LHCb, cos seus subdetectores e o imán. Segundo a funcionalidade, os subdetectores pódense dividir en dúas categorías: sistemas de reconstrución de trazas e identificación de partículas (PID).

C.3 Proba de Universalidade Leptónica de Sabor con desintegracións $D^0 \to K^-\ell^+\nu_\ell$

A Universalidade Leptónica de Sabor pódese probar estudando as relacións de fracción de ramificación, como se indica na Sección C.1. Para as transicións $c \to s\ell\nu_\ell$, o observable

considerado é $R_{\mu/e}$,

$$R_{\mu/e} = \frac{\mathcal{B}(D^0 \to K^- \mu^+ \nu_\mu)}{\mathcal{B}(D^0 \to K^- e^+ \nu_e)}. \tag{C.2}$$

A medida de $R_{\mu/e}$ ten como obxectivo realizar unha proba de LFU empregando desintegracións $D^0 \to K^- \ell^+ \nu_\ell$. A topoloxía para estas desintegracións represéntase na Figura 5.1. Os candidatos a D^0 orixínanse en decaementos *prompt*[1] $D^{*+} \to D^0 \pi^+$. Os candidatos D^{*+} son seleccionados para orixinarse directamente desde o punto de interacción pp (PV), onde o pión voa a través do detector producindo unha traza cun momento medio duns 5 GeV/c, e chamase pión *brando*. Finalmente, o D^0 decae a través da interacción feble despois dun voo duns centímetros formando un vértice de desintegración secundaria (SV), desprazado do PV. Téñase en conta que as desintegracións de carga conxugada están implícitas, a non ser que se indique o contrario.

Os principais retos deste estudo débense á presenza dun electrón e de neutrinos nos estados finais. Os electróns perden enerxía a través da radiación *bremsstrahlung*, polo que a resolución e a eficiencia de detección son inferiores á dos muóns (véxanse Sección 4.3.1.1 e Sección 4.3.2.1). Polo tanto, no canto de medir a razón de fracción de ramificación de muóns sobre electróns, $R_{\mu/e}$, prefírese a súa inversa:

$$R_{e/\mu} = R_{\mu/e}^{-1} = \frac{\mathcal{B}(D^0 \to K^- e^+ \nu_e)}{\mathcal{B}(D^0 \to K^- \mu^+ \nu_\mu)}. \tag{C.3}$$

Para ter en conta a presenza de neutrinos, desenvolvéronse dúas estratexias: o método chamado "cone closure" e o método "Global Fit" (GF) descritos en detalle na Sección 5.5. O algoritmo GF pretende dar conta do neutrino realizando un axuste á cinemática da desintegración.

O valor de $R_{e/\mu}$ obtense coa taxa do número de eventos de sinal, N_e e N_μ, corrixida polas eficiencias, $\varepsilon_{tot}(\ell)$,

$$R_{e/\mu} = \frac{N(D^0 \to K^- e^+ \nu_e)}{N(D^0 \to K^- \mu^+ \nu_\mu)} \times \frac{\varepsilon_{tot}(\mu)}{\varepsilon_{tot}(e)}. \tag{C.4}$$

Esta estratexia para obter a relación de fracción de ramificación é moi similar a outras probas de LFU, como a da análise $R(D^{(*)0})$. Para realizala, desenvólvense dous *templates* de axuste que permiten obter as producións do sinal $D^0 \to K^- \ell^+ \nu_\ell$. Unha vez avaliados, un dos dous métodos de axuste empregarase como referencia e o outro como comprobación.

As eficiencias da Ecuación (5.3) obtéñense co produto das contribucións,

$$\varepsilon_{tot}(\ell) = \varepsilon_{acc} \cdot \varepsilon_{rec|acc} \cdot \varepsilon_{sel|rec} \cdot \varepsilon_{PID|sel}. \tag{C.5}$$

A aceptancia de LHCb contabilízase en ε_{acc}; $\varepsilon_{rec|acc}$ representa a eficiencia de reconstrución despois de formar os candidatos na aceptancia do detector; $\varepsilon_{sel|rec}$ é a eficiencia de selección, despois de aplicar todos criterios de selección e $\varepsilon_{PID|sel}$ representa a eficiencia

[1] O decamento *prompt* é mediado pola interacción forte e as partículas do estado final prodúcense no mésmo vértice que a súa nai.

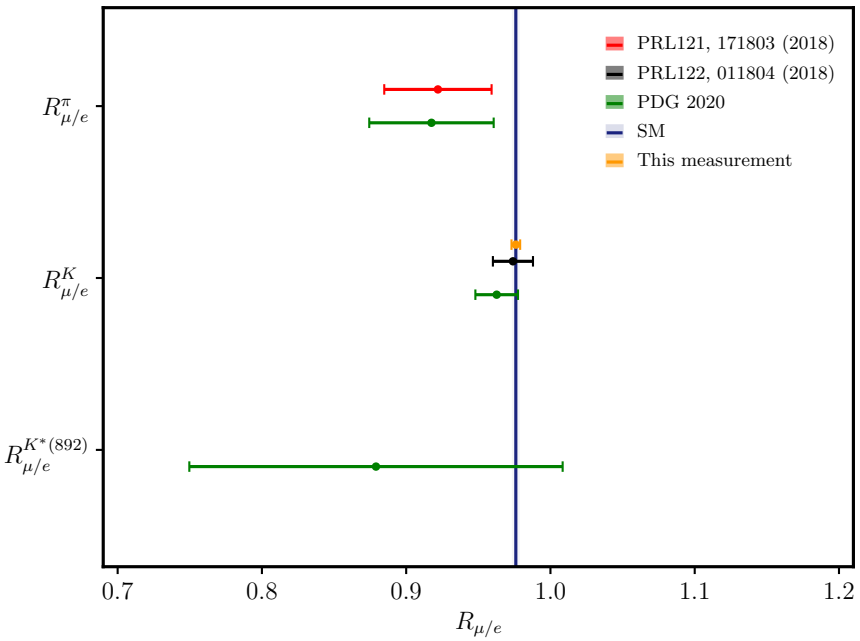

Figura C.2: Comparación das medidas de $R_{\mu/e}$ coas predicións teoricas. O resultado desta tese para $R_{\mu/e}$ está centrado no valor da predición teorica de modelo estándar.

de identificación de partículas dada a eficiencia de selección. Cada unha das eficiencias baséase no paso anterior e todas se calculan a partir da simulación, agás a eficiencia PID, que se calcula a partir de mostras de datos dedicadas, ben utilizando algoritmos PIDCalib (véxase a Sección 4.3.2) ou outros métodos desenvolvidos especificamente para esta análise, como os introducidos na Sección 4.3.2.1. Finalmente, co obxectivo de explotar a sensibilidade de $R_{e/\mu}$ a nova física, este estudo farase en intervalos da masa de dileptón ao cadrado, q^2. Isto non está incluído nesta tese, onde se presentan resultados preliminares en toda a rexión de q^2 integrado.

C.3.1 Modelos de axustes

As producións das desintegracións $D^0 \to K^-\mu^+\nu_\mu$ (N_μ) e $D^0 \to K^-e^+\nu_e$ (N_e) e, en consecuencia, $R_{e/\mu}$ (Eq. 5.3), extráense con dúas estratexias de axuste. Realízanse dous axustes bidimensionais simultáneos aos mesmos conxuntos de datos utilizando diferentes variables. Estes dous marcos ou *templates* denomínanse *YATF* e *SAGF*, onde se introduciron os acrónimos para diferenciar o axuste que usa os resultados do algoritmo de axuste global (GF), o *SAGF*, do YATF. As producións de sinal extraídas de ambos axustes

compáranse para comprobar a consistencia. Os dous modelos inclúen $R_{e/\mu}$ como

$$N_e = N_\mu \cdot R_{e/\mu}. \tag{C.6}$$

Isto garante que as incertezas se propaguen correctamente. O valor de $R_{e/\mu}$ cégase usando a aplicación `RooBlindCategory` [151], que aplica un desprazamento aleatorio do resultado central deixando a incerteza sen cambios. A semente deste desprazamento baséase na mesma cadea de caracteres para ambos os axustes. Deste xeito, é posible comparar os resultados para comprobar a consistencia dos dous axustes sen revelar o verdadeiro valor central. Nos dous axustes o sinal e as formas de fondo son tomadas da simulación mediante modelos bidimensionais e para cada modelo o único parámetro de axuste é a súa produción.

O axuste *YATF* usa a diferenza entre as masas visibles do D^{*+} e D^0 e a masa corrixida do D^0 como variables:

$$\Delta m_{\text{visible}} = m(K^-\ell^+\pi_s^+) - m(K^-\ell^+), \tag{C.7}$$

$$m_{\text{corr}}(D^0) = \sqrt{m(K\ell)^2 + {p'_{\text{T}}}^2} + |p'_{\text{T}}|, \tag{C.8}$$

onde p'_{T} é o momento transversal do sistema $K\ell$ con respecto da dirección de voo do D^0. O axuste está implementado usando o *framework* chamado `HistFactory`. Isto permite usar a técnica de Barlow-Beeston [152], incorporada para ter conta das incertezas estatísticas nos modelos.

O axuste *SAGF*, como suxire o acrónimo, depende dos resultados do algoritmo GF. A masa invariante do D^{*+}, $m_{GF}(D^{*+})$, obtense mediante o momento do neutrino estimado polo GF. A masa visible D^0, $m_{vis} = m(K\ell)$, é a outra variable de axuste.

Inicialmente, para ter os métodos o mais independentes posible, a idea era realizar un axuste analítico no SAGF; porén, despois dalgúns estudos preliminares, adoptouse un enfoque de axuste de modelo bidimensional polos dous modelos. O efecto do tamaño limitado das mostras de MC no resultado do axuste estímase como unha incerteza sistemática ao repetir o axuste utilizando novas mostras obtidas modificando cada intervalo do modelo cunha flutuación que segue a distribución de Poisson.

Ambos métodos de axuste dependen do feito de que as variables proporcionan unha boa separación entre os modos de sinal e de fondo. Para probar a coherencia entre as dúas estratexias, xéranse datos de pseudoexperimento con valores dados de $R_{e/\mu}$. Con estes datos móstranse ambos axustes para dar resultados compatibles, validando o método.

Os modelos bidimensionais prepáranse usando os mesmos conxuntos de datos de simulación para os dous axustes, ademais da pequena fracción de candidatos para os que o algoritmo de GF non consegue converxer (véxase Sección 5.5.3). As canles de desintegración consideradas nos modelos están listadas na Táboa 5.8 e son seleccionadas mediante cortes de PID sobre toda a cadea de decaemento.

As canles consideradas no modelo pódense clasificar nas seguintes tipoloxías:

i. **Canles de sinal.** $D^0 \to K^-\mu^+\nu_\mu$, modo muónico e $D^0 \to K^-e^+\nu_e$, modo electrónico, onde o D^0 vén de desintegracións $D^{*+} \to D^0\pi^+$.

ii. **Canles de fondo parcialmente reconstruídas** (Part-Reco), que conteñen un kaón e un leptón no estado final e unha partícula neutra que non se detecta. As canles consideradas son $D^{*+} \to D^0\pi^+$ con $D^0 \to K^-\ell^+\nu_\ell\pi^0$, onde a parella $K^-\pi^0$ pode ser non resoante ou de desintegracións de K^{*-}, $D^0 \to K^{*-}(\to K^-\gamma)\ell^+\nu_\ell$, $D^0 \to K^{*-}(\to K^-\pi^0)\ell^+\nu_\ell$ or $D^0 \to (K^{*-} \to \bar{K}^0\pi^-)\ell^+\nu_\ell$.

iii. **Canles de fondo mal identificadas** (misID) onde un pión ou un kaón se identifica como o leptón e/ou un pión se identifica como o kaón. O D^{*+} decae como $D^{*+} \to D^0\pi^+$. Onde a desintegración $D^0 \to \pi^-\ell^+\nu_\ell$ e as desintegracións hadronicas do D^0: $D^0 \to K^-K^+$, $D^0 \to K^-\pi^+\pi^0$, $D^0 \to K^-\pi^+\pi^+\pi^-$, $D^0 \to \pi^-\pi^+\pi^0$ e $D^0 \to K^-\pi^+$ son consideradas. Algunhas destas desintegracións tamén son parcialmente reconstruídas.

iv. **Desintegracións con pións aleatorios.** O pión brando procedente da desintegración $D^{*+} \to D^0\pi^+$ elíxese facéndoo coincidir cun D^0 na desintegración mentres que o candidato a D^{*+} non coincida coa mesma nai do D^0. Estes son un *proxy* do fondo combinatorio D^{*+}.

v. **Sinal co mesmo signo.** As desintegracións de $D^0 \to K^+\ell^+\nu_\ell$ empréganse como *proxy* combinatorio para os modos respectivos. Estes obtéñense polas liñas de separación dedicadas descritas na Sección 5.3.

Paga a pena notar que non todas as canles contribúen aos modos cos muóns e electróns. Isto compróbase mirando as taxas de identificación errónea. Para algunhas destas canles non sobrevive ningún candidato despois da selección do PID do modo muón ou electrón: todas as canles onde o leptón estaría mal identificado co outro leptón non se consideran no modelo porque a súa contribución é moi pequena. Ao final, dun total de 32 contribucións posibles, só se utilizan 21 para cada modo nos axustes, das que 11 son específicas de leptón (vexase Táboa 5.8). A cada canle, independentemente do axuste considerado, aplícanselle pesos relativos ao PID, á traza e á multiplicidade de eventos.

Para avaliar a calidade do axuste, prodúcense gráficos de *pull* en dúas dimensións (pull(i_x, i_y)) para os dous modos. Para considerar os erros do modelo total, estes calcúlanse do seguinte xeito. Sendo $(i_x, i_y)_{\text{datos}}$ e $(i_x, i_y)_{\text{modelo}}$ a poboación do intervalo (i_x, i_y) do histograma de datos e do modelo, respectivamente, pull(i_x, i_y) defínese como

$$\text{pull}(i_x, i_y) = \frac{(i_x, i_y)_{\text{data}} - (i_x, i_y)_{\text{model}}}{\sqrt{\sigma^2_{\text{data}} + \sigma^2_{\text{model}}}}, \tag{C.9}$$

onde a incerteza, σ_{datos}, é a raíz cadrada da ocupación do intervalo (i_x, i_y) e σ_{modelo} é o erro asociado ao intervalo (i_x, i_y) do histograma do modelo.

C.3.2 SAGF fitter

O axuste SAGF emprega un modelo bidimensional que considera simultaneamente a masa do sistema $K\ell$ e a masa D^{*+} reconstruída co algoritmo de GF (m_{GF}). As variables

empregadas no modelo usan unha división en 25×25 intervalos. As mostras de datos e simulación prodúcense co mesmo procedemento do axuste YATF, coa única adición de que o algoritmo GF teña éxito (véxase Sección 5.5.3); polo tanto, hai unha eficiencia do sinal lixeiramente menor debido a este requirimento adicional. As formas de modelo bidimensionais represéntanse nas Figuras 5.12 e 5.13 para o estado final con muón e electrón, respectivamente.

Na Figura C.3 amósanse as proxeccións do axuste nas dúas variables $m(K\ell)$ e m_{GF}, tanto para o estado final co muón como para co electrón. Os *pulls* bidimensionais obtidos usando a Ecuación (C.9) móstranse na Figura C.4. Todos os parámetros libres obtidos co axuste están listados na Táboa 5.10. Considerando as contribucións de fondo, unha gran fracción dos modos cun pión aleatorio son compatibles con cero, como é visible nas proxeccións de axuste e cando se comparan as producións. A produción do modo muón de sinal mídese como $N_{\mu}^{\mathrm{SAGF}} = (1.794 \pm 0.032) \times 10^5$, sendo as incertezas só debidas á estatística. Finalmente, obtemos $R_{e/\mu}^{\mathrm{SAGF}} = X.XXXX \pm 0.0027$ que, tendo conta da eficiencia dos cortes debidos ao axuste do GF (véxase Táboa 5.15), resulta $N_{\mu}^{\mathrm{SAGF}} = (2.135 \pm 0.038) \times 10^5$. Estes son compatibles co resultado do axuste YATF, $N_{\mu}^{\mathrm{YATF}} = (2.6470 \pm 0.0051) \times 10^5$ e $R_{e/\mu}^{\mathrm{YATF}} = X.XXXX \pm 0,002$ respectivamente.

C.3.3 Resultados cegados e conclusións

Dado que a análise aínda está cegada, non se coñece o resultado final de $R_{e/\mu}$. Non obstante, é posible avaliar as incertezas para poder comparar o valor cos outros resultados anteriores de $R_{e/\mu}$. O valor $R_{e/\mu}$ final obtido por esta análise é

$$R_{e/\mu} = x.xxx \pm 0.003\ (\mathrm{stat.}) \pm 0.014\ (\mathrm{syst.}), \tag{C.10}$$

onde a primeira incerteza é a estatística, mentres que a segunda é a estimación da sistemática obtida na Sección 5.8.

Para poder comparar este resultado co $R_{\mu/e}$ de medicións anteriores, investigouse $R_{e/\mu}^{-1}$. O valor central tómase da predición do SM [27] mentres que os erros propáganse da medida obtendo

$$R_{\mu/e} = R_{e/\mu}^{-1} = x.xxx \pm 0.003\ (\mathrm{stat.}) \pm 0.013\ (\mathrm{syst.}). \tag{C.11}$$

A Figura C.2 representa a comparación desta medida, centrada na predición do SM, coa medición anterior da colaboración BESIII e as razóns de fracción de ramificación.

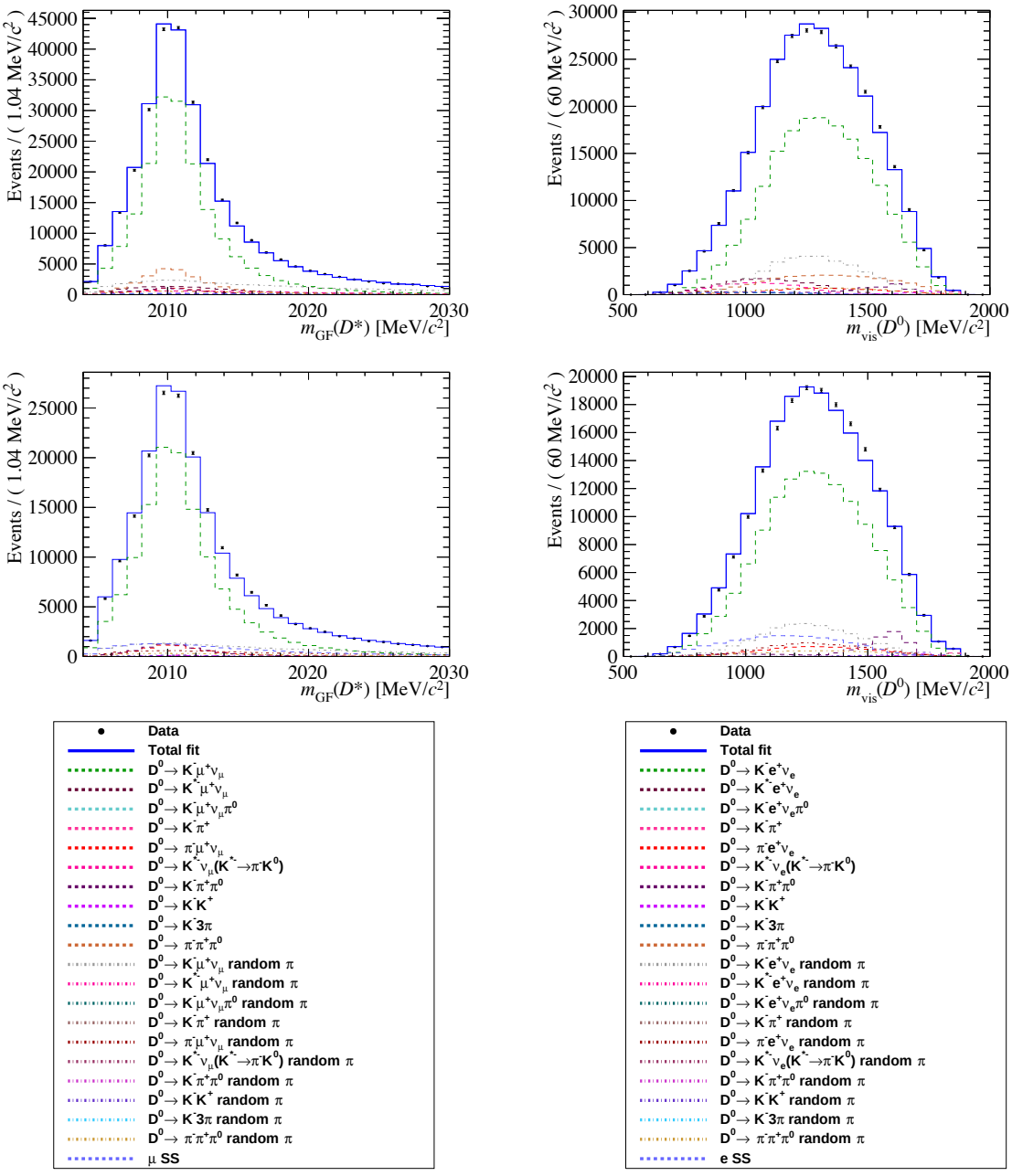

Figura C.3: Proxección dos resultados do axuste SAGF (m_{GF}-esquerda, $m(K\ell)$-dereita). Modo muón: parte superior, modo electrón: parte inferior.

Parameter	**Fit result**
$\boldsymbol{R_{e/\mu}}$	$x.xxx \pm 0.013$
$\boldsymbol{N_\mu(D^0 \to K^-\mu^+\nu_\mu)}$	179400 ± 3200
$N_\mu(D^0 \to K^{*-}\mu^+\nu_\mu)$	14200 ± 2100
$N_\mu(D^0 \to K^{*-}(\to \pi^- K^0_S)\mu^+\nu_\mu\ )$	9700 ± 1400
$N_\mu(D^0 \to K^-\mu^+\nu_\mu\pi^0)$	0 ± 660
$N_\mu(D^0 \to \pi^-\mu^+\nu_\mu)$	6700 ± 2500
$N_\mu(D^0 \to \pi^-\pi^+\pi^0)$	24100 ± 3000
$N_\mu(D^0 \to K^-\pi^+)$	323 ± 29
$N_\mu(D^0 \to K^-\pi^+\pi^0)$	6860 ± 640
$N_\mu(D^0 \to K^-\pi^+\pi^-\pi^+)$	1800 ± 1700
$N_\mu(D^0 \to K^-K^+)$	1200 ± 200
$N_\mu(D^0 \to K^+\mu^+\nu_\mu)$ SS	2700 ± 3800
$N_e(D^0 \to K^+e^+\nu_e)$ SS	16000 ± 740
$N_e(D^0 \to K^-e^+\nu_e\pi^0)$	0 ± 73
$N_e(D^0 \to \pi^-e^+\nu_e)$	7000 ± 240
$N_e(D^0 \to \pi^-\pi^+\pi^0)$	0 ± 190
$N_e(D^0 \to K^-\pi^+)$	293 ± 46
$N_e(D^0 \to K^-\pi^+\pi^0)$	7400 ± 350
$N_e(D^0 \to K^-\pi^+\pi^-\pi^+)$	0 ± 110
$N_e(D^0 \to K^-K^+)$	539 ± 200
Random π:	
$N_e(D^0 \to K^-e^+\nu_e)$	20100 ± 1700
$N_e(D^0 \to K^-K^+)$	1200 ± 300
$N_e(D^0 \to K^-\pi^+)$	294 ± 55
$N_e(D^0 \to K^-\pi^+\pi^0)$	100 ± 17
$N_e(D^0 \to \pi^-e^+\nu_e)$	8800 ± 1400
$N_e(D^0 \to \pi^-\pi^+\pi^0)$	4400 ± 1300
$N_\mu(D^0 \to K^-\pi^+\pi^-\pi^+)$	0 ± 190
$N_\mu(D^0 \to K^-\mu^+\nu_\mu)$	34800 ± 1600
$N_\mu(D^0 \to K^-\pi^+\pi^0)$	200 ± 200
$N_\mu(D^0 \to K^{*-}\mu^+\nu_\mu)$	0 ± 210
$N_\mu(D^0 \to K^{*-}(\to \pi^- K^0_S)\mu^+\nu_\mu)$	0 ± 150
$N_\mu(D^0 \to \pi^-\pi^+\pi^0)$	7700 ± 1300

Táboa C.1: Resultados do SAGF Fitter. O valor de $R_{e/\mu}$ e de N_μ^{SAGF} de sinal están representados en negriña. Na parte inferior da táboa amosanse todas as canles cun pión *random*.

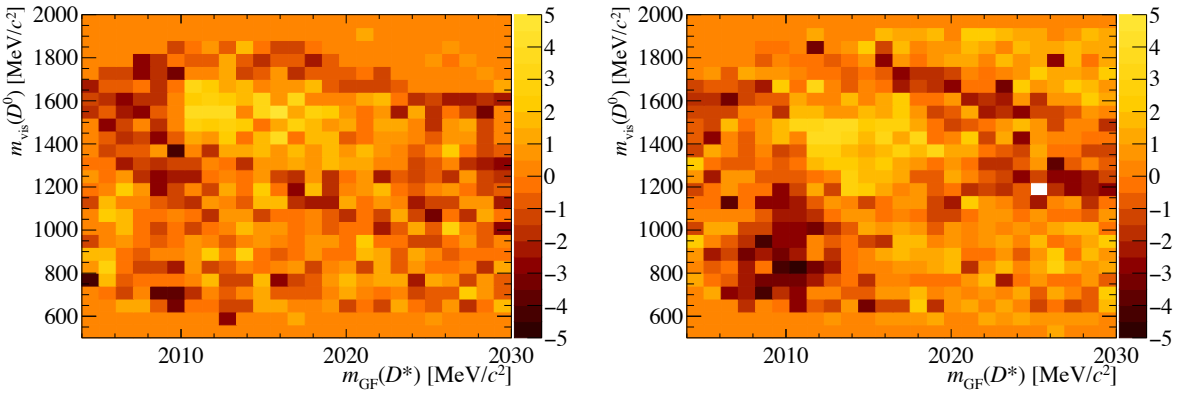

Figura C.4: *Pulls* bidimensionais do axuste SAGF. Modo muónico á esquerda, modo electrónico á dereita.

C.4 Proba de Universalidade Leptónica de Sabor con desintegracións $B \to D^{(*)0}\tau^+\nu_\tau$

Esta análise ten como obxectivo probar LFU medindo as razóns de fracción de ramificación $R(D^0)$ e $R(D^{*0})$, definidas como

$$R(D^0) = \frac{\mathcal{B}(B^+ \to \overline{D}^0\tau^+\nu_\tau)}{\mathcal{B}(B^+ \to \overline{D}^0\ell^+\nu_\ell)}, \tag{C.12}$$

$$R(D^{*0}) = \frac{\mathcal{B}(B^+ \to \overline{D}^{*0}\tau^+\nu_\tau)}{\mathcal{B}(B^+ \to \overline{D}^{*0}\ell^+\nu_\ell)}, \tag{C.13}$$

onde ℓ representa un electrón ou un muón. A topoloxía do decaemento do sinal móstrase na Figura 6.1. Algunhas características relevantes da estratexia de análise son:

- O leptón τ reconstrúese usando os modos de desintegración $\tau^+ \to \pi^+\pi^-\pi^+\overline{\nu}_\tau$ e $\tau^+ \to \pi^+\pi^-\pi^+\pi^0\overline{\nu}_\tau$.
- O $\overline{D}^0$ reconstrúese coa desintegración $\overline{D}^0 \to K^+\pi^-$.
- O mesón $\overline{D}^{*0}$ decae nunha $\overline{D}^0$ e unha partícula neutra: $\overline{D}^0\pi^0$, cunha fracción de ramificación de $(64,7 \pm 0,9)\%$ [1] ou $\overline{D}^{*0} \to \overline{D}^0\gamma$, con $\mathcal{B}$ de $(35,3 \pm 0,9)\%$ [1]. A partícula neutra adicional non se reconstrúe.

Do mesmo xeito que na análise $R_{e/\mu}$, presentada en Sección C.3, hai neutrinos no estado final, e as partículas visibles no estado final son catro pións cargados e un kaón. O uso de taxas permite investigar de forma independente o numerador e o denominador. Nesta tese, os denominadores de Ecuacións (C.12) e (C.13), $\mathcal{B}(B^+ \to \overline{D}^{(*)0}\ell^+\nu_\ell)$, tómanse de fontes externas. Estas fraccións de ramificación foron medidas polas colaboracións

CLEO, BaBar e Belle con boa precisión e recóllense na Táboa 6.1. Para os decaementos $B^+ \to \overline{D}^{(*)0}\tau^+\nu_\tau$ escóllese un modo de normalización co mesmo estado final que o decaemento do sinal. Deste xeito, as incertezas sistemáticas debidas á reconstrución son parcialmente canceladas na fracción. Na medición hadrónica anterior de $R(D^{*-})$ [53, 54], utilizouse o decaemento $B^0 \to D^{*-}3\pi$ como canle de normalización. Para este estudo, a desintegración $B^+ \to \overline{D}^0 3\pi$, é dicir, $B^+ \to \overline{D}^0\pi^+\pi^-\pi^+$, considerouse como primeira opción. Non obstante, a súa fracción de ramificación mídese cunha incerteza de case o 40% [1]. Polo tanto, optouse pola desintegración $B^+ \to \overline{D}^0 D_s^+$, onde se escolle que $D_s^+ \to 3\pi$. A relación de ramificación medida de $B^+ \to \overline{D}^0 D_s^+$ é $(9,9 \pm 0,1) \times 10^{-3}$ [1] e a da desintegración $D_s^+ \to 3\pi$ é igual a $(1,08 \pm 0,04)\%$ [1].

Considerando as canles de normalización, as Ecuacións (C.12) e (C.13) pódense reescribir como

$$R(D^{(*)0}) = \mathcal{K}(D^{(*)0}) \left(\frac{\mathcal{B}(B^+ \to \overline{D}^0 D_s^+)\mathcal{B}(D_s^+ \to 3\pi)}{\mathcal{B}(B^+ \to \overline{D}^{(*)0}\ell^+\nu_\ell)} \right)_{\text{ext.}} , \tag{C.14}$$

aquí, como se comentou anteriormente, as fraccións de ramificación do segundo factor son tomadas de fontes externas [1, 60]: $\mathcal{B}(B^+ \to \overline{D}^0 D_s^+) = (9.0 \pm 0.9) \times 10^{-3}$ e $\mathcal{B}(D_s^+ \to \pi^+\pi^-\pi^+) = (1.08 \pm 0.04)\%$. A proporción $\mathcal{K}(D^{(*)0})$ defínese como

$$\mathcal{K}(D^{(*)0}) = \frac{\mathcal{B}(B^+ \to \overline{D}^{*0}\tau^+\nu_\tau)}{\mathcal{B}(B^+ \to \overline{D}^0 D_s^+)\mathcal{B}(D_s^+ \to \pi^+\pi^-\pi^+)} . \tag{C.15}$$

Así, o obxectivo da análise é obter $\mathcal{K}(D^{(*)0})$ en función do sinal e as producións da normalización. Tendo en conta as eficiencias de sinal e normalización,

$$\mathcal{K}(D^{(*)0}) = \frac{N(B^+ \to \overline{D}^{(*)0}\tau^+\nu_\tau)}{N(B^+ \to \overline{D}^0 D_s^+)} \cdot \frac{\varepsilon_{\text{norm}}}{\varepsilon_{\text{sig}}} . \tag{C.16}$$

A relación de eficiencia $\varepsilon_{\text{norm}}/\varepsilon_{\text{sig}}$ está definida como

$$\frac{\varepsilon_{\text{norm}}}{\varepsilon_{\text{sig}}} = \frac{\varepsilon_{B^+\to\overline{D}^0 D_s^+}}{\varepsilon^{\tau^+\to\pi^+\pi^-\pi^+\overline{\nu}_\tau}_{B^+\to\overline{D}^{(*)0}\tau^+\nu_\tau}\mathcal{B}(\tau^+ \to \pi^+\pi^-\pi^+\overline{\nu}_\tau) + \varepsilon^{\tau^+\to\pi^+\pi^-\pi^+\pi^0\overline{\nu}_\tau}_{B^+\to\overline{D}^{(*)0}\tau^+\nu_\tau}\mathcal{B}(\tau^+ \to \pi^+\pi^-\pi^+\pi^0\overline{\nu}_\tau)} , \tag{C.17}$$

onde $\varepsilon_{B^+\to\overline{D}^0 D_s^+}$ é a eficiencia de normalización, $\varepsilon^{\tau^+\to 3\pi(\pi^0)\nu_\tau}_{B^+\to\overline{D}^{(*)0}\tau^+\nu_\tau}$ son as eficiencias dos sinais en relación aos modos de desintegración τ e as fraccións de ramificación das desintegracións do τ son $\mathcal{B}(\tau^+ \to \pi^+\pi^-\pi^+\overline{\nu}_\tau) = (0.0902 \pm 0.0005)$ e $\mathcal{B}(\tau^+ \to \pi^+\pi^-\pi^+\pi^0\overline{\nu}_\tau) = 0.0449 \pm 0.0005$ [1].

O sinal e as producións na Ecuación (6.5) obtéñense con dúas estratexias de axuste diferentes. Para obter $N(B^+ \to \overline{D}^{(*)0}\tau^+\nu_\tau)$, emprégase un modelo tridimensional que axusta ao momento transferido do sistema $\tau\nu$, q^2, o tempo de desintegración do tau, t_τ e a saída dun Boosted Decision Tree (BDT). Por outra banda, úsase un modelo unidimensional axustado á masa invariante $m(D^0 D_s^+)$ para obter a produción $N(B^+ \to \overline{D}^0 D_s^+)$.

Co obxectivo de illar o sinal e os modos de decaemento da normalización, é de suma importancia comprender todas as contribucións do fondo. As maiores orixínanse en desintegracións co mesmo estado final cargado de 4π e un K^+.

A principal compoñente de fondo antes da selección débese ás desintegracións *prompt* $B \to \overline{D}^0\pi^+\pi^-\pi^+(X)$, onde os tres pións se prodúcen no vértice de desintegración do B. Nesta fórmula X representa outras posibles partículas adicionais no estado final. Este fondo redúcese moito despois de aplicar a selección.

Un fondo máis irreducible, e por tanto máis resiliente á selección, son as desintegracións $B \to \overline{D}^0 D(X)$, onde o D significa un D_s^+, un D^0 ou un mesón D^+ que se desintegra no vértice 3π. Entre estes son especialmente relevantes os que proceden de desintegracións $D_s^+ \to \pi^+\pi^-\pi^+(X)$ inclusivas co D_s^+ decaendo no vértice 3π. Dado que estas canles de fondo non están controladas polos requirimentos de selección, desenvolvéronse dous modelos independentes para controlalas. Estes modelos amósanse na Figura 6.2. Os modelos utilízanse para corrixir a simulación, tanto para o sinal como para o axuste de normalización.

Outra contribución importante ao fondo débese ás desintegracións semitauónicas $B \to D^{**}\tau^+\nu_\tau$, onde D^{**} é un mesón D excitado diferente dun D^*. Estas non foron medidas, polo que se fai un procedemento de estimación para contabilizalas.

A principal contribución desta tese é o modelo para controlar as desintegracións de $D_s^+ \to \pi^+\pi^-\pi^+$, que se describe na seguinte sección. Finalmente, os resultados de $R(D^{(*)0})$ preséntanse na Sección C.4.2.

C.4.1 O modelo das desintegracións $D_s^+ \to \pi^+\pi^-\pi^+(X)$

Os decaementos $B \to \overline{D}^0 D_s^+(X)$ inclusivos coas desintegracións $D_s^+ \to \pi^+\pi^-\pi^+(X)$ son a maior contribución de fondo á mostra de sinal. É por isto que a súa descrición é crucial para a medida de $R(D^{(*)0})$. As desintegracións $D_s^+ \to \pi^+\pi^-\pi^+(X)$ inclusivas teñen unha taxa de ramificación maior que a desintegración exclusiva $D_s^+ \to \pi^+\pi^-\pi^+$. Esta diferenza débese á contribución de desintegracións que implican estados intermedios como η, η', K^0_S, ϕ e ω.

Para estimar a contribución destes modos aos antecedentes, proponse nesta tese unha estratexia innovadora: un procedemento de reponderación para corrixir a descrición de desintegracións D_s^+, tomada da simulación e validada cos datos. Este método de reponderación require unha descrición exhaustiva das desintegracións D_s^+ consideradas. Prodúcense un total de 9 mostras de control e realízase un axuste simultáneo para obter os pesos.

As desintegracións D consideradas que contribúen ao fondo $D_s^+ \to \pi^+\pi^-\pi^+(X)$ están listadas na Táboa 6.9, xunto coas súas fraccións de ramificación coñecidas [1, 171] e os valores destas fraccións de ramificación utilizadas como entrada para a simulación. É importante notar que as desintegracións $D_s^+ \to \eta'\pi^+\pi^-\pi^+$ e $D_s^+ \to \pi^+\pi^-\pi^+\pi^0$ non resoantes non se informan no PDG [1], pero foron incluídas na produción da simulación, anticipando a súa presenza nos datos.

As desintegracións D_s^+ pódense clasificar en diferentes categorías dependendo do estado final e da presenza dun estado intermedio lixeiro. A continuación, R representa un mesón η, ϕ ou ω. Tendo en conta isto, considéranse os seguintes estados finais:

- **Desintegracións $D_s^+ \to \pi^+\pi^-\pi^+$ exclusivas.**
- **Estados finais de 3 trazas con pións neutros adicionais.** Estes decaementos inclúen $D_s^+ \to R\pi^+(\pi^0)$ con $R \to \pi^+\pi^-\pi^0$, e $D_s^+ \to \pi^+\pi^-\pi^+\pi^0$ non resoante.
- **Estados finais de 5 trazas.** Estes modos teñen a topoloxía representada na Figura 6.19 e inclúen desintegracións $D_s^+ \to R\pi^+\pi^-\pi^+(\pi^0)$: $D_s^+ \to \eta'(\to \eta(\to \pi^+\pi^-\pi^0)\pi^+\pi^-)\pi^+$, $D_s^+ \to \eta'(\to \rho^0(\to \pi^+\pi^-)\gamma)\pi^+\pi^-\pi^+$, $D_s^+ \to \omega(\to \pi^+\pi^-\pi^0)\pi^+\pi^-\pi^+$, $D_s^+ \to \eta(\to \pi^+\pi^-\pi^0)\pi^+\pi^-\pi^+$, $D_s^+ \to \phi(\to \pi^+\pi^-\pi^0)\pi^+\pi^-\pi^+$ e $D_s^+ \to \pi^+\pi^-\pi^+\pi^-\pi^+$ non resoante. Para a desintegración $D_s^+ \to \eta\pi^+\pi^-\pi^+$, considérase a medida da fracción de ramificación da Ref. [171].
- **Estados finais de 5 trazas con caóns.** Estes inclúen $D_s^+ \to \phi\pi^+\pi^-\pi^+$, onde $\phi \to K^+K^-$. Este modo de desintegración modélase como espazo de fase na simulación, pero sábese que está dominado por desintegracións $D_s^+ \to \phi a_1(1260)^+$, onde $a_1(1260)^+ \to \rho^0\pi^+$ e $\phi \to K^+K^-$, cunha fracción de ramificación de $(0.74 \pm 0.12)\%$ [1].
- **Estados finais con $\eta \to \gamma\gamma$.** Estes inclúen todos os estados finais cun η que decae en dous fotóns: $D_s^+ \to \eta'(\to \eta\pi^+\pi^-)\pi^+(\pi^0)$, $D_s^+ \to \eta'(\to \eta\pi^0\pi^0)\pi^+\pi^-\pi^+$ e $D_s^+ \to \eta\pi^+\pi^-\pi^+$. Os dous últimos tamén se simulan como espazo-fase.
- **Desintegracións $D_s^+ \to \tau^+\nu_\tau$ tauonicas**, con desintegracións de τ en 3 pións.
- **Outras desintegracións D_s^+.** Ademais das anteriores, desintegracións do D_s^+ con fraccións de ramificación máis baixas inclúense na simulación: $D_s^+ \to K_S^0K_S^0\pi^+\pi^-\pi^+$, $D_s^+ \to K_L^0\pi^+\pi^-\pi^-$, $D_s^+ \to K_L^0K_L^0\pi^+\pi^-\pi^-$, $D_s^+ \to K^-\pi^+\pi^-$, $D_s^+ \to \phi e^+\nu_e$, $D_s^+ \to \phi\mu^+\nu_\mu$, $D_s^+ \to \eta e^+\nu_e$, $D_s^+ \to \eta\mu^+\nu_\mu$, $D_s^+ \to \eta' e^+\nu_e$, $D_s^+ \to \eta'\mu^+\nu_\mu$, $D_s^+ \to f_0(980)e^+\nu_e$, $D_s^+ \to f_0(980)\mu^+\nu_\mu$. Estas canles non están listadas no resumo da Táboa 6.9.
- **Desintegracións "Non D_s^+ ".** Son desintegracións residuais que superan os requisitos de selección, incluíndo desintegracións D^0 ou D^+, desintegracións de sinal, desintegracións *prompt* e fondo combinatorio.

Estes modos de desintegración D_s^+ están representados na Figura 6.18, que mostra as compoñentes utilizadas no modelo de axuste.

C.4.1.1 Mostras de control do decaemento $D_s^+ \to \pi^+\pi^-\pi^+(X)$

Para obter un modelo de desintegración fiable para desintegracións $D_s^+ \to \pi^+\pi^-\pi^+(X)$ inclusivas, prodúcense nove mostras aplicando seleccións dedicadas. Espérase que cada

mostra sexa sensible, polo menos, a un dos modos de desintegración mostrados na Táboa 6.9. Para producir estas mostras aplícanse os requisitos da selección de sinal, con excepción das condicións de illamento de vértices e $m(\pi^+\pi^-\pi^+)$.

Ademais, para enriquecer a mostra con desintegracións D_s^+, só se consideran eventos no intervalo q^2 $[3, 6.5]$ GeV$^2/c^4$. Esta selección suprime as desintegracións $B \to \overline{D}^0 D^0(X)$ e $B \to \overline{D}^0 D^+(X)$, que se atopan na rexión de alto q^2. Respecto da simulación, esta prodúcese coas fraccións de ramificación mostradas na Táboa 6.9.

Para producir mostras de control con trazas cargadas adicionais, empréganse as ferramentas de illamento descritas en Sección 6.3.3.1. Só se consideran as trazas con $\chi^2_{\rm IP}(\rm PV) > 4$ e $p_{\rm T} > 250$ GeV/c. Como exemplo, a topoloxía dun decaemento D_s^+ con dúas trazas cargadas adicionais móstrase na Figura 6.19(a). Ademais da ferramenta `TupleToolVtxIsolnPlus` [163], a saída do algoritmo `TupleToolIsoKS`, desenvolvido especialmente para este estudo, úsase para incluír mesóns $K^0_{\rm S}$ adicionais, reconstruídos usando o modo $K^0_{\rm S} \to \pi^+\pi^-$.

As partículas neutras no estado final son contabilizadas coas ferramentas introducidas na Sección 6.3.3.2. Os pións neutros e os mesóns η reconstrúense usando o estado final $\gamma\gamma$. Dado que a colisión protón-protón altamente enerxética produce moitos destes mesóns,seleccionáronse os candidatos π^0 e η co p_T máis alto no evento. Ademais, a masa π^0 debe estar no intervalo $|m(\gamma\gamma) - m(\pi^0)_{\rm PDG}| < 15$ GeV/c^2 cun nivel de confianza CL $> 0,2$. A masa invariante η é necesaria para situarse no intervalo $|m(\gamma\gamma) - m(\eta)_{\rm PDG}| < 30$ GeV/c^2 cun nivel de confianza CL $> 0,2$. A topoloxía dunha desintegración do mesón D_s^+ cun π^0 adicional móstrase na Figura 6.19(b).

As nove mostras de control producidas para o axuste do modelo do D_s^+ son as seguintes:

I. Desintegracións $D_s^+ \to \pi^+\pi^-\pi^-$ exclusivas. Son seleccionadas aplicando os mesmos requisitos de illamento que no sinal. Utilízase a distribución $m(\pi^+\pi^-\pi^+)$, que require estar dentro dunha xanela de masa de $[1.9, 2.0]$ GeV/c^2.

II. Desintegracións $D_s^+ \to \pi^+\pi^-\pi^+\pi^-\pi^+(X)$. Prodúcese unha mostra de control con dous pións cargados adicionais de signo oposto que apuntan ao vértice 3π (véxase Figura 6.19(a)). A distribución de masa $m(\pi^+\pi^-\pi^+\pi^-\pi^+)$ considérase no intervalo $[1.6, 2.1]$ GeV/c^2. Esta mostra de control é a máis sensible a desintegracións $D_s^+ \to \pi^+\pi^-\pi^+\pi^-\pi^+$, $D_s^+ \to \eta(\to \pi^+\pi^-\pi^0)\pi^+\pi^-\pi^+$, $D_s^+ \to \eta'(\to \eta(\to \pi^+\pi^-\pi^0)\pi^+\pi^-)\pi^+$ e $D_s^+ \to \omega(\to \pi^+\pi^-\pi^0)\pi^+\pi^-\pi^+$.

III. Desintegracións $D_s^+ \to K^+K^-\pi^+\pi^-\pi^+$. Para controlar estas desintegracións, engádense dous kaóns con carga de signo oposto ao vértice 3π. A variable característica desta mostra é a masa $m(K^+K^-\pi^+\pi^-\pi^+)$, que é necesaria para situarse arredor da masa coñecida do D_s^+. Esta mostra selecciona desintegracións puras de $D_s^+ \to \phi(\to K^+K^-)\pi^+\pi^-\pi^+$.

IV. Desintegracións $D_s^+ \to \eta'\pi^+\pi^-\pi^+$. Esta mostra de control prodúcese engadindo ao vértice 3π dous pións cargados de signo oposto e un mesón η que se desintegra

en dous fotóns. No axuste utilízase a distribución $m(5\pi\eta)$ no intervalo de masa $[1.6, 2.2]$ GeV/c^2. O candidato $\eta \to \gamma\gamma$ selecciónase nun cono de 0.50 arredor da dirección 3π. Para enriquecer a mostra en desintegracións $D_s^+ \to \eta'(\to \eta\pi^+\pi^-)\pi^+\pi^-\pi^+$, que nunca foron observadas, o mínimo da masa do pión con carga oposta $\min[m(\pi^+\pi^-)]$ requírese que estea na xanela de masa $[1.9, 2.0]$ GeV/c^2.

V. Desintegracións $D_s^+ \to K_S^0\pi^+\pi^-\pi^+$. Prodúcese unha mostra ao engadir un $K_S^0 \to \pi^+\pi^-$ ao vértice 3π. No axuste utilízase a masa $m(K_S^0\pi^+\pi^-\pi^+)$ que debe estar no intervalo $[1.9, 2.0]$ GeV/c^2. A parella de pións da desintegración K_S^0 debe ter unha masa invariante no intervalo $|m(\pi^+\pi^-) - m_{\rm PDG}(K_S^0)| < 30$ MeV/c^2. Esta mostra é sensible ás desintegracións de $D_s^+ \to K_S^0\pi^+\pi^-\pi^+$.

VI. Desintegracións $D_s^+ \to \eta\pi^+(\pi^0)$. O mesón η reconstrúese no seu modo $\pi^+\pi^-\pi^0$ anexando un π^0 ao vértice 3π. Requírese que a súa masa invariante estea nunha xanela arredor da masa coñecida do η. A variable utilizada é a masa dos catro pións: $m((\pi^+\pi^-\pi^0)_\eta\pi^+)$, onde o subíndice η indica a desintegración η reconstruída. Esta mostra é sensible ás desintegracións $D_s^+ \to \eta(\to \pi^+\pi^-\pi^0)\pi^+$ e $D_s^+ \to \eta(\to \pi^+\pi^-\pi^0)\pi^+\pi^0$.

VII. Desintegracións exclusivas $D_s^+ \to \pi^+\pi^-\pi^+\pi^0$. Esta mostra créase achegando un π^0 ao vértice 3π. A masa invariante $m(\pi^+\pi^-\pi^+\pi^0)$ é necesaria para situarse nunha xanela ± 30 MeV/c^2 arredor da masa coñecida do D_s^+, de xeito que só se seleccionan decaementos $D_s^+ \to \pi^+\pi^-\pi^+\pi^0$. A variable utilizada para esta mostra é o mínimo das masas $m(\pi_0^+\pi_1^-\pi^0)$ e $m(\pi_2^+\pi_1^-\pi^0)$, representada como $\min[m(\pi^+\pi^-\pi^0)]$. Esta mostra de control é sensible ás desintegracións: $D_s^+ \to \eta(\to \pi^+\pi^-\pi^0)\pi^+$, $D_s^+ \to \omega(\to \pi^+\pi^-\pi^0)\pi^+$, $D_s^+ \to \phi(\to \pi^+\pi^-\pi^0)\pi^+$ e $D_s^+ \to \pi^+\pi^-\pi^+\pi^0$ non resoantes. Aquí, non resoante indica que o sistema $\pi^+\pi^-\pi^0$ non forma ningún estado intermedio.

VIII. Desintegracións $D_s^+ \to \eta\pi^+\pi^-\pi^+$. A mostra prodúcese unindo un $\eta \to \gamma\gamma$ ao vértice 3π. Para seleccionar desintegracións exclusivas de $D_s^+ \to \eta\pi^+\pi^-\pi^+$, aplícase un veto ao mínimo das masas que conforman o mesón η e dous pións cargados, $\min[m(\eta\pi^+\pi^-)]$, de tal xeito que as desintegracións $\eta' \to \eta\pi^+\pi^-$ son suprimidas. A variable utilizada nesta mostra é a masa $m(\eta\pi^+\pi^-\pi^+)$, no intervalo $[1.9, 2.05]$ GeV/c^2. Polo tanto, esta mostra é sensible ás desintegracións $D_s^+ \to \eta(\to \gamma\gamma)\pi^+\pi^-\pi^+$.

IX. Desintegracións $D_s^+ \to \eta'\pi^+(\pi^0)$. A mostra prepárase unindo un candidato $\eta \to \gamma\gamma$ ao vértice 3π. Ao contrario da mostra anterior, é necesario que a masa $\min[m(\eta\pi^+\pi^-)]$ estea arredor da masa coñecida do η', concretamente no rango $[0.9, 1.01]$ GeV/c^2. A variable utilizada nesta mostra é $m((\eta\pi^+\pi^-)_{\eta'}\pi^+)$. Esta mostra de control é sensible ás desintegracións $D_s^+ \to \eta'(\to \eta(\to \gamma\gamma)\pi^+\pi^-)\pi^+$ e $D_s^+ \to \eta'(\to \eta(\to \gamma\gamma)\pi^+\pi^-)\pi^+\pi^0$.

Considerando todo isto, este modelo é engloba a maioría dos modos de desintegración $D_s^+ \to \pi^+\pi^-\pi^+(X)$, excepto as canles $D_s^+ \to \tau^+\nu_\tau$, $D_s^+ \to \omega\pi^+\pi^0$ e $D_s^+ \to \phi\pi^+\pi^0$. Na Táboa 6.10 resúmese a selección de todas as mostras de control e os modos de desintegración aos que se dirixen.

Correccións de estruturas resoantes de eventos simulados no espazo das fases

Para as desintegracións $D_s^+ \to \eta 3\pi$ e $D_s^+ \to \phi 3\pi$, investigáronse algunhas variables, coñecidas por ser sensibles ás contribucións resonantes, e que implican un procedemento de corrección. Estas variables son as masas $m(3\pi)$, $\min[m(\pi^+\pi^-)]$, $\max[m(\pi^+\pi^-)]$ e $m(K^+K^-)$ (esta última só para a desintegración $\phi \to K^+K^-$). Polo tanto, é posible explicar a presenza de contribucións resonantes nestas desintegracións, que orixinalmente se simulan como espazo de fase puro. As desintegracións $D_s^+ \to \eta 3\pi$ e $D_s^+ \to \phi 3\pi$ pondéranse de novo para ter en conta as contribucións resoantes $D_s^+ \to \eta\rho^0\pi^+$ e $D_s^+ \to \phi a_1^+(\to \rho^0\pi^+)$, respectivamente.

Na Figura C.5(a), represéntase a masa do sistema 3π na selección de decaementos $D_s^+ \to \phi 3\pi$ (mostra III). Antes da corrección, na Figura C.5(a) é visible unha estrutura de pico non incluída pola simulación. Isto débese a desintegracións $D_s^+ \to a_1(1260)^+\phi$. Despois da reponderación, no lado dereito da Figura C.5(a), a simulación describe mellor os datos.

Aplícase un procedemento análogo ás desintegracións $D_s^+ \to \eta 3\pi$. Na parte esquerda da Figura C.5(b) móstrase a distribución $m(\pi^+\pi^-)$. É visible unha estrutura de pico centrada arredor da masa coñecida do ρ^0 (~ 770 MeV/c^2) nos datos, que non se reproduce pola simulación antes da corrección (esquerda). Despois da reponderación á mostra $D_s^+ \to \eta\rho^0\pi^+$ o acordo entre simulación e datos mellora, como se ve na parte dereita da Figura C.5(b).

C.4.1.2 O modelo de axuste do D_s^+

No modelo de axuste que se propón para os decaementos do D_s^+ cada mostra pódese describir polo produto da función de densidade de probabilidade para unha desintegración D_s^+ e a súa produción. A distribución total obtense sumando sobre as desintegracións consideradas:

$$\sum_{j \in \text{desintegracións do } D_s^+} N_j^{(K)} \times \mathcal{P}_j^{(K)}(x^{(K)})\,, \tag{C.18}$$

onde o superíndice K indica a mostra, o subíndice j indica o modo de desintegración do D_s^+ e $x^{(K)}$ é a variable utilizada para describir cada mostra. Os producións pódense parametrizar en función da produción do $D_s^+ \to \pi^+\pi^-\pi^+$ observado na mostra de $D_s^+ \to \pi^+\pi^-\pi^+$ (mostra I) corrixida polas eficiencias relativas:

$$N_j^{(K)} = \left(\frac{\varepsilon_j^{(K)}}{\varepsilon_{D_s^+\to 3\pi}^{(\mathrm{I})}}\right) \times \left(\frac{\mathcal{B}_j}{\mathcal{B}(D_s^+ \to 3\pi)_{\mathrm{PDG}}}\right) \times N_{D_s^+\to 3\pi}^{(\mathrm{I})}, \tag{C.19}$$

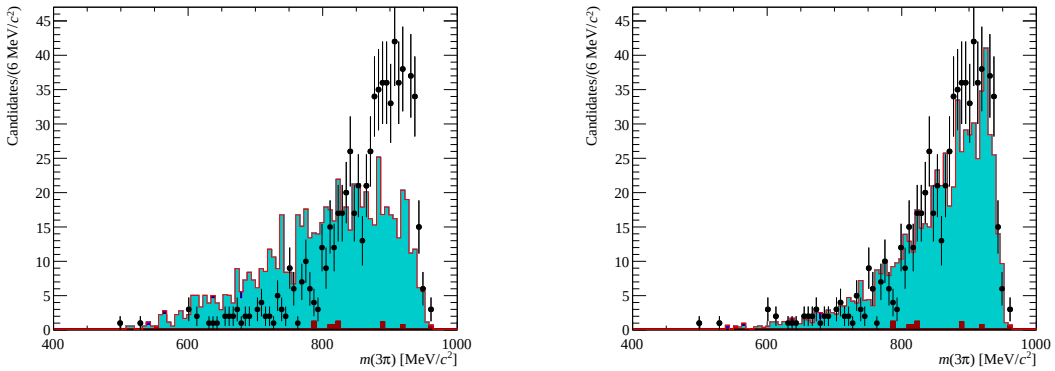

(a) Distribución de m(3π) seleccionando dous kaóns no estado final (mostra III)

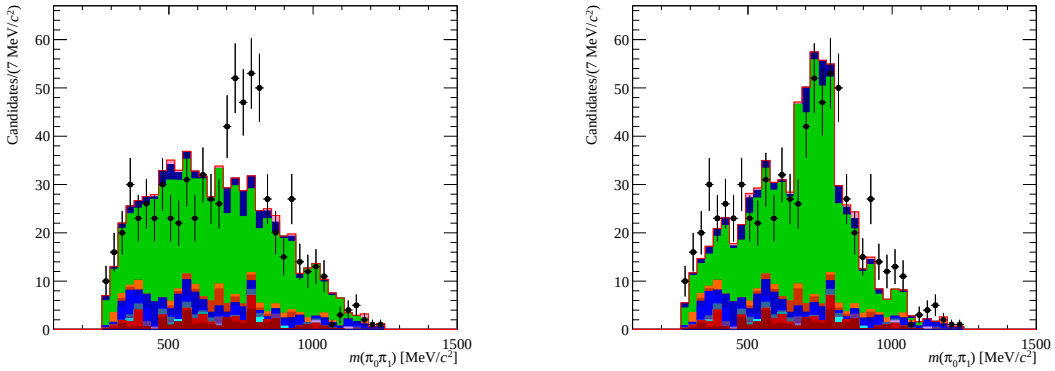

(b) Distribución de $m(\pi^+\pi^-)$ seleccionando η fóra do intervalo de masa η' (mostra VIII)

Figura C.5: Comparación antes (esquerda) e despois (dereita) da corrección dos modos resonantes. Arriba: $m(3\pi)$ ao seleccionar dous kaóns adicionais no estado final (mostra III); inferior: $m(\pi^+\pi^-)$ distribución seleccionando η fóra do intervalo de masas η'. Os puntos negros representan os datos, o modo $D_s^+ \to \phi(\to K^+K^-)3\pi$ móstrase en azul claro e a contribución de $D_s^+ \to \eta(\to \gamma\gamma)3\pi$ móstrase en verde.

sendo $\mathcal{B}(D_s^+ \to 3\pi)_{\rm PDG}$ a $D_s^+ \to \pi^+\pi^-\pi^+$ a fracción de ramificación coñecida e $\mathcal{B}_j$ a fracción de ramificación da desintegración j por determinar neste estudo. Esta fracción de ramificación pódese parametrizar aínda máis en función da fracción de ramificación utilizada para xerar a simulación, $\mathcal{B}_j^{(\rm sim)}$,

$$\mathcal{B}_j = w_j \times \mathcal{B}_j^{(\rm sim)}, \tag{C.20}$$

tal que, finalmente, para a mostra de control (K), o modelo vén dado por

$$f^{(K)} = \sum_{j \in D_s^+ \text{ decays}} w_j \times \left(\frac{\varepsilon_j^{(K)}}{\varepsilon_{D_s^+\to 3\pi}^{(\rm I)}} \right) \times \left(\frac{\mathcal{B}_j^{(\rm sim)}}{\mathcal{B}(D_s^+ \to 3\pi)_{\rm PDG}} \right) \times N_{D_s^+\to 3\pi}^{(\rm I)} \times \mathcal{P}_j^{(K)}(x^{(K)}) \,. \tag{C.21}$$

Neste punto, realízase un axuste simultáneo ás nove mostras de control. Os pesos w_j son os parámetros libres, con excepción das canles ás que o modelo non é sensible: $D_s^+ \to \tau^+\nu_\tau$, $D_s^+ \to \omega\pi^+\pi^0$ e $D_s^+ \to \phi\pi^+\pi^0$. Estes pesos de desintegracións fíxanse no axuste tendo en conta as súas fraccións de ramificación coñecidas como

$$w_j^{\rm fixed} = \frac{\mathcal{B}_j^{(\rm PDG)}}{\mathcal{B}_j^{(\rm sim)}} \,. \tag{C.22}$$

As desintegracións D_s^+ que se explican polo axuste son as descritas anteriormente na Sección C.4.1.1 e recollidas na lenda representada na ultima subfigura de Figura C.7. A canle "outras D_s^+ " inclúe o decaemento $D_s^+ \to K^+\pi^-\pi^+$ e outras posibles desintegracións do D_s^+ non consideradas nas categorías anteriores. Finalmente, a compoñente "non D_s^+ " inclúe todas as contribucións debidas a desintegracións procedentes de D^+, D^0 e desintegracións residuais que pasaron a selección debidas ao sinal, a eventos *prompt*, nos que os pións se producen no vértice do B, e o fondo combinatorio. O peso da compoñente "non D_s^+ " tamén se fixa no axuste.

C.4.1.3 Resultados do modelo do D_s^+

Os pesos devoltos polo axuste recóllense na Figura C.6 e na Táboa 6.11. As proxeccións de axuste para cada mostra represéntanse nas Figuras C.7 e C.8. Usando estes pesos é posible obter unha medida das fraccións de ramificación con respecto dun modo de referencia, ou sexa, a desintegración exclusiva $D_s^+ \to \pi^+\pi^-\pi^+$. Seguindo Ecuación (C.20), as fraccións de ramificación relativa son

$$\frac{\mathcal{B}_j}{\mathcal{B}(D_s^+ \to 3\pi^+)} = \frac{w_j \times \mathcal{B}_j^{(\rm sim)}}{w_{D_s^+\to 3\pi} \times \mathcal{B}_{D_s^+\to 3\pi}^{(\rm sim)}}, \tag{C.23}$$

onde as fraccións de ramificación co superíndice (sim) corresponden aos valores utilizados para xerar os eventos simulados (véxase Táboa 6.9). As fraccións de ramificación relativas

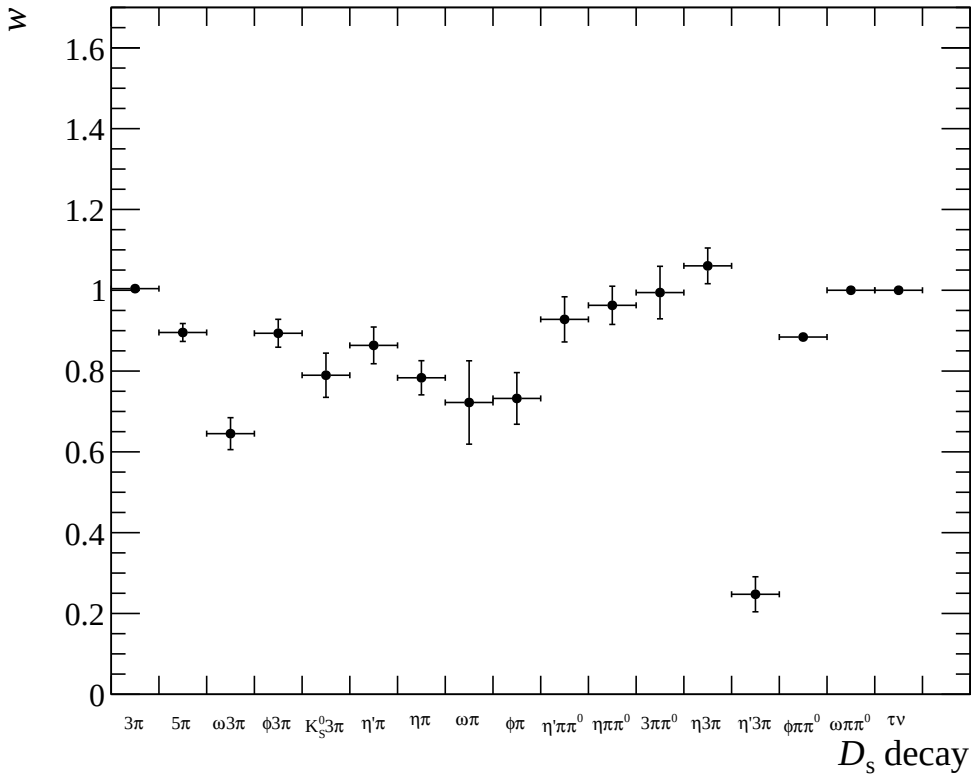

Figura C.6: Valores dos pesos para cada compoñente no modelo das desintegracións do D_s^+ devoltos polo axuste simultáneo ás mostras de control. Teñase en conta que os valores de $w_{D_s^+\to\tau^+\nu_\tau}$, $w_{D_s^+\to\omega\pi^+\pi^0}$ e $w_{D_s^+\to\phi\pi^+\pi^0}$ e $w_{D_s^+\to\ell^+\nu_\ell}$ fíxanse no axuste segundo as súas fraccións de ramificación coñecidas.

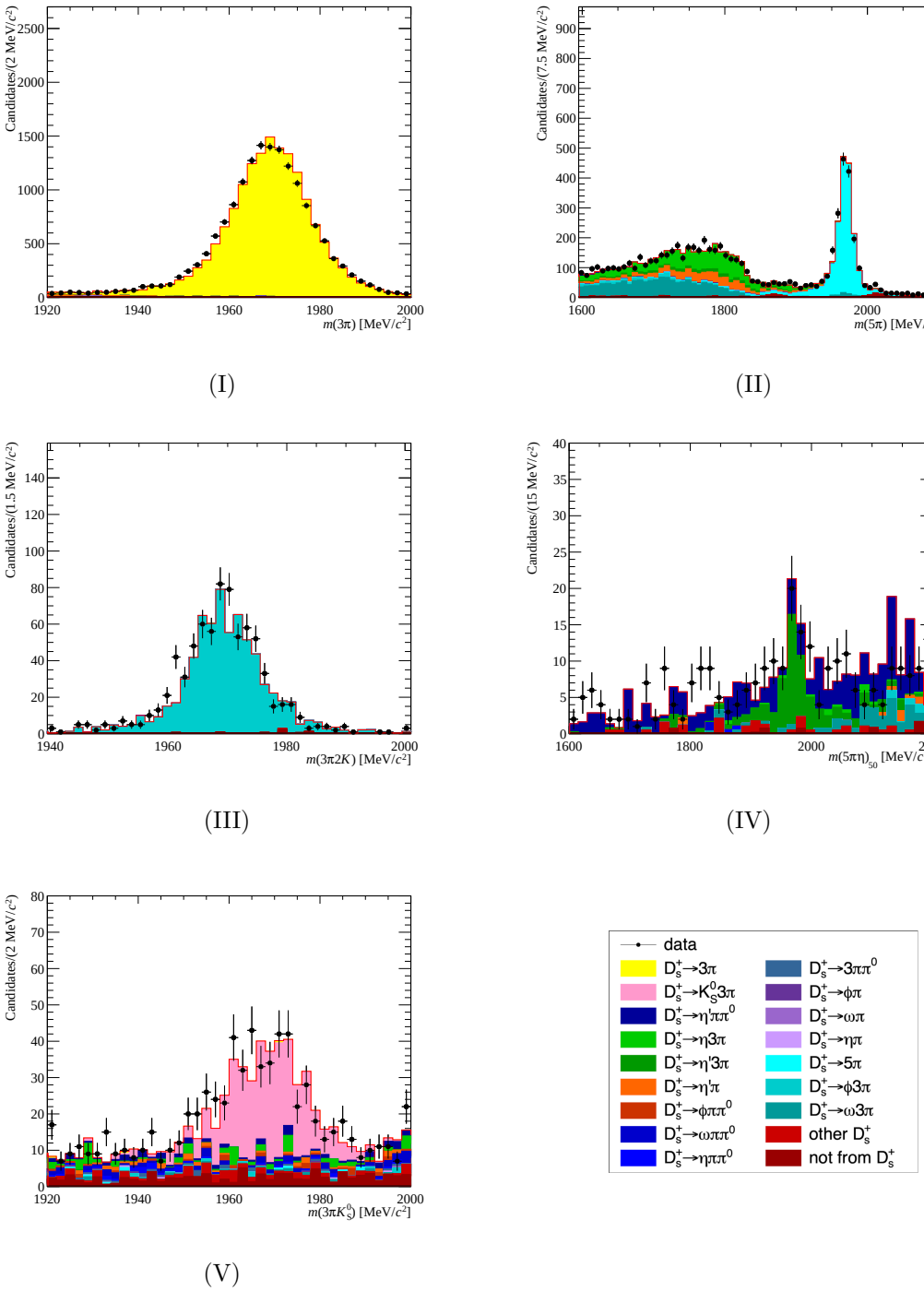

Figura C.7: Proxeccións das mostras de con trazas cargadas despois do axuste $D_s^+ \to \pi^+\pi^-\pi^+(X)$. Fila superior (de dereita a esquerda): $m(\pi^+\pi^-\pi^+)$, para desintegracións exclusivas de$D_s^+ \to \pi^+\pi^-\pi^+$, e distribución de $m(\pi^+\pi^-\pi^+\pi^-\pi^-)$, Fila do medio: distribucións de $m(K^+K^-\pi^+\pi^-\pi^-)$ (esquerda) e $m(5\pi\eta)$ con $\eta \to \gamma\gamma$. Fila inferior: distribución de $m(K^0_S(\to \pi^+\pi^-)\pi^+\pi^-\pi^+)$ e lenda.

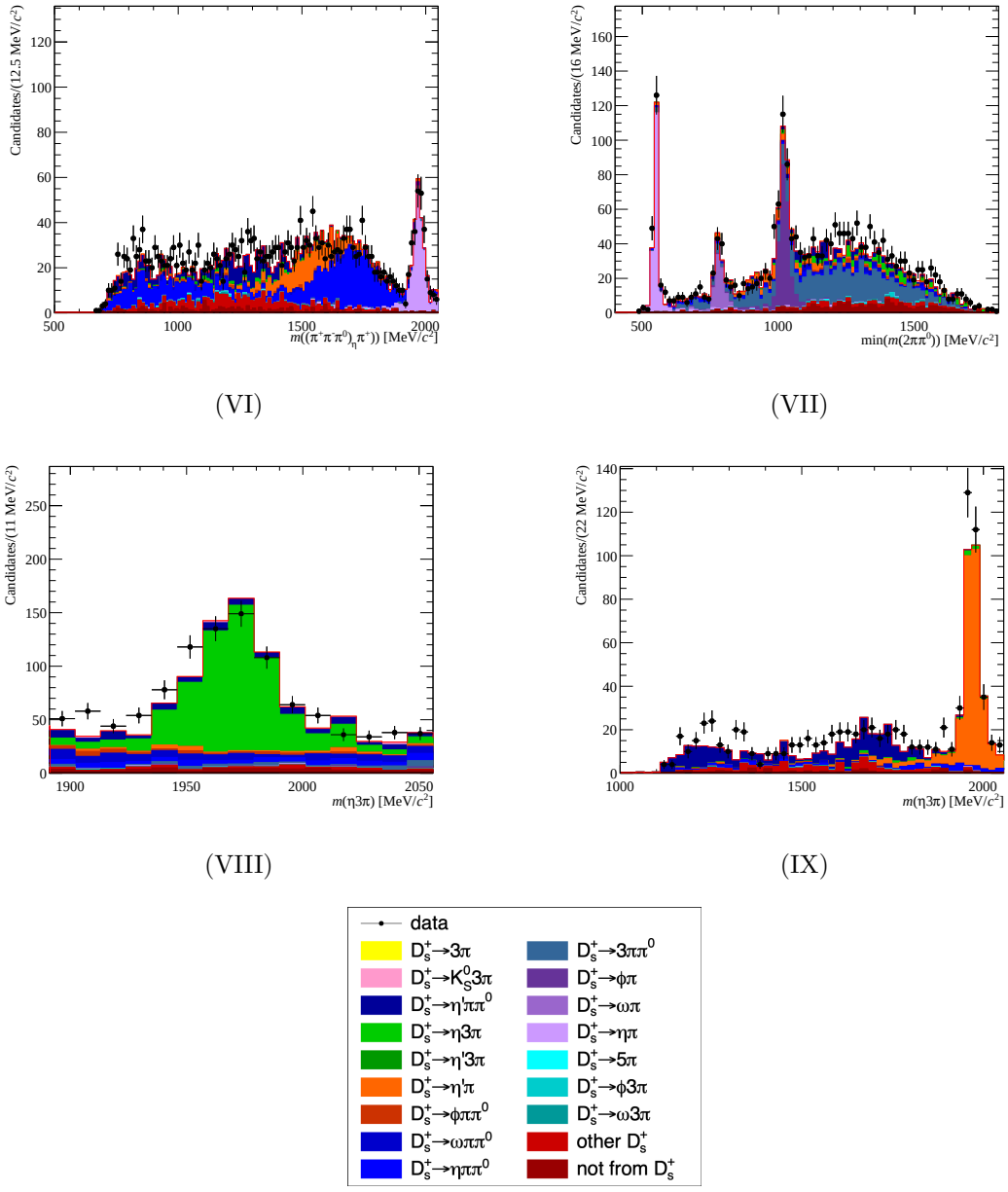

Figura C.8: Fila superior: $m\left((\pi^+\pi^-\pi^0)_\eta\pi^+(\pi^0)\right)$ para desintegracións inclusivas de $D_s^+ \to \eta\pi^+(X)$; $\min[m(\pi^+\pi^-\pi^0)]$ para mostras de $D_s^+ \to \pi^+\pi^-\pi^+\pi^0$ despois do axuste do modelo de D_s^+. Fila do medio: distribución de $m(\eta\pi^+\pi^-\pi^+)$ despois do axuste seleccionando eventos fóra (esquerda) e dentro (dereita) do intervalo de masa do η'.

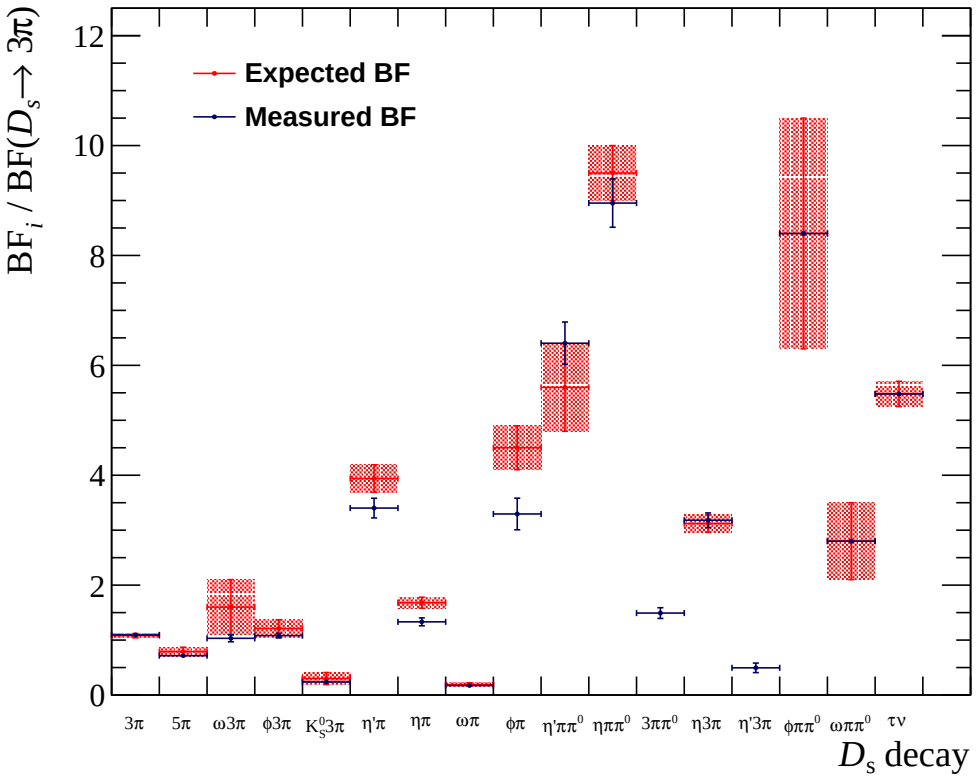

Figura C.9: Fraccións de desintegración relativas ao decaemento $D_s^+ \to \pi^+\pi^-\pi^+$ obtidas polo modelo do D_s^+ (azul) e das Refs. [1, 171] (vermello).

ao modo exclusivo $D_s^+ \to \pi^+\pi^-\pi^+$ móstranse na Táboa 6.12. A Figura C.9 mostra a comparación entre as fraccións de ramificación relativas medidas nesta tese e os mesmos valores das medidas anteriores, mostrados na Táboa 6.9 [1, 171]. Teñase en conta que as fraccións de ramificación de $D_s^+ \to \eta'\pi^+\pi^-\pi^+$ e as desintegracións non resoantes de $D_s^+ \to \pi^+\pi^-\pi^+\pi^0$ non se informan, xa que teñen non se observaron antes.

Pódese concluír que, en xeral, as fraccións de ramificación relativa obtidas neste estudo están de acordo cos valores do PDG dentro das incertezas. Ademais, usando as fraccións de ramificación relativa, este modelo tamén se pode empregar para producir novas mostras de simulación e para outros estudos de desintegracións semitauónicas que consideren desintegracións do τ en 3 pións.

C.4.2 Resultados cegados e conclusións

A principal contribución desta tese á análise de $R(D^{(*)0})$ é o modelo para controlar as desintegracións $D_s^+ \to \pi^+\pi^-\pi^+(X)$. Este modelo mostra moi bo acordo coas

medidas precedentes das canles consideradas. Empregando os resultados do modelo $D_s^+ \to \pi^+\pi^-\pi^+(X)$ e doutros modelos de fondo, corríxese a simulación. Polo tanto, é posible obter as producións de sinal e de normalización a traves de dous axustes. Do axuste á masa invariante na canle de normalización obtense $N_{\rm norm} = 3047 \pm 56$. Os valores de $N(B^+ \to \overline{D}^{*0}\tau^+\nu_\tau)$ e $N(B^+ \to \overline{D}^0\tau^+\nu_\tau)$ obteñense dun axuste simultaneo en tres dimencións, o q^2, o tempo de desintegración do τ, t_τ e a saída do BDT. Sendo $N(B^+ \to \overline{D}^{*0}\tau^+\nu_\tau) = xxx \pm 1096$ e $N(B^+ \to \overline{D}^0\tau^+\nu_\tau) = xxx \pm 1844$. A incerteza é só a debida á estatística.

Finalmente, usando estes valores e as eficiencias é posible obter o valor de $\mathcal{K}(D^{(*)0})$, definido na Ecuación (C.15). Este cálculase como

$$\begin{aligned}\mathcal{K}(D^{(*)0}) &= \frac{N(B^+ \to \overline{D}^{(*)0}\tau^+\nu_\tau)}{N(B^+ \to \overline{D}^0 D_s^+)} \times \\ &\times \frac{\varepsilon_{B^+\to\overline{D}^0 D_s^+}}{\varepsilon^{\tau^+\to 3\pi\overline{\nu}_\tau}_{B^+\to\overline{D}^{(*)0}\tau^+\nu_\tau}\mathcal{B}(\tau^+ \to 3\pi\overline{\nu}_\tau) + \varepsilon^{\tau^+\to 3\pi\overline{\nu}_\tau\pi^0}_{B^+\to\overline{D}^{(*)0}\tau^+\nu_\tau}\mathcal{B}(\tau^+ \to 3\pi\overline{\nu}_\tau)}\,, \quad \text{(C.24)}\end{aligned}$$

onde $\mathcal{B}(\tau^+ \to \pi^+\pi^-\pi^+\overline{\nu}_\tau) = (0.0902 \pm 0.0005)$ and $\mathcal{B}(\tau^+ \to \pi^+\pi^-\pi^+\pi^0\overline{\nu}_\tau) = 0.0449 \pm 0.0005$ [1]. Con todo o anterior, obtéñense os seguintes valores de $\mathcal{K}(D^{(*)0})$

$$\mathcal{K}(D^0) = xx \pm 22\ (\text{stat.}) \pm 0.35\ (\text{ext.})\,, \quad \text{(C.25)}$$
$$\mathcal{K}(D^{*0}) = xx \pm 16\ (\text{stat.}) \pm 0.74\ (\text{ext.})\,, \quad \text{(C.26)}$$

onde a primeira contribución de incerteza débese á estatística e a segunda ás fraccións de ramificación externa. A correlación entre as incertezas estatísticas é de $-0,91$ e entre as externas é de $+1$. A incerteza externa considérase desprezable con respecto da estatística.

Usando $\mathcal{K}(D^{(*)0})$ e as medidas externas $\mathcal{B}(B^+ \to \overline{D}^0 D_s^+) = (9.0 \pm 0.9) \times 10^{-3}$ e $\mathcal{B}(D_s^+ \to \pi^+\pi^-\pi^+) = (1,08 \pm 0,04)\%$, as fraccións de ramificación do $B^+ \to \overline{D}^{*0}\tau^+\nu_\tau$ e $B^+ \to \overline{D}^0\tau^+\nu_\tau$ pódense calcular como

$$\mathcal{B}(B^+ \to \overline{D}^{(*)0}\tau^+\nu_\tau) = \mathcal{K}(D^{(*)0}) \times \mathcal{B}(B^+ \to \overline{D}^0 D_s^+) \times \mathcal{B}(D_s^+ \to \pi^+\pi^-\pi^+)\,, \quad \text{(C.27)}$$

obtendo

$$\mathcal{B}(B^+ \to \overline{D}^0\tau^+\nu_\tau) = xx \pm 0.21\ (\text{stat.}) \pm 0.07\ (\text{ext.})\%\,, \quad \text{(C.28)}$$
$$\mathcal{B}(B^+ \to \overline{D}^{*0}\tau^+\nu_\tau) = xx \pm 0.15\ (\text{stat.}) \pm 0.15\ (\text{ext.})\%\,. \quad \text{(C.29)}$$

A correlación entre as fraccións de ramificación determinadas é a mesma que no caso de $\mathcal{K}(D^{(*)0})$, -0.91 e $+1$ para as incertezas estatísticas e externas, respectivamente. Sendo a medida de última xeración das fraccións de ramificación, [1]

$$\mathcal{B}(B^+ \to \overline{D}^0\tau^+\nu_\tau) = 0.77 \pm 0.25\%\,, \quad \text{(C.30)}$$
$$\mathcal{B}(B^+ \to \overline{D}^{*0}\tau^+\nu_\tau) = 1.88 \pm 0.20\%\,, \quad \text{(C.31)}$$

é posible sumar as incertezas do noso resultado para poder comparalas. Polo tanto,

$$\mathcal{B}(B^+ \to \overline{D}^0 \tau^+ \nu_\tau) = xx \pm 0.23 \text{ (stat.} + \text{ext.)}\% \,, \tag{C.32}$$

$$\mathcal{B}(B^+ \to \overline{D}^{*0} \tau^+ \nu_\tau) = xx \pm 0.22 \text{ (stat.} + \text{ext.)}\% \,, \tag{C.33}$$

cunha correlación de -0.37, o que resulta nunha medición competitiva coa media mundial.

Tendo todo isto en conta, as razóns LFU $R(D)$ e $R(D^*)$ pódense determinar como

$$R(D^{(*)0}) = \frac{\mathcal{B}(B^+ \to \overline{D}^{*0} \tau^+ \nu_\tau)}{\mathcal{B}(B^+ \to \overline{D}^0 D_s^+)\mathcal{B}(D_s^+ \to \pi^+\pi^-\pi^+)} \times \left(\frac{\mathcal{B}(B^+ \to \overline{D}^0 D_s^+)\mathcal{B}(D_s^+ \to 3\pi)}{\mathcal{B}(B^+ \to \overline{D}^{(*)0} \ell^+ \nu_\ell)} \right)_{\text{ext.}} , \tag{C.34}$$

e substituíndo as medidas externas [60] de $\mathcal{B}(B \to \overline{D}^0 \ell^+ \nu_\ell) = 2.30 \pm 0.06 \pm 0.08$ e $\mathcal{B}(B \to \overline{D}^{*0} \ell^+ \nu_\ell) = 5.58 \pm 0.07 \pm 0.21$, onde a primeira incerteza é estatística e a segunda é debido á sistemática, obtéñense os seguintes valores:

$$R(D^0) = xx \pm 0.093 \text{ (stat.)} \pm 0.034 \text{ (ext.)} \,\% \,, \tag{C.35}$$

$$R(D^{*0}) = xx \pm 0.026 \text{ (stat.)} \pm 0.029 \text{ (ext.)} \,\% \,. \tag{C.36}$$

cunha correlación de $-0,91$ e $+1$ para as incertezas estatísticas e externas, respectivamente. Este resultado inclúese en Figura C.10 en maxenta, xunto coas medicións $R(D)$ e $R(D^*)$ anteriores. Dado que o valor central está cegado a elipse céntrase no valor da predición do SM. A liña continua representa a incerteza estatística. A incerteza total, incluíndo tamén as incertezas externas, está representada pola liña discontinua. Non se mostra a incerteza sistemática xa que non foi avaliada no momento nin na elaboración desta tese.

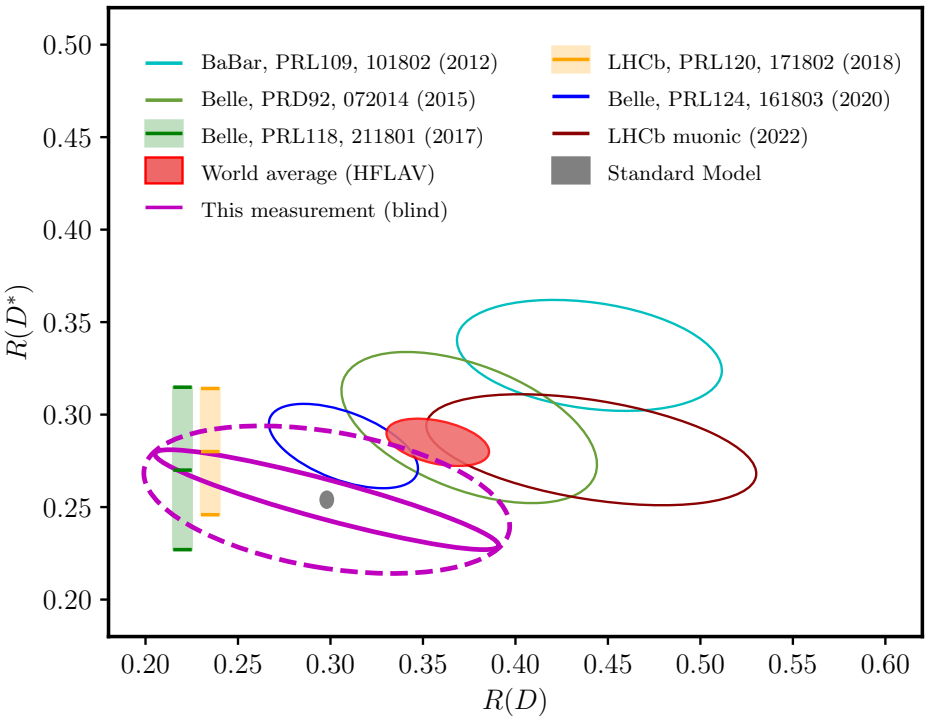

Figura C.10: Resultados de $R(D)$ e $R(D^*)$ (maxenta) comparados coa predición do modelo estandar e as medidas publicadas [44–51, 53, 54, 60]. A incerteza estatística é representada coa elipse en liña continua, mentres que a incerteza total (incluíndo as incertezas externas) coa elipse de liña descontinua e a incerteza sistematica non está incluída. A correlación está representada pola pendente da elipse. A predición do modelo estándar está representada polo punto gris, cuxa anchura reflicte a incerteza. A media das medidas está representada pola elipse vermella e os resultados previos están especificados na lenda (véxase Sección 3.2.2 para máis detalles).

C.5 Conclusións e perspectivas futuras

No SM, o acoplamento entre os leptóns e os bosóns gauge é independente da xeración de leptóns. Esta característica chámase Lepton Flavor Universality. Moitos novos escenarios de física prevén procesos de violación de LFU, que inclúen principalmente á terceira xeración [33]. Polo tanto, as comprobacións de LFU son unha das mellores sondas do SM.

O experimento LHCb demostrou ser unha excelente ferramenta para buscar NP, en particular para comprobacións de LFU. As últimas medicións de LHCb en procesos de correntes neutras e cargadas son as máis precisas na actualidade. Nos dous primeiros períodos de toma de datos LHCb recolleu datos correspondentes a unha luminosidade integrada de 9 fb^{-1}. A estatística aumentará significativamente co detector actualizado, que comezou o seu funcionamento en 2022. O LHCb Upgrade I, operando cunha luminosidade de ata $2 \times 10^{33}\,\text{cm}^2\,\text{s}^{-1}$ e enerxía centro de masa $\sqrt{s} = 14$ TeV, está previsto que acade unha luminosidade integrada de 50 fb^{-1} (300 fb^{-1}) na fin do Run 3 (Run 4) en 2025 (2030).

Nesta tese propóñense dúas análises de datos de LHCb, relativas ás desintegracións semileptónicas dos mesóns B e D. Ambas análises realízanse a cegas. Os principais estudos que fican para completar as dúas análises refírense á avaliación de incertezas sistemáticas.

O obxectivo da primeira análise é comprobar LFU medindo a razón

$$R_{\mu/e} = \frac{\mathcal{B}(D^0 \to K^- \mu^+ \nu_\mu)}{\mathcal{B}(D^0 \to K^- e^+ \nu_e)} \tag{C.37}$$

usando o decaemento $D^0 \to K^- \ell^+ \nu_\ell$. Esta é a primeira medición de LFU no sector de encanto nun colisor de hadróns. Os candidatos $D^0 \to K^- \ell^+ \nu_\ell$ son seleccionados a partir das desintegracións $D^{*+} \to D^0 \pi^+$ e o valor de $R_{e/\mu}$ obtense pola relación entre as producións do sinal e a relación de eficiencias entre os dous modos. O resultado é

$$R_{e/\mu} = x.xxx \pm 0,003\ (\text{stat.}) \pm 0,014\ (\text{syst.}), \tag{C.38}$$

onde a primeira contribución ás incertezas é estatística, e a segunda é unha estimación da incerteza sistemática. Para comparalo coas predicións teóricas e a medida do experimento BESIII calcúlase a $R_{\mu/e}$ inversa, propagando en consecuencia os erros,

$$R_{\mu/e} = R_{e/\mu}^{-1} = x.xxx \pm 0.003\ (\text{stat.}) \pm 0.013\ (\text{syst.}). \tag{C.39}$$

Este resultado móstrase na Figura 5.21 centrado no valor das predicións do SM. Comparado co resultado de BESIII, pode anticiparse que o de LHCb será máis preciso.

A segunda análise pretende medir os observables LFU $R(D^0)$ e $R(D^{*0})$, definidos na Ecuación (6.3). Esta é a primeira medición simultánea nun colisor de hadróns usando a desintegración hadrónica $\tau^+ \to \pi^+\pi^-\pi^+\overline{\nu}_\tau$ do leptón τ. O resultado cegado de $R(D^0)$ e $R(D^{*0})$ aparece na Figura C.10:

$$R(D^0) = x.xxx \pm 0.093\ (\text{stat.}) \pm 0.034\ (\text{ext.})\%\,, \tag{C.40}$$

$$R(D^{*0}) = x.xxx \pm 0.024\ (\text{stat.}) \pm 0.029\ (\text{ext.})\%\,, \tag{C.41}$$

onde a primeira contribución á incerteza débese á estatística e a segunda ás medicións externas de $\mathcal{B}(B \to D^{(*)0}\ell'^{+}\nu_\ell)$, $\mathcal{B}(B \to D^0 D_s^+)$ e $\mathcal{B}(D_s^+ \to \pi^+\pi^-\pi^+)$. As dúas medidas presentan unha correlación de $-0,91$ e $+1$ para as incertezas estatísticas e externas, respectivamente.

A principal contribución desta tese á análise $R(D^{(*)0})$ é un modelo usado para controlar as contribucións ao fondo das desintegracións $D_s^+ \to \pi^+\pi^-\pi^+(X)$ inclusivas. Unha das principais fontes de información deste estudo débese ás desintegracións $B^+ \to \overline{D}^0 D_s^+(X)$ dobremente encantadas. Coñecer as contribucións relativas das desintegracións inclusivas dos D en tres pións é de fundamental importancia, tamén para outras análises $R(H_c)$. Estes resultados aparecen na Figura C.9 e mostran un acordo coas medicións actuais. Ademais, é importante notar que foron medidas por primeira vez as fraccións parciais de desintegración das canles $D_s^+ \to \eta'\pi^+\pi^-\pi^+$ e $D_s^+ \to \pi^+\pi^-\pi^+\pi^0$.

List of Figures

List of Tables

Glossary

All acronyms and abbreviations used in this thesis are defined here. Some of these are re-defined also in the text for completeness.

$\mathcal{B}$ branching fraction or branching ratio

BGL Boyd-Grinstein-Lebed parameterisation

BK Beciveric-Kaidalov pole parameterisation

BSM Beyond the Standard Model

CERN European Organisation of Nuclear Research

CLN Caprini-Lellouch-Neubert parameterisation

DAQ Data Acquisition

DIRA(particle, PV) cosine of the angle between the particle momentum and the direction given by the position of the particle decay vertex and the best PV

DLL(x) $= \Delta\text{LL}(x - \pi) = \ln\left(\mathcal{L}^{\text{PID}}(x)/\mathcal{L}^{\text{PID}}(\pi)\right)$ also referred as PID(x)

DOF degrees of freedom

DOCA(i, j) Distance Of Closest Approach between the tracks associated to the i^{th} and j^{th} particles

EFT Effective Field Theory

HAMMER Helicity Amplitude Module for Matrix Element Re-weighting

h.c. Hermitian conjugate

HLT High Level Trigger

HPD Hybrid Photo-Detector

HQEFT Heavy Quark Effective Field Theory

ISGW2 Isgur-Scora-Grinstein-Wise parameterisation

IP impact parameter

χ^2_{IP} impact parameter significance

L0 Level Zero Trigger

LEP Large Electron-Positron collider

LFV Lepton Flavour Violation

LFU Lepton Flavour Universality

LHC Larghe Hadron Collider

LHCb Larghe Hadron Collider Beauty

LQCD Lattice QCD

LS Long Shutdown

MB minimum bias

MD Magnet Down

MC Monte Carlo

MU Magnet Up

MVA multivariate analysis

NN Neural Network

NP new physics

nSPDHits number of hits in the SPD detector

PDF probability density function

PDG Particle Data Group [1]

PID particle identification

PID(x) = DLL(x)

PHSP phase-space

PMT photomultiplier

PV primary vertex

QCD Quantum Chromodynamics

QED Quantum Electrodynamics

QFT Quantum Field Theory

ROC Receiver Operating Characteristic

SM Standard Model

SSB Spontaneous Symmetry Breaking

SUSY Supersymmetry

SV secondary vertex

PID particle identification

TIS Triggered Independently of Signal

TOS Triggered On Signal

TISTOS Combination of TIS and TOS trigger

VEV Vacuum Expectation Value

w.r.t. With respect to

Oggetto: Re: Permission to reuse figures from JINST 3 (2008) S08005
Mittente: Permissions <permissions@ioppublishing.org>
Data: 12/10/22, 09:44
A: Alessandra Gioventù <alessandra.gioventu@cern.ch>
CC: jinst-eo <jinst-eo@jinst.sissa.it>

Dear Alessandra Gioventù,

Thank you for your email. Your additional permission has been granted below:

> Thank you for your request to reproduce material published by IOP Publishing *in your thesis,* ***"Tests of Lepton Flavour Universality with semileptonic D and B decays at the LHCb experiment"***
>
> ***Regarding:***
>
> - ***Figure 2.1*** *from* ***"The LHCb Detector at the LHC"***
>
> We are happy to grant permission for the use you request on the terms set out below.
>
> # License to publish material published by IOP Publishing
>
> Please provide the below to your new publisher as proof of permission.
>
> **Conditions**
>
> Non-exclusive, non-transferrable, revocable, worldwide, permission to use the material in print and electronic form will be granted **subject to the following conditions:**
>
> - Permission will be cancelled without notice if you fail to fulfil any of the conditions of this letter.
> - You will make reasonable efforts to contact the author(s) to seek consent for your intended use. Contacting one author acting expressly as authorised agent for their co-authors is acceptable.
> - You will reproduce the following prominently alongside the material:
>   - the source of the material, including author, article title, title of journal, volume number, issue number (if relevant), page range (or first page if this is the only information available) and date of first publication. This information can be contained in a footnote or reference note; or
>   - a link back to the article (via DOI); and
>   - ***if practical and IN ALL CASES for works published under any of the Creative Commons licences the words "© IOP Publishing Ltd and SISSA. Reproduced by permission of IOP Publishing. All rights reserved"***
> - The material will not, without the express permission of the author(s), be used in any way which, in the opinion of IOP Publishing, could distort or alter the author(s)' original

> intention(s) and meaning, be prejudicial to the honour or reputation of the author(s) and/or imply endorsement by the author(s) and/or IOP Publishing and/or SISSA.
> - Payment of £0 is received in full by IOP Publishing prior to use.
>
> This permission does not apply to any material/figure which is credited to another source in our publication or has been obtained from a third party. Express permission for such materials/figures must be obtained from the copyright owner.
>
> Kind regards,
>
> Sophie

Copyright & Permissions Team
Sophie Brittain - Rights & Permissions Assistant
Cameron Wood - Legal & Rights Adviser
Contact Details
E-mail: permissions@ioppublishing.org

For further information about copyright and how to request permission:
https://publishingsupport.iopscience.iop.org/copyright-journals/
See also: https://publishingsupport.iopscience.iop.org/
Please see our Author Rights Policy https://publishingsupport.iopscience.iop.org/author-rights-policies/
Please note: We do not provide signed permission forms as a separate attachment. Please print this email and provide it to your publisher as proof of permission. **Please note**: Any statements made by IOP Publishing to the effect that authors do not need to get permission to use any content where IOP Publishing is not the publisher is not intended to constitute any sort of legal advice. Authors must make their own decisions as to the suitability of the content they are using and whether they require permission for it to be published within their article.

From: Alessandra Gioventù <alessandra.gioventu@cern.ch>
Sent: 10 October 2022 11:40
To: Permissions <permissions@ioppublishing.org>
Cc: jinst-eo <jinst-eo@jinst.sissa.it>
Subject: Re: Permission to reuse figures from JINST 3 (2008) S08005

To whom it may concern,

in the previous mail I missed to list a figure from the same paper, i.e. **Figure 2.1**.
Could you please grant me the permission also for this?

Thank you and sorry for the oversight.

Best regards,
Alessandra Gioventù

Il 05/10/22 14:27, Permissions ha scritto:

> Dear Alessandra Gioventù,

Thank you for your request to reproduce material published by IOP Publishing *in your thesis,* ***"Tests of Lepton Flavour Universality with semileptonic D and B decays at the LHCb experiment"***

Regarding:

- ***Figures 5.1, 5.35a, 6.1, 6.2a, 6.4a, 6.21, 6.46, 6.47, 10.1, 10.2, 10.7*** *from* ***"The LHCb Detector at the LHC"***

We are happy to grant permission for the use you request on the terms set out below.

License to publish material published by IOP Publishing

Please provide the below to your new publisher as proof of permission.

Conditions

Non-exclusive, non-transferrable, revocable, worldwide, permission to use the material in print and electronic form will be granted **subject to the following conditions:**

- Permission will be cancelled without notice if you fail to fulfil any of the conditions of this letter.
- You will make reasonable efforts to contact the author(s) to seek consent for your intended use. Contacting one author acting expressly as authorised agent for their co-authors is acceptable.
- You will reproduce the following prominently alongside the material:
  - the source of the material, including author, article title, title of journal, volume number, issue number (if relevant), page range (or first page if this is the only information available) and date of first publication. This information can be contained in a footnote or reference note; or
  - a link back to the article (via DOI); and
  - ***if practical and IN ALL CASES for works published under any of the Creative Commons licences the words "© IOP Publishing Ltd and SISSA. Reproduced by permission of IOP Publishing. All rights reserved"***
- The material will not, without the express permission of the author(s), be used in any way which, in the opinion of IOP Publishing, could distort or alter the author(s)' original intention(s) and meaning, be prejudicial to the honour or reputation of the author(s) and/or imply endorsement by the author(s) and/or IOP Publishing and/or SISSA.
- Payment of £0 is received in full by IOP Publishing prior to use.

This permission does not apply to any material/figure which is credited to another source in our publication or has been obtained from a third party. Express permission for such materials/figures must be obtained from the copyright owner.

Kind regards,

Sophie
Copyright & Permissions Team
Sophie Brittain - Rights & Permissions Assistant
Cameron Wood - Legal & Rights Adviser
Contact Details
E-mail: permissions@ioppublishing.org

For further information about copyright and how to request permission:
https://publishingsupport.iopscience.iop.org/copyright-journals/
See also: https://publishingsupport.iopscience.iop.org/
Please see our Author Rights Policy https://publishingsupport.iopscience.iop.org/author-rights-policies/
Please note: We do not provide signed permission forms as a separate attachment. Please print this email and provide it to your publisher as proof of permission. **Please note**: Any statements made by IOP Publishing to the effect that authors do not need to get permission to use any content where IOP Publishing is not the publisher is not intended to constitute any sort of legal advice. Authors must make their own decisions as to the suitability of the content they are using and whether they require permission for it to be published within their article.

From: Alessandra Gioventù <alessandra.gioventu@cern.ch>
Sent: 03 October 2022 09:54
To: Permissions <permissions@ioppublishing.org>
Subject: Permission to reuse figures from JINST 3 (2008) S08005

To whom it may concern,
I am Alessandra Gioventù, a PhD student in experimental particle physics at the University of Santiago de Compostela (Spain).
I would like to use some figures from the paper
The LHCb detector at the LHC, LHCb collaboration et al., JINST 3 (2008) S08005
These are the following:

- 5.1
- 5.35a
- 6.1
- 6.2a
- 6.4a
- 6.21
- 6.46
- 6.47
- 10.1
- 10.2
- 10.7

The title of my thesis is “Tests of Lepton Flavour Universality with semileptonic D and B decays at the LHCb experiment”
Could you grant me the permission to use it?

Thank you very much in advance.

Best regards,
Alessandra Gioventù

--
Alessandra Gioventù PhD student
Instituto Galego de Física de Altas Enerxías - Universidade de Santiago de Compostela

Rúa de Xoaquín Díaz de Rábago s/n, Campus Vida - Universidade de Santiago de Compostela, Santiago de Compostela, 15705, Spain

IGFAE: ale.gioventu@usc.es Tel: +34 8818 13983
CERN: alessandra.gioventu@cern.ch Tel: +41 22 76 76585

--
Alessandra Gioventù PhD student
Instituto Galego de Física de Altas Enerxías - Universidade de Santiago de Compostela

Rúa de Xoaquín Díaz de Rábago s/n, Campus Vida - Universidade de Santiago de Compostela, Santiago de Compostela, 15705, Spain

IGFAE: ale.gioventu@usc.es Tel: +34 8818 13983
CERN: alessandra.gioventu@cern.ch Tel: +41 22 76 76585

References

[1] Particle Data Group, R. L. Workman *et al.*, *Review of particle physics*, Prog. Theor. Exp. Phys. **2022** (2022) 083C01. (Cited on pages xvi, xviii, xx, 4, 11, 14, 15, 27, 28, 29, 81, 88, 107, 108, 109, 132, 135, 136, 137, 138, 150, 159, 160, 202, 203, 204, 205, 214, 215, 224, 225, 227, and 230.)

[2] LHCb collaboration, R. Aaij *et al.*, *Observation of two new Ξ_b^- baryon resonances*, Phys. Rev. Lett. **114** (2015) 062004, `arXiv:1411.4849`. (Cited on pages 5 and 37.)

[3] LHCb collaboration, R. Aaij *et al.*, *Observation of $J/\psi p$ resonances consistent with pentaquark states in $\Lambda_b^0 \to J/\psi p K^-$ decays*, Phys. Rev. Lett. **115** (2015) 072001, `arXiv:1507.03414`. (Cited on pages 5 and 37.)

[4] S. L. Glashow, *Partial-symmetries of weak interactions*, Nuclear Physics **22** (1961) 579. (Cited on page 5.)

[5] S. Weinberg, *A model of leptons*, Phys. Rev. Lett. **19** (1967) 1264. (Cited on page 5.)

[6] A. Salam and J. C. Ward, *Electromagnetic and weak interactions*, Physics Letters **13** (1964) 168. (Cited on page 5.)

[7] C. S. Wu *et al.*, *Experimental test of parity conservation in beta decay*, Phys. Rev. **105** (1957) 1413. (Cited on page 5.)

[8] F. Englert and R. Brout, *Broken symmetry and the mass of gauge vector mesons*, Phys. Rev. Lett. **13** (1964) 321. (Cited on page 7.)

[9] P. W. Higgs, *Broken symmetries and the masses of gauge bosons*, Phys. Rev. Lett. **13** (1964) 508. (Cited on page 7.)

[10] B. T. Cleveland *et al.*, *Measurement of the solar electron neutrino flux with the homestake chlorine detector*, The Astrophysical Journal **496** (1998) 505. (Cited on pages 8 and 11.)

[11] Super-Kamiokande Collaboration, Y. Fukuda *et al.*, *Evidence for oscillation of atmospheric neutrinos*, Phys. Rev. Lett. **81** (1998) 1562. (Cited on pages 8 and 11.)

[12] M. V. Diwan, V. Galymov, X. Qian, and A. Rubbia, *Long-baseline neutrino experiments*, Annual Review of Nuclear and Particle Science **66** (2016) 47. (Cited on pages 8 and 11.)

[13] N. Cabibbo, *Unitary symmetry and leptonic decays*, Phys. Rev. Lett. **10** (1963) 531. (Cited on pages 9, 11, and 17.)

[14] M. Kobayashi and T. Maskawa, *CP-violation in the renormalizable theory of weak interaction*, Prog. Theor. Phys. **49** (1973) 652. (Cited on page 9.)

[15] L. Wolfenstein, *Parametrization of the kobayashi-maskawa matrix*, Phys. Rev. Lett. **51** (1983) 1945. (Cited on page 10.)

[16] S. L. Glashow, J. Iliopoulos, and L. Maiani, *Weak interactions with lepton-hadron symmetry*, Phys. Rev. D **2** (1970) 1285. (Cited on pages 11 and 17.)

[17] Z. Maki, M. Nakagawa, and S. Sakata, *Remarks on the Unified Model of Elementary Particles*, Progress of Theoretical Physics **28** (1962) 870, arXiv:https://academic.oup.com/ptp/article-pdf/28/5/870/5258750/28-5-870.pdf. (Cited on page 11.)

[18] C. N. Yang and R. L. Mills, *Conservation of isotopic spin and isotopic gauge invariance*, Phys. Rev. **96** (1954) 191. (Cited on page 11.)

[19] A. D. Sakharov, *Violation of cp invariance, c asymmetry, and baryon asymmetry of the universe*, Soviet Physics Uspekhi **34** (1991) 392. (Cited on page 12.)

[20] M. Fael and C. Greub, *Next-to-leading order prediction for the decay* $\mu \to e\ (e^+e^-)\ \nu\,\overline{\nu}$, JHEP **01** (2017) 084, arXiv:1611.03726. (Cited on page 13.)

[21] A. Pich, *Tau physics: theoretical perspective*, Nuclear Physics B - Proceedings Supplements **98** (2001) 385. (Cited on page 13.)

[22] S. Bifani, S. Descotes-Genon, A. Romero Vidal, and M.-H. Schune, *Review of Lepton Universality tests in B decays*, J. Phys. G **46** (2019) 023001, arXiv:1809.06229. (Cited on pages 16, 18, and 221.)

[23] G. Buchalla, A. J. Buras, and M. E. Lautenbacher, *Weak decays beyond leading logarithms*, Rev. Mod. Phys. **68** (1996) 1125. (Cited on page 17.)

[24] A. J. Buras, *Weak hamiltonian, cp violation and rare decays*, 1998. Appear in Probing the standard model of particle interactions. Proceedings, Summer School in Theoretical Physics, NATO Advanced Study Institute, 68th session, Les Houches, France, July 28-September 5, 1997, doi: 10.48550/ARXIV.HEP-PH/9806471. (Cited on page 17.)

[25] M. Neubert, *Heavy quark effective theory*, Subnucl. Ser. **34** (1997) 98, arXiv:hep-ph/9610266. (Cited on page 17.)

[26] K. G. Wilson, *Non-lagrangian models of current algebra*, Phys. Rev. **179** (1969) 1499. (Cited on page 18.)

[27] S. Fajfer, I. Nišandžć, and U. Rojec, *Discerning new physics in charm meson leptonic and semileptonic decays*, Phys. Rev. D **91** (2015) 094009, arXiv:1502.07488. (Cited on pages 19, 26, 28, 104, and 199.)

[28] J. Koponen *et al.*, *The shape of the $D \to K$ semileptonic form factor from full lattice QCD and V_{cs}*, arXiv:1305.1462. (Cited on page 20.)

[29] HPQCD collaboration, B. Chakraborty *et al.*, *Improved Vcs determination using precise lattice QCD form factors for $D \to K\ell\nu$*, Phys. Rev. D **104** (2021) 034505, arXiv:2104.09883. (Cited on pages 20, 26, 27, and 221.)

[30] N. Isgur, D. Scora, B. Grinstein, and M. B. Wise, *Semileptonic B and D decays in the quark model*, Phys. Rev. D **39** (1989) 799. (Cited on pages 21, 74, and 128.)

[31] D. Scora and N. Isgur, *Semileptonic meson decays in the quark model: An update*, Phys. Rev. D **52** (1995) 2783. (Cited on pages 21, 74, and 128.)

[32] D. Becirevic and A. B. Kaidalov, *Comment on the heavy $\to$ light form-factors*, Phys. Lett. B **478** (2000) 417, arXiv:hep-ph/9904490. (Cited on pages 21 and 74.)

[33] S. Fajfer, J. F. Kamenik, and I. Nišandžić, *$B \to D^* \tau \overline{\nu}_\tau$ sensitivity to new physics*, Phys. Rev. D **85** (2012) 094025, arXiv:1203.2654. (Cited on pages 21, 22, 173, and 218.)

[34] I. Caprini, L. Lellouch, and M. Neubert, *Dispersive bounds on the shape of $\overline{B} \to D^{(*)} \ell \overline{\nu}$ form-factors*, Nucl. Phys. B **530** (1998) 153, arXiv:hep-ph/9712417. (Cited on page 23.)

[35] C. G. Boyd, B. Grinstein, and R. F. Lebed, *Constraints on form-factors for exclusive semileptonic heavy to light meson decays*, Phys. Rev. Lett. **74** (1995) 4603, arXiv:hep-ph/9412324. (Cited on page 23.)

[36] C. G. Boyd, B. Grinstein, and R. F. Lebed, *Model independent determinations of $\overline{B} \to D\ell\overline{\nu}, D^*\ell\overline{\nu}$ form-factors*, Nucl. Phys. B **461** (1996) 493, arXiv:hep-ph/9508211. (Cited on pages 23 and 24.)

[37] C. G. Boyd, B. Grinstein, and R. F. Lebed, *Precision corrections to dispersive bounds on form-factors*, Phys. Rev. D **56** (1997) 6895, arXiv:hep-ph/9705252. (Cited on page 23.)

[38] D. Bigi and P. Gambino, *Revisiting $B \to D\ell\nu$*, Phys. Rev. D **94** (2016) 094008, arXiv:1606.08030. (Cited on pages 23, 29, 31, 128, 131, 221, and 228.)

[39] Belle II collaboration, *Belle II luminosity page*, https://confluence.desy.de/display/BI/Belle+II+Luminosity. Last visited on 15^{th} November 2022. (Cited on page 26.)

[40] BESIII collaboration, M. Ablikim, *et al.*, *Study of the $D^0 \to K^- \mu^+ \nu_\mu$ dynamics and test of lepton flavor universality with $D^0 \to K^- \ell^+ \nu_\ell$ decays*, Phys. Rev. Lett. **122** (2019) 011804, arXiv:1810.03127. (Cited on pages 26 and 27.)

[41] BESIII collaboration, M. Ablikim *et al.*, *Improved measurement of the absolute branching fraction of* $D^+ \to \bar{K}^0\mu^+\nu_\mu$, Eur. Phys. J. **C76** (2016) 369, arXiv:1605.00068. (Cited on page 27.)

[42] BESIII collaboration, M. Ablikim *et al.*, *Measurement of the branching fraction for the semileptonic decay* $D^{0(+)} \to \pi^{-(0)}\mu^+\nu_\mu$ *and test of lepton flavor universality*, Phys. Rev. Lett. **121** (2018) 171803, arXiv:1802.05492. (Cited on pages 26 and 27.)

[43] BESIII collaboration, M. Ablikim *et al.*, *Study of Dynamics of* $D^0 \to K^-e^+\nu_e$ *and* $D^0 \to \pi^-e^+\nu_e$ *Decays*, Phys. Rev. **D92** (2015) 072012, arXiv:1508.07560. (Cited on pages 27 and 74.)

[44] BaBar collaboration, J. P. Lees *et al.*, *Evidence for an excess of* $\bar{B} \to D^{(*)}\tau^-\bar{\nu}_\tau$ *decays*, Phys. Rev. Lett. **109** (2012) 101802, arXiv:1205.5442. (Cited on pages 29, 30, 162, and 217.)

[45] BaBar collaboration, J. P. Lees *et al.*, *Measurement of an Excess of* $\bar{B} \to D^{(*)}\tau^-\bar{\nu}_\tau$ *Decays and Implications for Charged Higgs Bosons*, Phys. Rev. D **88** (2013) 072012, arXiv:1303.0571. (Cited on pages 29, 30, 162, and 217.)

[46] Belle collaboration, M. Huschle *et al.*, *Measurement of the branching ratio of* $\bar{B} \to D^{(*)}\tau^-\bar{\nu}_\tau$ *relative to* $\bar{B} \to D^{(*)}\ell^-\bar{\nu}_\ell$ *decays with hadronic tagging at Belle*, Phys. Rev. D **92** (2015) 072014, arXiv:1507.03233. (Cited on pages 29, 30, 162, and 217.)

[47] LHCb collaboration, R. Aaij *et al.*, *Measurement of the ratio of branching fractions* $\mathcal{B}(\overline{B}^0 \to D^{*+}\tau^-\overline{\nu}_\tau)/\mathcal{B}(\overline{B}^0 \to D^{*+}\mu^-\overline{\nu}_\mu)$, Phys. Rev. Lett. **115** (2015) 111803, Publisher's Note ibid. **115** (2015) 159901, arXiv:1506.08614. (Cited on pages 29, 30, 37, 162, and 217.)

[48] Belle collaboration, S. Hirose *et al.*, *Measurement of the* τ *lepton polarization and* $R(D^*)$ *in the decay* $\bar{B} \to D^*\tau^-\bar{\nu}_\tau$, Phys. Rev. Lett. **118** (2017) 211801, arXiv:1612.00529. (Cited on pages 29, 30, 162, and 217.)

[49] Belle collaboration, S. Hirose *et al.*, *Measurement of the* τ *lepton polarization and* $R(D^*)$ *in the decay* $\bar{B} \to D^*\tau^-\bar{\nu}_\tau$, Phys. Rev. Lett. **118** (2017) 211801, arXiv:1612.00529. (Cited on pages 29, 30, 162, and 217.)

[50] Belle collaboration, G. Caria *et al.*, *Measurement of* $\mathcal{R}(D)$ *and* $\mathcal{R}(D^*)$ *with a semileptonic tagging method*, Phys. Rev. Lett. **124** (2020) 161803, arXiv:1910.05864. (Cited on pages 29, 30, 162, and 217.)

[51] LHCb collaboration, R. Aaij *et al.*, *Simultaneous extraction of the branching fraction ratios* $\mathcal{R}(D)$ *and* $\mathcal{R}(D^*)$ *with the Run 1 dataset using the* $\tau^+ \to \mu^+\nu_\mu\bar{\nu}_\tau$ *decay*, arXiv:2302.02886, For submission to PRL. (Cited on pages 29, 30, 128, 162, and 217.)

[52] LHCb collaboration, R. Aaij *et al.*, *Measurement of the ratio of branching fractions* $\mathcal{B}(B_c^+ \to J/\psi\tau^+\nu_\tau)/\mathcal{B}(B_c^+ \to J/\psi\mu^+\nu_\mu)$, Phys. Rev. Lett. **120** (2018) 121801, arXiv:1711.05623. (Cited on page 29.)

[53] LHCb collaboration, R. Aaij *et al.*, *Measurement of the ratio of the* $\mathcal{B}(B^0 \to D^{*-}\tau^+\nu_\tau)$ *and* $\mathcal{B}(B^0 \to D^{*-}\mu^+\nu_\mu)$ *branching fractions using three-prong* τ*-lepton decays*, Phys. Rev. Lett. **120** (2018) 171802, arXiv:1708.08856. (Cited on pages 29, 30, 37, 108, 116, 136, 162, 168, 203, and 217.)

[54] LHCb collaboration, R. Aaij *et al.*, *Test of lepton flavor universality by the measurement of the* $B^0 \to D^{*-}\tau^+\nu_\tau$ *branching fraction using three-prong* τ *decays*, Phys. Rev. **D97** (2018) 072013, arXiv:1711.02505. (Cited on pages 29, 30, 37, 108, 116, 136, 162, 168, 203, and 217.)

[55] LHCb collaboration, R. Aaij *et al.*, *Observation of the decay* $\Lambda_b^0 \to \Lambda_c^+\tau^-\bar{\nu}_\tau$, Phys. Rev. Lett. **128** (2021) 191803, arXiv:2201.03497. (Cited on pages 29 and 168.)

[56] A. Y. Anisimov, I. M. Narodetskii, C. Semay, and B. Silvestre-Brac, *The* B_c *meson lifetime in the light-front constituent quark model*, Physics Letters B **452** (1999) 129. (Cited on page 29.)

[57] V. V. Kiselev, *Exclusive decays and lifetime of* B_c *meson in QCD sum rules*, arXiv:hep-ph/0211021. (Cited on page 29.)

[58] M. A. Ivanov, J. G. Körner, and P. Santorelli, *Exclusive semileptonic and nonleptonic decays of the* B_c *meson*, Phys. Rev. D **73** (2006) 054024. (Cited on page 29.)

[59] E. Hernández, J. Nieves, and J. M. Verde-Velasco, *Study of exclusive semileptonic and nonleptonic decays of* B_c^- *in a nonrelativistic quark model*, Phys. Rev. D **74** (2006) 074008. (Cited on page 29.)

[60] Y. Amhis *et al.*, *Averages of b-hadron, c-hadron, and* τ*-lepton properties as of 2021*, arXiv:2206.07501. (Cited on pages 29, 30, 31, 74, 108, 109, 160, 162, 203, 216, 217, and 221.)

[61] M. Bordone, M. Jung, and D. van Dyk, *Theory determination of* $\bar{B} \to D^{(*)}\ell^-\bar{\nu}$ *form factors at* $\mathcal{O}(1/m_c^2)$, Eur. Phys. J. C **80** (2020) 74, arXiv:1908.09398. (Cited on pages 29, 31, and 221.)

[62] P. Gambino, M. Jung, and S. Schacht, *The* V_{cb} *puzzle: An update*, Phys. Lett. B **795** (2019) 386, arXiv:1905.08209. (Cited on pages 29, 31, and 221.)

[63] F. U. Bernlochner, Z. Ligeti, M. Papucci, and D. J. Robinson, *Combined analysis of semileptonic B decays to D and* D^**:* $R(D^{(*)})$*,* $|V_{cb}|$*, and new physics*, Phys. Rev. D **95** (2017) 115008, arXiv:1703.05330, [Erratum: Phys.Rev.D 97, 059902 (2018)]. (Cited on pages 29, 31, and 221.)

[64] S. Jaiswal, S. Nandi, and S. K. Patra, *Extraction of $|V_{cb}|$ from $B \to D^{(*)}\ell\nu_\ell$ and the Standard Model predictions of $R(D^{(*)})$*, JHEP **12** (2017) 060, arXiv:1707.09977. (Cited on pages 29, 31, and 221.)

[65] BaBar collaboration, J. P. Lees *et al.*, *Extraction of form Factors from a Four-Dimensional Angular Analysis of $\overline{B} \to D^*\ell^-\overline{\nu}_\ell$*, Phys. Rev. Lett. **123** (2019) 091801, arXiv:1903.10002. (Cited on pages 29, 31, and 221.)

[66] G. Martinelli, S. Simula, and L. Vittorio, *$|V_{cb}|$ and $R(D)^{(*)}$) using lattice QCD and unitarity*, Phys. Rev. D **105** (2022) 034503, arXiv:2105.08674. (Cited on pages 29, 31, and 221.)

[67] D. Bigi, P. Gambino, and S. Schacht, *$R(D^*)$, $|V_{cb}|$, and the Heavy Quark Symmetry relations between form factors*, JHEP **11** (2017) 061, arXiv:1707.09509. (Cited on pages 29, 31, 128, 131, 221, and 228.)

[68] Fermilab Lattice, MILC collaboration, A. Bazavov *et al.*, *Semileptonic form factors for $B \to D^*\ell\nu$ at nonzero recoil from 2 + 1-flavor lattice QCD*, arXiv:2105.14019. (Cited on pages 29, 31, and 221.)

[69] HPQCD collaboration, H. Na *et al.*, *$B \to D\ell\nu$ form factors at nonzero recoil and extraction of $|V_{cb}|$*, Phys. Rev. D **92** (2015) 054510, arXiv:1505.03925, [Erratum: Phys.Rev.D 93, 119906 (2016)]. (Cited on pages 31 and 221.)

[70] M. Bordone, G. Isidori, and A. Pattori, *On the Standard Model predictions for R_K and R_{K^*}*, Eur. Phys. J. C **76** (2016) 440, arXiv:1605.07633. (Cited on page 32.)

[71] W. Altmannshofer, C. Niehoff, P. Stangl, and D. M. Straub, *Status of the $B \to K^*\mu^+\mu^-$ anomaly after Moriond 2017*, Eur. Phys. J. C **77** (2017) 377, arXiv:1703.09189. (Cited on page 32.)

[72] L.-S. Geng *et al.*, *Towards the discovery of new physics with lepton-universality ratios of $b \to s\ell\ell$ decays*, Phys. Rev. D **96** (2017) 093006, arXiv:1704.05446. (Cited on page 32.)

[73] B. Capdevila *et al.*, *Patterns of New Physics in $b \to s\ell^+\ell^-$ transitions in the light of recent data*, JHEP **01** (2018) 093, arXiv:1704.05340. (Cited on page 32.)

[74] LHCb collaboration, R. Aaij *et al.*, *Test of lepton universality with $B^0 \to K^{*0}\ell^+\ell^-$ decays*, JHEP **08** (2017) 055, arXiv:1705.05802. (Cited on pages 32 and 33.)

[75] LHCb collaboration, R. Aaij *et al.*, *Test of lepton universality in beauty-quark decays*, Nature Physics **18** (2022) 277, arXiv:2103.11769. (Cited on pages 32 and 33.)

[76] LHCb collaboration, R. Aaij *et al.*, *Measurement of lepton universality parameters in $B^+ \to K^+\ell^+\ell^-$ and $B^0 \to K^{*0}\ell^+\ell^-$ decays*, arXiv:2212.09153, submitted to Phys. Rev. D. (Cited on pages 32 and 33.)

[77] LHCb collaboration, R. Aaij *et al.*, *Test of lepton universality in $b \to s\ell^+\ell^-$ decays*, arXiv:2212.09152, submitted to Phys. Rev. Lett. (Cited on pages 32 and 33.)

[78] S. Descotes-Genon, T. Hurth, J. Matias, and J. Virto, *Optimizing the basis of $B \to K^*\ell\ell$ observables in the full kinematic range*, JHEP **05** (2013) 137, arXiv:1303.5794. (Cited on page 32.)

[79] LHCb collaboration, R. Aaij *et al.*, *Angular analysis of the $B^+ \to K^{*+}\mu^+\mu^-$ decay*, Phys. Rev. Lett. **126** (2021) 161802, arXiv:2012.13241. (Cited on page 32.)

[80] LHCb collaboration, R. Aaij *et al.*, *Measurement of CP-averaged observables in the $B^0 \to K^{*0}\mu^+\mu^-$ decay*, Phys. Rev. Lett. **125** (2020) 011802, arXiv:2003.04831. (Cited on page 32.)

[81] CMS collaboration, A. M. Sirunyan *et al.*, *Angular analysis of the decay $B^+ \to K^*(892)^+\mu^+\mu^-$ in proton-proton collisions at $\sqrt{s} = 8$ TeV*, JHEP **04** (2021) 124, arXiv:2010.13968. (Cited on page 32.)

[82] ATLAS collaboration, M. Aaboud *et al.*, *Angular analysis of $B_d^0 \to K^*\mu^+\mu^-$ decays in pp collisions at $\sqrt{s} = 8$ TeV with the ATLAS detector*, JHEP **10** (2018) 047, arXiv:1805.04000. (Cited on page 32.)

[83] CMS collaboration, A. M. Sirunyan *et al.*, *Measurement of angular parameters from the decay $\mathrm{B}^0 \to \mathrm{K}^{*0}\mu^+\mu^-$ in proton-proton collisions at $\sqrt{s} = 8$ TeV*, Phys. Lett. B **781** (2018) 517, arXiv:1710.02846. (Cited on page 32.)

[84] Belle collaboration, S. Wehle *et al.*, *Lepton-Flavor-Dependent Angular Analysis of $B \to K^*\ell^+\ell^-$*, Phys. Rev. Lett. **118** (2017) 111801, arXiv:1612.05014. (Cited on page 32.)

[85] LHCb collaboration, R. Aaij *et al.*, *Measurements of the S-wave fraction in $B^0 \to K^+\pi^-\mu^+\mu^-$ decays and the $B^0 \to K^*(892)^0\mu^+\mu^-$ differential branching fraction*, JHEP **11** (2016) 047, Erratum ibid. **04** (2017) 142, arXiv:1606.04731. (Cited on page 32.)

[86] LHCb collaboration, R. Aaij *et al.*, *Differential branching fraction and angular analysis of $\Lambda_b^0 \to \Lambda\mu^+\mu^-$ decays*, JHEP **06** (2015) 115, Erratum ibid. **09** (2018) 145, arXiv:1503.07138. (Cited on page 32.)

[87] LHCb collaboration, R. Aaij *et al.*, *Measurement of the Z + b-jet cross-section in pp collisions at $\sqrt{s} = 7$ TeV in the forward region*, JHEP **01** (2015) 064, arXiv:1411.1264. (Cited on page 32.)

[88] LHCb collaboration, R. Aaij *et al.*, *Differential branching fractions and isospin asymmetries of $B \to K^{(*)}\mu^+\mu^-$ decays*, JHEP **06** (2014) 133, arXiv:1403.8044. (Cited on page 32.)

[89] Belle collaboration, J.-T. Wei *et al.*, *Measurement of the Differential Branching Fraction and Forward-Backward Asymmetry for $B \to K^{(*)}\ell^+\ell^-$*, Phys. Rev. Lett. **103** (2009) 171801, arXiv:0904.0770. (Cited on page 33.)

[90] BaBar collaboration, J. P. Lees *et al.*, *Measurement of Branching Fractions and Rate Asymmetries in the Rare Decays $B \to K^{(*)}\ell^+\ell^-$*, Phys. Rev. D **86** (2012) 032012, arXiv:1204.3933. (Cited on page 33.)

[91] Belle collaboration, A. Abdesselam *et al.*, *Test of Lepton-Flavor Universality in $B \to K^*\ell^+\ell^-$ Decays at Belle*, Phys. Rev. Lett. **126** (2021) 161801, arXiv:1904.02440. (Cited on page 33.)

[92] LHCb collaboration, R. Aaij *et al.*, *Tests of lepton universality using $B^0 \to K^0_S\ell^+\ell^-$ and $B^+ \to K^{*+}\ell^+\ell^-$ decays*, Phys. Rev. Lett. **128** (2022) 191802, arXiv:2110.09501. (Cited on page 33.)

[93] BELLE collaboration, S. Choudhury *et al.*, *Test of lepton flavor universality and search for lepton flavor violation in $B \to K\ell\ell$ decays*, JHEP **03** (2021) 105, arXiv:1908.01848. (Cited on page 33.)

[94] LHCb collaboration, R. Aaij *et al.*, *Test of lepton universality using $\Lambda_b^0 \to pK^-\ell^+\ell^-$ decays*, JHEP **05** (2020) 040, arXiv:1912.08139. (Cited on page 33.)

[95] L. Evans and P. Bryant, *LHC Machine*, JINST **3** (2008) S08001. (Cited on page 35.)

[96] E. Mobs, *The CERN accelerator complex in 2019. Complexe des accélérateurs du CERN en 2019*, , General Photo. (Cited on pages 36 and 221.)

[97] ATLAS collaboration, G. Aad *et al.*, *The ATLAS experiment at the CERN large hadron collider*, JINST **3** (2008) S08003. (Cited on page 37.)

[98] CMS collaboration, S. Chatrchyan *et al.*, *The CMS experiment at the CERN LHC*, JINST **3** (2008) S08004. (Cited on page 37.)

[99] ATLAS collaboration, G. Aad *et al.*, *Observation of a new particle in the search for the Standard Model Higgs boson with the ATLAS detector at the LHC*, Physics Letters B **716** (2012) 1. (Cited on page 37.)

[100] CMS collaboration, S. Chatrchyan *et al.*, *Observation of a new boson at a mass of 125 GeV with the CMS experiment at the LHC*, Physics Letters B **716** (2012) 30. (Cited on page 37.)

[101] ALICE collaboration, K. Aamodt *et al.*, *The ALICE experiment at the CERN LHC*, JINST **3** (2008) S08002. (Cited on page 37.)

[102] LHCb collaboration, A. A. Alves Jr. *et al.*, *The LHCb detector at the LHC*, JINST **3** (2008) S08005. (Cited on pages 37, 40, 41, 43, 44, 47, 48, 49, 54, 55, 62, 194, 221, 222, and 224.)

[103] CMS and LHCb collaborations, V. Khachatryan *et al.*, *Observation of the rare $B^0_s \to \mu^+\mu^-$ decay from the combined analysis of CMS and LHCb data*, Nature **522** (2015) 68, arXiv:1411.4413. (Cited on page 37.)

[104] LHCb collaboration, R. Aaij *et al.*, *Observation of CP violation in charm decays*, Phys. Rev. Lett. **122** (2019) 211803, arXiv:1903.08726. (Cited on page 37.)

[105] LHCb collaboration, R. Aaij *et al.*, *First observation of CP violation in the decays of B^0_s mesons*, Phys. Rev. Lett. **110** (2013) 221601, arXiv:1304.6173. (Cited on page 37.)

[106] LHCb collaboration, R. Aaij *et al.*, *Observation of CP violation in two-body B^0_s-meson decays to charged pions and kaons*, JHEP **03** (2021) 075, arXiv:2012.05319. (Cited on page 37.)

[107] LHCb collaboration, R. Aaij *et al.*, *Measurement of the nuclear modification factor and prompt charged particle production in pPb and pp collisions at $\sqrt{s_{NN}} = 5$ TeV*, Phys. Rev. Lett. **128** (2022) 142004, arXiv:2108.13115. (Cited on page 37.)

[108] LHCb collaboration, R. Aaij *et al.*, *Measurement of the W boson mass*, JHEP **01** (2022) 036, arXiv:2109.01113. (Cited on page 37.)

[109] LHCb collaboration, R. Aaij *et al.*, *Observation of a narrow pentaquark state, $P_c(4312)^+$, and of two-peak structure of the $P_c(4450)^+$*, Phys. Rev. Lett. **122** (2019) 222001, arXiv:1904.03947. (Cited on page 37.)

[110] LHCb collaboration, R. Aaij *et al.*, *Search for dark photons produced in 13 TeV pp collisions*, Phys. Rev. Lett. **120** (2018) 061801, arXiv:1710.02867. (Cited on page 37.)

[111] T. Sjöstrand, S. Mrenna, and P. Skands, *A brief introduction to PYTHIA 8.1*, Comput. Phys. Commun. **178** (2008) 852, arXiv:0710.3820. (Cited on page 37.)

[112] LHCb collaboration, C. Elsässer, *$\bar{b}b$ production angle plots*, https://lhcb.web.cern.ch/lhcb/speakersbureau/html/bb_ProductionAngles.html. Last visited on 8^{th} July 2022. (Cited on pages 38 and 221.)

[113] LHCb collaboration, *Nu, mu and pile-up. the lhcb definitions of what we see and what we don't see*, https://twiki.cern.ch/twiki/bin/view/LHCb/NuMuPileUp, 2002. (Cited on page 38.)

[114] LHCb collaboration, R. Aaij *et al.*, *LHCb detector performance*, Int. J. Mod. Phys. **A30** (2015) 1530022, arXiv:1412.6352. (Cited on pages 39 and 221.)

[115] LHCb collaboration, *LHCb VELO (VErtex LOcator): Technical Design Report*, CERN-LHCC-2001-011, 2001. (Cited on page 41.)

[116] LHCb collaboration, *LHCb VELO Upgrade Technical Design Report*, CERN-LHCC-2013-021, 2013. (Cited on pages 41 and 164.)

[117] R. Aaij *et al.*, *Performance of the LHCb Vertex Locator*, JINST **9** (2014) P09007, arXiv:1405.7808. (Cited on pages 42 and 55.)

[118] LHCb collaboration, *LHCb RICH: Technical Design Report*, CERN-LHCC-2000-037, 2000. (Cited on page 42.)

[119] LHCb collaboration, *LHCb inner tracker: Technical Design Report*, CERN-LHCC-2002-029, 2002. (Cited on page 43.)

[120] LHCb collaboration, *LHCb outer tracker: Technical Design Report*, CERN-LHCC-2001-024, 2001. (Cited on page 45.)

[121] LHCb collaboration, *LHCb magnet: Technical Design Report*, CERN-LHCC-2000-007, 2000. (Cited on page 46.)

[122] LHCb collaboration, *LHCb calorimeters: Technical Design Report*, CERN-LHCC-2000-036, 2000. (Cited on page 46.)

[123] L. Capriotti, *Searches for new physics in violation of strong CP symmetry and lepton universality with the LHCb experiment*, PhD thesis, Manchester University, 2018, Presented 26 Apr 2018. (Cited on pages 46, 60, 101, 221, 222, and 223.)

[124] W. R. Leo, *Techniques for Nuclear and Particle Physics Experiments: A How-to Approach*, Springer, 1994. (Cited on page 47.)

[125] C. Abellan Beteta *et al.*, *Calibration and performance of the LHCb calorimeters in Run 1 and 2 at the LHC*, arXiv:2008.11556, submitted to JINST. (Cited on pages 47 and 222.)

[126] H. Fessler *et al.*, *A Tower structured scintillator lead photon calorimeter using a novel fiber optics readout system*, Nucl. Instrum. Meth. **A228** (1985) 303. (Cited on page 48.)

[127] G. S. Atoyan *et al.*, *Lead-scintillator electromagnetic calorimeter with wavelength shifting fiber readout*, Nucl. Instrum. Meth. A **320** (1992) 144 . (Cited on page 48.)

[128] F. Archilli *et al.*, *Performance of the muon identification at LHCb*, JINST **8** (2013) P10020, arXiv:1306.0249. (Cited on page 49.)

[129] LHCb collaboration, *LHCb trigger system: Technical Design Report*, CERN-LHCC-2003-031, 2003. (Cited on page 50.)

[130] G. Dujany and B. Storaci, *Real-time alignment and calibration of the LHCb Detector in Run II*, J. Phys. Conf. Ser. **664** (2015) 082010. (Cited on page 50.)

[131] R. Aaij *et al.*, *Performance of the LHCb trigger and full real-time reconstruction in Run 2 of the LHC*, JINST **14** (2019) P04013, arXiv:1812.10790. (Cited on pages 50, 51, 167, 222, 224, and 227.)

[132] LHCb collaboration, R. Aaij *et al.*, *Measurement of the track reconstruction efficiency at LHCb*, JINST **10** (2015) P02007, arXiv:1408.1251. (Cited on page 54.)

[133] LHCb collaboration, R. Aaij *et al.*, *Measurement of the electron reconstruction efficiency at LHCb*, JINST **14** (2019) P11023, arXiv:1909.02957. (Cited on pages 55, 56, 57, and 222.)

[134] R. Forty, *Rich pattern recognition for lhcb*, Nuclear Instruments and Methods in Physics Research Section A: Accelerators, Spectrometers, Detectors and Associated Equipment **433** (1999) 257. (Cited on page 59.)

[135] L. Anderlini *et al.*, *The PIDCalib package* , CERN, Geneva, 2016. (Cited on pages 59 and 121.)

[136] M. Pivk and F. R. Le Diberder, *sPlot: A statistical tool to unfold data distributions*, Nucl. Instrum. Meth. **A555** (2005) 356, arXiv:physics/0402083. (Cited on page 59.)

[137] M. Clemencic *et al.*, *The LHCb simulation application, Gauss: Design, evolution and experience*, J. Phys. Conf. Ser. **331** (2011) 032023. (Cited on page 61.)

[138] T. Sjöstrand, S. Mrenna, and P. Skands, *PYTHIA 6.4 physics and manual*, JHEP **05** (2006) 026, arXiv:hep-ph/0603175. (Cited on page 61.)

[139] D. J. Lange, *The EvtGen particle decay simulation package*, Nucl. Instrum. Meth. **A462** (2001) 152. (Cited on page 61.)

[140] P. Golonka and Z. Was, *PHOTOS Monte Carlo: A precision tool for QED corrections in Z and W decays*, Eur. Phys. J. **C45** (2006) 97, arXiv:hep-ph/0506026. (Cited on page 61.)

[141] Geant4 collaboration, S. Agostinelli *et al.*, *Geant4: A simulation toolkit*, Nucl. Instrum. Meth. **A506** (2003) 250. (Cited on page 61.)

[142] Geant4 collaboration, J. Allison *et al.*, *Geant4 developments and applications*, IEEE Trans. Nucl. Sci. **53** (2006) 270. (Cited on page 61.)

[143] D. Müller, M. Clemencic, G. Corti, and M. Gersabeck, *ReDecay: A novel approach to speed up the simulation at LHCb*, Eur. Phys. J. C **78** (2018) 1009, arXiv:1810.10362. (Cited on pages 61 and 112.)

[144] G. A. Cowan, D. C. Craik, and M. D. Needham, *RapidSim: an application for the fast simulation of heavy-quark hadron decays*, Comput. Phys. Commun. **214** (2017) 239, arXiv:1612.07489. (Cited on page 61.)

[145] LHCb collaboration, R. Aaij *et al.*, *Measurements of charm mixing and CP violation using $D^0 \to K^\pm\pi^\mp$ decays*, Phys. Rev. **D95** (2017) 052004, Erratum ibid. **D96** (2017) 099907, arXiv:1611.06143. (Cited on page 71.)

[146] LHCb collaboration, R. Aaij *et al.*, *Measurement of D^0–$\overline{D}^0$ mixing parameters and search for CP violation using $D^0 \to K^+\pi^-$ decays*, Phys. Rev. Lett. **111** (2013) 251801, arXiv:1309.6534. (Cited on page 71.)

[147] A. Rogozhnikov, *Reweighting with Boosted Decision Trees*, J. Phys. Conf. Ser. **762** (2016) 012036, arXiv:1608.05806, https://github.com/arogozhnikov/hep_ml. (Cited on page 72.)

[148] A. Gioventù, *Test of lepton flavour universality with charm semileptonic decays*, 2018. MSc thesis. (Cited on page 75.)

[149] W. E. Johns, *Measurements of the semileptonic decay of the neutral charmed meson $D^0 \to K^-\mu^+$ muon-neutrino*, PhD thesis, Colorado U., 1995. (Cited on page 78.)

[150] F. James and M. Roos, *Minuit: A System for Function Minimization and Analysis of the Parameter Errors and Correlations*, Comput. Phys. Commun. **10** (1975) 343. (Cited on page 82.)

[151] R. Brun *et al.*, *root-project/root: v6.18/02*, 2019. doi: 10.5281/zenodo.3895860. (Cited on pages 82, 84, and 197.)

[152] R. Barlow and C. Beeston, *Fitting using finite Monte Carlo samples*, Comput. Phys. Commun. **77** (1993) 219. (Cited on pages 85, 89, 154, and 197.)

[153] L. Anderlini *et al.*, *The PIDCalib package*, LHCb-PUB-2016-021, 2016. (Cited on pages 86 and 100.)

[154] LHCb collaboration, *L0 hadron tables*, https://gitlab.cern.ch/lhcb-TrackingAlignment/l0hadrontables. (Cited on page 98.)

[155] https://twiki.cern.ch/twiki/bin/view/LHCbInternal/LHCbTrackingEfficiencies. (Cited on page 100.)

[156] CLEO collaboration, J. E. Bartelt *et al.*, *Measurement of the $B \to D\ell\nu$ Branching Fractions and Form Factor*, Phys. Rev. Lett. **82** (1999) 3746, arXiv:hep-ex/9811042. (Cited on page 109.)

[157] BaBar collaboration, B. Aubert *et al.*, *Measurement of $|V_{\rm cb}|$ and the Form-Factor Slope in $\overline{B} \to D\ell^-\overline{\nu}_\ell$ Decays in Events Tagged by a Fully Reconstructed B Meson*, Phys. Rev. Lett. **104** (2010) 011802, arXiv:0904.4063. (Cited on page 109.)

[158] Belle collaboration, R. Glattauer *et al.*, *Measurement of the decay $b \to d\ell\nu_\ell$ in fully reconstructed events and determination of the Cabibbo-Kobayashi-Maskawa matrix element $|V_{cb}|$*, Phys. Rev. D **93** (2016) 032006, arXiv:1510.03657. (Cited on page 109.)

[159] CLEO collaboration, N. E. Adam *et al.*, *Determination of the $\overline{B} \to D^*\ell\overline{\nu}$ decay width and $|V_{\rm cb}|$*, Phys. Rev. D **67** (2003) 032001, arXiv:hep-ex/0210040. (Cited on page 109.)

[160] BaBar collaboration, B. Aubert *et al.*, *A Measurement of the branching fractions of exclusive $\overline{B} \to D^{(*)}(\pi)l^-\overline{\nu}_l$ decays in events with a fully reconstructed B meson*, Phys. Rev. Lett. **100** (2008) 151802, arXiv:0712.3503. (Cited on page 109.)

[161] BaBar collaboration, B. Aubert *et al.*, *Measurement of the Decay $B^- \to D^{*0}e^-\overline{\nu}_e$*, Phys. Rev. Lett. **100** (2008) 231803, arXiv:0712.3493. (Cited on page 109.)

[162] M. Williams *et al.*, *The HLT2 Topological Lines*, . (Cited on page 114.)

[163] LHCb collaboration, `TupleToolVtxIsoln`*: Tupletool for vertex isolation*, https://gitlab.cern.ch/lhcb/Analysis/-/blob/run2-patches/Phys/DecayTreeTuple/src/TupleToolVtxIsoln.cpp. (Cited on pages 118, 139, and 206.)

[164] H. Voss, A. Hoecker, J. Stelzer, and F. Tegenfeldt, *TMVA - Toolkit for Multivariate Data Analysis with ROOT*, PoS **ACAT** (2007) 040. (Cited on page 120.)

[165] B. Garcia Plana, *Tests of Lepton Flavour Universality using semitauonic B decays in the LHCb experiment at CERN*, PhD thesis, Universidade de Santiago de Compostela, 2022, Presented 27 July 2022. (Cited on page 121.)

[166] F. U. Bernlochner *et al.*, *Das ist der HAMMER: Consistent new physics interpretations of semileptonic decays*, The European Physical Journal C **80** (2020) . (Cited on page 128.)

[167] S. Faller, A. Khodjamirian, C. Klein, and T. Mannel, *$B \to D^{(*)}$ Form Factors from QCD Light-Cone Sum Rules*, Eur. Phys. J. C **60** (2009) 603, arXiv:0809.0222. (Cited on pages 128, 131, and 228.)

[168] F. U. Bernlochner and Z. Ligeti, *Semileptonic $B_{(s)}$ decays to excited charmed mesons with e, μ, τ and searching for new physics with $R(D^{**})$*, Phys. Rev. D **95** (2017) 014022, arXiv:1606.09300. (Cited on pages 135 and 228.)

[169] F. U. Bernlochner, M. Franco Sevilla, D. J. Robinson, and G. Wormser, *Semitauonic b-hadron decays: A lepton flavor universality laboratory*, Rev. Mod. Phys. **94** (2022) 015003, arXiv:2101.08326. (Cited on pages 135, 175, and 224.)

[170] LHCb collaboration, R. Aaij *et al.*, *Precise measurement of the f_s/f_d ratio of fragmentation fractions and of B^0_s decay branching fractions*, Phys. Rev. **D104** (2021) 032005, arXiv:2103.06810. (Cited on page 136.)

[171] BESIII collaboration, M. Ablikim *et al.*, *Study of the Decay $D_s^+ \to \pi^+\pi^+\pi^-\eta$ and Observation of the W-annihilation Decay $D_s^+ \to a_0(980)^+\rho^0$*, arXiv:2106.13536. (Cited on pages 136, 137, 138, 150, 204, 205, and 214.)

[172] Particle Data Group, P. A. Zyla *et al.*, *Review of Particle Physics*, PTEP **2020** (2020) 083C01. (Cited on page 152.)

[173] T. Skwarnicki, *A study of the radiative cascade transitions between the Upsilon-prime and Upsilon resonances*, PhD thesis, Institute of Nuclear Physics, Krakow, 1986, DESY-F31-86-02. (Cited on page 152.)

[174] R. J. Barlow and C. Beeston, *Fitting using finite Monte Carlo samples*, Comput. Phys. Commun. **77** (1993) 219. (Cited on page 157.)

[175] LHCb collaboration, *LHCb PLUME: Probe for LUminosity MEasurementt*, CERN-LHCC-2021-002, 2021. (Cited on page 164.)

[176] LHCb collaboration, *LHCb SMOG Upgrade*, CERN-LHCC-2019-005, 2019. (Cited on page 164.)

[177] LHCb collaboration, *LHCb Framework TDR for the LHCb Upgrade II Opportunities in flavour physics, and beyond, in the HL-LHC era*, CERN-LHCC-2021-012, 2022. (Cited on pages 164 and 224.)

[178] LHCb collaboration, *LHCb Tracker Upgrade Technical Design Report*, CERN-LHCC-2014-001, 2014. (Cited on pages 164, 165, and 224.)

[179] LHCb collaboration, *LHCb PID Upgrade Technical Design Report*, CERN-LHCC-2013-022, 2013. (Cited on page 164.)

[180] LHCb collaboration, *LHCb Trigger and Online Upgrade Technical Design Report*, CERN-LHCC-2014-016, 2014. (Cited on page 166.)

[181] LHCb collaboration, *LHCb Upgrade GPU High Level Trigger Technical Design Report*, CERN-LHCC-2020-006, 2020. (Cited on page 166.)

[182] R. Aaij *et al.*, *A comprehensive real-time analysis model at the LHCb experiment*, JINST **14** (2019) P04006, arXiv:1903.01360. (Cited on page 166.)

[183] R. Aaij *et al.*, *The LHCb Upgrade I*, LHCb-DP-2022-002, in preparation. (Cited on pages 167 and 224.)

In The Standard Model, the coupling between the leptons and the gauge bosons is independent of the lepton generation. This is called Lepton Flavour Universality (LFU). This thesis aims to test LFU by studying two different processes involving D and B meson decays using data recorded by the LHCb experiment. The first LFU test aims to measure the branching fraction ratio $R(\mu/e)=BF(D0\to K\mu\nu)/BF(D0\to Ke\nu)$. The result, which is still blinded, presents an uncertainty of $0.003(stat)\pm0.013(syst)$. The second LFU test is a simultaneous measurement of R(D0) and R(D*0), defined as $BF(B\to D(*)0\tau\nu)/BF(B\to D(*)0l\nu)$, where $(l=\mu,e)$. This thesis presents a model implemented to study one of the main background components of this study, the inclusive $Ds\to3\pi(X)$ decays, where the Ds decays in the τ decay vertex.